

**This PDF was created from the British Library's microfilm copy of the original thesis. As such the images are greyscale and no colour was captured.**

**Due to the scanning process, an area greater than the page area is recorded and extraneous details can be captured.**

**This is the best available copy**

**D46551'83**

Attention is drawn to the fact that the copyright of this thesis rests with its author.

This copy of the thesis has been supplied on condition that anyone who consults it is understood to recognise that its copyright rests with its author and that no quotation from the thesis and no information derived from it may be published without the author's prior written consent.

**IV**

248

D 46551/83

RAY C.P

248.

Some Aspects of Crack Initiation in Mild Steel Subjected to  
Fatigue Stressing in a Corrosive Environment

by

G P Ray BSc MSc CEng MIM MICorrT MIMF

A report presented in partial fulfilment of the requirements  
of the PhD Degree of COUNCIL OF NATIONAL ACADEMIC AWARDS.

City of London Polytechnic  
Sir John Cass School of Science  
and Technology  
Department of Metallurgy and Materials  
LONDON

1983

### Abstract

Some aspects of the corrosion fatigue crack initiation in EN 1 type mild steel have been studied.

Results of the electrochemical investigations show that the application of both static and compressive stresses enhance anodic dissolution. Application of cyclic stress assists the breakdown of the surface film resulting in localised attack.

Metallographic studies indicate that a sulphur enriched band of ferrite exists around the non-metallic inclusions and corrosion occurs in this contaminated band with and without applied stress. Cyclic stress enhances the formation and coalescence of micropits at and around the inclusions leading to the nucleation of cracks. Preferential attack also occurs at the ferrite - pearlite interfaces, at slip band - matrix interfaces, and at grain boundaries. All these modes of attack can lead to crack nucleation.

It has also been found that non-metallic inclusions can act as sites for hydrogen blisters; this may assist the nucleation of cracks.

ACKNOWLEDGEMENTS

I am indebted to Dr J G N Thomas of the National Physical Laboratory and Dr R A Jarman for their continuous help and encouragement. Thanks are also due to Dr L L Shreir, Dr M Clarke and Dr C J L Booker for the provision of the laboratory facilities.

<u>Contents</u>		Page
Chapter 1	Introduction	1
Chapter 2	Literature Survey	3
2.1	Phenomenon of corrosion fatigue and its characteristics	3
2.2	Principal variables in corrosion fatigue	4
2.3	Mechanisms of crack initiation	10
2.3.1	Mechanisms under air fatigue conditions	10
2.3.2	Mechanisms under corrosion fatigue conditions, classical concepts	14
2.3.3	The effect of chloride and sulphide ions in the corrosion of carbon steels	26
2.3.4	Dissolution of iron carbides	40
2.3.5	Mechanisms under corrosion fatigue conditions, modern concepts	43
Chapter 3	Experimental	48
3.1	Introduction	48
3.2	Material	49
3.3	Electrolyte	49
3.4	Electrochemical tests	49
3.4.1	Anodic polarisation tests	49
3.4.1.1	Specimen preparation	50
3.4.1.2	Apparatus	50
3.4.1.3	Procedure	52
3.4.2	Scratching electrode tests	53
3.4.2.1	Specimen preparation	53
3.4.2.2	Apparatus	53
3.4.2.3	Procedure	54

Contents

	Page
Chapter 3.4.3 Measurement of potential inside a notch	55
3.4.3.1 Specimen preparation	55
3.4.3.2 Apparatus	55
3.4.3.3 Procedure	56
3.4.4 Measurement of potential of specimen subjected to tensile stress	57
3.4.4.1 Specimen preparation	57
3.4.4.2 Apparatus	57
3.4.4.3 Procedure	57
3.4.5 Reverse bend fatigue tests - 0.02 to 0.2 Hz	57
3.4.5.1 Specimen preparation	57
3.4.5.2 Apparatus	58
3.4.5.3 Procedure	58
3.4.6 Reverse bend fatigue tests - 24 Hz	59
3.4.6.1 Specimen preparation	59
3.4.6.2 Apparatus	59
3.4.6.3 Procedure	60
3.5 Immersion tests	60
3.5.1 Specimen preparation	60
3.5.2 Apparatus	61
3.5.3 Procedure	61
3.6 Metallurgical examination: Rotating bend fatigue tests - 47 Hz	61
3.6.1 Specimen preparation	61
3.6.2 Apparatus	61
3.6.3 Procedure	62
3.6.3.1 Scanning electron microscopic examination	62
3.6.3.2 Transmission electron microscopic examination	63

<u>Contents</u>		Page
Chapter 4	Results	65
4.1	Anodic polarisation tests	65
4.2	Scratching electrode tests	68
4.3	Measurements of potential inside a notch	69
4.4	Measurement of potential of specimen subjected to tensile stress	69
4.5	Reverse bend fatigue tests - 0.02 to 0.2 Hz	71
4.6	Reverse bend fatigue tests - 24 Hz	73
4.7	Immersion tests	75
4.8	Metallurgical examinations: Rotating bend fatigue tests - 47 Hz	75
4.8.1	Scanning electron microscopic examination	75
4.8.2	Transmission electron microscopic examination	78
Chapter 5	Discussion	85
5.1	Introduction	85
5.2	Anodic polarisation tests	85
5.3	Scratching electrode test	94
5.4	Measurement of potential inside a notch	97
5.5	Measurement of potential of specimens subjected to tensile stress	101
5.6	Reverse bend fatigue tests - 0.02 to 0.2 Hz	105
5.7	Reverse bend fatigue tests - 24 Hz	111
5.8	Immersion tests	114
5.9	Metallurgical examinations: Rotating bend fatigue tests - 47 Hz	115
5.9.1	Scanning electron microscopic examination	115
5.9.2	Transmission electron microscopic examination	131
5.10	General discussion	137
Chapter 6	Conclusion	144

## 1 INTRODUCTION

The adverse effect of corrosive environment and cyclic stress or strain on the properties of materials has been defined as corrosion fatigue. Many engineering components fail by this process. Early studies presented corrosion fatigue data in terms of conventional S-N curves without much indications of the proportion of the components' lives spent in the nucleation of cracks whereas recent investigations have mostly concentrated on the fracture-mechanical approach to crack propagation.

The nucleation event by which corrosion affects the fatigue process is still a matter of debate. In the absence of acute discontinuities the fatigue failure of ductile metals in air is known to occur in two stages, namely crack initiation stage I and crack propagation stage II. In stage I, cracking occurs along slip planes at approximately  $45^\circ$  to the applied stress whereas in stage II, the crack changes direction and travels normal to the applied stress. In a corrosive environment this two stage-process is also observed. The greatest effect of corrosion appears to occur in the crack initiation stage, and at low stresses cathodic polarisation prevents the formation of cracks at  $45^\circ$  indicating that cracks in stage I are associated with anodic dissolution of the metal. Among the various theories proposed, pitting, preferential dissolution, film rupture, adsorption of species from surrounding aqueous environment, slip-dissolution-reverse slip, and enhanced slip due to unlocking of piled-up dislocations have received considerable attention. However, none of these models has been found to be universally applicable.

It is possible that fatigue crack initiation in the presence of aggressive environments does not occur by the same mechanism for every material.

In many engineering alloys cracks may nucleate at some weakly constrained interface or at stress concentrations associated with discontinuities in the structure. However, surface discontinuities can result in significant changes in solution composition from those represented by the bulk solution. Consequently, it may be misleading to assume that surface discontinuities are only of significance in the context of stress concentration. Non-metallic inclusions present in the material may act as sites for  $H_2S$  generation and a low energy path for hydrogen diffusion in the material. Localised corrosion also rapidly occurs in the vicinity of the non-metallic inclusions developing voids or micropits. The crevices and subsequent pits appear to serve as sites for the nucleation of cracks. In this context it appears that a study of the electrochemical behaviour and of the changes in surface topology of the metal subjected to cyclic strain is of major importance in corrosion fatigue.

The present investigation is concerned with some aspects of crack initiation in smooth surfaced EN 1 type mild steel specimens in 0.6 M sodium chloride solution at room temperature. The aim of the work was to investigate the electrochemical changes that occur during corrosion fatigue over a range of cycling frequencies and to examine the changes in surface morphologies at 47 Hz, by using optical, scanning and transmission electron microscopy. The thesis presents the results of this investigation.

## 2. LITERATURE SURVEY

### 2.1 Phenomenon of Corrosion Fatigue and its Characteristics

Corrosion fatigue is a failure mode of metals and alloys due to the combined action of cyclic stress or strain and an aggressive environment. The damage due to this combined action is greater than the sum of the damage arising from cyclic stresses and that due to corrosion. That is, a specimen subjected to air fatigue prior to introduction into an aggressive environment does not necessarily exhibit an increased corrosion rate, nor does a pre-corroded specimen show appreciable reduction in fatigue life when it is subjected to a cyclic stress.

The first reported observation of corrosion fatigue was mentioned by Haigh<sup>1</sup>. McAdam<sup>2-5</sup> systematically investigated the effect of aggressive environment on fatigue life of metals and termed the failure due to the combined action of corrosion and cyclic stresses as "corrosion fatigue".

Much of the earlier work was concerned with the accumulation of data for different materials in a variety of corrosive environments. Between 1939-1965, some important researches were performed by Evans and his co-workers on electrochemical aspects of the subject. Extensive reviews of these and earlier works were made by Gough<sup>6</sup>, Gould<sup>7</sup>, Gilbert<sup>8</sup>, Waterhouse<sup>9</sup>, Duquette<sup>10,11</sup>, and Pelloux et al<sup>12</sup>. In recent years, interests have generated mainly due to North Sea oil and submarine failure problems and the subject is receiving a great deal more attention<sup>13-16</sup>.

Corrosion fatigue is characterised by a reduction of endurance values compared with that obtained in air. In steels, a fatigue limit is not observed and hence failure is possible even at very low stresses.

According to Gilbert<sup>8</sup>, other characteristics are:

- i) Corrosion fatigue cracks are usually transcrystalline, although in some cases these may be intercrystalline.
- ii) Corrosion fatigue usually produces a large number of cracks on the surface.
- iii) Corrosion fatigue in immersed condition is an electrochemical phenomenon, as shown by cathodic protection or by adding suitable inhibitors to the corroding solution.
- iv) Corrosion fatigue limits are often relatively insensitive to changes in metallurgical conditions, such as those produced by cold working and heat treatment.

## 2.2 Principal Variables in Corrosion Fatigue

The principal variables may be described as temperature, pH, potential, frequency, loading mode, alloying and heat treatments, presence of oxygen, salt concentration, mean stress and tensile strength.

### a) The effect of temperature

The effect of temperature on corrosion fatigue failure was investigated by Gould<sup>17</sup>. He found that the fatigue life of mild steel was considerably reduced in the  $10^7$  cycle range with the rise in temperature from 15 to 35°C. Cornet and Golan<sup>18</sup>, however, observed that in 0.4M sodium chloride solutions, drill rod showed improved performance at temperatures around the boiling point of water.

They suggested that this improvement was due to the uniform distribution of shallower pits and that the ratio of cathodic areas was higher at lower temperatures. Watanabe and Mukai<sup>19</sup> reported that in mild steel specimens immersed in 0.6M sodium chloride solutions, an increase in temperature from 20 to 50°C resulted in a 50% reduction in cycles to failures. However, the tests were carried out at very high cyclic stress level ( $\pm 460$  Mpa,  $R = -1$ ) and may not be applicable for low stress - long life specimens.

b) The effect of pH

Simnad and Evans<sup>20</sup> studied the effect of pH on the corrosion fatigue behaviour of steel and observed that greater damage was caused in 0.1M HCl than in neutral KCl solution. Radd et al<sup>21</sup> found a "fatigue limit" of mild steel in 0.6M sodium chloride solution at pH 12.1 and above, and suggested that "corrosion fatigue" is a result of differential aeration cells producing pits on the metal surface and that a high pH provided diffusion barriers to oxygen set up by ferrous hydroxide films on the surface. Duquette<sup>22</sup> observed that in 0.5M sodium chloride solution there was a rapid reduction in life of low carbon steel as the pH fell below 4 and a marked increase in life where pH was increased above 10. The specimen endurance appeared to be nearly constant between pH 4 to 10 for a given stress range.

c) The effect of frequency

Corrosion fatigue is influenced by the frequency of cyclic stressing since corrosion is time dependent.

Endo and Miyas<sup>23</sup> studied the effect of frequency on 0.44% carbon steel specimens in tap water and 0.2M sodium chloride solution and observed that endurance limit was reduced when the frequency was lowered. However, reduction of frequency from 42.5 Hz to 4 Hz showed an increase in the time to failure.

Watanabe and Mukai<sup>19</sup> found that for mild steel notched plate specimens in a dripping 0.5M sodium chloride solution, the number of cycles to failure, for frequencies less than 1.7 Hz, decreased as the cyclic frequency was reduced. If the frequency was lowered sufficiently, the number of cycles to failure approached a constant value.

In general, a reduction of frequency under corrosion fatigue conditions will reduce the number of cycles to failure but will increase the time to failure. If the frequency is reduced sufficiently, the number of cycles to failure becomes independent of frequency.

d) The effect of loading mode

The fatigue strength in a corrosive atmosphere is also affected by the method of testing. Endurance values of steel in sea water were found to be considerably higher in direct tension tests than those obtained in rotating beam or reverse bend type of tests<sup>9</sup>.

Gough and Sopwith<sup>24, 25</sup> obtained ratios of fatigue strength at  $50 \times 10^6$  cycles in direct tension against bending tests of 0.86 to 1.26 for steel in a salt spray environment. Gould<sup>26</sup>, however, observed that for steel in seawater, endurance was several times as great in direct tension as in bending.

Knight<sup>27</sup> quoted results of tests in air on 12.7 mm thick steel cantilever specimens with longitudinal no-load-carrying fillet welded joints. Evidence indicated that the bending specimens had fatigue lives between 3 to 4 times as long as axially loaded equivalent specimens. A similar effect was noted for four welded specimens fabricated from 38 mm thick plate, but other evidence obtained from 25.4 mm and 38 mm thick welded bending specimens indicated no increase in life compared with axially loaded specimens. Bending tests on cantilever welded specimens in salt solutions gave fatigue lives greater than those normally associated with equivalent specimens subjected to axial loading and tested in air which appeared to indicate that the loading mode could have a significant effect on endurance values for specimens tested under corrosion fatigue conditions<sup>26, 27</sup>.

e) The effect of alloying and heat treatment

Alloying and heat treatment normally have little effect on the corrosion fatigue behaviour of steels unless corrosion resistance is improved. Hence, the use of low alloy steels and high carbon steels is not beneficial in most corrosive media, whereas in air, their fatigue limit increases directly with their ultimate tensile strength<sup>10</sup>. This has been confirmed by the work on mild and low alloy steels in river water<sup>28</sup> and that on marine piston rods in sea water<sup>29</sup>.

f) The effect of Oxygen

The presence of dissolved oxygen influences the corrosion fatigue characteristics. Binnie<sup>30</sup> observed that the fatigue life of 0.33 C steel was reduced if the sodium chloride solution was dripped through air instead of through purified hydrogen. Duquette and Uhlig<sup>22</sup> investigated the influence of dissolved oxygen on the fatigue behaviour of 0.18% carbon steel in distilled water and in 0.5 M sodium

chloride solution. Their results show that the deaeration of the media caused the reappearance of a fatigue limit indicating that the presence of dissolved oxygen is necessary for corrosion fatigue to occur. However, chloride ions alone in deaerated solution can lower fatigue life although it does not affect the fatigue limit<sup>22</sup>. This tendency for the fatigue limit to reappear in completely deaerated sodium chloride solution was also observed by other investigators<sup>31</sup>. Their results showed that complete deaeration of the sodium chloride solution caused a reappearance of the fatigue limit observed in dry air tests, indicating that dissolved oxygen is essential to the corrosion fatigue mechanism in neutral pH solution.

Conflicting evidence regarding the effect of oxygen was provided by Watanabe and Mukai<sup>19</sup>. They tested notched mild steel specimens in sea water, with air, oxygen, and argon bubbled through it, for a relatively low values of endurance ( $10^5$  cycles), and observed little difference in the S-N relationship. It is possible that the expulsion of dissolved oxygen by the bubbling of argon does not act as a method for reducing corrosion fatigue, even though it may reduce the corrosion rate of the surface considerably. Type of specimen, i.e. notched or plain, may also have a bearing on the apparent difference in results<sup>27</sup>.

g) The effect of salt concentration

The effect of salt concentration on fatigue behaviour of steels were studied by McAdam<sup>4, 5</sup>, Gould<sup>17</sup>, and by Cornet and Golan<sup>18</sup>. Gould studied the effect on mild steel in distilled water and in various concentrations of KCl and observed that solutions ranging from 2 M to 1/40 M had similar effects on corrosion fatigue, but with concentrations below 1/40 M the effect approached that of distilled water.

McAdam investigated the effect of hard well water, soft water, river and fresh water. The well water contained 100 ppm  $\text{CaCO}_3$ , 100 to 200 ppm chloride and 50 ppm sulphate. There were 30 ppm sulphate and 5 ppm chloride in the soft water. The river water had one sixth to one third the salinity of sea water whereas the fresh water contained up to 20 ppm alkalinity and 5 ppm chloride. The results indicated that the hard and soft water were about equally damaging while the salt water was considerably more damaging than the fresh water.

Endo and Miyas <sup>23</sup> investigated the S-N relationship in tap and salt water at the same cycle frequency and observed that fatigue strength was reduced considerably in salt water environment.

h) The effect of mean stress

Ohuehida, quoted by Knight <sup>27</sup>, performed bending fatigue tests on plain cantilever specimens of 20 mm thick high strength steel plate and found that mean stress had a profound effect on fatigue strength. The effect of reducing the mean stress from half the stress range ( $R = 0$ ) to zero ( $R = -1$ ) was to increase the fatigue strength stress range, at  $2 \times 10^6$  cycles, by 36% for specimens tested in dripping fresh water and 26% for those tested in air. He also showed that, at  $10^7$  cycles, the corrosion fatigue strength increased by a factor of approximately 4 as the mean stress was reduced from a tensile value of 392 MPa to a compressive value of 98 MPa. However, the relationship between mean stress and corrosion fatigue strength is not linear. He plotted stress range values appropriate to  $5 \times 10^6$  cycles against mean stress and found that tensile mean stress had little effect on corrosion fatigue strength, unless part of the cyclic waveform became compressive, whereas an increase in tensile mean stress for plain specimens tested in air resulted in a significant reduction in fatigue strength.

However, when the mean stress was compressive, a significant increase of corrosion fatigue strength was noted.

j) The effect of tensile strength

In rotary bending tests for  $10^7$  cycles, Kitagawa<sup>32</sup> observed that the fatigue limit for specimens tested in air was dependent on tensile strength while in tap water, tensile strength had very little effect on the fatigue limit.

Knight<sup>27</sup> observed that in dripping salt water, "there is no fatigue benefit to be gained from using material with the higher tensile strength". Higher strength steels also had lower corrosion fatigue strength at high endurance values.

k) Potential

This is considered in the subsequent sections.

2.3 Mechanisms of crack initiation

2.3.1 Mechanisms under air fatigue conditions

Earlier investigations on crack initiation have been reviewed by Thompson and Wadsworth<sup>33</sup>. Most of these studies were made by using optical microscopy. These works suggested that slip steps developed on the metal surface during fatigue process and with increased number of cycling, the active planes became concentrated into slip bands from which cracks developed<sup>34-37</sup>. It was found that in alpha-iron the slip bands had a rather different appearance from the fcc metals in that the slip was more wavy and that fatigue cracks formed in the positions of maximum resolved shear stress<sup>36</sup>. Thompson et al<sup>37</sup> showed that the crack nucleation was a surface phenomenon and occurred early in life when lives were long and the material was pure.

Smith<sup>38</sup> observed that in aluminium at low stresses, the persistent slip bands, or incipient cracks, appeared dotted. If the stresses were reduced further this feature became more pronounced. These dots were found to be pointed pits, a few microns deep on the surface. Similar markings were also observed by other investigators<sup>39-41</sup>. It was envisaged that these pits represented an early stage of crack formation and later on in the test these linked up to produce macroscopic surface cracks.

Ewing and Humphrey<sup>34</sup> observed that the surface of the broad slip bands frequently rose above the surface of the surrounding material but the rise was gradual and progressive across the band. This phenomenon was observed by Forsyth and other investigators<sup>42-45</sup>. They concluded that the extrusions and the reverse of extrusions - intrusions formed by relative slips on parallel planes within the slip bands and that the intrusions extended into cracks.

These earlier studies identified that plastic strain was a prerequisite for fatigue, and localisation of strain was most effective in nucleating cracks.

Much of the recent work has been summarised by Grosskreutz<sup>46</sup> and Laird and Duquette<sup>11</sup>.

The taper sectioning technique - a modern development - has shown that the embryonic cracks, observed in the earlier work, develop by void formation in the slip bands below the notch<sup>47</sup>. Later work<sup>48</sup> has established that the supposed voids are, however, continuation of tubular holes extending from the surface of persistent slip bands.

The dislocation structure associated with the slip bands have been investigated and the general conclusion is that a dislocation cell structure is always associated with the bands <sup>49, 50</sup>. The slip bands appear to grow by a series of dislocation avalanches on selected slip planes <sup>51</sup>.

The persistent slip band develops where the saturated stage of hardness has been established. Seger, quoted by Laird <sup>11</sup>, has suggested that the interaction between dislocations and clustered vacancies, i.e. dislocation loops, during fatigue deformation lead to the concentration of slip on a relatively small number of persistent glide bands. During saturation the dislocation array is unstable. A local increase in the stress can be expected to trigger the release of stored dislocations by the agency of a single free dislocation and thus to form a persistent slip band. The trigger for releasing the avalanche can be provided by local stress concentrations caused by random slip effects either at the surface, or at grain boundaries on the surface. The latter are particularly favoured because persistent slip bands in fatigue frequently start at grain boundaries and develop transgranularly <sup>11</sup>.

Cottrell and Hull <sup>52</sup> proposed a duplex slip mechanism for metals which can exhibit slip on more than one set of planes under test conditions and consequently form extrusions and intrusions by one full cycle of stress. This is based on the mechanical movement of atoms by assuming that two intersecting slip planes operate sequentially during both the tension and compression halves of the stress cycle. This mode predicts a close association between extrusions and intrusions. Theoretically, these will appear in neighbouring slip bands whereas in practice they appear to occur together in the same band <sup>53</sup>.

Other models leading to the formation of extrusions and intrusions <sup>54-56</sup>, and crack initiation <sup>57</sup> have been proposed, and these have been summarised by Kennedy <sup>53</sup>.

Wood <sup>47</sup> has suggested that slip causes significant changes in local surface contours and the formation of surface microcracks is primarily a geometric consequence of to and fro slip movements within broad slip bands.

In many materials containing more than one phase, fatigue crack initiation takes place by means of mechanisms similar to those observed for pure, single phase materials. Low carbon steels exhibit slip bands and grain boundary cracking <sup>46</sup>. In commercial multiphase alloy materials, however, other mechanisms may also occur. Two of the mechanisms have received recent attention <sup>58-60</sup>. The first involves re-resolution of the second phase precipitate which normally provides strength. The second relies on the presence of undissolved second phase or impurities which provide a local stress concentration for the nucleation of cracks.

If a second phase precipitate can be sheared by a dislocation, then the possibility exists that repeated back and forth motion of dislocations in fatigue will reduce the average precipitate size to a point at which the second phase reverts into solid solution. Such behaviour has been observed in high purity Al-Cu and Al-Zn-Mg systems <sup>58-60</sup>. It has been suggested that the process starts in slip bands where the activity of the dislocation is high, and spreads as the bands widen and multiply. The material is softened due to the reversion of the precipitate. This aids the development of the slip band and shortens the period required to initiate cracks therein. Reversion by shearing of carbide precipitate in low carbon steels has been observed during fatigue <sup>60</sup>.

The most common site for crack initiation in commercial material is the non-coherent particle which intersects the surface. These particles may be undissolved second phases, impurities, or the products of improper heat treatment. Prior to crack initiation, the stress concentration around some second phases causes concentrated slip bands to develop. Fatigue cracks, however, do not initiate in these bands<sup>46</sup>. Cracks initiate at the matrix - second phase interface around which no visible slip occurs. It has been reported that examination of the as-received material failed to reveal any significant number of pre-cracked second phase from which fatigue cracks could begin<sup>46</sup>. It is envisaged that the interfaces are probably weak and consequently provide suitable nuclei for crack initiation. Tiny voids at the interface were noticed during fatigue tests<sup>46</sup>. Continued cycling opened these voids until they became propagating fatigue cracks. The crack initiation mechanism appeared to be one in which disbonding of the interface occurred without the assistance of detectable plastic deformation. The larger second phases and clusters of these constituents are normally favoured sites, possibly because the interface is weaker.

In pearlitic steel, 0.78% C, Taylor et al<sup>61</sup> found a build up of dislocations in the ferrite during cycling. These researchers observed that in both fine and coarse lamellar pearlitic structures, the major initiation sites were slip bands, ferrite-cementite interfaces and pearlite cell boundaries. In spheroidal carbide material, the sites were slip bands and ferrite grain boundaries.

### 2.3.2 Mechanisms under corrosion fatigue conditions: classical concepts

Theories concerning the crack initiation process in aqueous environment can be divided into five principal categories involving pitting,

preferential dissolution of plastically deformed areas of metal with undeformed areas acting as cathode, electrochemical attack at ruptures in an otherwise protective surface film, reduction of surface energy of the metal due to environmental adsorption and increased propagation of microcracks, and hydrogen embrittlement.

a) Pitting mechanism

One of the earliest proposed mechanisms of corrosion fatigue is the concept of corrosion-induced pit formation and the concentration of stress at the base of the pits. This mechanism was based on the experimental evidence by McAdam and co-workers<sup>4, 5</sup> who observed that pre-corroded steels in soft and hard waters had lower fatigue limits and that the fatigue cracks originated from the pits on the surface. However, corrosion fatigue also occurs in environments where pitting does not occur, e.g. low carbon steels in acid solutions<sup>11</sup>. In addition, the fatigue life of steel specimens can be reduced by the application of small anodic currents in deaerated solutions in which pits do not form. Fatigue tests performed in 0.5 M sodium chloride + sodium hydroxide solution at pH 12, where only a few randomly distributed pits are observed, exhibit fatigue limits similar to those observed in air. Laird and Duquette<sup>11</sup> suggested that results of this type are not unexpected since corrosion induced pits tend to be hemispherical in nature and the stress concentration factor associated with surface-connected hemispherical pits is not large.

In low carbon steels fatigued in neutral sodium chloride solution, Duquette and Uhlig<sup>62, 63</sup> observed deep pit-like configurations oriented at approximately 45 degrees to the specimen surface. However, no cracks were found to emerge from such pits.

Examination of specimens cycled for longer periods showed that the extent of growth of initiated fatigue cracks was always equivalent to pit depth, with no fatigue cracks associated with pits. At large numbers of cycles, branched fatigue cracks are associated with surface pits but, at these cracks lengths, the problem is one of propagation and not initiation. It has been suggested that pits are the result and not the cause of corrosion fatigue cracking. The cracks are initiated and then broadened by the corrosive environment to produce the evidence of pit associated cracking reported by previous investigators <sup>63</sup>.

Although it is difficult to prove which came first, the pits or the cracks, there is evidence in some cases that pits act as precursors for crack initiation. Rollins et al <sup>14</sup> observed that the corrosion fatigue fractures in 1% C, 1% Cr steel occurred in a number of stages involving pitting. These investigators suggested that the corrosive solution provides the initial pit and allows rapid removal of dynamically yielding metal from the tip, thereby controlling the initial stages of the corrosion fatigue processes. Jack and Peterson <sup>64</sup> observed that pits were precursors and were critical stress raisers for crack initiation process, and suggested that pits were present without cracks and the cracks were associated with pits in the failure of rotor shafts. It has also been suggested elsewhere that pits can act as stress raisers and reduce the fatigue limit <sup>65, 66</sup>.

b) Preferential dissolution mechanism

This theory suggests that the deformed areas, such as regions of intense slip, act as anodes whilst the undeformed part of the metal behaves as a cathode <sup>67</sup>. The effect of cold work on corrosion rate is thought to be associated with the increase in dislocation density,

and the inherent reactivity of the screw dislocations at a metal surface, relative to the undislocated lattice has been shown by etch pitting studies<sup>68, 69</sup>. It has been suggested that etch pits occur in pure metals because the spiral lattice arrangement around a screw dislocation ensures that an edge is maintained as the metal dissolves. Segregation and precipitation of impurities may take place preferentially in the strained lattice around dislocations resulting in the development of local corrosion cells and pitting at individual dislocations<sup>70, 71</sup>. Cabrerra and Levine<sup>72</sup> have shown that dissolution is easier from sites on the slip steps produced by deformation than from the unstepped crystal surface. These reserchers also suggested the presence of kinks on the slip steps and emphasised that these areas were more active than other sites on the slip steps.

The changes in the corrosion rate of metals subjected to prior deformation has been extensively investigated. Whitwham and Evans<sup>73</sup> observed that prior deformation on annealed and cold worked steel wires had no effect on the number of cycles to failure in acid solutions. The principal cause of failure was the transgranular cracks which originated in slip bands at the steel surface. A small percentage of intergranular cracks was also observed. From these observations, the authors concluded that the failure was caused by distorted metal acting as anode with undeformed metal as cathode. Very fine cracks then advanced by a combination of electrochemical and mechanical action. They also suggested that when the cyclic stress was applied, atoms at the crack tip became electrochemically more active, i.e. were in a higher energy state, relative to the atoms in the specimen body. Therefore, the cyclically deformed metal at the crack tip dissolves preferentially and crack growth is accelerated.

Electrochemical heterogeneity has also been proposed to explain the corrosion fatigue phenomenon. Lihl<sup>74</sup> has suggested that slip band precipitation of impurities is induced by cyclic deformation of alloys and this increases electrochemical reactivity. It has also been reported that electrochemical heterogeneity arose during cyclic stressing creating conditions for increased attack<sup>10</sup>. Prior deformation, on the other hand, had no appreciable effect on corrosion fatigue behaviour<sup>11</sup>. Hence it has been suggested that some dynamic process produces preferential dissolution of slip bands resulting in premature crack initiation. Changes in electrochemical corrosion potentials in the active direction during early stages of corrosion fatigue tests have been reported in support of the deformed - undeformed galvanic couple theory<sup>11</sup>. Spahn<sup>75</sup> attributed the shift in potential to localised corrosion occurring at emerging anodic slip steps. Crack initiation itself was not attributed directly to preferential dissolution, but rather to a corrosion created notch resulting in a sufficient stress concentration to initiate mechanical cracking. Laird and Duquette<sup>11</sup> quoted Evans and Simnad's observation on a potential shift which was attributed to one or more of three possibilities: a depolarisation of both anodic and cathodic sites, the anodic shift being more dominant: a reduction of the electrolyte path between local anodes and cathodes: and a shift of the open circuit potential of local anodic areas in the active direction due to the energy increase of plastic deformation.

The corrosion of iron and steels in oxygen containing neutral solutions is independent of cold work since under these conditions corrosion is controlled by the diffusion rate of dissolved oxygen in solution and is independent of metallurgical variables<sup>76</sup>.

However, when the corrosion reaction is the activation controlled reduction of hydrogen ions, which is markedly influenced by metallurgical variables<sup>136</sup>, the effects of plastic deformation are quite evident. Foroulis and Uhlig<sup>77</sup> found no effect of cold work on the corrosion rate of pure iron in acids but observed that pure iron containing carbon and nitrogen behaved in a similar manner to mild steel, i.e. corrosion rates were accelerated in acid solutions. They attributed increased corrosion rates to a subdivision of low overvoltage impurities due to deformation thus increasing the efficiency of the cathodic processes.

Green and Saltzman<sup>78</sup>, however, observed that plastic deformation had a marked effect on the corrosion rates of pure iron wire provided that the degree of deformation was extremely large. They attributed this to an increase in the number and/or the activity of the dislocations at the surface which acted as sites for anodic dissolution due to the lower bonding energies of iron atoms at these points.

Finley and Myers<sup>79</sup> observed that formation of passive films was more difficult on cold worked materials than on annealed materials and passivating currents were also higher. It is possible that due to the strain field, the surface films on the cold worked materials had a higher concentration of defects which could lead to higher ionic diffusion rates.

Doruk<sup>80</sup> studied the effect of alternating stresses on the polarisation of mild steel in acid solutions. The slope of the linear polarisation curve was found to increase with fatigue cycling indicating a decreasing tendency of the material to polarise and

this was accompanied by a continuous shift of the corrosion potential to a less noble value. In addition, there was an abrupt change in the rate at which the polarisation slope changed with time. The initial increase in the slope was ascribed to the increase in the number of intrusions and extrusions with continued deformation indicating an increase in the number of anodic sites. It was assumed that local action cells were created by the process of deformation with the tip of intrusions acting anodically. It was also suggested that the surface roughened and enlarged due to deformation and had a lower hydrogen overvoltage due to its improved catalytic activity. The sudden change of the slope in the polarisation curve was considered to be associated with the transition from crack initiation to crack propagation.

Duquette and Uhlig<sup>62, 63</sup>, in their investigation on the corrosion fatigue properties of 0.18% C steel in 0.5 M sodium chloride solution observed that a minimum critical corrosion rate was necessary to produce corrosion fatigue failure. The critical current density was found to be 2 micro-amp/sq cm, which was equivalent to an average removal of  $1 \times 10^{-4}$  atom layers across the surface per stress cycle. Assuming that the dissolution occurred preferentially at the slip steps they concluded that the area of active slip step sites was small compared with the remainder of the surface. Laird and Duquette<sup>11</sup> also suggested that the dissolution process in corrosion fatigue was located at slip steps produced at the surface. The dissolution effectively unlocks otherwise blocked slip and accelerates extrusion - intrusion phenomena, thus leading to crack initiation and initial growth.

Uhlig<sup>81</sup> suggested that the effect of dissolution above a critical corrosion rate was to induce or accelerate plastic flow of the stressed metal and hence facilitate the formation of intrusions and extrusions resulting in fatigue damage. It has been shown that dissolution can accelerate the creep rate of copper<sup>82, 83</sup>. This was attributed to the formation of divacancies which diffused into the metal to aid dislocation climb.

To examine the effect of dynamically imposed deformation on corrosion behaviour Duquette and Uhlig<sup>62, 63</sup> potentiostatically applied cathodic potential on low carbon steel specimens which were subjected to high cycle fatigue tests at above and below the air-fatigue limits. These researchers observed that in both neutral and acid solutions, polarisation to the calculated open circuit, i.e. equilibrium, potential reestablished the fatigue curve obtained in air. It was concluded that the application of a cathodic potential prevented crack re-initiation below the fatigue limit and that the mechanism proposed by Evans and Simnad was not relevant. Laird and Duquette<sup>11</sup> suggested that if the crack initiation sites were more active due to temperature effects or if the deformed metal were more anodic than the undeformed part, then a more active cathodic potential would be required to prevent crack initiation. Although the possibility that anodic and cathodic depolarisation occurs can not be discounted by potentiostatic experiments, the fatigue life of steels in deaerated solution and under carefully controlled anodic current indicates that the total fatigue life compares directly with specimens cyclically stressed at the normal corrosion potential. Hence it is concluded that a higher corrosion rate does not occur in cyclically fatigue steels and that polarisation is not affected<sup>11</sup>.

Rollins et al <sup>14</sup> used the two stage technique of Simnad and Evans <sup>84</sup> to investigate the corrosion fatigue properties of high carbon steel in sodium chloride solutions of varying concentrations and concluded that corrosion was more important in the initiation stage and the essential stages of crack initiation involved pitting and cyclic strain enhanced dissolution.

c) Film rupture mechanism

According to this mechanism, the surface film formed on exposure in aqueous environments is ruptured by slip steps. This newly emergent surface becomes anodic to the large oxide film acting as the cathode. Laute, quoted by Duquette <sup>10</sup>, observed that low test frequencies prolonged fatigue lives probably by allowing repair of the film and thereby reducing anodic dissolution of bare metal. Simnad and Evans <sup>84</sup> also suggested the possibility of a film rupture mechanism in neutral solutions. They concluded that this mechanism did not apply in acid solutions since oxide films are soluble. In addition, in sodium hydroxide + sodium chloride solutions of pH 12 where steels show passive behaviour indicating the presence of a surface film of probably absorbed  $\text{OH}^-$ , the fatigue limit is unaffected <sup>63</sup>. It has also been observed that the electrode potential of a steel drops significantly in fatigue tests with a high rate of change being observed at higher stresses. <sup>10</sup>. This potential fall continues during a particular alternating stress experiment, but reaches a steady state in static tests. Continuous reduction of electrode potential has been attributed to the opening of microcracks and the destruction of a protective film. Furthermore, it had also been observed that when a grooved specimen is subjected to alternating stress, the bottom of the groove tends to be anodic relative to the sides of the notch and to the surface of the specimen.

Laird and Duquette <sup>11</sup> have also suggested that even where cathodic films are present, the stresses generated by high cycle fatigue tests either are not sufficient to rupture the surface films or slip bands emerge at low enough rates so that film repair takes place more rapidly than the occurrence of corrosion damage due to a galvanic couple between freshly emerging metal and the film.

d) Adsorption mechanism

The influence of adsorbed species from a surrounding aqueous environment on the mechanical properties of solids and its relevance to fatigue behaviour have been discussed by Benedicks <sup>85</sup>. He suggested that the tensile and fatigue strengths could be reduced by wetting the surface with water or alcohol but be increased with organic agents. The liquid wetting the surface reduces the surface energy causing a dilation of the solid body. The subsequent deformation is thereby made easier, the effect increases with increasing surface tension of the liquid. This theory, based on the reduction of surface energy, has received considerable attention from Russian investigators, such as Rebinder and co-workers, and Karpenko <sup>10</sup>. The Rebinder mechanism proposed preferential adsorption of surface active agents in pre-existing microcracks on the metal surface with consequent build up of pressures in the cracks. This creation of large pressures would allow the cracks to propagate at a reduced stress level. This mechanism was later modified to include a reduction of surface energy due to the adsorbing species and an ease of production of slip bands at the surface in the presence of surfactants <sup>11</sup>.

The Rebinder effect has been explained differently by other workers<sup>86-89</sup>. In their investigation on creep properties of zinc and cadmium wires, these researchers suggested that the reduction of creep strength was due to an environmental dissolution of a strong, adherent surface oxide by a liquid environment. In the absence of aqueous environment, the oxide film appears to act as a barrier to the emergence of dislocations, and hence, slip step formation, and exerts sufficient back stresses in the slip planes to significantly strengthen the metal. Liquid environments, particularly acids, dissolve the film and allow the slip process to occur more easily at the surface. According to Laird and Duquette<sup>11</sup>, this mechanism cannot be accepted as a universal explanation to the Rebinder effect since a similar phenomenon is observed in gold where oxide film does not exist.

This mechanism although attractive does not, however, explain why initiation of a crack in steels in neutral solution is influenced by deaeration even when strongly adsorbing, e.g. chloride ions, are present. Significant changes in fatigue behaviour of mild steel were observed by very small impressed currents in deaerated salt solutions<sup>62, 63</sup>. The fatigue behaviour was found to be independent of corrosion rate only at moderate or at high current densities. Kramer<sup>90</sup> suggested that the Rebinder effect was observed because the surface active species caused significant dissolution initially. The explanation of the effects may then be associated with the requirements of a minimum corrosion rate for corrosion fatigue crack initiation, as suggested by Duquette and Uhlig<sup>63</sup>, higher dissolution rates above the critical value having little additional effect<sup>91</sup>.

e) Hydrogen absorption mechanism

The first evidence that hydrogen may be responsible for corrosion fatigue failure was observed by Simnad and Evans<sup>20</sup> who reported that in acid solutions cathodic polarisation was not effective in preventing failure of mild steel. Other investigators<sup>92-95</sup> have also suggested the role of hydrogen in corrosion fatigue failure. Liddiard et al<sup>92</sup> observed that in the absence of cathodic polarisation, and with zero mean stress, cracks developed initially at  $45^\circ$  and grew later to an angle of  $90^\circ$ . Cathodic polarisation was found to prevent the formation of cracks at  $45^\circ$ . However, corrosion fatigue life was increased due to an increase in the number of cracks at  $90^\circ$ . If the mean stress was equal to three times the alternating stress, cracks only appear at  $90^\circ$  even in the absence of cathodic polarisation. In this case, cathodic polarisation did not prolong corrosion fatigue life<sup>95</sup>. It was concluded that cracks at  $45^\circ$  were connected with anodic dissolution at the tip of the crack while cathodic reaction, if it was oxygen reduction, occurred on the surface of the metal outside the crack. Cracking at  $90^\circ$  was considered to be associated with hydrogen evolution which would explain why cathodic protection was not effective in prolonged corrosion fatigue life. The amount of hydrogen produced on the external surface would have been increased by cathodic protection. It has been suggested that hydrogen can diffuse into microcavities beneath the surface and, under the action of a mean tensile stress, can develop the cavity into a crack perpendicular to the applied stress. Holshouser and Bennett<sup>96, 97</sup> observed evolution of hydrogen bubbles in aluminium alloys whenever the stress range used was sufficient to produce cracking. In the absence of moisture, or if the stress was too low for cracking, evolution of hydrogen was not observed.

Jackson<sup>98</sup> reported that stress increased the diffusion rate of hydrogen in steels and the rate was also faster in regions of cold work<sup>99</sup>. Hence, hydrogen may be expected to diffuse rapidly in the regions where fatigue deformation has taken place.

Recent investigations<sup>100-102</sup> in connection with offshore technology have demonstrated the beneficial effects of cathodic protection in reducing the risk of corrosion fatigue failure. Conflicting evidence, however, was provided by Watanabe and Mukai<sup>19</sup>. They observed that under high strain and low frequency conditions, cathodic protection was ineffective in improving endurance. It was suggested that under these conditions, hydrogen embrittlement occurred.

### 2.3.3 The effect of chloride and sulphide ions in the corrosion of carbon steels

There is no generally accepted explanation for the role that the chloride ion plays in the corrosion of iron. The environmental effects, including the presence and concentration of various anions in the corrosion process, are considered to be important. These have been reviewed by Foley<sup>103</sup>.

The halogen containing ions, such as chlorides, are almost always associated with the pitting of metals and alloys. Chloride is one of the most aggressive of the halogen containing anions and gives rise to pitting particularly in near neutral solutions, as strongly acid solutions are conducive to uniform attack. Pits tend to initiate at grain boundaries<sup>104</sup>, sub-grain boundaries and also inside sub grains<sup>105</sup>. On the surface of passivated iron, pits nucleate quite randomly<sup>106</sup>. For commercial steels, however, pits tend to initiate at metallurgical inhomogeneities<sup>107-119</sup>. Sulphide inclusions are the most effective initiators of pits in mild steel.

In 1933, Tronstad and Sejersted<sup>120</sup> examined the effect of varying sulphur content in a carbon steel and found that in sodium chloride solution, anodic attack occurred on the metal immediately around certain sulphide inclusions leading to localised corrosion. Their results suggest that active sites consist of sulphides of manganese and iron. These investigators, however, considered that the localised attack at sulphide inclusions occurred because of the presence of crevices of capillary size which formed due to the differences in the thermal expansion or lack of proper adhesion between the metal and the sulphide.

Sulphur has been known to exert a more or less detrimental influence on the corrosion of steel, especially in acid solution<sup>121</sup>. Stern<sup>122</sup> investigated the effect of alloying elements commonly found in steel when added to pure iron exposed to 0.1 M citric and malic acids, and 0.7 M sodium chloride solution at pH 1 and 3. He observed that sulphur, phosphorus, and carbon were detrimental to corrosion resistance. However, copper and manganese were effective in reducing the damaging effect of sulphur.

Wranglen<sup>108</sup> reinterpreted the results obtained by Stern<sup>122</sup> and observed that (1) when sulphur was added the dissolution rate of pure iron increased in acids due to the "couple action Fe (of high sulphur content) - FeS, resulting in pitting", and (2) the dissolution of FeS in acids released sulphide ions which adsorb on the metal surface and catalyse the anodic dissolution reaction. Additions of manganese or copper to pure iron per se accelerates the dissolution rate but counteracts the detrimental effect of sulphur by reducing the sulphur content in solid solution in Fe.

In the case of manganese addition, the sulphur content of the ferrite is reduced by the formation of manganese sulphide. Although MnS is nearly inert electrochemically due to its low conductivity, and FeS, a good electronic conductor with low hydrogen overvoltage, is an efficient cathode, MnS is more soluble in acids than FeS. Addition of copper counteracts the second reaction by reacting with sulphide ions to form  $\text{Cu}_2\text{S}$  which is insoluble in acids and, although conducting, is not quite active as a local cathode<sup>108</sup>.  $\text{Cu}_2\text{S}$  may not form as a separate phase. However, copper enriches sulphide inclusions. Salmon Cox and Charles<sup>123</sup> observed that in a steel containing 0.24% copper some of the sulphide inclusions contained 2-4% copper. Cleary and Green<sup>124</sup> investigated the effect of composition on weight losses on various steels and concluded that in steels containing more than 0.01% copper, sulphur has no effect on corrosion rate.

The presence of phosphorus and sulphur reduces the cathodic polarisation much more than anodic polarisation<sup>122, 125</sup>. Therefore, a shift of corrosion potential in the positive direction will be expected. According to Wranglen<sup>108</sup>, this is true only for phosphorus which promotes general corrosion. With sulphur, producing localised attack, a large shift of potential occurs in the negative direction even in the presence of manganese or copper. He suggests that the pitting nature of the corrosion makes the polarisation measurements uncertain and the separation of anodic and cathodic areas means that the cathodic polarisation due to strongly increased hydrogen evolution outside the pits is mainly measured while the anodic polarisation occurring inside the pits is not properly included in the corrosion potential.

Janik-Czachor et al <sup>110</sup> studied the effect of sulphur and manganese on localised corrosion of iron in a buffered potassium chloride solution. In their experiments, sulphur and manganese contents in the iron were varied. Electron microprobe and microscopic examination revealed that  $(\text{Mn}, \text{Fe})\text{S}_x$  inclusions were the source of pit nucleation. In steels with a high concentration of manganese, the sulphide inclusions were rich in manganese and at a low concentration of manganese the sulphides were rich in iron. In the case of inclusions rich in manganese, both the inclusions and the matrix were attacked and crevices were produced around the inclusions. In the case of inclusions rich in iron, the metal around the inclusions were attacked but the inclusion itself was not.

Electrochemical investigations <sup>110</sup> of the alloys showed that the critical pitting potential, irrespective of sulphur content of the alloys, was lower than that for ultrapure iron. It was found that even materials with low manganese content had sulphides rich in manganese and these were the main source of pit nucleation. It was concluded that since manganese was found within all the pits examined, independent of concentration, pits were predominantly formed on sulphides rich in manganese. The corrosion attack started at the interface between the inclusion and the passive metal indicating the weak spot in the passivating oxide film. Szummer and Janik-Czachor <sup>112</sup> investigated the effect of chloride ions on localised corrosion at sulphide inclusions in iron and observed that chloride accumulation occurred at the boundaries of the inclusions and was accompanied by potassium. Since both chloride and potassium ions were present in the corrosive solution it implied that traces of solution were trapped in the microcrevices between the matrix and the inclusions or in the anodic products.

They also found areas containing a high concentration of chloride away from any inclusion. These discrete areas, or "microstains", were much smaller than the areas of chloride accumulation at the sulphide inclusions and also contained potassium. Their results showed that the formation of pits was preceded by a local concentration of chlorides at the surface of iron. Since the accumulation of chloride ions was greater at non-metallic inclusions, pits developed first at these sites. In the absence of inclusions, e.g. in high purity iron, the "microstains" would be sites for pit initiation.

Wranglen<sup>108, 113, 115</sup> has suggested that the methods of casting and heat treatment of steels cause difference in corrosion rates. He studied the differences between the active and inactive sulphides in continuous cast steel (CCS) and ingot cast steel (ICS) by using an etching method, termed as a micro-corrosion test (MCT) which consisted of exposing a freshly polished specimen to 0.5 M sodium chloride solution for 30 seconds. The active sulphide inclusions caused attack in the immediate surroundings within the test period whereas the inactive sulphides did not. He defined the pitting susceptibility of the material as the ratio of the number of active sulphides to that of inactive sulphides when the specimen was examined at a magnification of 400.

He found that pronounced localised corrosion occurred in the case of some CCS in which the ratio of active to inactive sulphides was above 1. Insignificant general corrosion was observed in ICS having a ratio of active to inactive sulphides 0.16 - 0.26. The high susceptibility to localised corrosion of CCS could be eliminated by proper annealing before rolling.

He found no difference between the composition of active and inactive sulphides or of the sulphides in ICS and CCS after rolling. All the sulphides were normal manganese sulphide inclusions containing about 90% MnS. He, therefore, concluded that the difference between active and inactive sulphides was the difference in composition of the surrounding matrix.

According to Wranglen<sup>113, 115</sup>, sulphide inclusions in carbon steel and nickel are more noble than the surrounding matrix which is therefore attacked preferentially. All sulphides in carbon steel are attacked depending on the time of exposure of the material in the test solution. Existing voids between the inclusion and the matrix also act as starting points of the attack. Around active sulphides the attack is particularly rapid due to the high activity of the sulphur contaminated matrix in the immediate vicinity of these inclusions. This activity has been attributed to the large area of contact between the finely divided MnS precipitate and the iron. The sulphide ions are responsible for accelerating both corrosion processes - the anodic process which is iron dissolution and the local cathodic reaction which is in the active area and consists mainly of hydrogen evolution. The main cathodic process, oxygen reduction, however, occurs on the surrounding matrix which is not contaminated by sulphur. It has been emphasised that the smaller sulphide particles have a higher solubility than larger particles and that the anodic sites, due to the hydrolysis of metal ions, tend to become acidic, enhancing dissolution of sulphides with the formation of  $H_2S$  and  $HS^-$  ions. Even in neutral solution, both MnS and FeS have sufficient solubility to produce a significant concentration of  $HS^-$  ions, accelerating localised corrosion.  $S^{2-}$  and  $HS^-$  ions possess high electric polarisability and consequently strongly adsorb on metal surfaces.

In strongly acid solution this may lead to inhibition whereas in weakly acid, neutral and alkaline solution this may result in a reduction of activation overpotential.

The active sulphides, after a short period of time, are undermined and become detached creating a micropit. In normal carbon steels containing a small proportion of active sulphides, most pits stop growing after reaching a depth of 100 - 200 microns. Under favourable conditions, e.g. below deposits of dirt, some pits may continue to grow leading to penetration <sup>113, 115</sup>.

In the presence of a small proportion of active sulphides, general corrosion is expected since the dissolution of the sulphur contaminated matrix surrounding the active inclusions tends to expose uncontaminated steel. The presence of a higher proportion of active sulphides, however, tends to favour further localised corrosion. In this case, the dissolution of contaminated matrix appears to expose a new active volume around an underlying sulphide forming a macroscopic, self-generating pit.

In the propagation stage, according to Wranglen <sup>103, 105</sup>, an oxygen concentration cell is formed with the interior of the pit acting as a small anode and its surrounding surface as a large cathode. From the bottom and side walls of the pit iron is dissolved anodically. The  $\text{Fe}^{2+}$  ions tend to migrate and diffuse outwards, while the anions, e.g. chloride ions, migrate into the pit. Wranglen suggests the following conditions for the autocatalytic nature of pitting:

- i) Within the pit preventing passivation, limited availability of oxygen; migration of anions from the bulk solution into the pit resulting in a high concentration of chloride ions; decrease in pH due to hydrolysis of  $\text{Fe}^{2+}$  ions and due to magnetite formation.

In 0.5 M sodium chloride solutions, the electrolyte in the pit may possibly be about 1 M solution of  $\text{FeCl}_2$ . The pH of the electrolyte, on hydrolysis of  $\text{Fe}^{2+}$  ions, is calculated to be 3.5 if  $[\text{Fe}^{2+}]$  is assumed to be 1 M. However, the hydrolysis of  $\text{Fe}^{2+}$  ions occurs to a very small extent. The reaction which contributes principally to the acidification of the electrolyte inside the pit is that which produces magnetite. Within the pit dissolution of sulphide also occurs forming  $\text{H}_2\text{S}$  and  $\text{HS}^-$ .

ii) In the mouth of the pit, the formation of a "hydrate blister" forms a barrier to diffusion and maintains the difference in concentration between the bulk solution and the solution inside the pit. The concentration gradient is associated with the oxygen concentration cell which is the driving force for pitting corrosion.

iii) Outside the pit, oxygen reduction, partial cathodic protection and the formation of higher pH condition occur.

Szklarska-Smialowska<sup>111</sup> observed that the difference between active and inactive sulphides in mild steel was not made clear by Wranglen since the composition of the sulphides was the same. It was emphasised that the number of active sites formed during localised attack depended upon the concentration of chloride ions and the potential. The number of active sites may be higher with higher chloride concentration and at more positive potentials; and under different experimental conditions, even the inactive sites may behave as active ones. Therefore the designations active and inactive sulphides should be related to the specific experimental conditions<sup>111</sup>.

Eklund<sup>126, 127</sup> examined the effect of slag inclusions in steel on localised corrosion. The steel plates, both continuously cast and ingot forms, were normalised at  $900^\circ\text{C}$  for one hour after rolling.

The samples were immersed in an air-saturated solution of 0.1 M sodium chloride solution for periods of two to sixteen minutes. The corroded sites in each sample counted with the aid of an image analysing computer. He observed that the immersion time had no marked influence on the number of corroded sites and that manganese sulphides had no effect on the initial corrosion of the material investigated. In the initial corrosion process, inclusions consisting of calcium aluminates which were surrounded by a rim of  $(CaMn)S$ , having a high Ca content, were considered to be active. The difference between active and inactive sulphides was attributed to the difference in composition of the rim indicating a solid solubility at both ends of the CaS - MnS system.

The activity of the sulphide ions, which are present as  $HS^-$ , is higher near the inclusions than in the bulk solution at the commencement of the test <sup>126</sup>. This leads to a rapid breakdown of the oxide film since the sulphide ions attack the oxide film faster than the chloride ions. The area in the immediate vicinity of an inclusion becomes anodic in relation to the remainder of the matrix during the initial stage of the corrosion process. The development of smaller anodic areas surrounded by larger cathodic areas gives rise to a rapid attack on the active sites. Eklund stated that no conclusion could be drawn from these experiments regarding the corrodability of the material over extended periods.

It has been suggested that the sulphide rims form due to an enrichment of sulphur in the solidification front and to a reaction between sulphur and the calcium aluminates <sup>126</sup>. A higher aluminium content results in a higher frequency of pit nuclei, i.e. a greater number of Ca-rich sulphides. The Mn:S ratio or the casting technique has no influence on the initial stages of the corrosion process <sup>126</sup>.

Wranglen <sup>113</sup> suggested that CaS is an exceptionally active and water soluble inclusion. In its presence the area around it acts as a sacrificial anode providing cathodic protection to the matrix around neighbouring normal manganese sulphide inclusions whose activity may thereby be concealed.

King et al <sup>128, 129</sup> investigated the effect of chemically prepared iron sulphides on the corrosion of mild steel. They observed that ferrous sulphide, mackinawite ( $\text{FeS}_{1-x}$ ), was highly corrosive. The pH has only a small effect on the total corrosion, indicating that hydrogen evolution is the controlling reaction on the corrosion rate. It has been suggested that the corrosiveness of iron sulphides is associated with the sulphur content of the compound <sup>129</sup>. Corrosion of mild steel is due to the formation of a galvanic cell, iron sulphide/iron, and hydrogen evolution occurs on the iron sulphides which acts as cathodes.

Wallwork and Harris <sup>114</sup> studied the corrosion rates and the nature of the corroding surface of a number of different types of steel and of pure iron with less than 20 ppm total metallic impurities. The killed, semi-killed and rimmed steels were of similar composition. The specimens made from these materials were annealed and metallographically polished prior to immersion in sulphuric acid (pH 5) in which they were rotated at approximately 8 Hz. The concentration of iron in solution was analysed over a period of time and it was found that the fully killed steel dissolved at double the rate of pure iron after six hours. In the case of rimmed steel, a change in the rate of attack with increased time was noted. This was considered to be associated with the penetration through the outer rim into the more impure core.

Metallographic examination showed that pure iron had developed large pits which followed a marked crystallographic pattern <sup>114</sup>. The rimmed steel which was relatively free of inclusions in the outer rim also exhibited similar pits, but the depth appeared to be less. The fully killed steel, however, had a more general attack with some smaller, rounded pits.

Wallwork and Harris <sup>114</sup> also investigated the effect of the MCT described by Wranglen <sup>115</sup>, on continuously cast and ingot steels in the as-rolled conditions. The inclusions in both steels were similar but less inclusion was detected in CCS than ingot steels. The inclusions in the CCS were, however, distinctly different from those in the material used by Wranglen <sup>115</sup>.

The results of the MCT showed the initiation of pits on the surface but no significant difference was observed between the two types of steel. After reimmersion for ten minutes in the test solution, specimens exhibited extensive pitting at sites that were not associated with the pits produced during the shorter time MCT. It was concluded that further corrosion did not necessarily occur by the growth of the pits already formed and that under the conditions of testing used, the MCT was not suitable for distinguishing between ICS and CCS and the test could even be misleading. It was also observed that most pits were not always associated with the inclusions. However, where pitting was associated with an inclusion, it was a MnS inclusion and the attack was not general along the inclusions.

Localised corrosion of mild steel in neutral chloride solutions was studied by Gainer and Wallwork <sup>116</sup> using a scanning microprobe potentiometer.

This apparatus measures potential variations on a corroding metal surface and records the information in the form of a potential distribution map as a function of time. Active, active to passive, and passive regions can be recognised from these maps and located on the specimen surface.

Their results suggested that pitting of mild steel occurs in three stages: pit initiation, pit coalescence, and pit propagation<sup>116</sup>. The initiation stage was shown to depend primarily on the presence of metallurgical heterogeneities in the metal. Among the heterogeneities, sulphide inclusions are the most effective pit initiation sites. The anodic nature of the individual inclusion is influenced by the composition, size, and the inclusion density i.e. number of inclusions per unit area. If the Mn:S ratio of the steel is approximately 12, then the activity of the inclusions is independent of composition. Inclusions are identified as (Mn, Fe)S inclusions and are present in all the regions. However, if the Mn:S ratio is about 3, the activity varies with the composition. The majority of the inclusions are duplex FeS + MnS; some (Mn, Fe)S inclusions are also present in the passive regions. Increasing the FeS content of these inclusions increases their activity towards pit initiation. The active region contains inclusions with low FeS content. The transition region is at a Mn:S ratio of approximately 5.

Gainer and Wallwork<sup>116</sup> found that FeS + MnS duplex inclusions with high FeS concentration (approximately 50 wt percent) were more efficient in initiating pits than the (Mn, Fe)S inclusions. The effectiveness decreased in the order FeS + MnS > (Mn, Fe)S > grain boundary triple points.

Since in the conventional steelmaking practice the Mn:S ratio is greater than 4, to avoid FeS formation and prevent hot shortness, normally (Mn, Fe)S inclusions form in the steel. The sulphides are anodic relative to the matrix and, if present in sufficient densities, form anodic regions on the metal surface which are more active than the surrounding metal. Within these regions large sulphide particles initiate micropits at the matrix-inclusion interface, where the current density is highest, by electrochemical dissolution of the steel.

It was found that not all inclusions in the anodic regions form micropits<sup>116</sup>. Microprobe analysis results indicated that the compositions of the active and inactive sulphides were the same. Gainer and Wallwork concluded that the activity of the individual inclusions was influenced by the inclusion size and the presence of other inclusions nearby. Large sulphide inclusions tend to initiate micropits in preference to smaller ones. However, if only small inclusions are present, then these will form micropits if the inclusion density is sufficiently high in the matrix. Inclusions may also be inactive due to the cathodic protection provided by the adjacent sulphides which have initiated micropits. They also emphasised that the inclusion density for an active area was not absolute value but depended on the density within other regions.

Within the active regions, where the sulphide density is highest, coalescence of the micropits occurs leading to the formation of macropits. As macropits develop, more sulphides are exposed, new micropits are initiated and further coalescence occurs. If the macropits have the correct geometry to generate an autocatalytic process within the pit, pit propagation follows resulting in general pitting corrosion.

Propagation may cease by an induced cathodic current from more active pits nearby, precipitation of corrosion product on the sites of metal dissolution, or by a pit geometry which does not produce or destroys the concentration gradient between the electrolyte within the pit and the bulk solution.

In the passive regions, inclusions are small in size and low in density. These regions are cathodically protected by the areas of higher inclusion density and size. An active area may also become passive in the presence of a very strongly anodic region in its vicinity. Thus the theory of pit initiation and coalescence, suggested by Gainer and Wallwork<sup>116</sup> concludes that the pitting tendency of sulphides depends on the size and density of the inclusions.

Adrian et al<sup>130</sup> suggested that development of micropit was not associated either with a local cathode effect or with an increased anodic activity around the sulphide inclusions. In carbon steels, pits formed at manganese-rich sulphides due to (i) the preferential dissolution of sulphides under specific potential conditions, (ii) crevices formed at the matrix-inclusion phase boundary upon cooling from the melting temperature due to different coefficients of expansion, or (iii) the stimulating effect of dissolved sulphide ions on the anodic dissolution in the areas surrounding the inclusions.

On the basis of evidence published so far, it becomes apparent that the precise mechanism for the initiation of a micropit and its propagation has not been resolved. However, it appears that anodic dissolution is enhanced about inclusions particularly in regions of high inclusion density. The possible mechanism for enhanced anodic activity around the inclusions may include

(i) cathodic reduction on more noble sulphide inclusions creating a local galvanic effect, (ii) stimulation of the anodic process by  $\text{HS}^-$  from dissolving inclusions, and (iii) variation in the exchange current density of the sulphide rich matrix<sup>131</sup>. Recent investigations on pitting in alloy steels have also suggested that most susceptible sites for nucleation of pits in these materials are the (Mn, Fe)S inclusions<sup>107, 109, 112, 117, 132, 133</sup>.

#### 2.3.4 Dissolution of iron carbides

Most of the alloys used in industry are heterogeneous. The dissolution behaviour of a material is considerably influenced by these heterogeneities. The presence of carbides in steel can greatly affect the behaviour of the material when exposed to an aggressive environment.

Rapid attack on grey cast iron in sulphuric and hydrochloric acids has been attributed to the carbide particles which act as efficient cathodes to the anodic ferrite matrix.<sup>134</sup> It has also been suggested that the corrosion rate of steels in citric acid increases in the presence of massive cementite which assists cathodic process<sup>135</sup>. Foroulis<sup>136</sup> observed that the presence of a needle like precipitate increased the corrosion rate of an Fe-Si-C alloy in 0.1 M hydrochloric acid.

At elevated temperature steels with a spheroidised structure corrodes more rapidly than those with pearlite structure. Manuel<sup>137</sup> investigated the corrosion behaviour of a fine grained medium manganese steel in both normalised and spheroidised conditions in dichromate - sulphuric acid solution at 82° C and found that a spheroidised steel corroded more rapidly than the normalised one.

Cleary and Green <sup>124</sup>, however, observed that in 0.1 M sulphuric acid, the corrosion rate depended upon the distribution of iron carbide in the material. They found that the dissolution rate increased as the average pearlite lamellae spacing decreased. According to these researchers, a pearlite structure corroded faster than spheroidised material, and steels containing fine pearlite corroded more rapidly than those with coarse pearlite. Evans <sup>138</sup>, however, reported that in caustic solutions the carbide phase of pearlite was preferentially attacked.

Staicopolus <sup>139</sup> studied the cathodic polarisation characteristics of cementite in 0.5 M sodium chloride solution. He found that cementite was an active cathodic site in the corrosion of steel since it did not polarise at low current densities. At high current densities, however, cementite rapidly polarised to the potential which was characteristic of iron under similar current density conditions. He attributed this behaviour to chemical decomposition of cementite to iron and various hydrocarbons under the influence of cathodically evolved hydrogen. These gases were analysed by mass spectrometry and the presence of hydrocarbons was confirmed.

Green and Parkins <sup>140</sup> investigated the electrochemical properties of cementite in nitrite solution. They observed that cementite underwent relatively little cathodic polarisation at low current densities and appeared to be an efficient site for cathodic discharge during the corrosion reaction. At high current densities the electrode surface appeared to be denuded of carbon and to take on the properties of an iron surface.

Anodic polarisation curves of iron carbides in 5 M ammonium nitrate solution in the temperature ranges of 25° C to 100° C were determined by Flis<sup>141</sup>. He found that as temperature increased the carbide became more active and the dissolution rate at a given potential increased.

Cron et al<sup>142</sup> investigated the dissolution behaviour of Fe - Fe<sub>3</sub>C structure in Fe - 0.45% C alloy and observed that in the acid range iron did not dissolve at potentials more negative than -620 mV (SHE). As the pH increased the range of potentials in which passivity occurred also increased.

The results of their study suggest that the (i) dissolution of the carbide occurs at -1000 mV (SHE) in the pH 4 hydrochloric acid solution, possibly due to the reduction of carbide to iron and methane, or iron and methanol; (ii) dissolution behaviour changes as anions are changed at pH 4 and pH 14; (iii) mode of attack changes as a function of potential, e.g. at pH 4 in sulphuric acid, the interface dissolves at low potentials, while the carbide dissolves at higher potentials; (iv) iron carbide has higher reactivity than carbon, because of its higher energy due to the strained cementite lattice. It is also possible that the cementite is reactive because the carbon "may not allow the iron in the carbide to passivate. Thus the carbide will be rapidly attacked with the iron going into solution and the carbon left as an amorphous powder. The appearance of a powdery carbon on the surface of corroding steel has been observed".

The attack at the interface between carbide and ferrite occurs only in specific instances, e.g. in the pH 4 sulphuric acid, attack occurs at -500 mV (SHE) but does not occur at -215 mV or +800 mV (SHE).

They suggested that the interface was attacked because of the segregation of minor elements, such as P and S, to this area. These elements rejected from the carbide upon precipitation are present in greater concentrations at the interface than in the bulk of the matrix.

Foroulis and Uhlig<sup>125</sup> studied the effects of cold work on pure iron, iron-carbon, and iron-nitrogen alloys and found that the presence of dislocations and substructure did not increase the corrosion rate of pure iron. Segregation of carbon atoms, however, to these defects influences the corrosion rate by creating more efficient cathodic sites on the surface. Chance<sup>143</sup> investigated the effect of heat treatment and plastic deformation on the corrosion of low carbon steel. He concluded that heat treatment promoting precipitation and growth of iron carbides in the ferrite matrix causes increased corrosion after the metal has been plastically deformed. Fracturing of the carbide particles and parting of the carbide-ferrite interface caused by the displacement of the carbide particle during deformation create capillary paths which tend to be sites for entrapment of corrosive substances. This can lead to reduced corrosion resistance in low carbon steels.

#### 2.3.5 Mechanisms under corrosion fatigue conditions: modern concepts

Most of the previously proposed models of crack initiation generally fail to satisfy all of the experimental observations and it has been suggested that no single mechanism is possibly responsible for the behaviour of metals and alloys under corrosion fatigue conditions<sup>10, 11</sup>.

According to Parkins<sup>144, 145</sup>, environments that promote cracking in a given material under nominally static loading will also promote fracture under cyclic loading conditions, by essentially the same mechanism when the frequency of loading is not too high. Thus the selective dissolution process and the hydrogen embrittlement mechanism of stress corrosion cracking may also operate under corrosion fatigue conditions.

Recently Rollins et al<sup>14</sup> have suggested that in high carbon steels the environment is of primary importance in the crack initiation stage of fracture and that corrosion fatigue processes involve preliminary pitting by a differential aeration corrosion mechanism. Superimposition of alternating stress causes depolarisation of the cell and consequently enhanced dissolution at the tip. The fracture of the films of corrosion products causes localisation of attack which results in sharpening of the pit. The decrease of the area of the anode relative to the cathode causes a corresponding increase in anodic current density which enhances the pit extension rate. At this stage, in aerated salt solutions, the corrosion process is controlled by the anodic exchange current since both electrodes are effectively depolarised by the alternating stress, the resistance between anode and cathode is not large and oxygen has easy access to the cathode. In the second stage, plastic deformation occurs at the base of the pit and this has the effect of increasing the anodic exchange current. Provided the cathodic reaction keeps pace, there is a rapid increase in the rate of metal dissolution and this extends the pit into a crack.

Patel et al<sup>15, 147</sup> proposed a slip - dissolution - reverse slip model for anodic corrosion fatigue in which the formation of a slip step at the metal surface in regions of localised strain ruptures the passive surface oxide layer and exposes fresh,

active metal on the face of the slip step. This newly exposed metal is anodic to the surrounding passivated metal and therefore undergoes rapid electrochemical dissolution. When slip reversal occurs along the same plane or on a plane close to the original, the formation of a notch results. These researchers suggest that for corrosion fatigue crack development, the minimum dissolution rate will be that to remove one atomic layer of metal from the slip step. In addition, the slip step has to reverse back into the metal to be effective in crack development and the wedge created has to be large enough to exert a significant stress concentration effect during the next cycle. It appears that the dissolution rate within the pit or notch needs to be small relative to the effect of strain, otherwise a sharp crack will not form. Consequently, electrochemical conditions in the pit may not be of direct importance to crack initiation by this mechanism<sup>131</sup>.

Anodic and cathodic reactions on mild steel in aqueous chloride solution are significantly stimulated by cyclic plastic deformation during both the tensile and compressive strain reversals<sup>15</sup>. It has also been reported that the cathodic corrosion fatigue depends on the absorption of hydrogen<sup>16, 147</sup>. The hydrogen formed on the metal surface can enter the metal by diffusion. Alternatively it may be drawn into the metal, if it is adsorbed on the slip steps, when the cycle is reversed<sup>148</sup>. An alternative mechanism, known as the enhanced slip model, postulates that crack initiation in a corrosive environment is a result of a selective corrosion process of specific sites on the metal surface<sup>11, 63</sup>. The localised electrochemical dissolution results in the formation of numerous persistent slip bands.

These bands are preferentially attacked because the localised dissolution at these emerging bands reduces the resistance of the surface to dislocation egress by unlocking piled-up dislocations, resulting in the formation of intrusions and extrusions. Moskovitz and Pelloux<sup>149</sup> suggest that any proposed model should be able to account for the existence of a critical current density below which accelerated crack initiation does not occur, as observed by Uhlig et al<sup>63, 81</sup>. Slip - dissolution - reverse slip models describe this critical current density as the dissolution rate required to remove one atom layer of metal in the time a slip step is exposed to the electrolyte, so that a notch will form upon slip reversal. However, the enhanced slip mechanism describes the critical current density as removing considerably less than one atom layer per cycle, which is insufficient to result in notch formation<sup>149</sup>.

It is possible that fatigue crack initiation in the presence of aggressive environments does not occur by the same mechanism for every material. In many engineering alloys cracks may nucleate at some weakly constrained interface or because of a stress concentration associated with discontinuities in the structure. Parkins<sup>144, 150</sup>, however, suggests that surface discontinuities can result in considerable changes in solution composition from those represented by the bulk solution and that to assume that surface discontinuities are only of significance in the context of stress concentration can be misleading.

Lees<sup>151</sup> investigated the susceptibility of cold worked C-Mn steel to environmental sensitive cracking in acidic sulphate solutions and concluded that (Mn, Fe)S inclusions played an important role in both crack initiation and propagation.

In cold worked material they act as sites for H and  $H_2S$  formation at the crack tip. Inclusions act as local sites for  $H_2S$  generation, cathodic sites for  $H_3O^+$  reduction and low energy paths for H diffusion in the material.

Preliminary work on corrosion fatigue of EN 1 type mild steel in 0.6 M sodium solution shows that localised corrosion rapidly occurs in the vicinity of non-metallic inclusions developing voids or microcracks <sup>152</sup>. The crevices and subsequent pits appear to serve as sites for enhanced stress concentration since crack initiation seems to occur due to the coalescence of these crevices.

For 18% manganising steel in 0.6 M sodium chloride solution initiation was found to be associated with iron silicate inclusions <sup>153</sup>. It has been suggested that in BS 4360 50D steel in 0.6 M sodium chloride solution corrosion fatigue cracks form initially at inclusions <sup>154</sup>.

### 3 EXPERIMENTAL

#### 3.1 Introduction

The accelerating influence of an aqueous environment on fatigue crack initiation has been attributed to stress intensification at a localised corroded area, yield assisted dissolution, dissolution of metal exposed at rupture in passive films, reduced surface energy requirements for crack development and local embrittlement by hydrogen. According to circumstances, all these effects - either singly or in combination - may be responsible for nucleation of a crack.

On an active metal surface, disturbances created by fatigue may stimulate electrochemical activity and to observe these phenomena in the present work, corrosion fatigue tests were performed, and metallographic and electrochemical techniques were used to examine the changes in electrochemical activity and surface morphology.

For metallographic examinations, corrosion fatigue tests were carried out by using a Schenck rotating bend fatigue testing machine (47 Hz). Since this machine was not suitable for electrochemical measurements, a slow strain (0.02-1 Hz) reverse bend fatigue testing machine was constructed whilst for faster strain rates, an Avery reverse bend fatigue testing machine (24 Hz) was used.

To provide a greater consistency in the saline environment e.g. to prevent any increase in salinity due to evaporation or build up of corrosion product, or any drop in pH of the electrolyte, a constant flow of sodium chloride solution was allowed through a glass cell past the specimen.

Where it was not possible to use a glass cell, as in the Avery machine, a pool of liquid was created on the specimen surface and a flow of fresh solution was allowed to drip into the pool. In the case of rotating bend fatigue tests, the electrolyte was drip fed.

### 3.2 Material

The material used in this investigation was commercially available EN 1 type mild steel with the chemical analysis conforming to 0.11% C, 0.41% Mn, 0.016% Si, 0.07% S, 0.18% P, 0.05% Cr, and 0.02% Ni. In addition, Mo, Al, Co, Cu, Nb, Sn and V were present at less than 0.01% level.

The mechanical properties of the steel are:

Ultimate tensile strength : 565 - 596 MPa

Elongation : 9 - 13%

Reduction of Area : 48 - 57%

The structure of the material in the "as received" condition is shown in Figure E 1.

### 3.3 Electrolyte

Solutions were prepared from "Laboratory Reagent" grade sodium chloride, dissolved in de-ionised water to a concentration of 0.6 M, with a pH of 6.5. All tests were performed at room temperature of  $22 \pm 1^\circ \text{C}$ .

### 3.4 Electrochemical tests

#### 3.4.1 Anodic polarisation tests

Anodic polarisation tests were performed potentiostatically under static and flowing electrolyte conditions without externally applied stress. Tests were also made in flowing electrolyte with an externally applied cyclic stress.

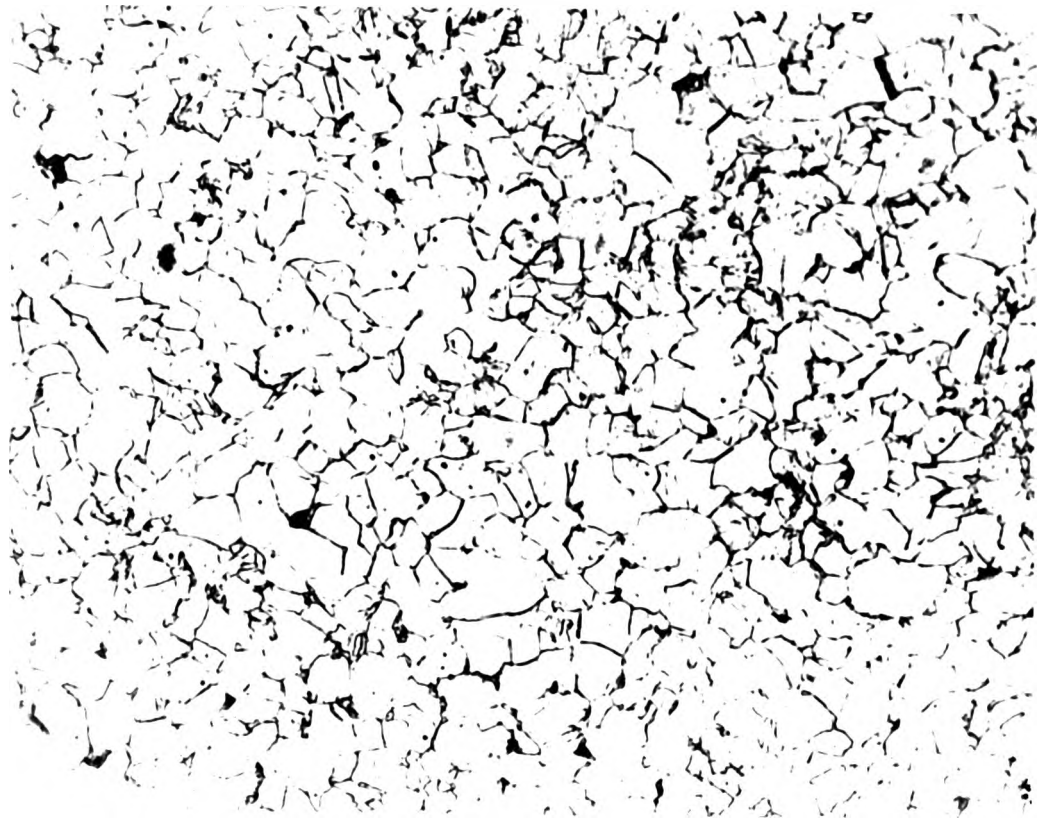


Fig E 1: Optical micrograph of the structure of mild steel in the wrought condition. x 140

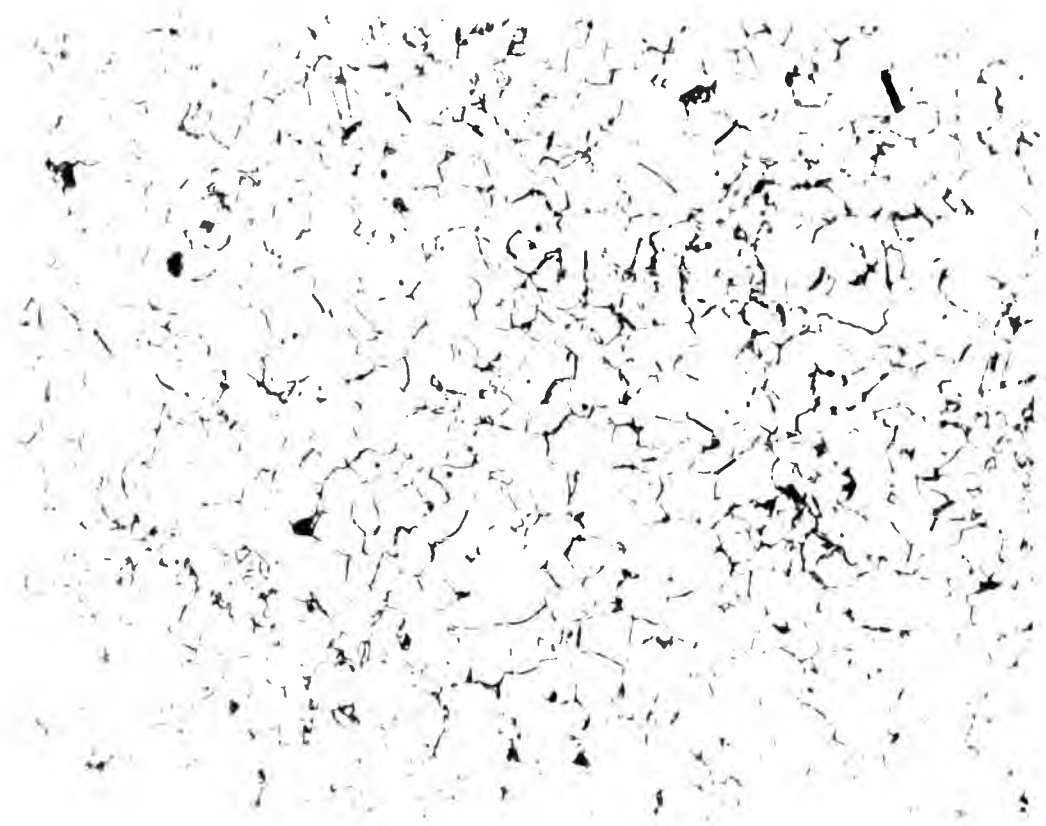


Fig. 1: Optical micrograph of the structure of mild steel in the wrought condition. x 140

Potentiationkinetic polarisation tests were also performed under static and flowing electrolyte conditions without externally applied stress.

#### 3.4.1.1 Specimen preparation

The specimens were made from flat pieces of mild steel measuring 6.4 mm x 3.2 mm x 304 mm. They were sectioned parallel to the rolling direction and surface defects were removed by grinding the specimens with successive grades of silicon carbide papers followed by polishing with 1  $\mu$ m diamond paste. These were then coated with Lacomit leaving an area of known dimensions exposed on one face of the specimen.

When cyclic stress was applied, a gauge length of 7 mm long, 5 mm wide and 1.5 mm thick, was made by grinding the test pieces on one face. Surfaces of the specimens were then prepared as described previously.

The specimens were stored in a desiccator until required.

#### 3.4.1.2 Apparatus

For the static electrolyte condition a large pyrex glass beaker was used as the container for the electrolyte to assist aeration of the solution, for both potentiostatic and potentiokinetic polarisation tests. The counter electrode was a platinum gauze encased in a polythene tube with a glass wool plug inserted in one end to make provision for the gas to escape. The calomel reference electrode was placed directly above the exposed area. The distance between the specimen and the reference electrode was kept to a minimum throughout the test. No external stress was applied to the specimen.

For potentiostatic tests, under flowing electrolyte condition, the connection to the calomel electrode was made through a glass capillary placed directly above the exposed area. The experimental arrangement is shown in Figure E 2. The flow of the electrolyte was controlled to avoid any turbulence in the glass cell. The distance between the specimen and the tip of the capillary was kept to a minimum throughout the tests. No external stress was applied to the specimens.

A machine was constructed to provide facilities for electrochemical measurements on test pieces during cyclic stressing by reverse bending in the prescribed aqueous environment (Figure E 3). The specimen was mounted horizontally in the machine, clamped at one end while the other end was held in a yoke connected to a mechanism applying the stress. To avoid electrical interference, the test piece was isolated electrically from the machine by insulating inserts fitted to the clamps and the yoke.

The stress was applied to the specimen by means of an eccentrically driven shaft which provided the stroke of the machine. Individual stress ranges were obtained by re-positioning the shaft in the drive conversion plate. Electrical resistance strain gauges placed at different positions on dummy specimens were used to establish stress ranges. The machine was capable of producing sinusoidal waveform, symmetrically disposed about zero mean stress. The rate of cycling could be varied electronically between 0.02 to 1 Hz.

When external stress (169 MPa) was applied, the specimens were fitted to a reverse bend fatigue testing machine (Figure E 3) and a glass cell (Figure E 2) was used as a container for the electrolyte.

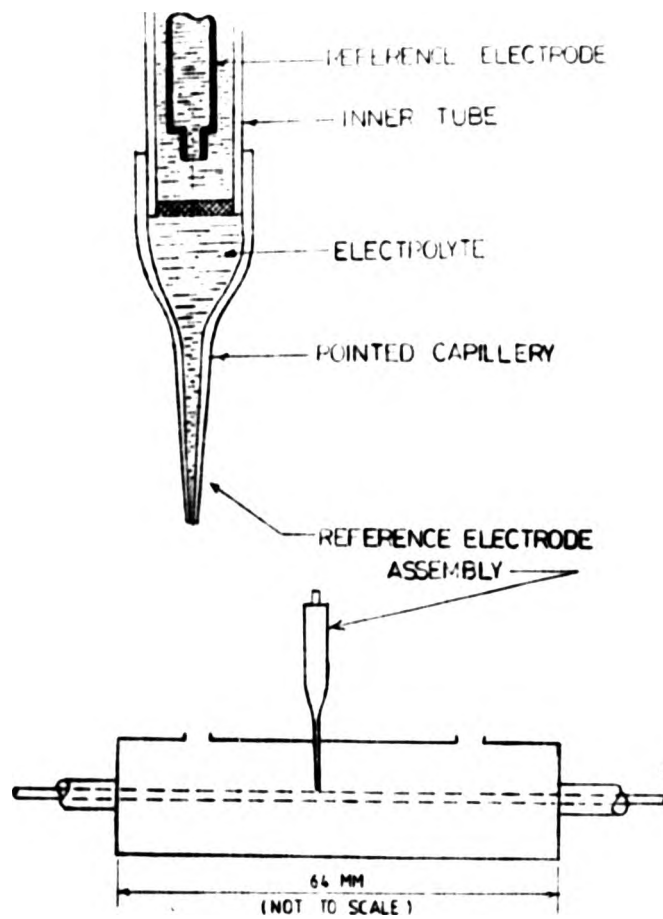


Fig E 2: Arrangement of reference and working electrodes for anodic polarisation tests in flowing electrolyte.

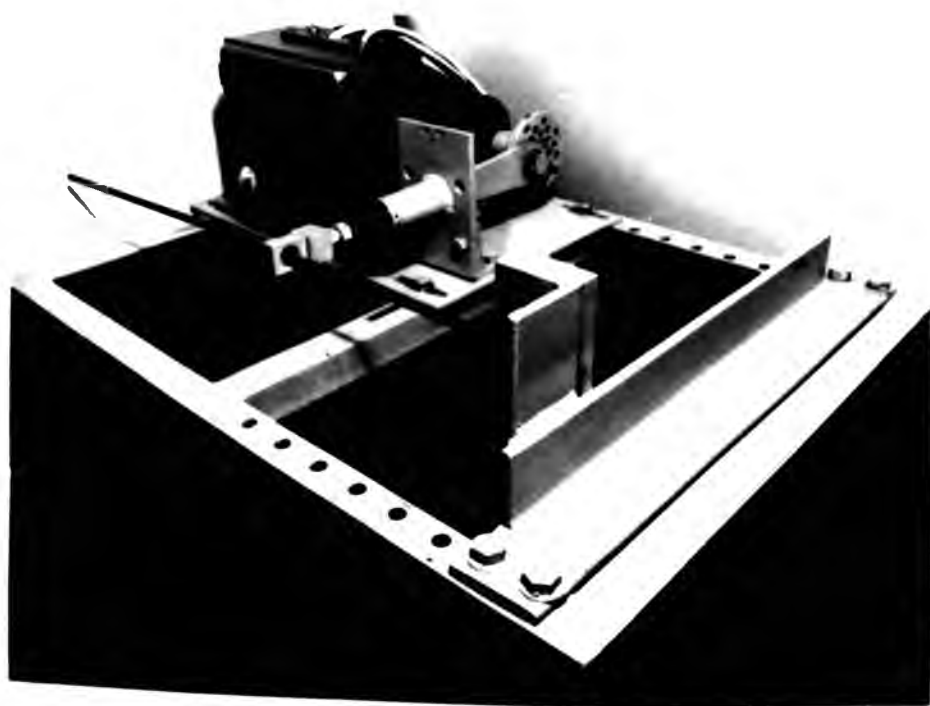


Fig E 3: Reverse bend slow strain fatigue testing machine. Rate of cycling 0.02 to 1 Hz.

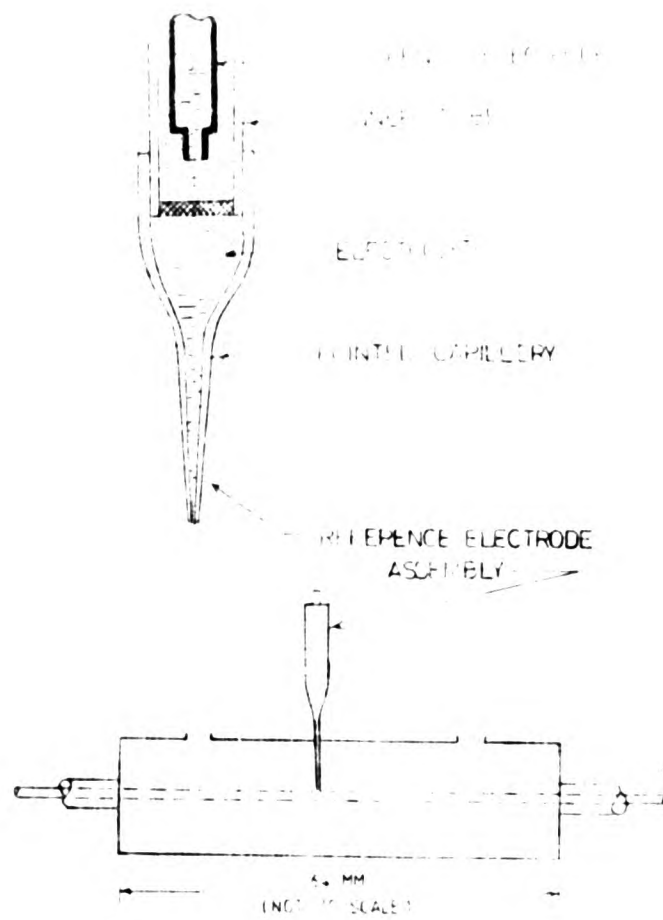


Fig. 2: Arrangement of reference and working electrodes for anodic polarisation tests in flowing electrolyte.

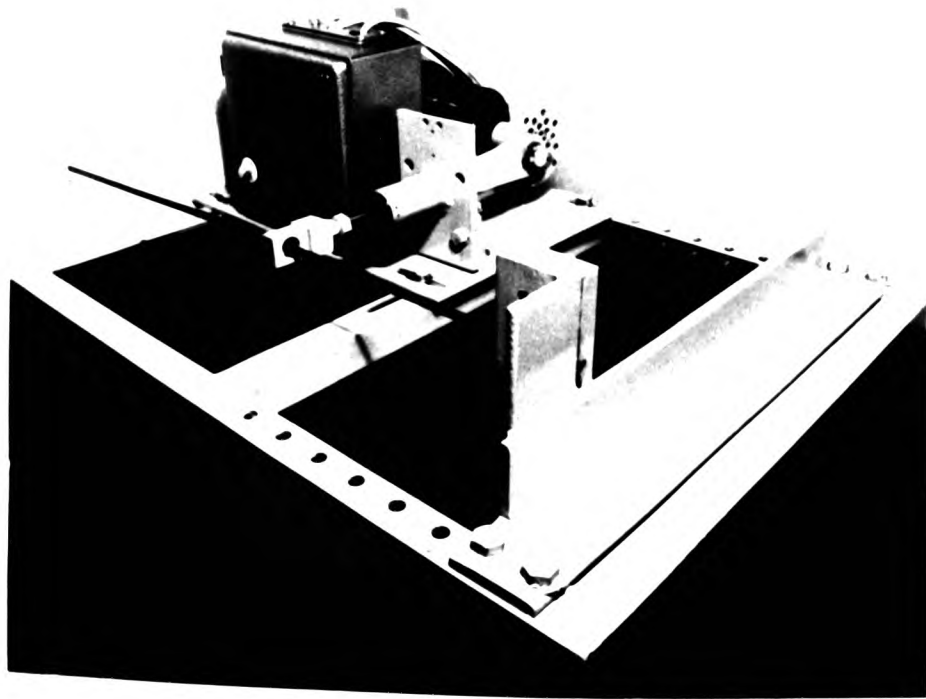
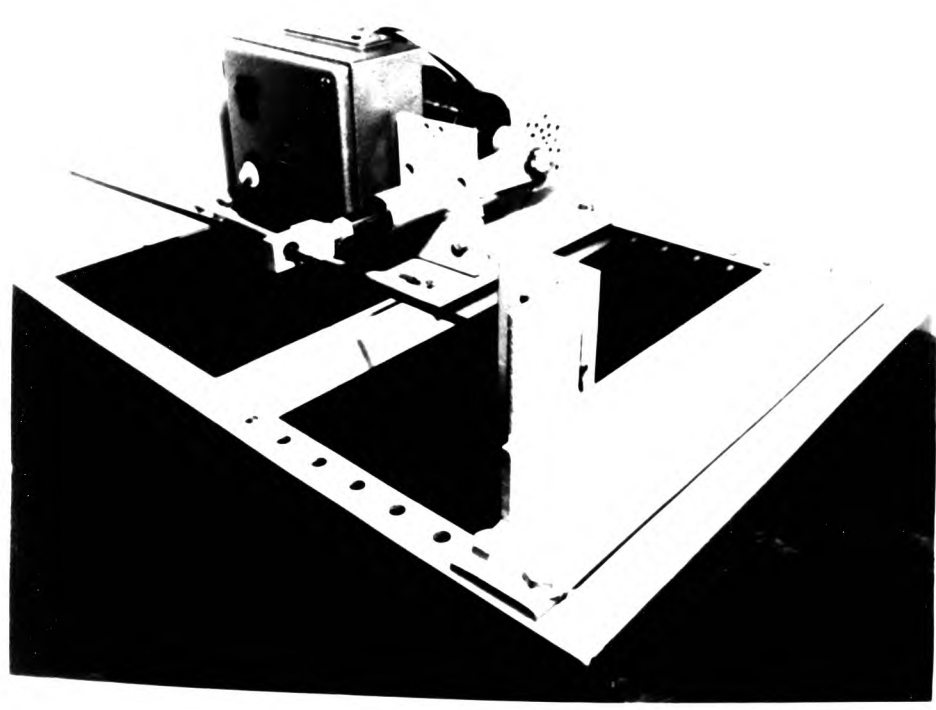


Fig. 3: Reverse bend slow strain fatigue testing machine. Rate of cycling 0.02 to 1 Hz.



1. Diagram of the reference and control circuit for the  
classification test of the sub-element.



The connection to the calomel reference electrode was made through a thin PVC tube with a taper end. This part of the tube was placed on to the exposed surface of the specimen and the tube was secured to the coated part by using rubber "O" rings. This system avoided the risk of breakage of the reference electrode due to the movement of the specimen and thus contaminating the electrolyte. The tests were performed potentiostatically in flowing electrolyte. A Wenking potentiostat was used for all the tests.

During development trials it was observed that similar results were obtained whether the connections to the reference electrode were made through a tapered PVC capillary tube, through a glass capillary or by placing the reference electrode directly above the metal surface. Consequently, whenever there was any risk of contaminating the electrolyte, tests were performed using a PVC capillary tube.

For potentiokinetic polarisation tests under flowing electrolyte conditions, the polarisation study was carried out using an 'Accuron' potentiostat with a built-in Linear Sweep Generator, under conditions similar to that used for the potentiostatic study.

No external stress was applied to the specimens.

#### 3.4.1.3 Procedure

For potentiostatic polarisation tests, the specimens were immersed in the electrolyte and the tests commenced immediately a fixed cathodic current density of  $200 \mu\text{A}/\text{cm}^2$  was obtained. Potential was increased by 10 mV steps at 60 seconds interval. The change in the potential and the current was recorded from the potentiostat meter.

For potentiokinetic polarisation tests, under stagnant and flowing electrolyte condition, the specimens were immersed in the electrolyte and tests commenced immediately at -1000 mV (SCE).

The specimen was made more positive at a rate of 0.2 mV per second. The change in the potential and current was recorded on a x-y plotter.

When cyclic stress was applied, the procedure used was similar to that described previously for the potentiostatic polarisation test. The difference was that the potential of the specimen was decreased to obtain the prescribed cathodic current density at which the polarisation test commenced, and the fatigue machine was switched on. The rate of cycling was 0.2 Hz. The specimens were stressed to 169 MPa at  $R = -1$ .

Several tests were performed for each type of test condition employed and for each test a new specimen was used. In all cases, the cathodic current or cathodic potential, where appropriate, was applied as the specimen was immersed in the electrolyte.

#### 3.4.2 Scratching electrode tests

Scratching electrode tests were performed in flowing electrolyte without an applied stress.

##### 3.4.2.1 Specimen preparation

The surface preparation of the specimen was as described in 3.4.1.1. The specimens were coated with Lacomit leaving an area, 4 mm wide, 7 mm long, exposed on one face of the specimens.

##### 3.4.2.2 Apparatus

The specimen was fitted to a reverse bend fatigue testing machine (Figure E 3) and a glass cell (Figure E 2) was used as a container for the electrolyte. Connection to the reference electrode was made through a tube made of PVC material with a taper end which was secured to the specimen by using rubber "O" rings.

The reference electrode was placed in a glass beaker separate from the corrosion cell. The flexible tube was connected to a glass capillary, shown in Figure E 4, one end of which was placed in the beaker containing the reference electrode. The glass cell and the capillary tube contained the same test solution. During the performance trials, it was observed that the potential measured by using the capillary tube was the same as that obtained by placing the reference electrode on the specimen surface. A Vibron electrometer was used for measurement of potential. The counter electrode, for passing current, was a platinum gauze cylinder encased in a polythene tube with a glass wool plug inserted at one end. A Wenking potentiostat and a Bryans 28000 series chart recorder were used for the measurement of current. The experimental arrangement is shown in Figure E 5.

#### 3.4.2.3 Procedure

After immersion of the specimen, changes in potential were recorded. Electrolyte was fed continuously by gravity, avoiding any turbulence of the solution in the cell. No stress was applied to the specimen.

On achieving a steady state potential, the surface of the specimen was scratched gently with a glass rod to remove the surface film without, as far as possible, agitating the electrolyte. The shift in potential was recorded.

For current measurement, a similar technique was used. The applied potential was  $-680$  mV (SCE).

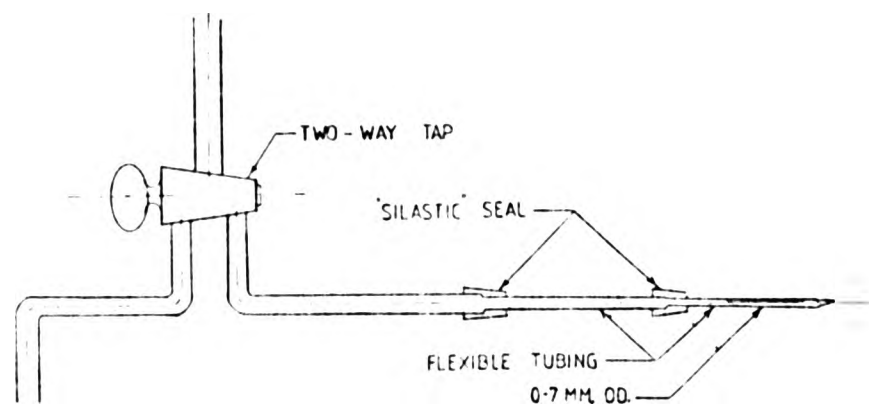


Fig 4: Glass capillary connected to flexible tubing.

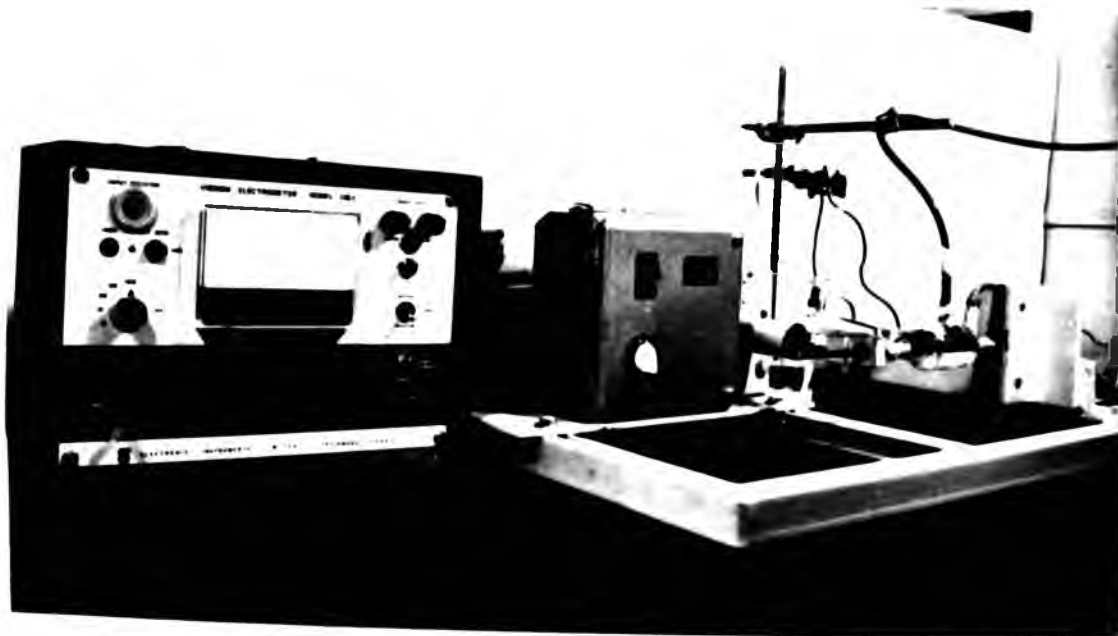


Fig 5: Experimental arrangement for electrochemical and reverse bend test.

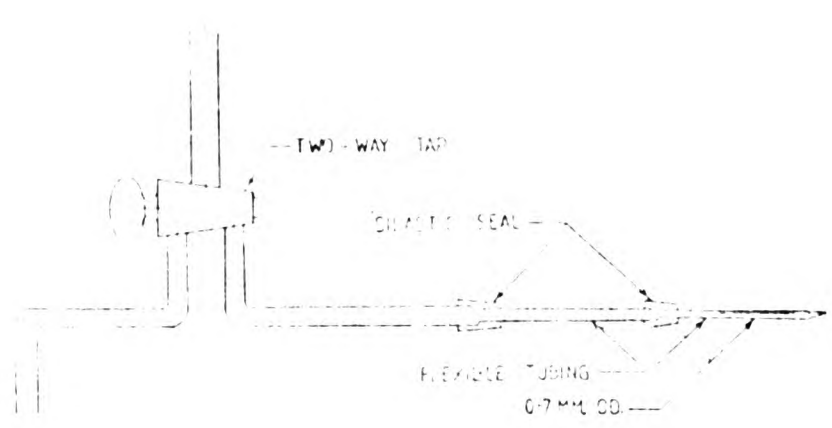


Fig. 4: Glass capillary connected to flexible tubing.

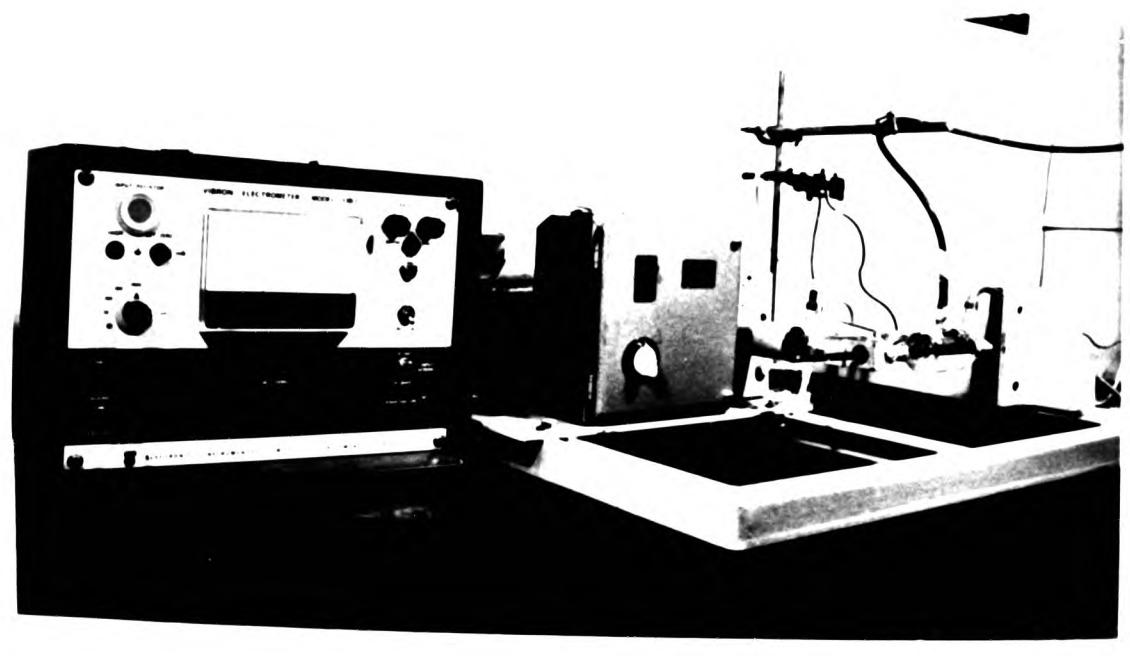


Fig. 5: Experimental arrangement for electrochemical and reverse bend test.

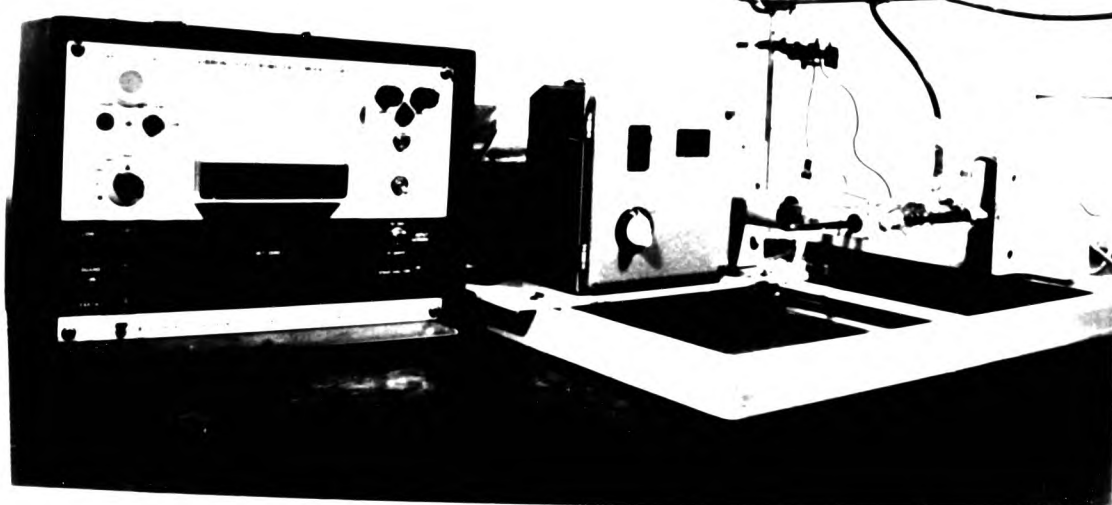


Fig. 1. Schematic diagram of the experimental setup.

### 3.4.3 Measurement of potential inside a notch

#### 3.4.3.1 Specimen preparation

The surface preparation of the specimens was as described in 3.4.1.1. The specimens were then coated with Lacomit leaving an area exposed on one face of the specimen.

A notch of approximately 2.5 mm deep was machined with a miniature drill of 1 mm diameter on the exposed surface.

#### 3.4.3.2 Apparatus

The specimen was fitted to the reverse bend fatigue testing machine (Figure E 3). A glass cell was used for flowing electrolyte. A 0.7 mm diameter tube made of PVC type material was inserted in the notch and connected to a standard calomel electrode. The reference electrode was placed in a glass beaker separate from the corrosion cell. The flexible tube was connected to a glass capillary, shown in Figure E 4, one end of which was placed in the beaker containing the reference electrode. The glass cell, capillary tube and the beaker contained the same test solution.

Potential of the external surface of the specimen was also measured through a similar tube connected to a second calomel electrode. Prior to the commencement of the test the potential difference between the reference electrodes were checked and no variation was observed. Two Wenking potentiostats were used to measure the potentials. The experimental arrangement was similar to that shown in Figure E 5.

#### 3.4.3.3 Procedure

After immersion of the specimen, changes in potential were recorded on a Bryans 28000 series chart recorder. Electrolyte was fed continuously by gravity avoiding any turbulence of the solution in the cell.

In a separate series of experiments, a static stress of 15 MPa was applied for 7 hours and then the stress was reduced to zero. Finally, the specimen was subjected to a static compressive stress of 100 MPa for 60 minutes. The initial and final potentials were recorded in both cases.

In all cases, to measure the surface potential, the taper end of the tube connected to the reference electrode via a glass capillary was placed approximately 4 mm away from the mouth of the notch. Potentials were measured using two separate reference electrodes located in two beakers containing the same test solution. The PVC capillary tube was inserted in the notch prior to the immersion of the specimen in the electrolyte. Only the potential of the external surface was measured when a static compressive stress of 100 MPa was applied.

In another series of experiments, to measure the pH of the notch electrolyte, the PVC tube was not fitted initially with the test solution. A short time after the immersion of the specimen, with the external surface potential at approximately  $-610$  mV (SCE), the liquid in the notch was extracted through the capillary tube. Indicator papers were placed at the end of the tube to measure pH. No external potential was applied to the specimen.

### 3.4.4 Measurements of potential of specimens subjected to tensile stress

#### 3.4.4.1 Specimen preparation

The specimens were made from flat pieces of mild steel, measuring 6.4 mm x 3.2 mm x 304 mm. Some of these specimens were annealed at 650° C for 3 hours in argon and furnace cooled. These were sectioned parallel to the rolling direction with a gauge length of 6.4 mm x 1.5 mm x 7 mm. The surface preparation of the specimens was as described in 3.4.1.1. The specimens were then coated with Lacomit leaving an area, 7 mm long and 4 mm wide, exposed on one face of the specimens.

#### 3.4.4.2 Apparatus

The specimen was fitted to a Monsanto-Hounsfield tensometer machine and a glass cell was used as a container for the electrolyte. Connection to the saturated calomel electrode was made through a PVC tube with a taper end which was secured to the specimen by using rubber "O" rings. A Wenking potentiostat and a Bryans 28000 series recorder was used to measure and record potentials.

Stagnant electrolyte was used for this series of tests.

#### 3.4.4.3 Procedure

After immersion of the specimen a load was applied and the potential was measured while the load was maintained at that level.

Potential measurements were carried out after successive increments of load.

### 3.4.5 Reverse bend fatigue tests - 0.02 to 0.2 Hz

#### 3.4.5.1 Specimen preparation

The specimens were prepared as described in 3.4.4.1.

#### 3.4.5.2 Apparatus

The reverse bend fatigue testing machine is shown in Figure E 3. The stress is applied to the specimen by means of an eccentrically driven shaft which provides the stroke of the machine. Individual stress ranges may be obtained by re-positioning the shaft in the drive conversion plate. The rate of cycling can be varied electronically between 0.02 to 1 Hz.

Glass cells were made for immersion of the specimens which were held in position by rubber bungs with holes slightly larger than the dimensions of the specimens. The rubber bungs were also coated with Lacomit to avoid contamination. The gap between the specimens and the bungs was filled with two pack "Silastic" silicone product and Araldite was used outside the cell to prevent leakage of the electrolyte. The experimental arrangement is shown in Figure E 5.

Connection to the saturated calomel electrode was made through a tube made of PVC type material, with a taper end which was secured to the specimen by using rubber "O" rings. The distance between the specimen and the taper end was kept to a minimum throughout the tests. The counter electrode was a platinum gauze cylinder encased in a polythene tube with a glass wool plug inserted in one end.

#### 3.4.5.3 Procedure

Prior to the corrosion fatigue tests, corrosion current was measured without an applied stress. Current was also measured with monotonically applied load. The specimen was stressed in compression for a period, unloaded, and then held in tension.

#### 3.4.5.2 Apparatus

The reverse bend fatigue testing machine is shown in Figure E 3. The stress is applied to the specimen by means of an eccentrically driven shaft which provides the stroke of the machine. Individual stress ranges may be obtained by re-positioning the shaft in the drive conversion plate. The rate of cycling can be varied electronically between 0.02 to 1 Hz.

Glass cells were made for immersion of the specimens which were held in position by rubber bungs with holes slightly larger than the dimensions of the specimens. The rubber bungs were also coated with Lacomit to avoid contamination. The gap between the specimens and the bungs was filled with two pack "Silastic" silicone product and Araldite was used outside the cell to prevent leakage of the electrolyte. The experimental arrangement is shown in Figure E 5.

Connection to the saturated calomel electrode was made through a tube made of PVC type material, with a taper end which was secured to the specimen by using rubber "O" rings. The distance between the specimen and the taper end was kept to a minimum throughout the tests. The counter electrode was a platinum gauze cylinder encased in a polythene tube with a glass wool plug inserted in one end.

#### 3.4.5.3 Procedure

Prior to the corrosion fatigue tests, corrosion current was measured without an applied stress. Current was also measured with monotonically applied load. The specimen was stressed in compression for a period, unloaded, and then held in tension.

During corrosion fatigue tests, changes in potential and corrosion current were recorded. After immersion of the specimens in the electrolyte the rest potential was measured and the test commenced almost immediately. The stresses applied were 0, 198/200 and 247 MPa. Electrical resistance gauges on dummy specimens were used to establish stress ranges. Both the potential and the current were recorded on a Bryans 28000 series recorder. A Vibron was used to monitor the potential while a Wenking potentiostat was used for measuring current. The rate of cycling was 0.02 to 0.2 Hz. The electrolyte was fed by gravity avoiding turbulence of the solution in the cell.

#### 3.4.6 Reverse bend fatigue tests - 24 Hz

##### 3.4.6.1 Specimen preparation

Specimens were made from mild steel sheet material to the specification in Figure E 6.

The surface preparation of the specimens was as described in

3.4.1.1. The ends of the specimens were coated with Lacomit to isolate them electrically from the rest of the machine. The sides of the specimens were also coated with Lacomit. For comparison purposes, specimens with mill scales were also tested; these were only degreased with acetone.

##### 3.4.6.2 Apparatus

A Standard "Avery" reverse bend fatigue testing machine was used for tests. The rate of cycling was 24 Hz.

Since it was not possible to construct a test cell, a pool with a narrow outlet was made with Araldite on the top surface of the specimen to hold the electrolyte in place, while the reverse side was left exposed to the ambient environment.

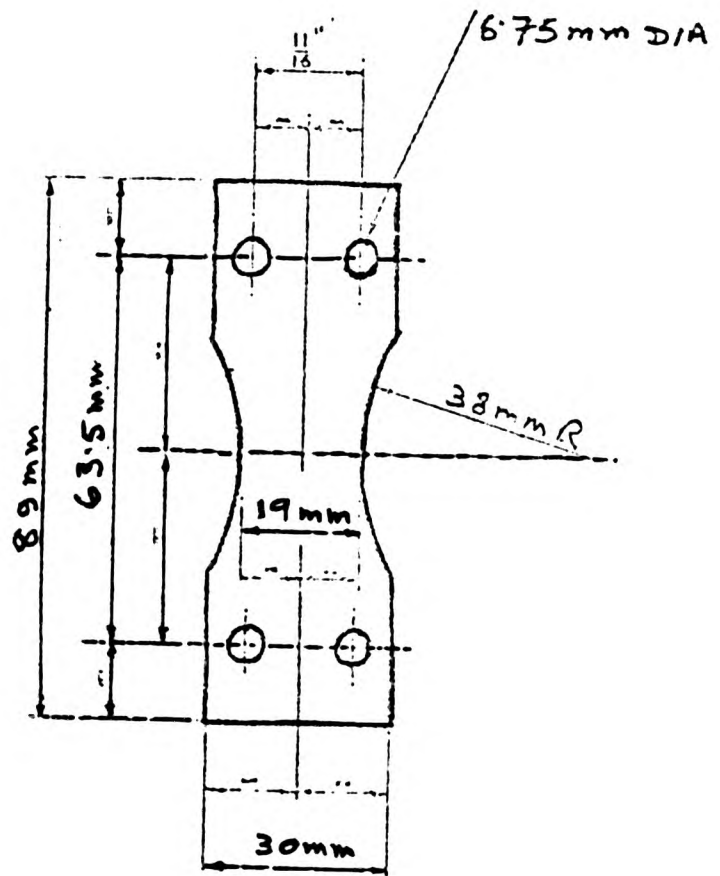


Fig E 6: Reverse bend fatigue test specimen (24 Hz).

Connection to the saturated calomel reference electrode was made through a thin PVC type tube with a taper end which was secured to the specimen by using rubber "O" rings. The distance between the specimen and the taper end was kept to a minimum throughout the tests.

The counter electrode was a platinum gauze cylinder encased in cotton wool which formed part of the drip feed system of the electrolyte (Figure E 7). The distance between the tip of the cotton wool casing and the surface of the specimen was kept to a minimum so that there was a continuous electrical path between the counter and the working electrode.

#### 3.4.6.3 Procedure

During corrosion fatigue tests, changes in potential and corrosion current were recorded using a Wenking potentiostat and a Bryans 28000 series chart recorder. The stresses applied were 170 and 277 MPa for polished and 170 MPa for mill scaled specimens. Higher stresses were not used for mill scaled specimens since it was observed, during the performance trials, that failure at higher stresses generally occurred at the edge of or underneath the Araldite. Disbonding also occurred between Araldite and the metal surface with the consequence that air bubbles were introduced into the PVC capillary tube. This resulted in the breakdown of the electrical circuit. Longitudinal and transverse surfaces of the specimens were examined using optical and scanning electron microscopy.

### 3.5 Immersion tests

#### 3.5.1 Specimen preparation

The specimens were made from wrought mild steel bars to the specification shown in Figure E 8. These were sectioned parallel to the

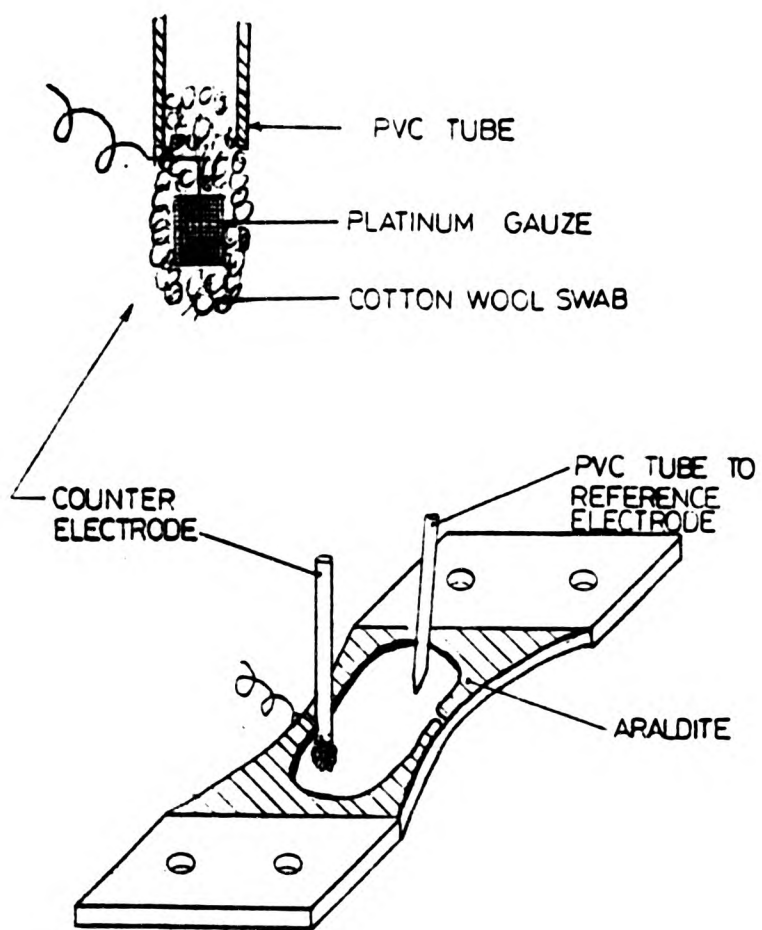


Fig E 7: Experimental arrangement of reverse bend fatigue test specimens (24 Hz).

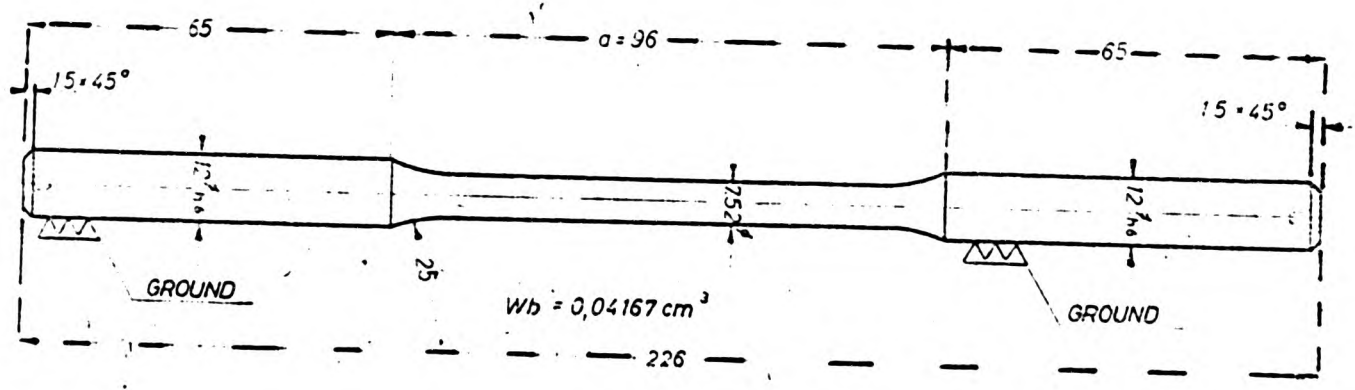


Fig E 8: Rotating bend fatigue test (47 Hz) specimen.

rolling direction. The surface preparation of the specimens was as described in 3.4.1.1. Some of the specimens were annealed at 925° C for 3 hours in argon and furnace cooled before grinding and polishing.

### 3.5.2 Apparatus

A pyrex beaker was used for immersion tests. For examination of the specimen surfaces scanning electron microscope, principal X-ray emission spectra of chemical elements (Link Systems Ltd), and JEOL 3A electron probe micro-analyser were used.

### 3.5.3 Procedure

Inclusions were analysed using a stationary beam with the specimen moving across at 10  $\mu\text{m}$  per minute. A beam current of approximately  $2 \times 10^{-2}$  amps was used. Specimens were also examined using scanning electron microscopy.

## 3.6 Metallurgical examinations: Rotating bend fatigue tests - 47 Hz

### 3.6.1 Specimen preparation

The specimen preparation was as described in 3.5.1.

### 3.6.2 Apparatus

Standard Schenck rotating bend fatigue testing machines were used for the tests. The rate of cycling was 47 Hz.

A perspex chamber, consisting of two halves, was employed as the test cell. Sodium chloride solution was drip-fed onto the centre of the rotating specimens through a PTFE nozzle, the distance between the specimen surface and the nozzle being kept to a minimum.

### 3.6.3 Procedure

#### 3.6.3.1 Scanning electron microscopic (SEM) examination

Fatigue tests were performed at 47 Hz. The stresses applied to the specimens ranged from ~~177~~<sup>183</sup> to 309 MPa.

In order to study the change in surface morphology of the specimens due to straining, scanning electron microscopy was used. Transverse surfaces of the fractured surfaces were also examined.

Immediately after completion of each test exposure, the specimens were cleaned in 1% hot tri-ammonium citrate solution to remove corrosion products and chloride ions from the surface and crevices<sup>197</sup>, washed in de-ionised water followed by alcohol and finally dried in warm air. The longitudinal surfaces of the test specimens were examined by using scanning electron microscopy (Hitachi S 410 and Philips 200) and principal X-ray emission spectra of chemical elements (Link Systems Ltd).

The approximate pH of the solution within the crevices and micropits was measured by freezing the fatigued specimens in situ in liquid nitrogen followed by pressing pH indicator papers at the corroded area on the external surfaces of the specimens. Some of these frozen specimens were also fractured and the pH was measured by pressing the indicator paper on the fractured surface.

Attempts were made to measure potentials during the fatigue tests. The drip-fed system of the electrolyte consisted of a flexible polyester tube with a cotton wool plug inserted at one end. The distance between the tip of the cotton wool and the surface of the specimen was kept to a minimum so that there was a continuous electrical path between the saturated calomel reference electrode, which was placed in the reservoir containing the electrolyte, and the working electrode.

Tests were interrupted to stop the rotating specimens and the connection to the working electrode was made as quickly as possible. The potentials were measured without unloading the stressed specimens. However, the measurements were fraught with difficulties and the results were not always reproducible. For this reason it was not pursued further.

#### 3.6.3.2 Transmission electron microscopic (TEM) examination

Fatigue tests were performed at 47 Hz. The stresses applied to the specimens ranged from 95 to 309 MPa.

In order to study the change of surface morphology of the specimens due to straining, fatigue tests were interrupted at various intervals to obtain plastic replicas for observation using transmission electron microscopy. Immediately after the interruption of each test the specimen was cleaned in 1% hot tri-ammonium citrate solution, in situ, to remove corrosion products and chloride ions from the surfaces and crevices<sup>197</sup>, washed in de-ionised water followed by alcohol.

Indirect carbon replicas were obtained using a standard technique. This involved moistening a cellulose acetate film in acetone and pressing it against the specimen surface to be examined. In practice, two plastic replicas were made. The first was discarded, its function being to clean the surface, and the second was used in the production of carbon replica. The second replica was placed in an evaporating unit and after evacuation, gold-palladium alloy was deposited at an angle of  $45^{\circ}$  after the initial deposition of carbon directly from two carbon electrodes. The replica with carbon and gold-palladium alloy shadowing was removed from the chamber and cut into pieces approximately 3 mm square.

These were then immersed in successive solvents, e.g. in acetone to remove plastic, in "Inhibisol" to dissolve grease, and in methylated spirit to remove contaminants. The remaining shadowed carbon replicas were examined using AEI EM6G electron microscope, replicas being taken from the longitudinal surfaces of the specimens.

## 4 RESULTS

### 4.1 Anodic polarisation tests

Two main types of experiments were performed : anodic potentiokinetic polarisation from a low potential not sufficiently negative for complete reduction of the air-formed oxide film, and anodic potentiostatic polarisation from a fixed current density. Both stagnant and flowing electrolyte conditions were used. To observe the influence of cyclic stress on the anodic polarisation, the condition of 169 MPa at  $R = -1$  was also superimposed in potentiostatic tests.

It has been suggested that the breakdown potentials,  $E_b$ , determined with anodic polarisation are most reproducible with highly polished surfaces<sup>155</sup>. For this reason, polished surfaces were used for all tests. Where the breakdown potential is not clearly defined in the polarisation curves, potentials at which a marked increase in anodic current occurs during polarisation, indicating the onset of rapid dissolution of iron, have been recorded. The potentials refer to the saturated calomel electrode (SCE) and the current densities to the geometric areas.

Typical potentiostatic curves, in aerated 0.6 M sodium chloride solution of pH 6.5 with and without stress, are shown in Figures R 1a to R 3a. These curves have been re-drawn with current densities on expanded linear scales to clarify the peak positions in the curves (Figures R 1b to R 3b). Typical potentiokinetic polarisation curves are shown in Figure R 4.

## 4 RESULTS

### 4.1 Anodic polarisation tests

Two main types of experiments were performed : anodic potentiokinetic polarisation from a low potential not sufficiently negative for complete reduction of the air-formed oxide film, and anodic potentiostatic polarisation from a fixed current density. Both stagnant and flowing electrolyte conditions were used. To observe the influence of cyclic stress on the anodic polarisation, the condition of 169 MPa at  $R = -1$  was also superimposed in potentiostatic tests.

It has been suggested that the breakdown potentials,  $E_b$ , determined with anodic polarisation are most reproducible with highly polished surfaces<sup>155</sup>. For this reason, polished surfaces were used for all tests. Where the breakdown potential is not clearly defined in the polarisation curves, potentials at which a marked increase in anodic current occurs during polarisation, indicating the onset of rapid dissolution of iron, have been recorded. The potentials refer to the saturated calomel electrode (SCE) and the current densities to the geometric areas.

Typical potentiostatic curves, in aerated 0.6 M sodium chloride solution of pH 6.5 with and without stress, are shown in Figures R 1a to R 3a. These curves have been re-drawn with current densities on expanded linear scales to clarify the peak positions in the curves (Figures R 1b to R 3b). Typical potentiokinetic polarisation curves are shown in Figure R 4.

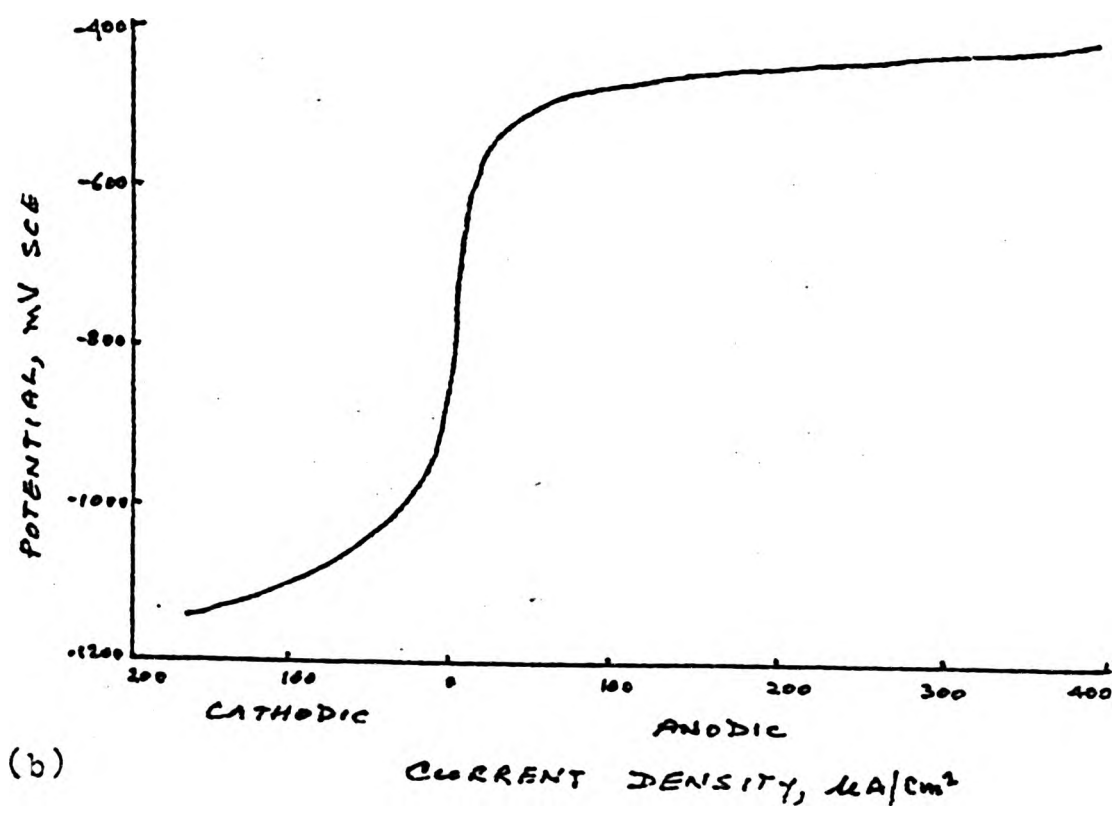
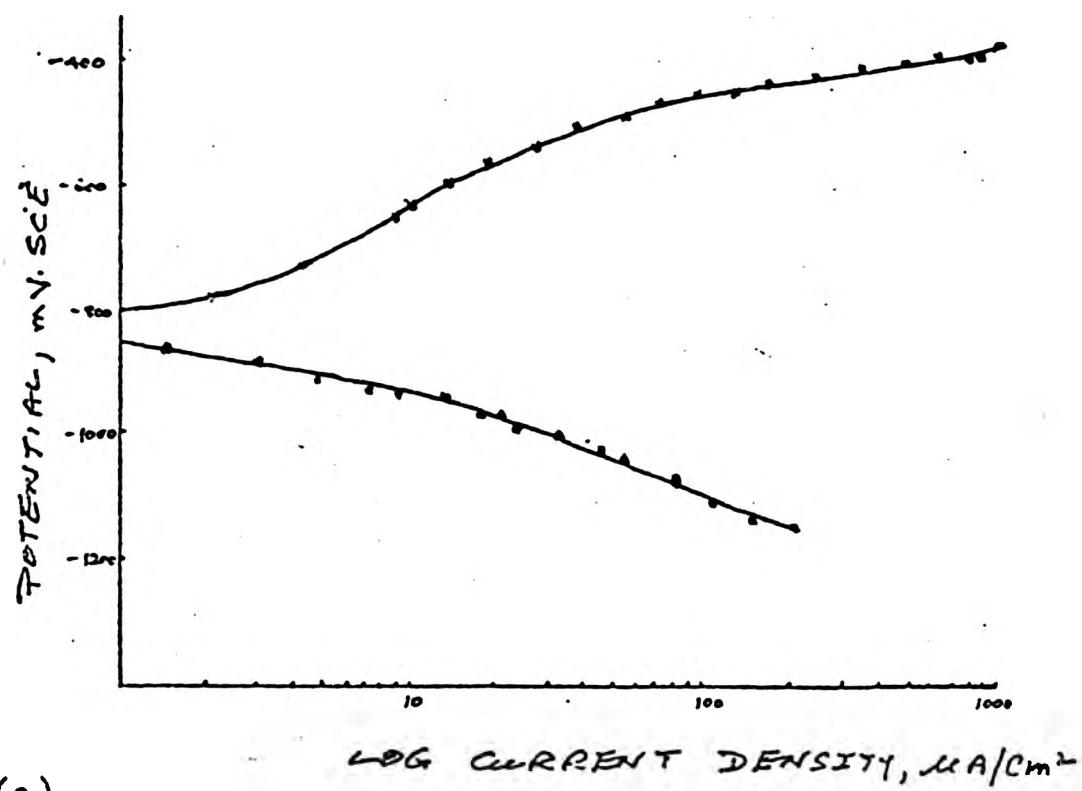
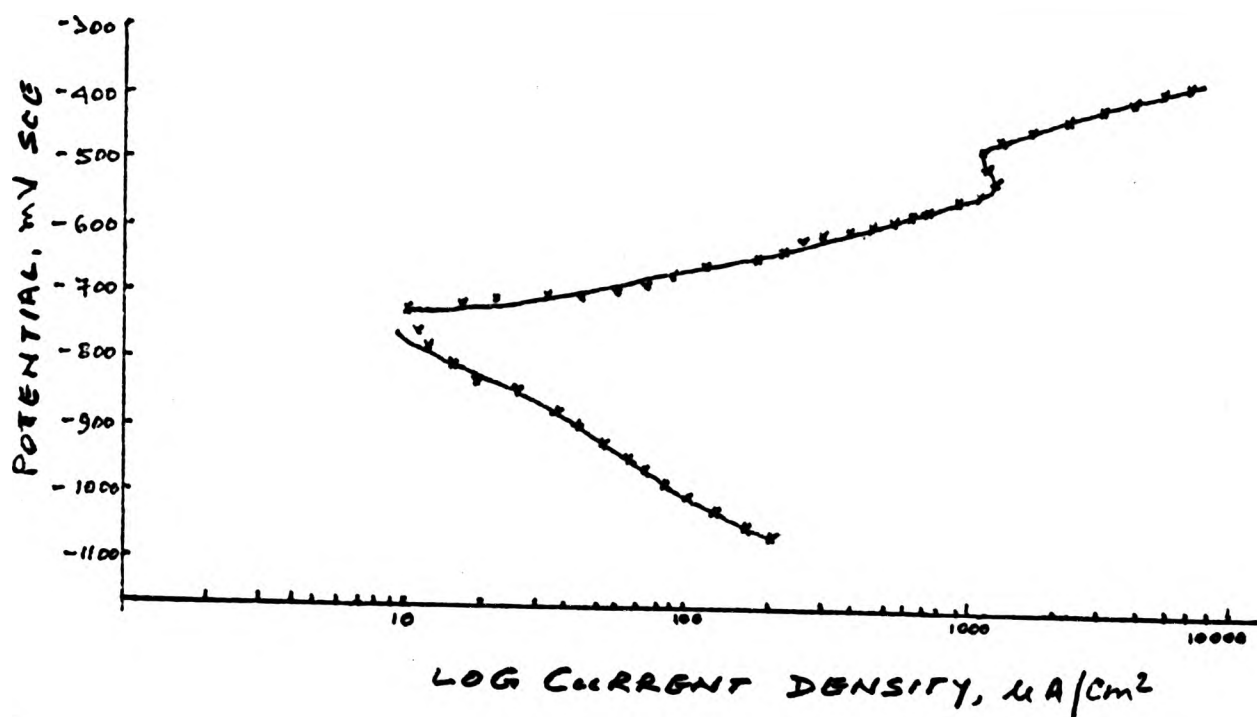
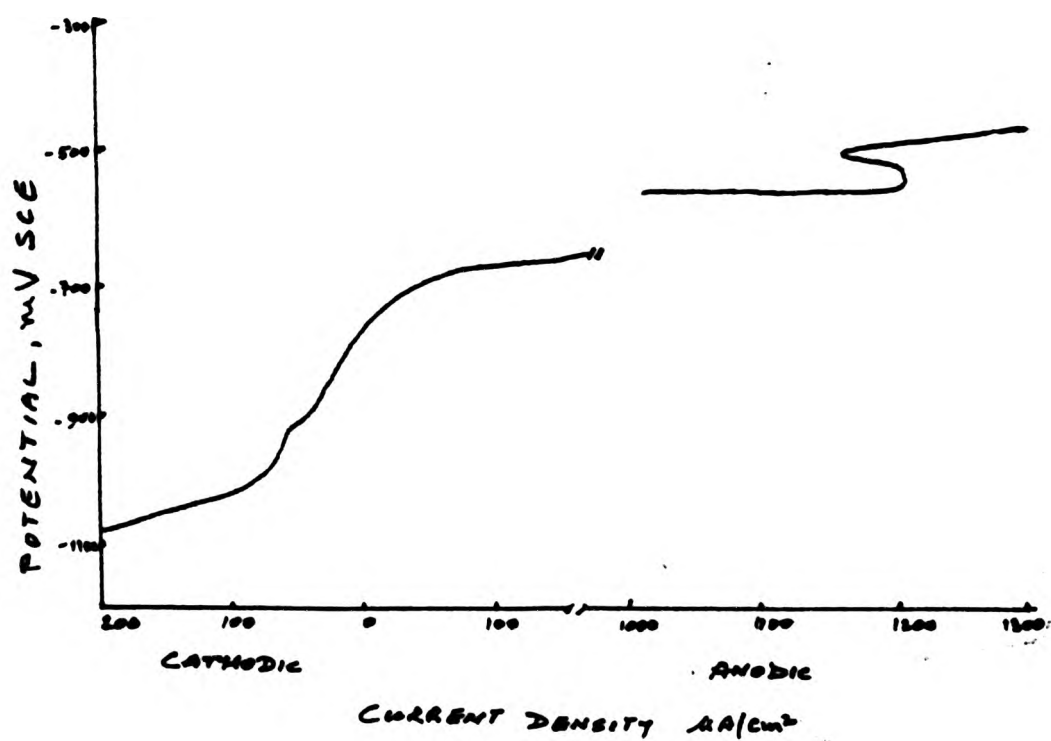


Fig R 1: Typical potentiostatic polarisation curve for mild steel in 0.6 M sodium chloride solution in stagnant condition without an applied stress. Current density is plotted on (a) log and (b) linear scales.



(a)



(b)

Fig R 2: Typical potentiostatic polarisation curve for mild steel in 0.6 M sodium chloride solution in flowing electrolyte. Current density is plotted on (a) log and (b) linear scales.

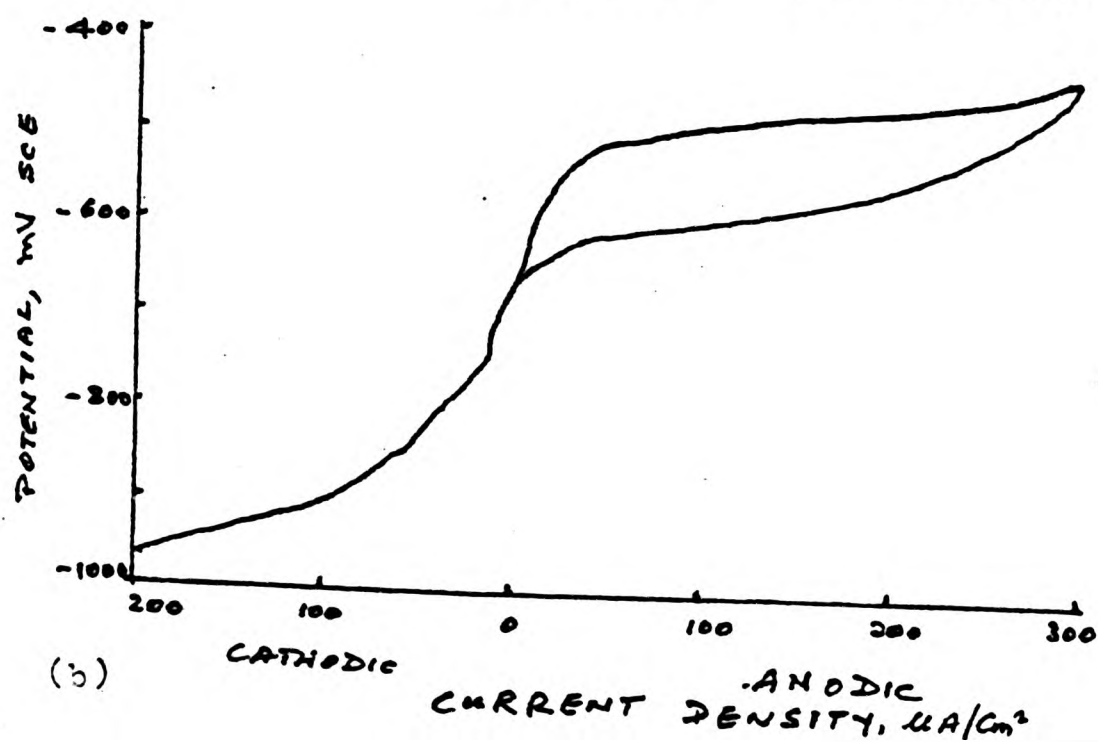
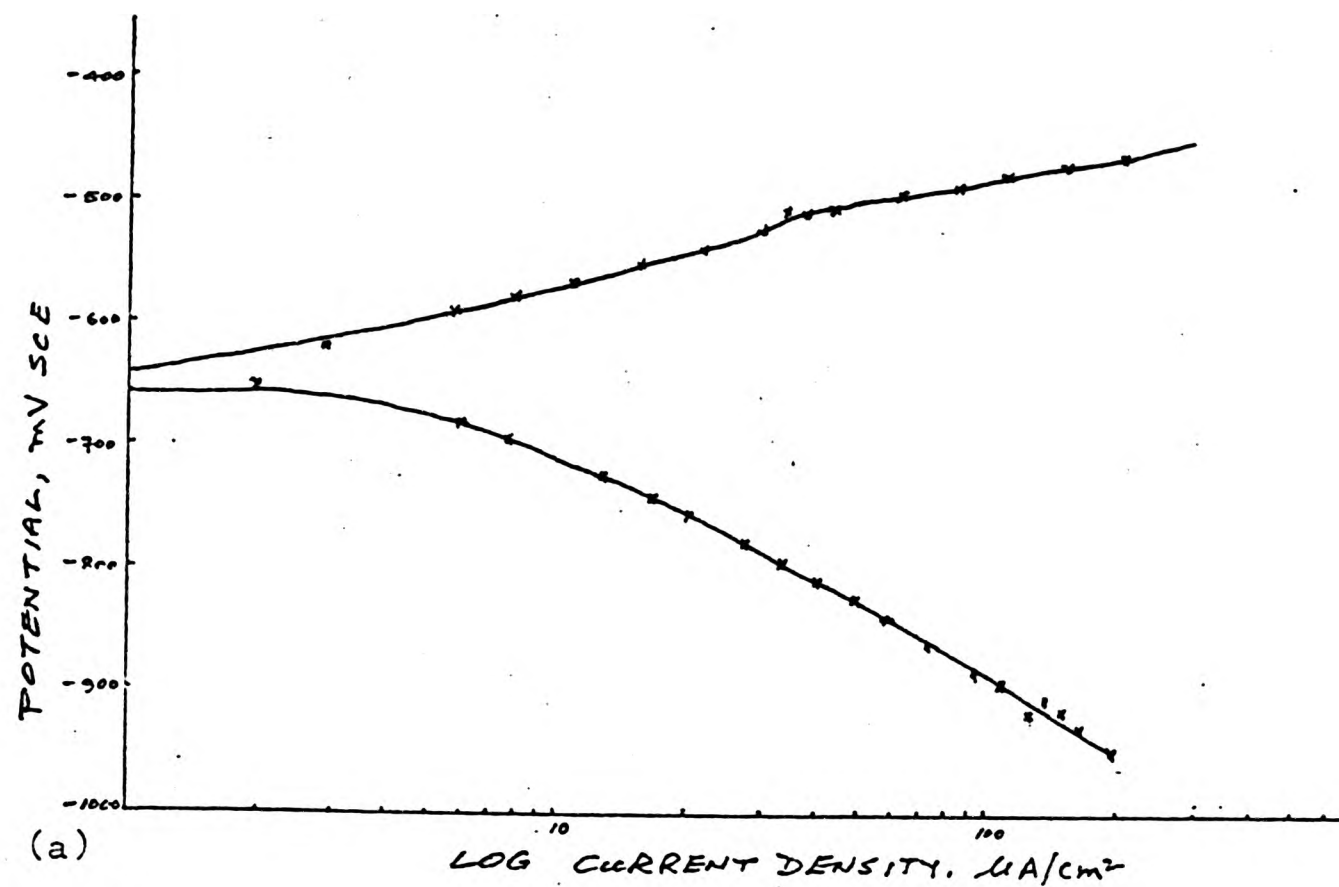


Fig R 3: Typical potentiostatic polarisation curve for mild steel in 0.6 M sodium chloride solution in flowing electrolyte. Current density is plotted on (a) log and (b) linear scales. Stress: 169 MPa, R=-1.

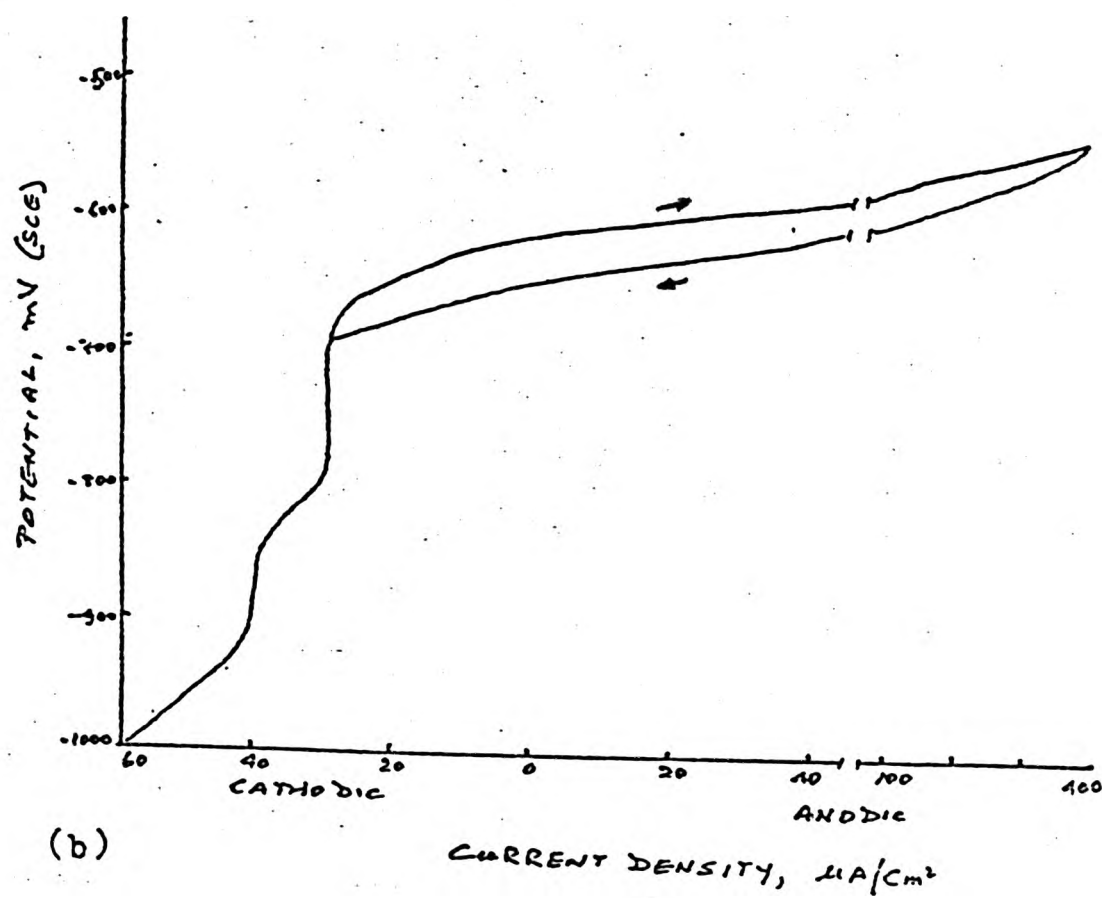
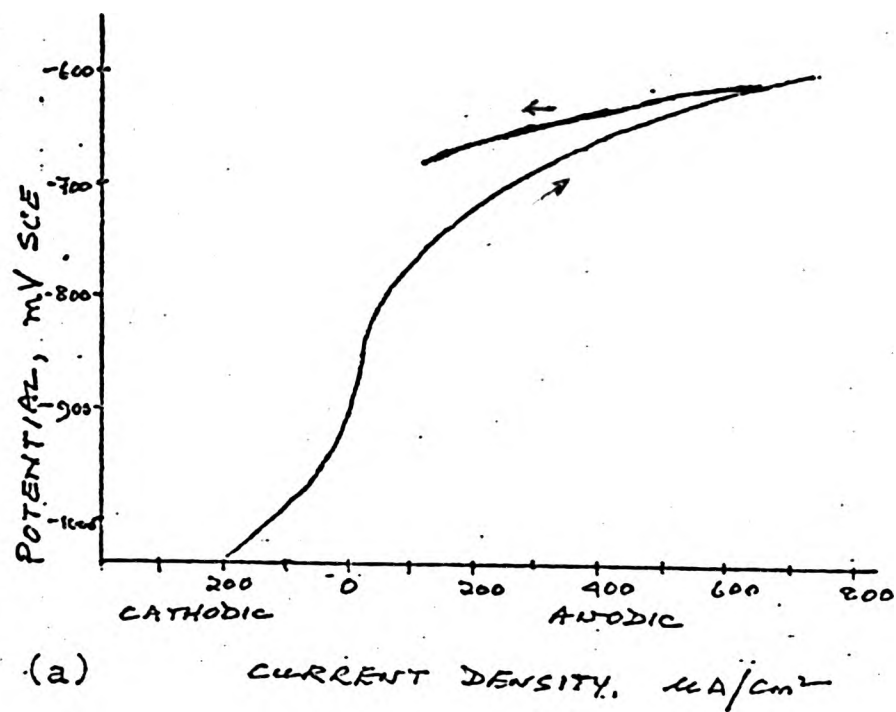


Fig R 4: Typical potentiokinetic polarisation curves for mild steel in 0.6 M sodium chloride solution in (a) stagnant and (b) flowing electrolyte conditions without an applied stress.

T A B L E I

Summary of Results of Anodic Polarisation of Mild Steel in Sodium Chloride Solutions

	<u>Potentiostatic Tests</u>				<u>Potentiokinetic Tests</u>	
	<u>Stagnant electrolyte</u>		<u>Flowing electrolyte</u>		<u>Stagnant electrolyte</u>	<u>Flowing electrolyte</u>
	No stress	No stress	Cyclic stress	No stress	No stress	No stress
Zero current (mV SCE)	-830 <sup>+</sup>	-750 <sup>+</sup>	-650 <sup>+</sup>	-860	-615	
E <sub>p</sub> (mV SCE)	-	-	-650	-	-690	
E <sub>b</sub> (mV SCE)	-550	-700 <sup>*</sup>	-550 <sup>*</sup>	-690 <sup>*</sup>	-630 <sup>*</sup>	
i <sub>pass</sub> ( $\mu\text{A}/\text{cm}^2$ )	5	-	-	-	-	
E <sub>Corr</sub> (mV SCE)	-810	-770	-620	-	-	
i <sub>Corr</sub> ( $\mu\text{A}/\text{cm}^2$ )	2.1	3	4.3	-	-	

+ estimated value from graph

\* denotes a marked increase in anodic current

The zero currents observed during potentiostatic tests are approximately at  $-830$  mV in stagnant solution and  $-750$  mV in flowing electrolyte at zero stress. Under cyclic stress at  $0.2$  Hz ( $169$  MPa,  $R = -1$ ) the zero current was noted at nearly  $-650$  mV in flowing electrolyte.

$E_{\text{corr}}$   $I_{\text{corr}}$  values are calculated by drawing straight lines along the linear portions of the anodic and cathodic curves of  $E$  vs  $\log i$  plots. The results are summarised in Table I.

When the curves are re-drawn on expanded linear scales, Figures R 1b to R 3b, some features which have not been so evident in Figures R 1a to R 3a tend to appear somewhat more prominent. The " $E_b$ " values calculated from the re-drawn curves are:  $-550$  mV in stagnant and  $-700$  mV in flowing electrolytes at zero stress. Under cyclic stress, " $E_b$ " appears to be  $-550$  mV. It has also been possible to show the presence of an hysteresis loop with  $E_p$ , the potential, at  $-650$  mV (Figure R 3b).

In flowing electrolyte with zero stress, a small peak current at approximately  $1000 \mu\text{A}/\text{cm}^2$  in the anodic portion of the curve is observed at  $-550$  mV (Figure R 2a). On the re-drawn curve (Figure R 2b), a marked increase in current is observed at approximately  $-700$  mV and the peak current possibly suggesting the formation followed by breakdown of an oxide film is also noted.

In potentiokinetic polarisation tests, the zero currents were observed at  $-860$  mV and  $-615$  mV in stagnant and flowing electrolytes respectively. The results are summarised in Table I.

Comparison of the two curves in Figure R 4, shows that in stagnant solution for some reason the polarisation curve is displaced from the cathodic to the anodic region over a narrow range of potentials in which the current recorded appears to be essentially constant. This potential region possibly corresponds to that of oxygen reduction. The pH of the solution after the test was found to be approximately 5 although at the commencement of the test the pH value of the electrolyte was 6.5. In flowing electrolyte the pH of the solution before and after the tests was the same.

#### 4.2 Scratching electrode tests

The potential and corrosion current against time curves are shown in Figure R 5.

The corrosion current with an applied potential equivalent to -680 mV (SCE) exhibited a relatively steady increase until a scratch was made to displace the surface of the film. An instantaneous change of current in cathodic direction was observed. However, this change was not permanent and the subsequent anodic current was found to be higher than that obtained initially.

Figure R 5b shows the potential against time curve after the steady state was nearly achieved. The removal of the surface film with a glass rod exhibited a change in potential in a more positive direction. The return of the potential to its original value was practically instantaneous. Subsequently it moved to a more negative direction than that obtained prior to the scratching of the specimen surface.

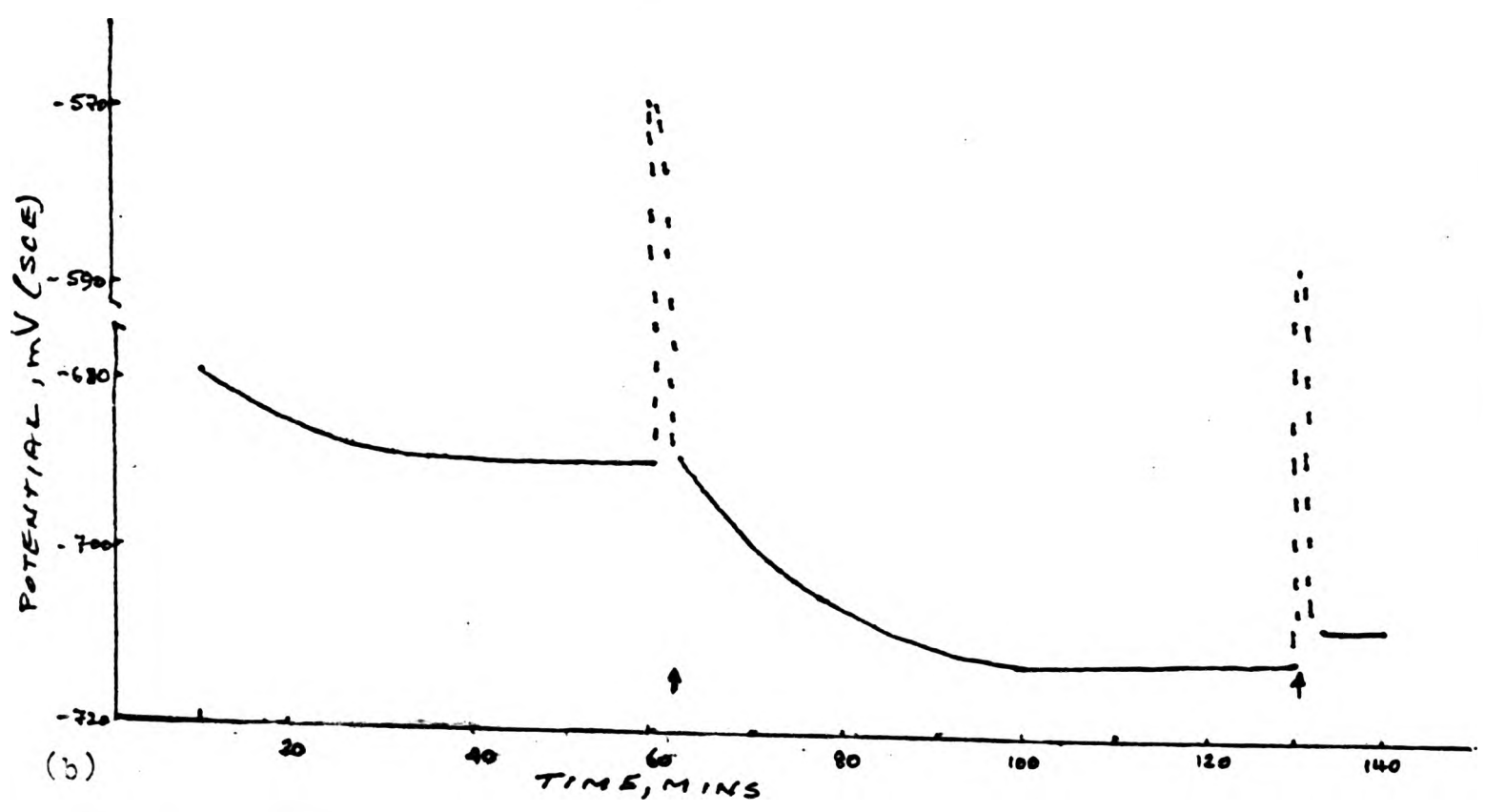
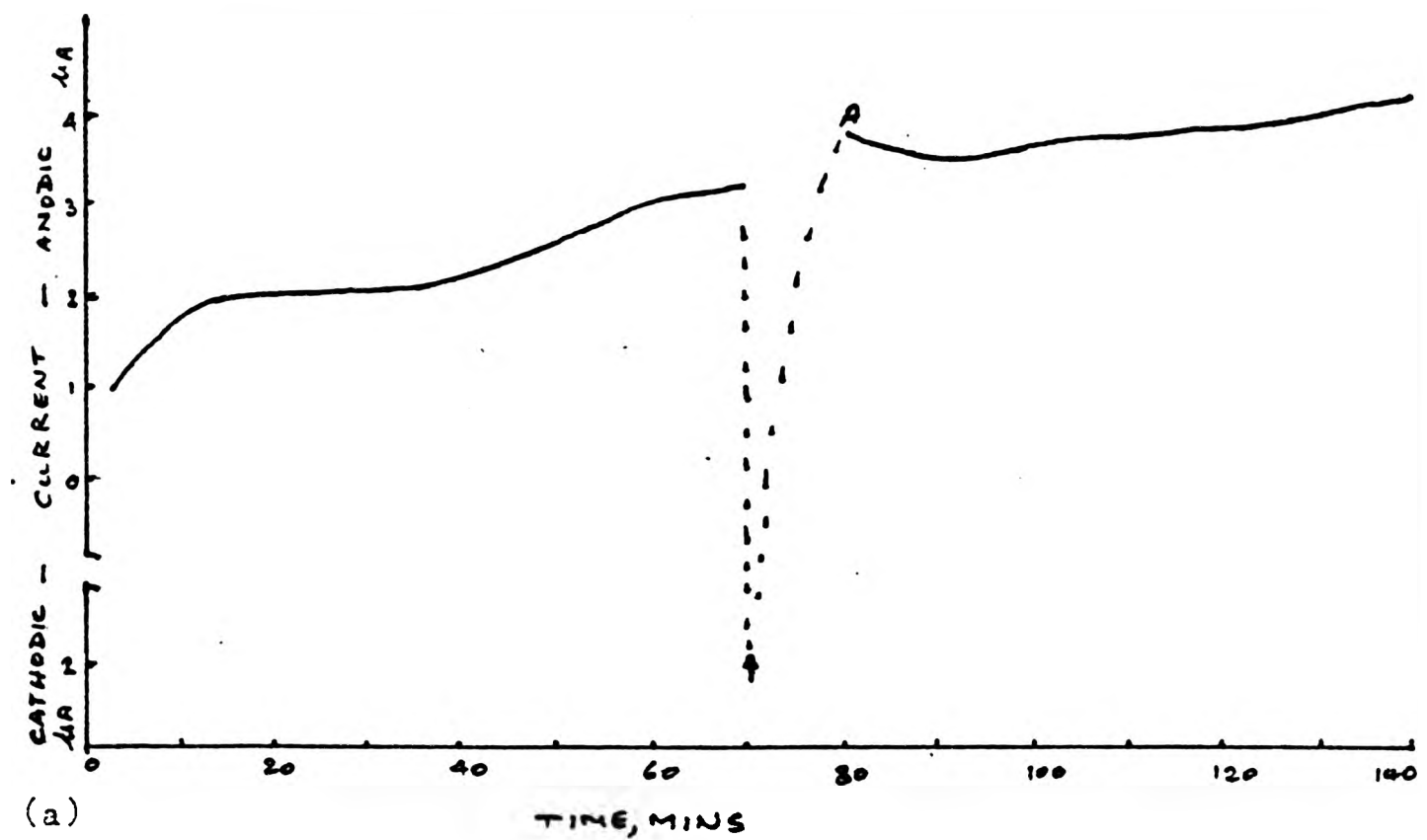


Fig R 5: Typical current and potential curves for mild steel in 0.6 M sodium chloride solution in flowing electrolyte. Arrows indicate scratching of the specimen surface. Current vs time and potential vs time curves are shown in (a) and (b) respectively.

#### 4.3 Measurement of potential inside a notch

Typical potential vs time curves are shown in Figure R 6. The curves indicate that the potentials gradually decreased and attained a steady state value after approximately 20 hours. The potential inside the notch, after an hour was -643 mV (SCE) while that on the external surface was -610 (SCE). The final potentials thus recorded after 24 hours were -673 mV (SCE) inside the notch and -638 mV (SCE) on the external surface approximately 4 mm away from the mouth of the notch. In the series of measurements, the potential difference between the external surface and inside the notch never exceeded 35 mV. For each test a new specimen was used. The tests were performed at  $20^{\circ}\text{C} \pm 1^{\circ}\text{C}$ , without any applied stress.

On application of a static tensile stress of 15 MPa, the initial potentials inside the notch and on the external surface were found to be the same, i.e. -675 mV(SCE). These gradually decayed to -689 mV (SCE) inside the notch and -690 mV (SCE) on the surface after 7 hours. On application of the static compressive stress, the initial measurement showed that the potential on the external surface remained the same. It, however, decayed with time.

The pH values of the electrolytes extracted from the notch were found to vary between 4.5 and 5.

#### 4.4 Measurement of potential of specimen subjected to tensile stress

Typical potential vs time curves are shown in Figure R 7. For annealed material (Figure R 7a), at zero stress, the potential was -607 mV (SCE) while after the application of a tensile stress of 62 MPa, the potential moved immediately to -613 mV (SCE).

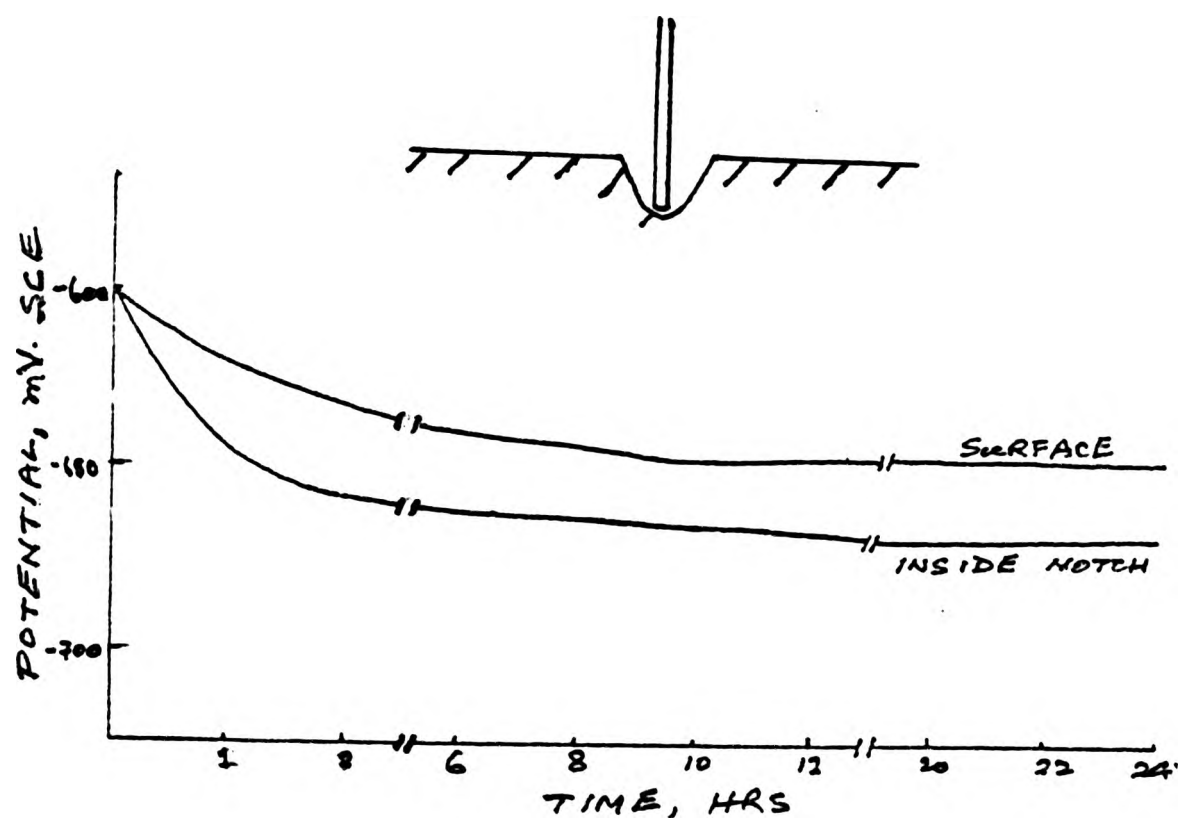


Fig R 6: Typical potential vs time curves for mild steel in 0.6 M sodium chloride solution in flowing electrolyte, indicating the potential drop inside a notch. The inset shows a schematic arrangement of capillary tube inside the notch.

This small potential shift, however, was not permanent. The change of potential was gradual prior to the application of further stress. The load was maintained while the potential measurements were performed.

On increasing the stress from 62 MPa to 124 MPa, the potential after a short period shifted in a positive direction to -585 mV (SCE). This potential shift was also not permanent and the potential returned near to its original value with the passage of time. On further increase of stress, no such large shift in potential in either positive or negative direction was observed. At 247 MPa a small change in potential in the positive direction was recorded.

In the wrought material, a large shift in potential in the positive direction was also observed at a slightly higher stress namely at 173 MPa. A shift in the more negative direction occurred at 199 and 212 MPa. It was observed that for annealed materials at 222 MPa, and for wrought material at 199 MPa, there was a sudden extension of the specimens indicated by the dropping of the mercury level in the loading beam system of the tensometer. The negative shift of potential occurred when this extension was recorded. This tends to suggest that the potential peaks observed for both these materials were possibly due to some surface phenomenon.

It has been observed in potentiokinetic study elsewhere<sup>185</sup> that a passivating surface film forms on mild steel in 0.1 M sodium hydroxide solution, at pH 12.5 when  $E_b$  and  $E_{pp}$  values were found to be +610 and -700 mV (SCE) respectively.

To observe whether the potential shift was due to the mechanical breakdown of a protective surface film, the wrought material was tested in a solution of 0.1 M sodium hydroxide solution, pH 12.5,

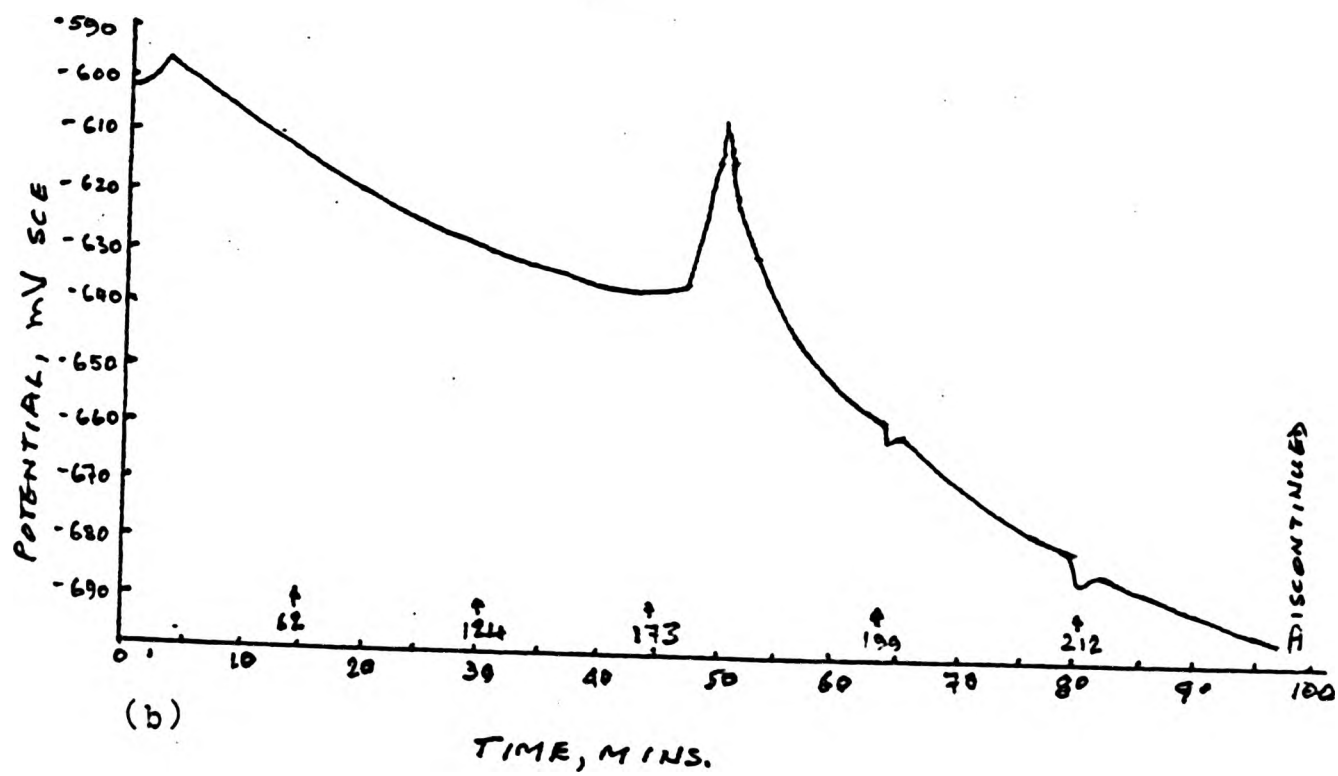
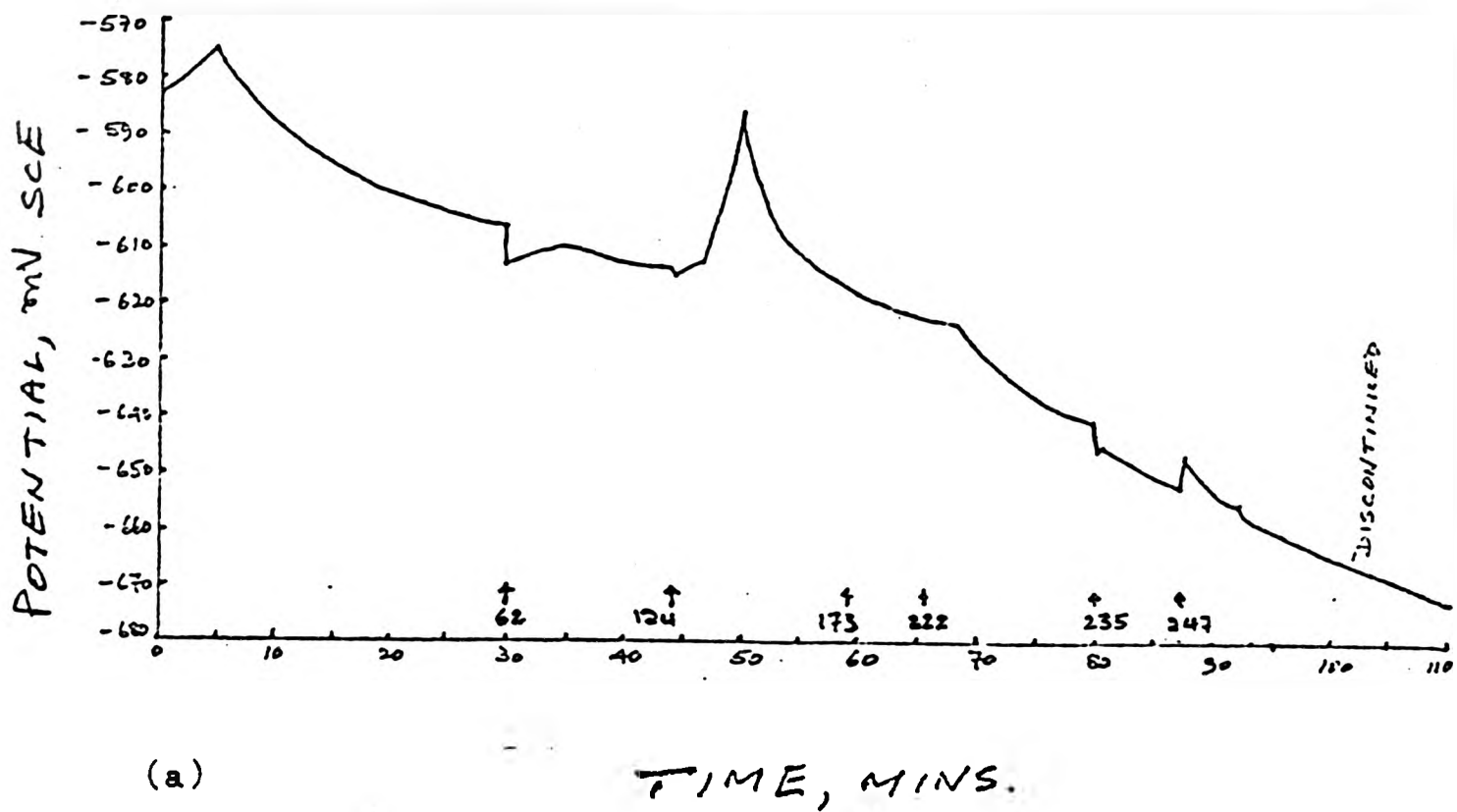


Fig R 7: Typical potential vs time curves for mild steel in 0.6 M sodium chloride solution with applied tensile stress for (a) annealed and (b) wrought material. Fig R 7 (c) shows potential vs time curve for wrought material in 0.1 M sodium hydroxide solution.

in incremental load. The potential vs time curve is shown in Figure R 7c.

#### 4.5 Reverse bend fatigue test - 0.02 to 0.2 Hz

The results of this series of tests are shown in Figure R 8. The corrosion current vs time curve (Figure R 8a) at zero stress in stationary conditions shows that the anodic current does not increase rapidly but tends to fluctuate with time. The applied potential was -650 mV (SCE).

Figure R 8b shows the results when the specimen was subjected to compressive and tensile stresses. After immersion of the test piece, a control potential of -660 mV (SCE) was applied. The specimen was stressed in compression at 200 MPa and was held for a period. The result shows fluctuating anodic current increasing with time. When the specimen was unloaded and held for a short period, anodic current continued to increase. On application of tensile stress the anodic current was found to increase more rapidly. Figure R 8b also shows current peaks observed on unloading and loading (dotted lines).

Plastic deformation has been found to occur when a specimen was subjected to tensile at 199 MPa (Figure R 7b). Increase in corrosion current when the specimen was in compression may also be considered due to the plastic deformation. Even though the macroscopic surface area may actually decrease the change in shape may still cause metal surface to be exposed to the corroding solution.

The stress/current vs time relationship over the first few cycles for tests carried out at 198 MPa,  $R = -1$ , with an applied potential of -560 mV (SCE), at 0.07 Hz, are shown in Figure R 8c.

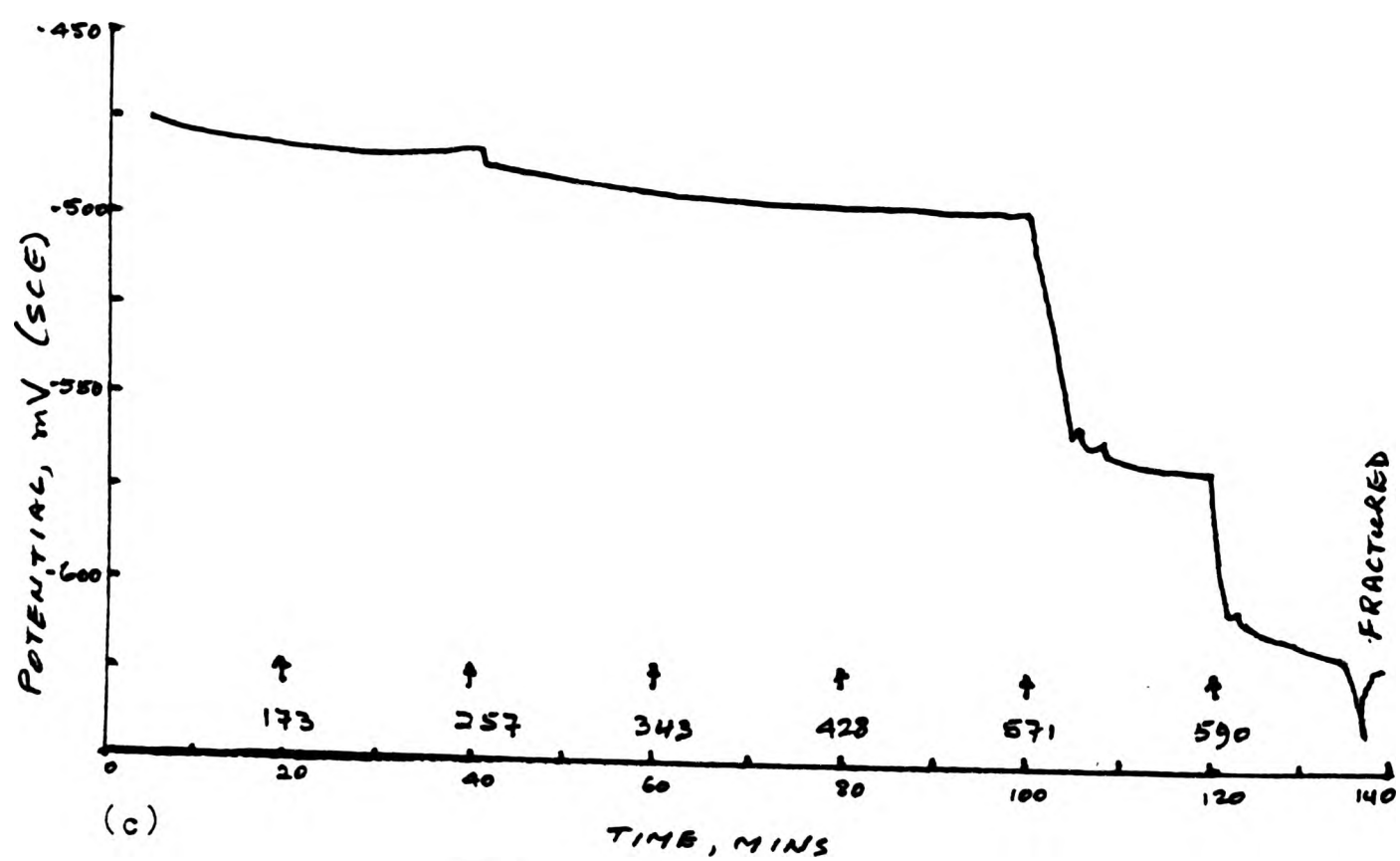
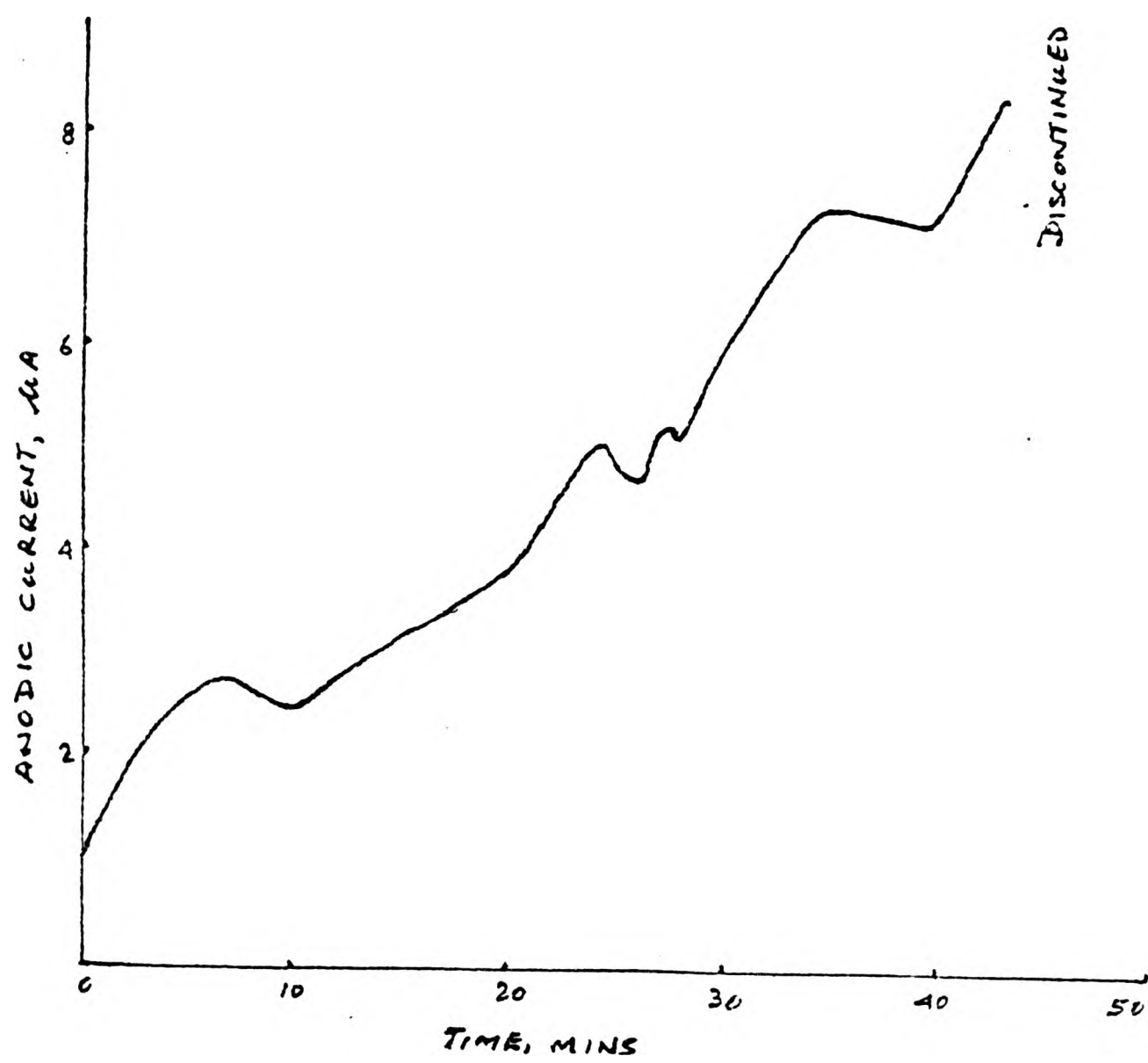
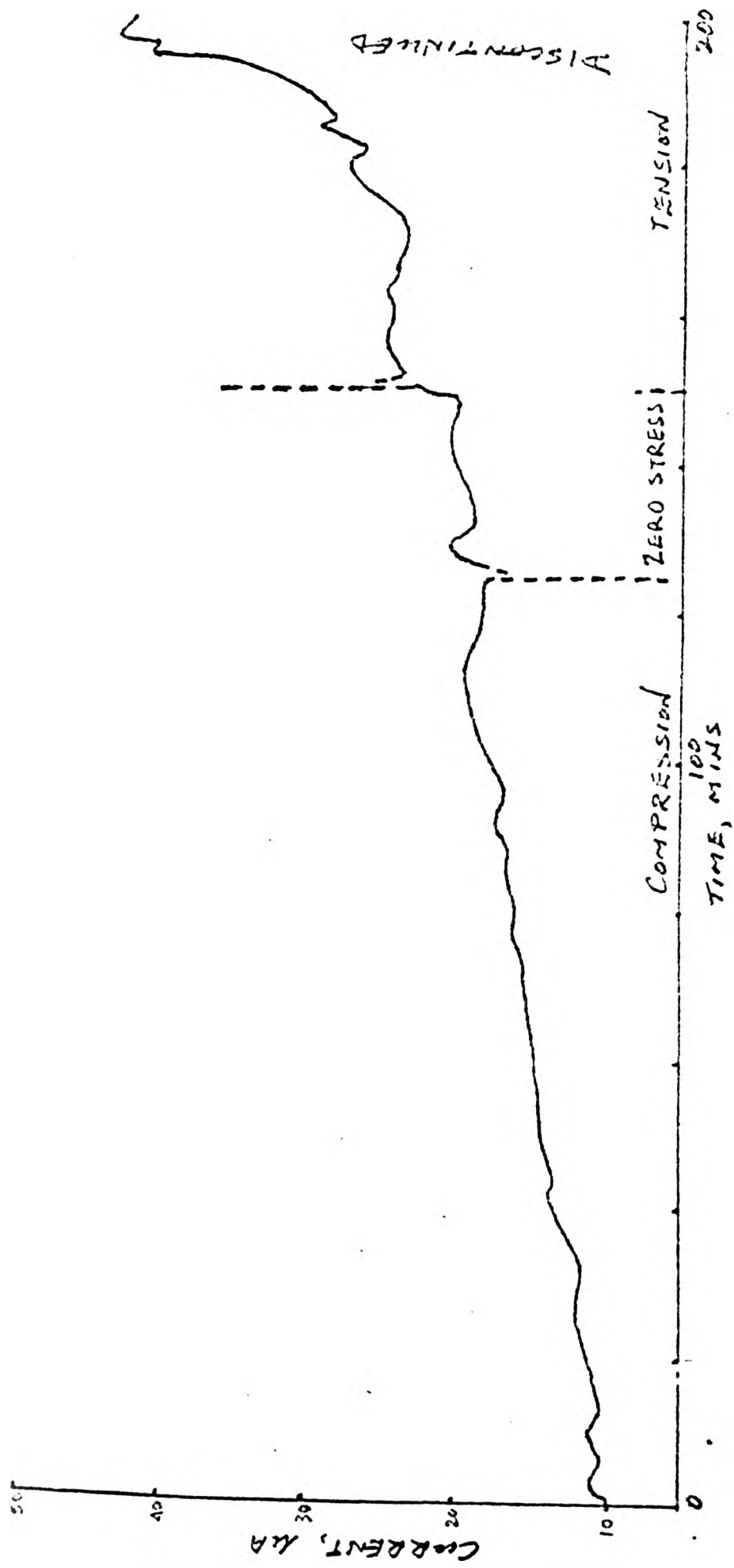


Fig R 7: Typical potential vs time curves for mild steel in 0.6 M sodium chloride solution with applied tensile stress for (a) annealed and (b) wrought material. Fig R 7 (c) shows potential vs time curve for wrought material in 0.1 M sodium hydroxide solution.



(a) Corrosion current vs time curve at zero stress in stationary condition at an applied potential of -650 mV (SCE).

Fig R 8: Typical curves for mild steel in 0.6 M sodium chloride solution.



(b) Corrosion current vs time under compressive and tensile stress in stationary condition at  $-660$  mV (SCE) applied potential, 200 MPa.

Fig R 8: Typical curves for mild steel in 0.6 M sodium chloride solution.

The slow strain reversals were necessary to observe the positions of the current and load peaks.

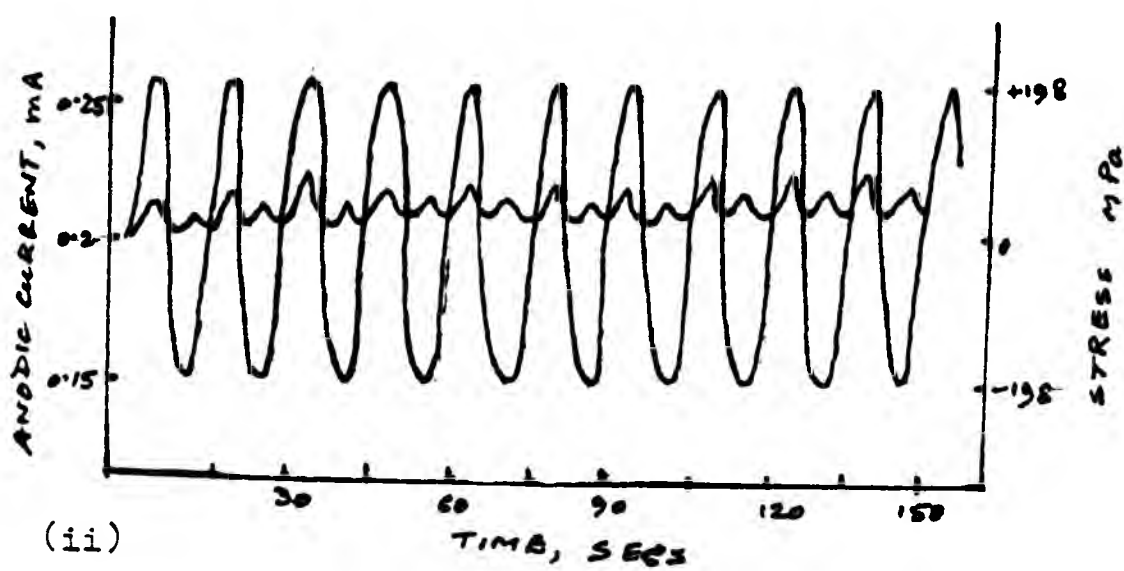
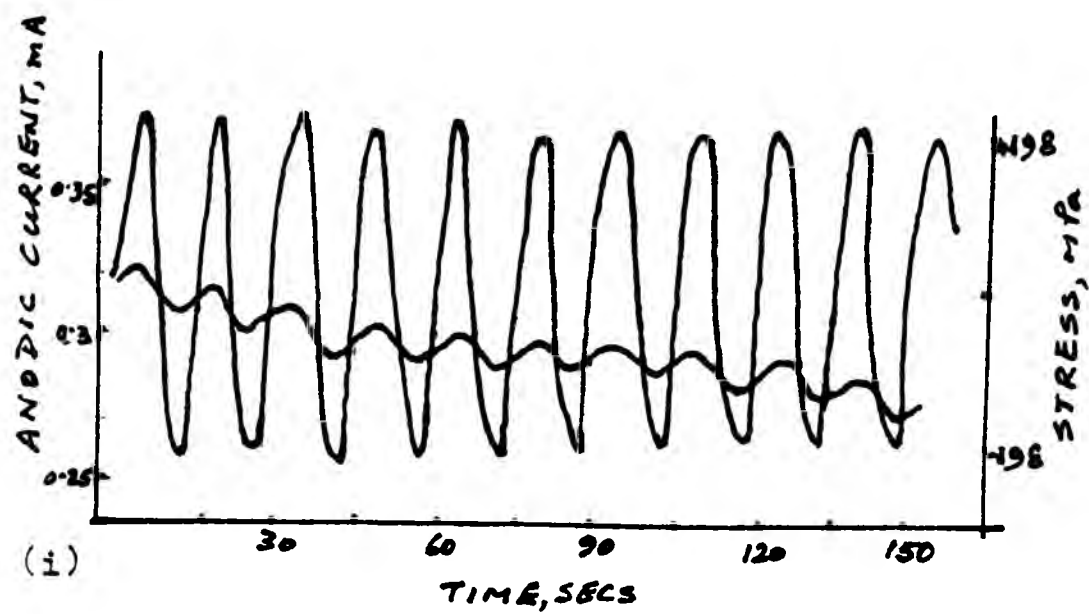
The results show that if a film or scale exists on the surface, the mean current initially tends to move in the cathodic direction with the current maxima and minima occurring immediately before or after the attainment of maximum tensile and compressive loads respectively (Figure R 8c (i)). Approximately 20 minutes after the commencement of the test, current changes direction. When the mean current moves in the anodic direction (Figure R 8c (ii)) the current peaks for some of the time appear to synchronise with the load cycle. Some of the current peaks appear to occur just before or after the load maximum and minimum.

There is a transition period between the cathodic and anodic movement when the mean current is stable. During this period the current maxima and minima tend to coincide with the tensile and compressive load cycles.

When the specimen contains only the air formed film the tendency of the movement of the mean current remains the same. However, the period during which the mean current moves in the cathodic direction and that of the transition region are shorter, (Figures R 8c (iii) and R 8c (iv)).

Changes in potential of a corrosion fatigue test specimen under static condition were recorded and are shown in Figure R 8d. The curve shows that the potential gradually decreases and attain a steady value,  $-650$  mV (SCE), after nearly 16 hours.

Results of fatigue tests at 198 MPa, exhibiting the change in potential and current are shown in Figures R 8e and R 8f respectively.

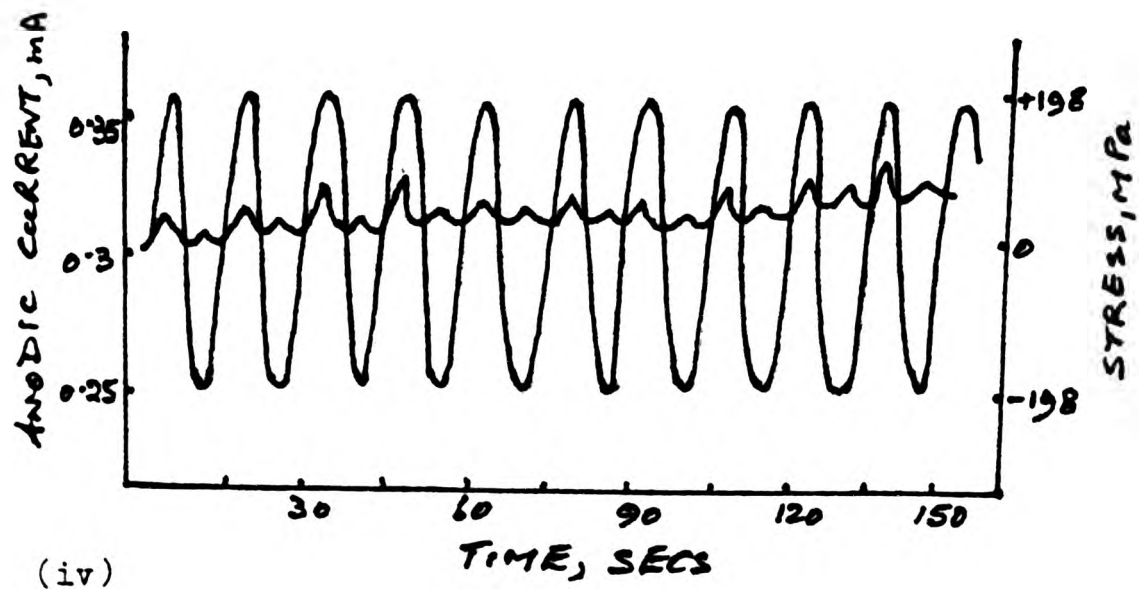
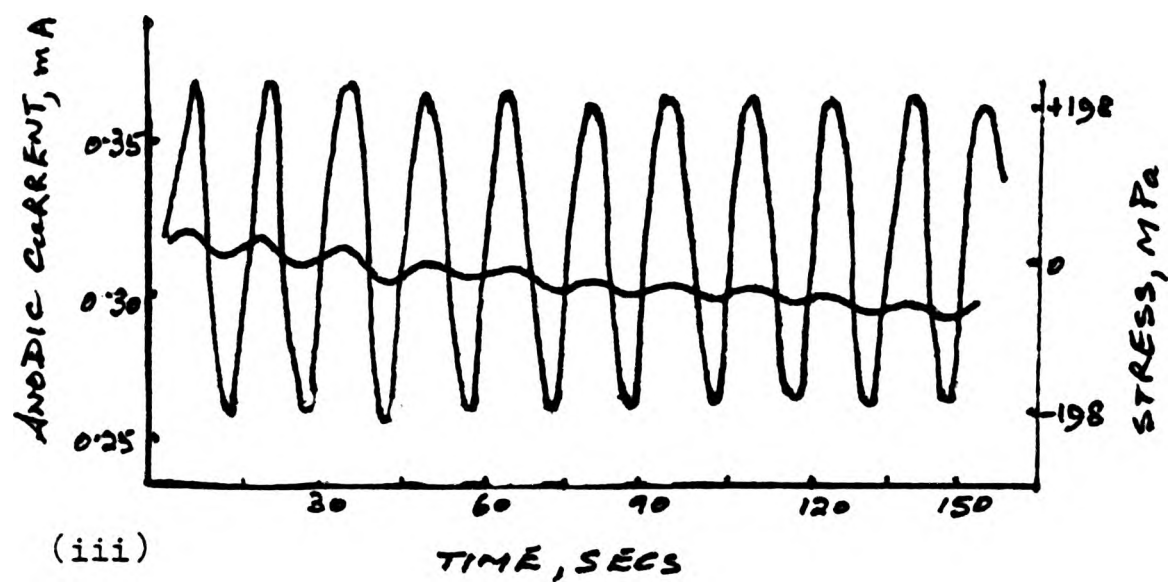


(c) Anodic current and stress as a function of time for a specimen under cyclic stress, 198 MPa,  $R=-1$ , at 0.07 Hz with an applied potential of -560 mV (SCE).

(i) immediately after commencement of test,

(ii) approximately 20 minutes after commencement of test. Specimen with surface scale of hydrated oxide.

Fig R 8: Typical curves for mild steel in 0.6 M sodium chloride solution.

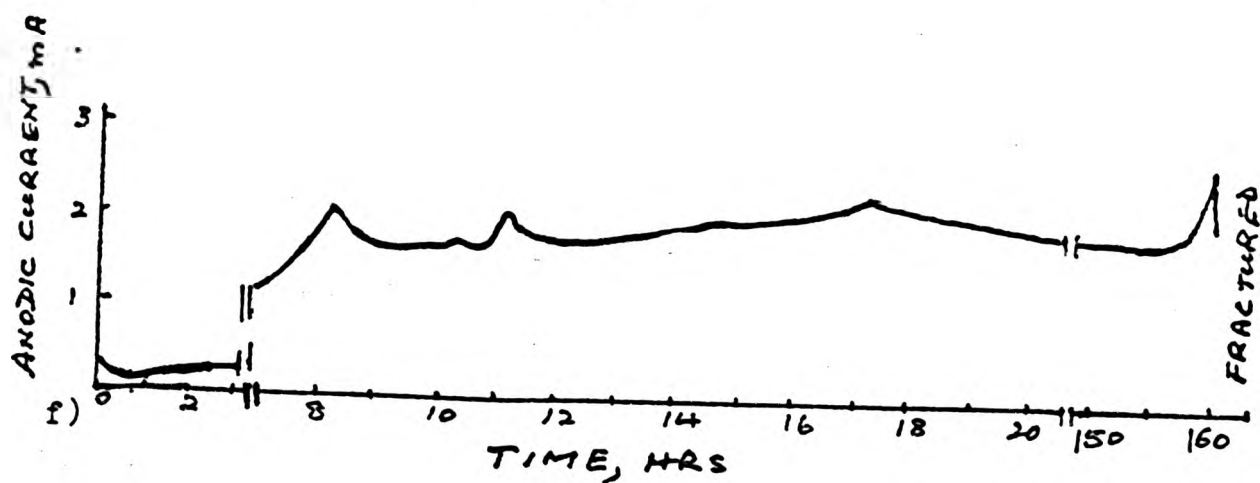
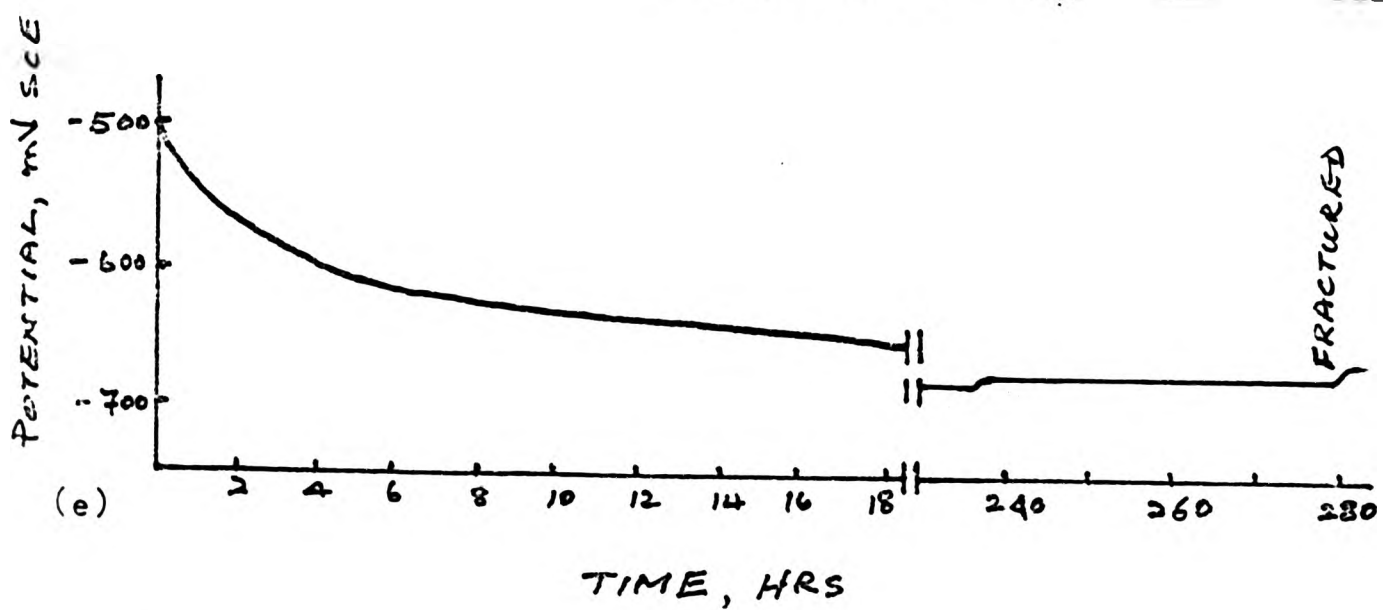
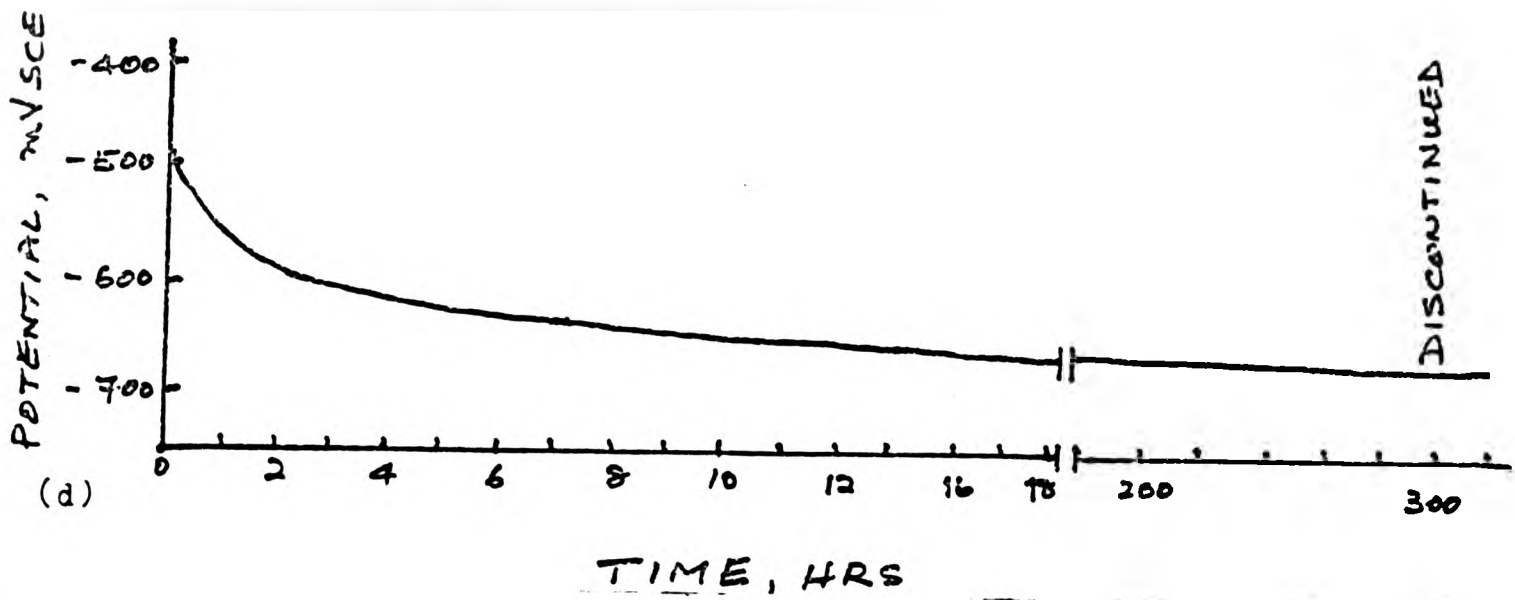


(c) Anodic current and stress as a function of time for a specimen under cyclic stress, 198 MPa,  $R=-1$ , at 0.07 Hz with an applied potential of -560 mV (SCE).

(iii) immediately after commencement of test,

(iv) approximately 20 minutes after commencement of test. Specimen with air formed oxide film.

Fig R 8: Typical curves for mild steel in 0.6 M sodium chloride solution.



Potential vs time curves (d) at zero stress in stationary condition and (e) with an applied cyclic stress of 198 MPa,  $R=-1$ , at 0.2 Hz. Corrosion current vs time curve at 198 MPa,  $R=-1$ , 0.2 Hz is shown in (f).

Fig R 8: Typical curves for mild steel in 0.6 M sodium chloride solution.

For the measurement of current, the applied potential was equivalent to the rest potential,  $E_R$ , - 560 mV (SCE).

On the application of stress, a momentary shift in potential in the positive direction (not shown in Figure R 8e), similar to that observed in Figure R 5, is found to take place. Potential, however, gradually moves towards a more negative value with the passage of time and a steady value of -680 mV is obtained after approximately 150 hours. There is a slight increase in potential prior to the fracture of the specimen (Figure R 8e).

The corrosion current as a function of time is shown in Figure R 8f. There is a decrease initially and then a rapid rise of current accompanied by a peak at approximately 8 hours, i.e. at about 4560 reversals. The applied potential was -560 mV (SCE).

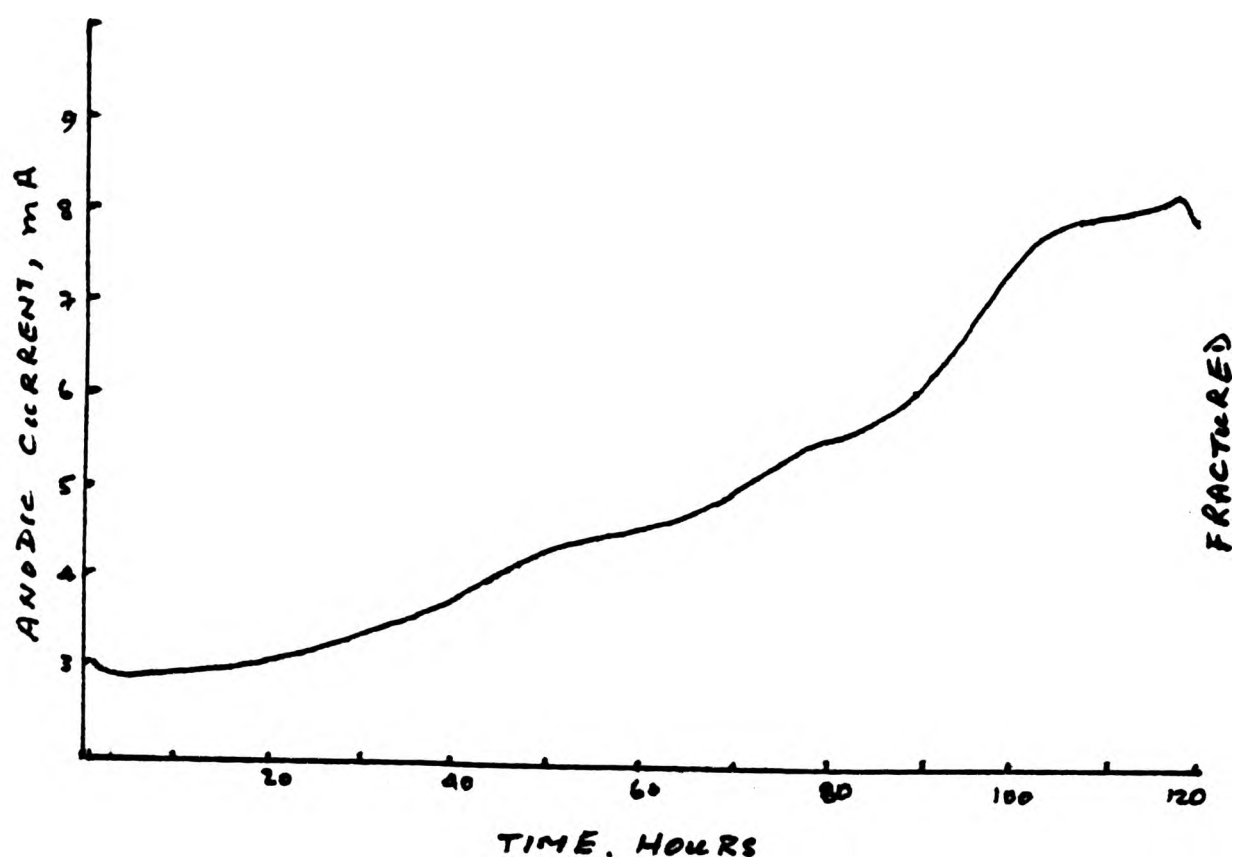
Similar tests were performed at 247 MPa,  $R = -1$ . 0.2 Hz, with an applied potential of -560 mV (SCE). Corrosion current vs time curve is shown in Figure R 8g.

Figure R 8h shows the potential vs time curve at 247 MPa,  $R = -1$ . 0.02 Hz.

#### 4.5 Reverse bend fatigue tests - 24 Hz

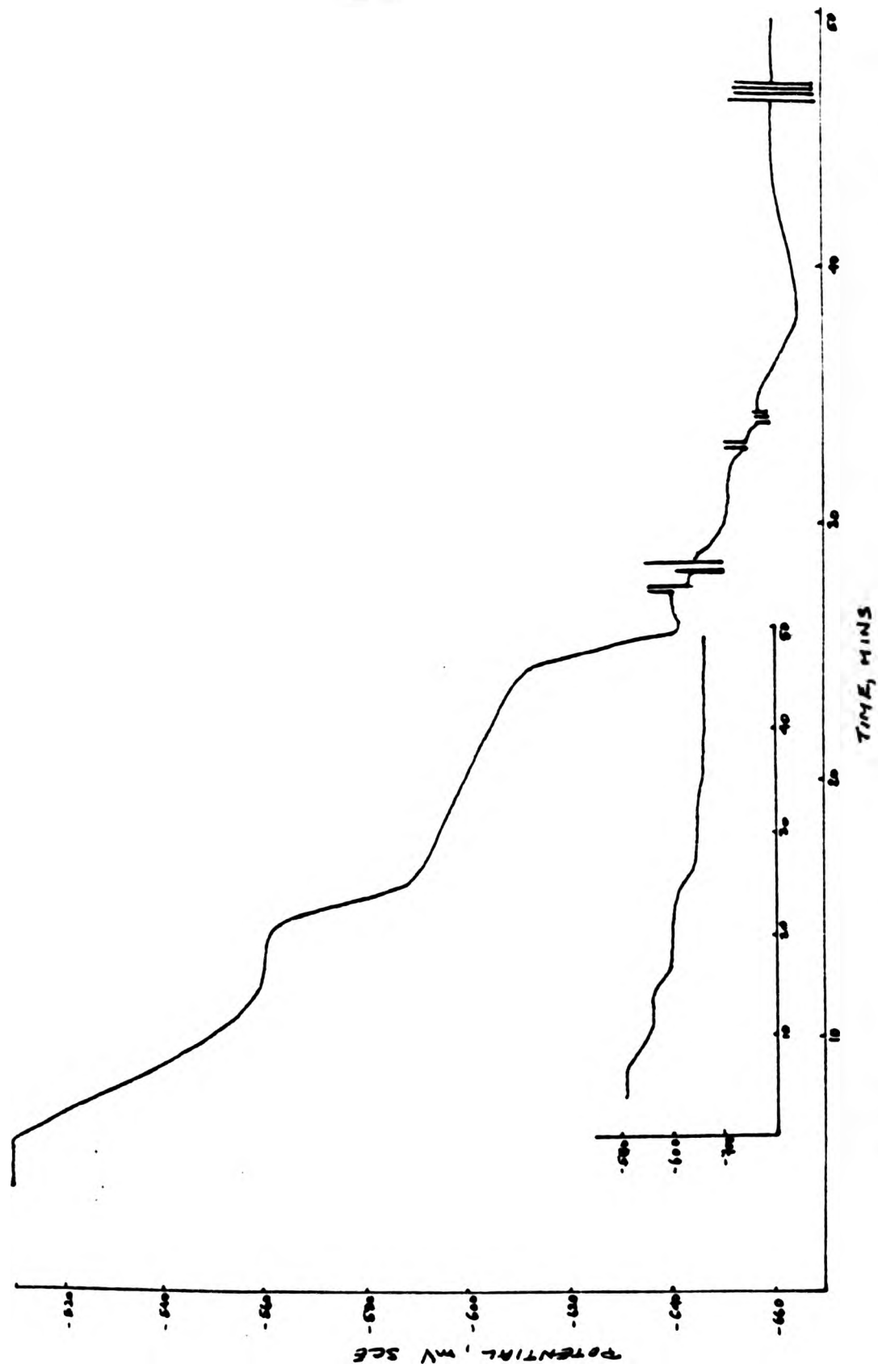
Results of fatigue tests at 170 and 294 MPa for polished and at 170 MPa for mill scaled specimens exhibiting change of potential and current as functions of time are shown in Figure R 9.

For the measurement of current the respective applied potentials were -560 mV (SCE) for polished and -440 mV (SCE) for mill scaled specimens. These were the potentials observed immediately after the "pool" was filled with the electrolyte.



(g) Corrosion current vs time curve at 247 MPa,  $R=-1$ , 0.2 Hz with an applied potential of -560 mV (SCE).

Fig R 8: Typical curves for mild steel in 0.6 M sodium chloride solution.



(h) Potential vs time curve with an applied stress of 247 MPa,  $R=-1$ ,  
0.02 Hz.

Fig R 8: Typical curves for mild steel in 0.6 M sodium chloride solution.

On the application of cyclic stress, 170 MPa,  $R = -1$ , a potential shift in the positive direction was observed for polished specimens (Figure R 9a). It gradually decays with the passage of time. A potential peak is observed after nearly 50 minutes. The potential appears to decay somewhat more rapidly after this peak.

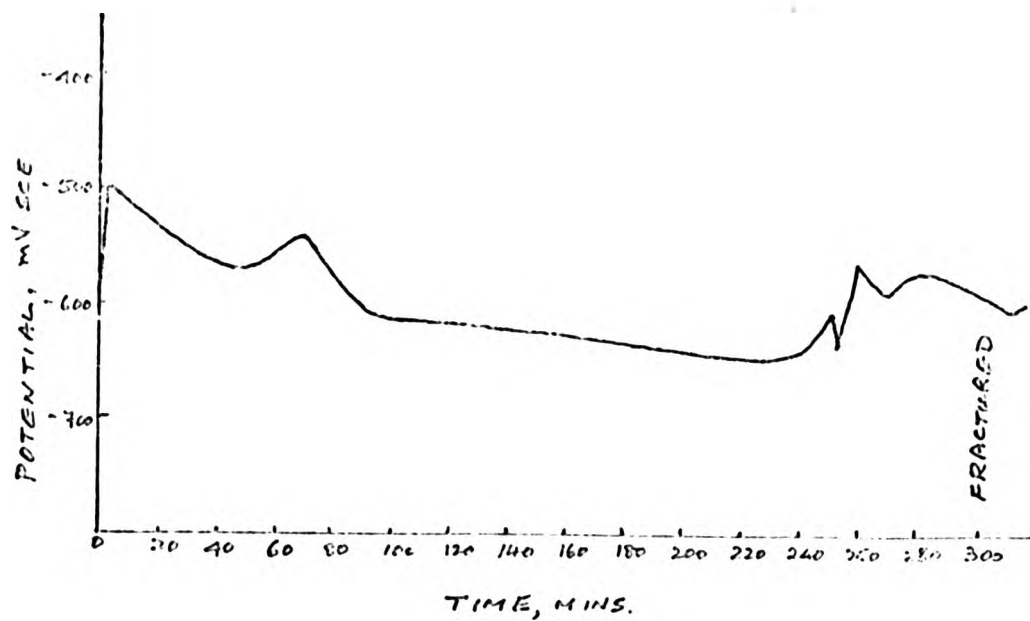
Figure R 9b show the fracture surface of the specimen after 300 minutes, i.e.  $4.25 \times 10^5$  reversals, indicating the presence of a pit from which a crack appears to emanate.

The corrosion current vs time curve (Figure R 9c) shows a considerable increase after nearly 20 minutes. Figure R 9d exhibits the dissolution of ferrite in a pearlitic area on the longitudinal surface of the specimen after the test was discontinued (Figure R 9c).

At 277 MPa, potential decays quite rapidly (Figure R 9e). Considerable fluctuations of potential are also observed.

A test at 277 MPa,  $R = -1$ , was interrupted at approximately 90 minutes and the longitudinal surface was examined using optical microscopy. Figure R 9f shows the presence of surface cracks. A second series of tests were stopped at various intervals, sectioned, and the transverse surfaces were examined using optical microscopy. The specimens were sectioned near the place where cracks appeared on the surface. Figures R 9g and R 9h exhibit the presence of a pit with a crack emanating from the bottom of the pit.

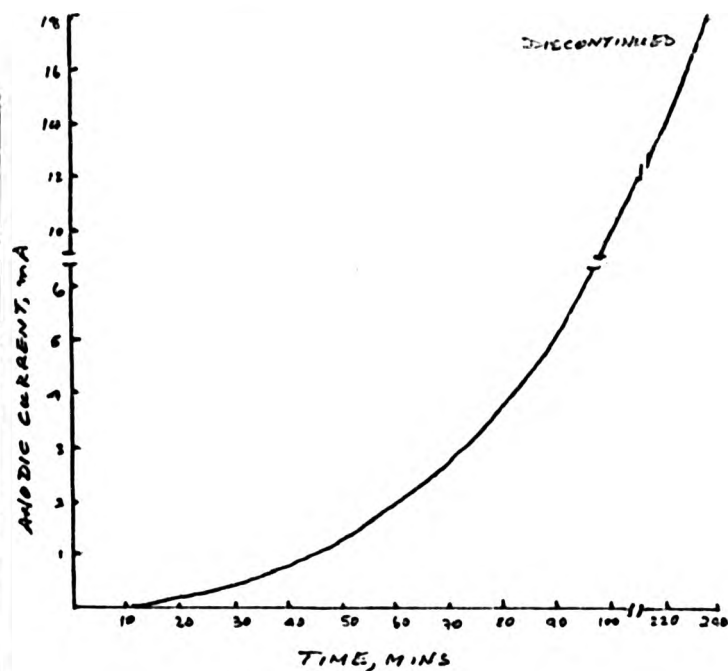
For mill scaled specimens, no potential shift in the positive direction was observed on application of stress (Figure R 9j). Peaks were noted after approximately 110 and 300 minutes with a sharp decrease in potential at the appearance of a series of cracks on the surface at around 360 minutes. To observe the specimen surface,



(a)



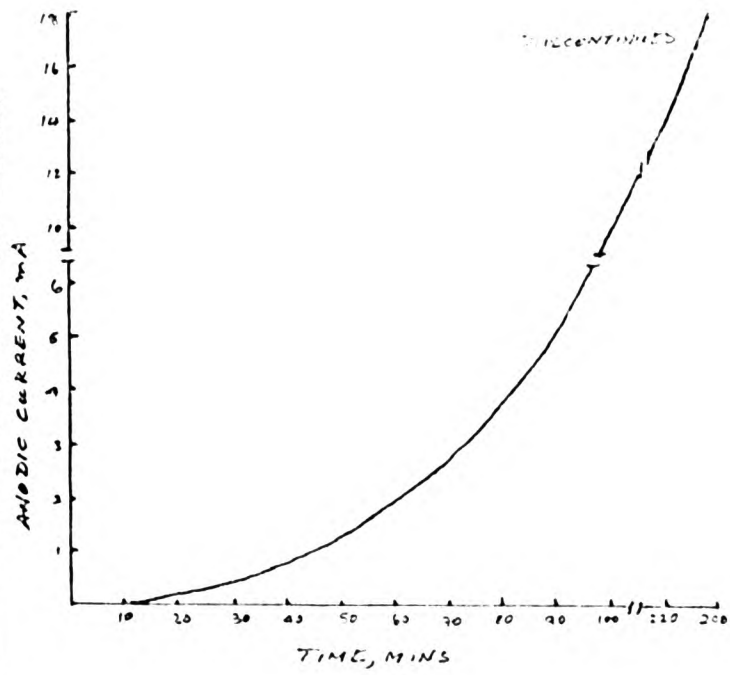
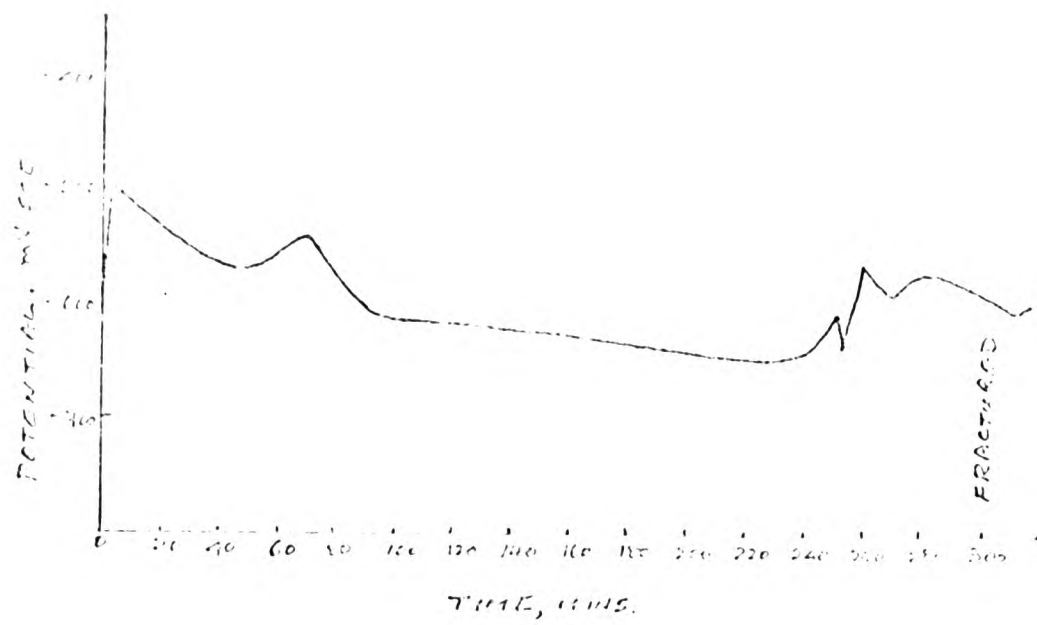
(b)



(c)

Typical (a) potential vs time and (c) corrosion current vs time curves for polished mild steel specimens in 0.6 M sodium chloride solution at 170 MPa,  $R=-1$ . The applied potential for (c) is -560 mV (SCE). (b) Fracture surface of a potential vs time (a) curve specimen after 300 minutes. Arrow indicates the presence of a pit from which a crack appears to emanate.

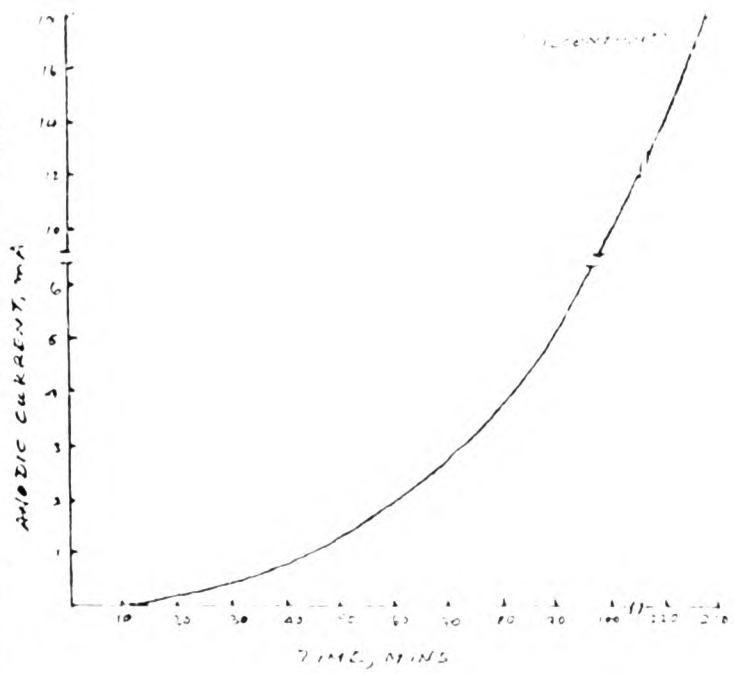
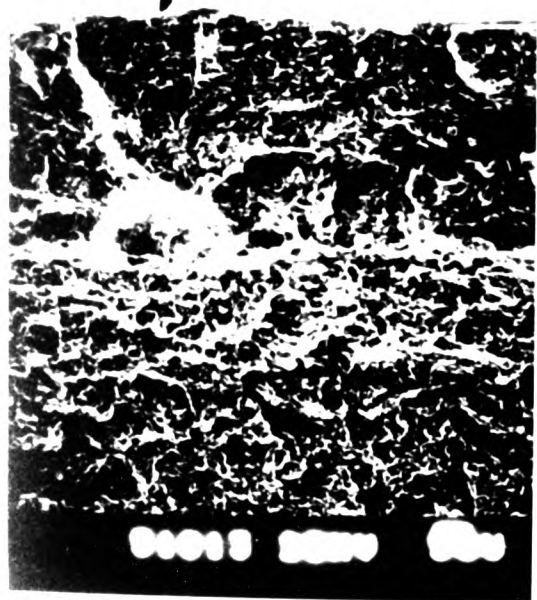
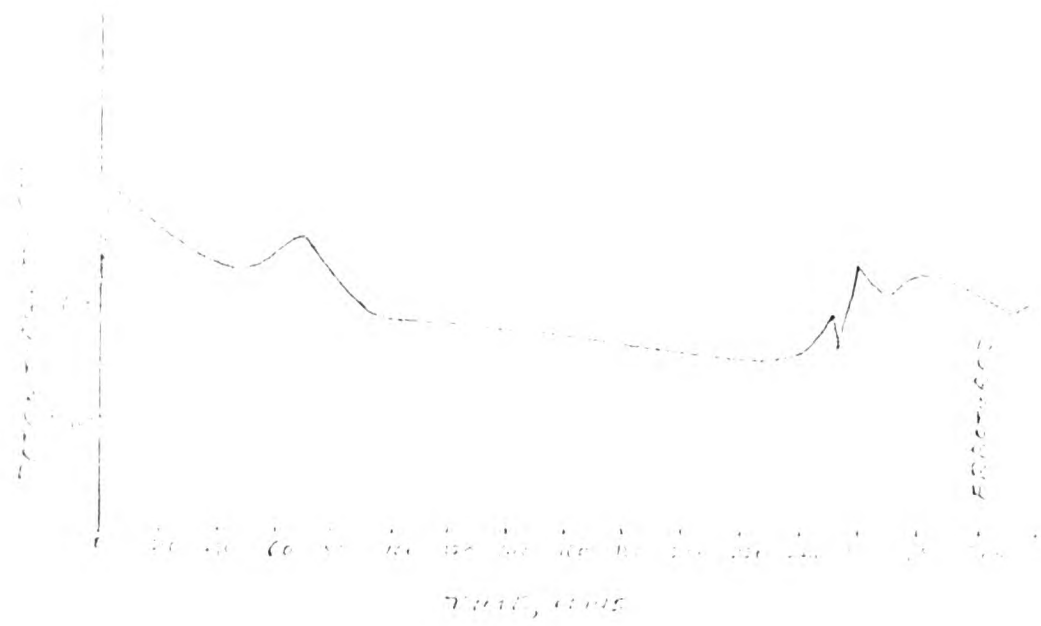
15 R 9: Reverse bend fatigue test at 24 Hz.



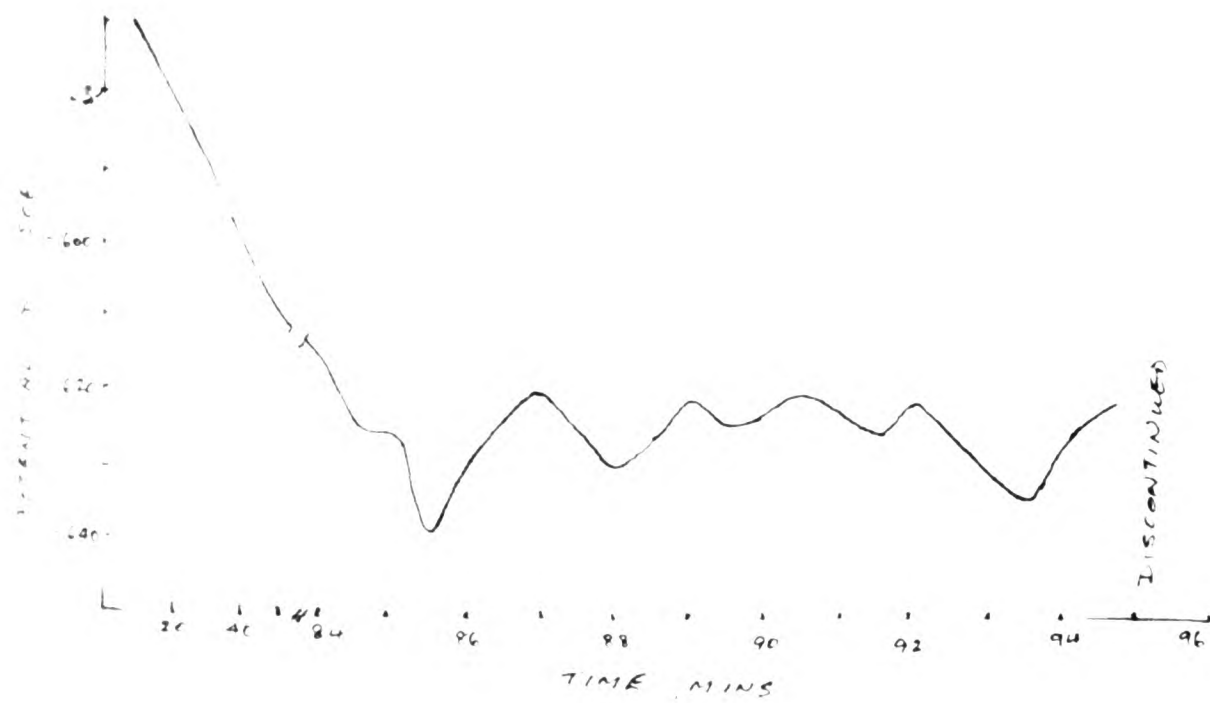
(c)

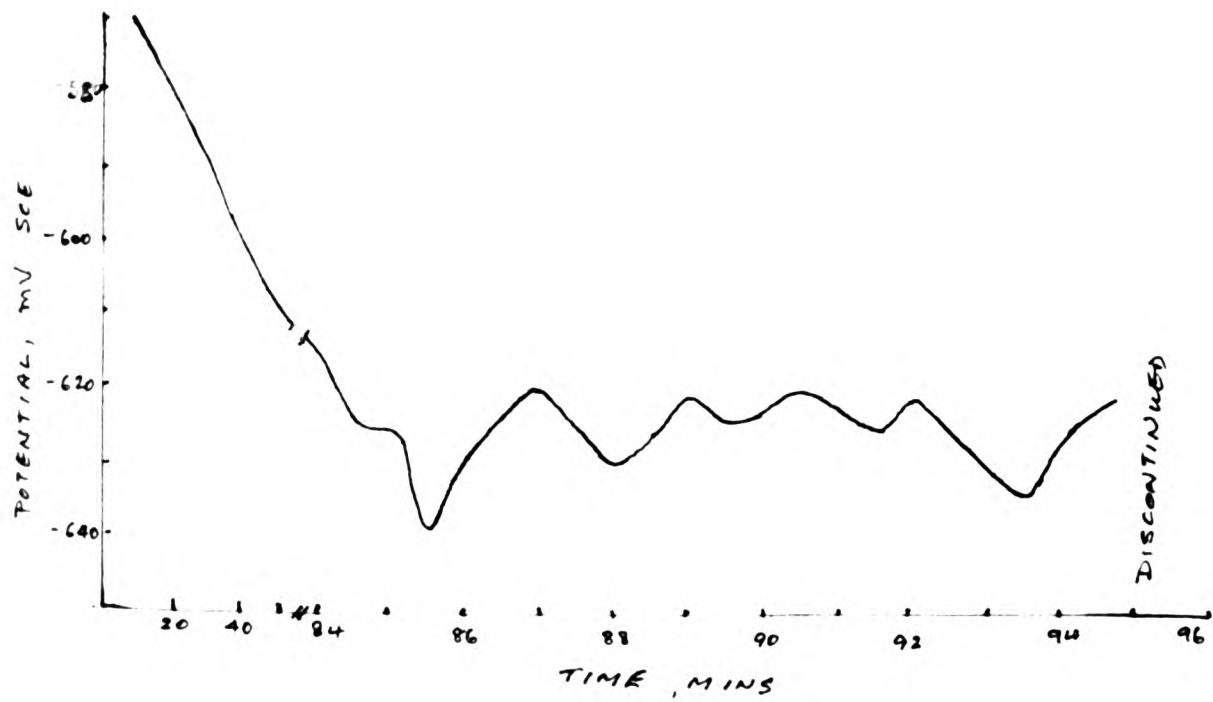
Typical (a) potential vs time and (c) corrosion current vs time curves for polished mild steel specimens in 1.0 M sodium chloride solution at 170 MPa, R=-1. The applied potential for (c) is -560 mV (SCE). (b) Fracture surface of a potential vs time (a) curve specimen after 30 minutes. Arrow indicates the presence of a pit from which a crack is seen to emanate.

Specimen (c) failed in test at 14 hr.



The first curve shows the current response to a step potential. The initial rise to 8.5 MA is due to the charging of the double layer. The subsequent drop to a steady-state value of 2.5 MA is characteristic of a diffusion-controlled process. The second rise at 150 seconds is due to a change in the electrode surface area or a change in the concentration of the electroactive species.

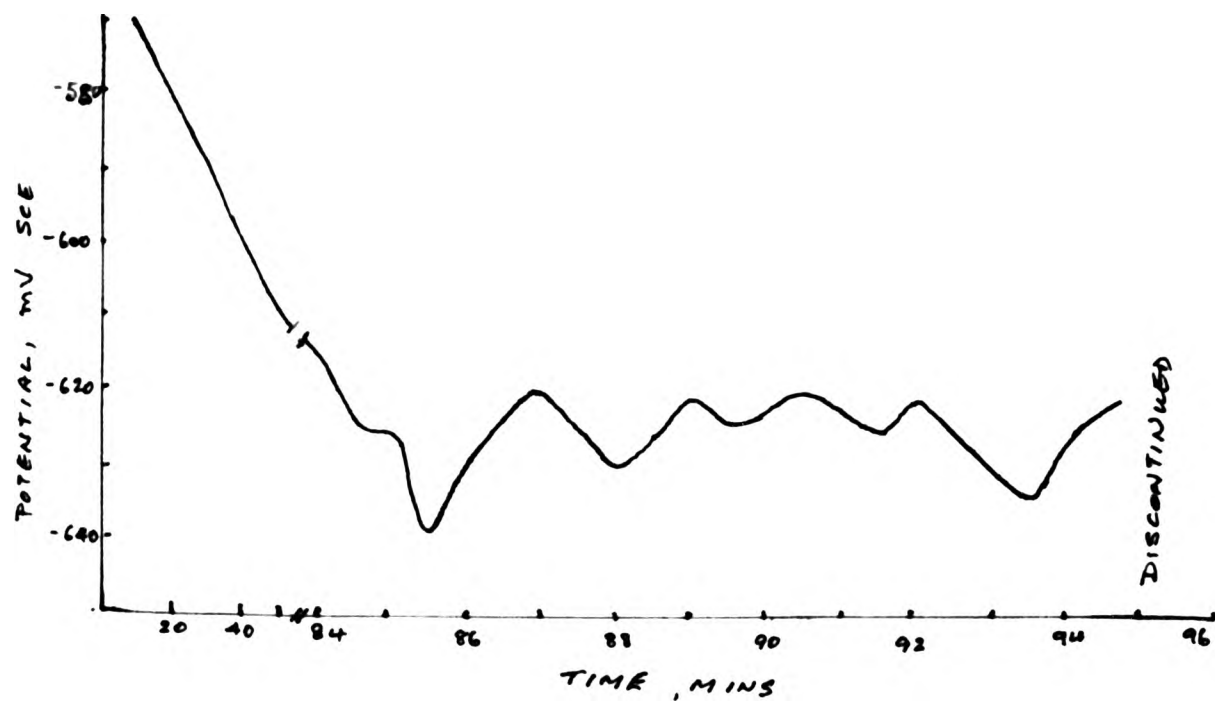




Plot of potential vs time curve for specimen after  
 water immersion in solution in early stage of  
 metal potential vs time curve for specimen after  
 immersion in solution in early stage of metal.

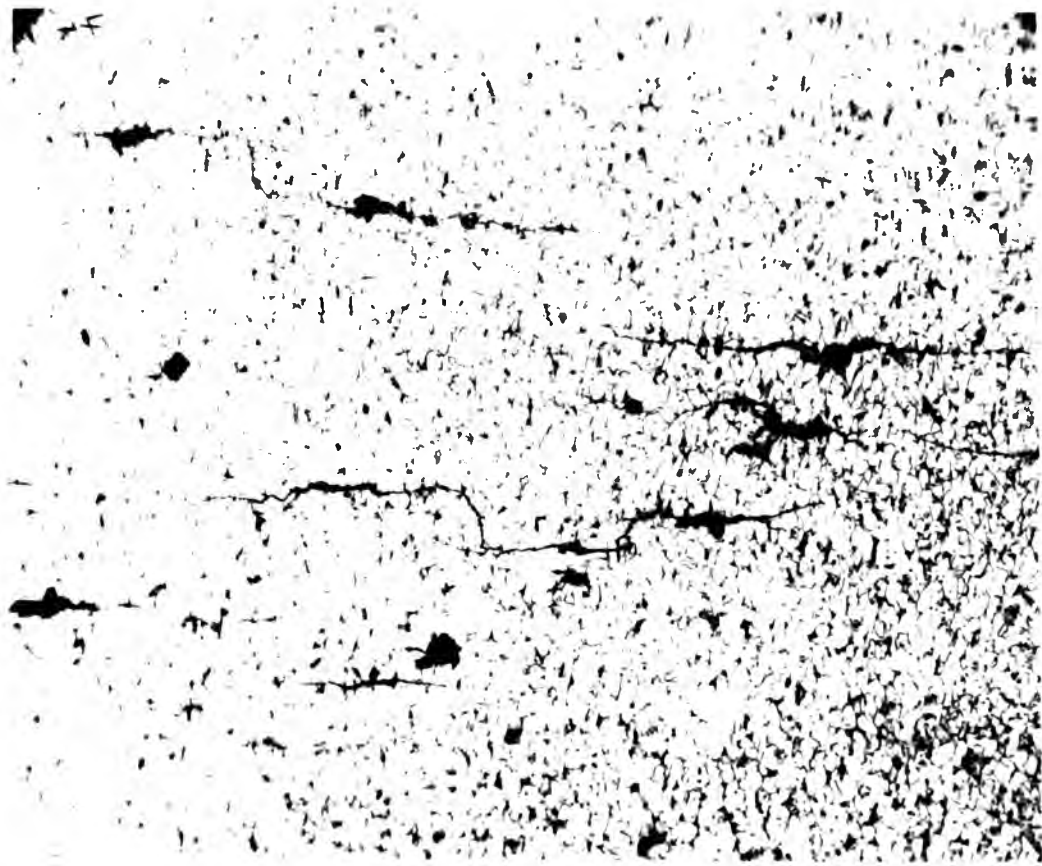


(d)



(a) surface of a current vs time curve (c) specimen after 40 minutes showing dissolution in pearlitic areas. (e) typical potential vs time curve for polished mild steel specimen in 0.1 M sodium chloride solution at 277 MPa, 25°C.

(f) typical current vs time test at 400 mV.



(f)



(g)

Micrographs of the (f) longitudinal (x 50) and (g) transverse (x 290) surfaces of polished mild steel specimens in 0.6 M sodium chloride solution at 277 MPa,  $R=-1$ , after  $1.28 \times 10^5$  and  $6.25 \times 10^5$  reversals respectively. Figure (f) shows surface cracks whilst (g) exhibits the initiation of a crack from a pit. Etch: 2% Nital.

Fig R 9: Reverse bend fatigue test at 24 Hz.



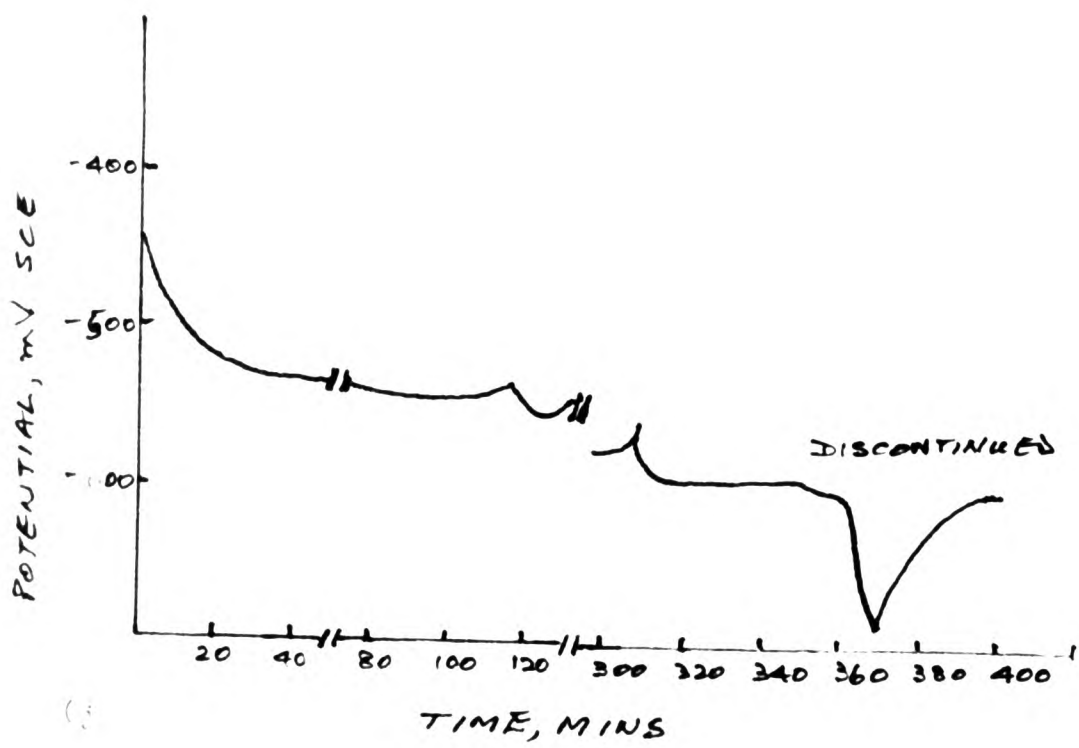
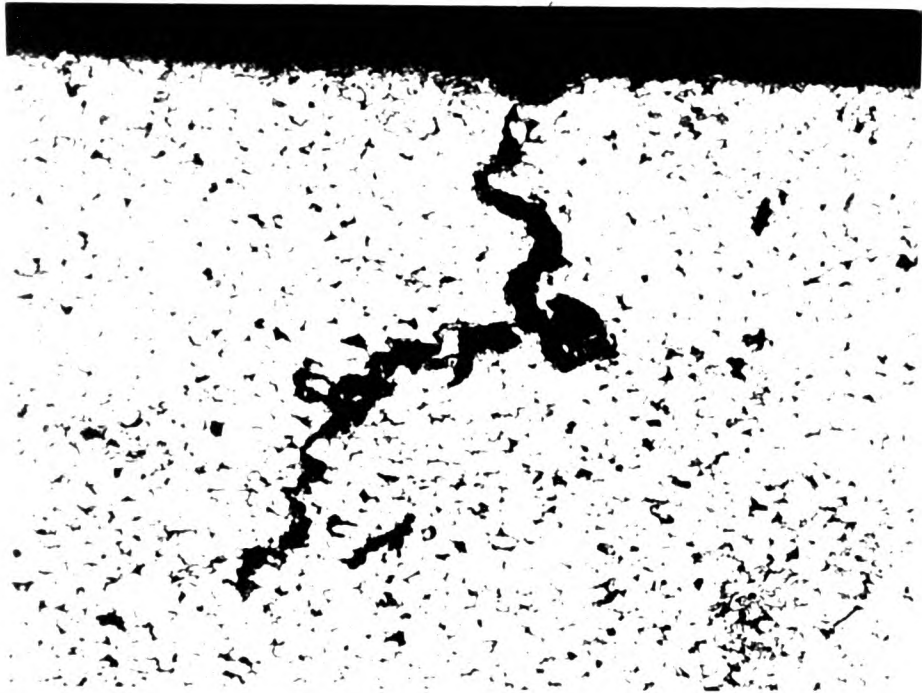
Micrographs of the (f) longitudinal ( $\times 50$ ) and (g) transverse ( $\times 290$ ) surfaces of polished mild steel specimens in 0.6 M sodium chloride solution at 277 MPa,  $R=-1$ , after  $1.8 \times 10^5$  and  $0.25 \times 10^5$  reversals respectively. Figure (f) shows surface cracks whilst (g) exhibits the initiation of a crack from a pit. Etch: 2% Nital.

Reverse bend fatigue test at 24 Hz.

Faint, illegible text, possibly bleed-through from the reverse side of the page.

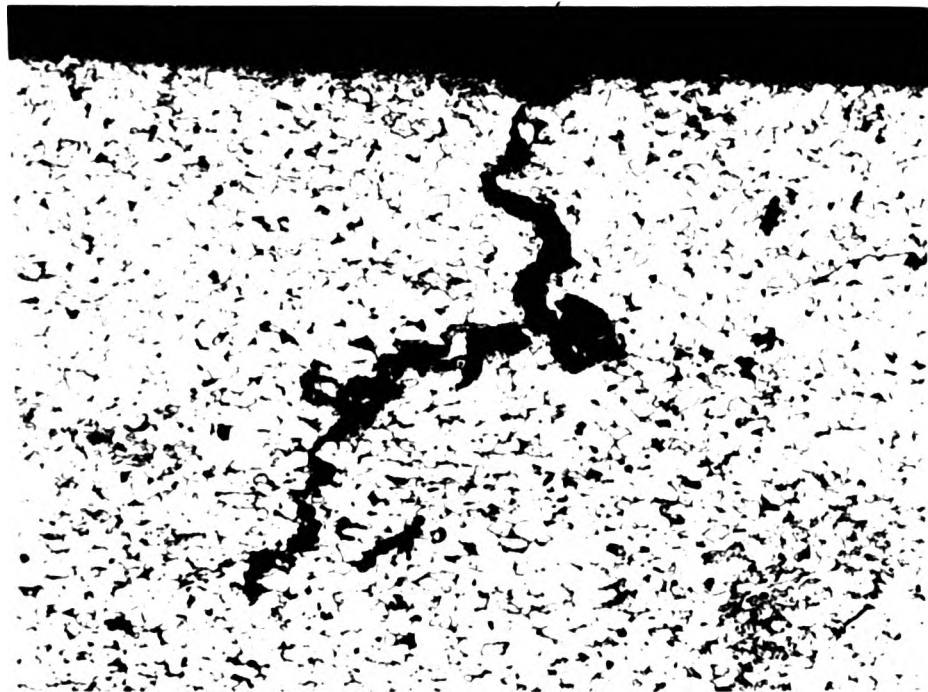


Faint, illegible text at the bottom of the page, possibly bleed-through or a very light print.



A scan of the iron-oxide surface (x 200) made by  
 differential scanning calorimetry (DSC) after 2.4 x 10<sup>18</sup>  
 electrons in a 100°C solution of 0.1 M ferrous chloride. The scan exhibits a  
 peak at 110°C. The scan was made at a heating rate  
 of 10°C/min. The scan was made at a scan rate  
 of 10°C/min. The scan was made at a scan rate  
 of 10°C/min.

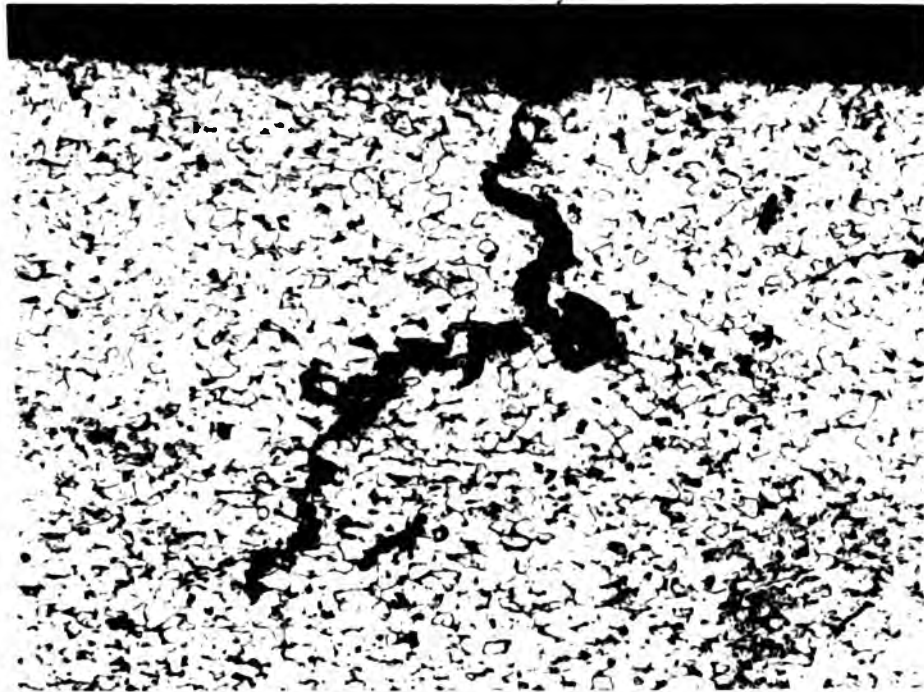
Figure 1. DSC scan of the iron-oxide surface.



(j)

Micrograph of the transverse surface (x 75) of a polished mild steel specimen at 277 MPa, R=-1, after  $8.36 \times 10^5$  reversals in 0.6 M sodium chloride solution exhibiting a crack emanating from a pit. Etch: 2% Nital. (j) Typical potential vs time curve for mill scaled specimen at 170 MPa, R=-1, in 0.6 M sodium chloride solution.

is reverse bend fatigue test at 4 MPa.



(h)



(j)

(h) Micrograph of the transverse surface (x 75) of a polished mild steel specimen at 277 MPa,  $R=-1$ , after  $8.36 \times 10^5$  reversals in 0.6 M sodium chloride solution exhibiting a crack emanating from a pit. Etch: 2% Nital. (j) Typical potential vs time curve for mill scaled specimen at 170 MPa,  $R=-1$ , in 0.6 M sodium chloride solution.

Fig R 9: Reverse bend fatigue test at 24 Hz.

tests were interrupted after 300 and 360 minutes and the specimens were examined using scanning electron microscopy. Cracks on, and dissolution of, mill scale were noted (Figures R 9k and R 9l).

The current vs time curve (Figure R 9m) shows a gradual increase of corrosion current initially. Considerable increase is observed after nearly 220 minutes, i.e.  $3.1 \times 10^5$  reversals, possibly indicating the breakdown of mill scale. Figure R 9n exhibits the surface of a specimen after the interruption of a test at approximately  $3.4 \times 10^5$  reversals, indicating dissolution of the mill scale and formation of cracks on the surface of the steel.

#### 4.7 Immersion tests

Results of the examination of the steel surfaces before and after the immersion tests are shown in Figure R 10.

Figure R 10a exhibits the results of the analysis of the inclusions on the surface of a wrought specimen. It indicates that in some cases the only element detectable, other than S, is Mn (Trace  $A_{Fe} - A_{Mn}$ ) whilst in others Fe is also present (Trace  $B_{Fe} - B_{Mn}$ ) but this is associated with a corresponding reduction in the Mn content. Presence of S in the inclusions is shown in Figure R 10b.

Figures R 10c and R 10d exhibit the elements present in inclusions on the specimen surface after immersion in 0.6 M sodium chloride solution for 5 minutes and 5 hours respectively.

Figures R 10e and R 10f exhibit the scanning electron micrographs after immersion for 20 and 17 hours respectively.

#### 4.8 Metallurgical examinations: Rotating bend fatigue tests - 47 Hz

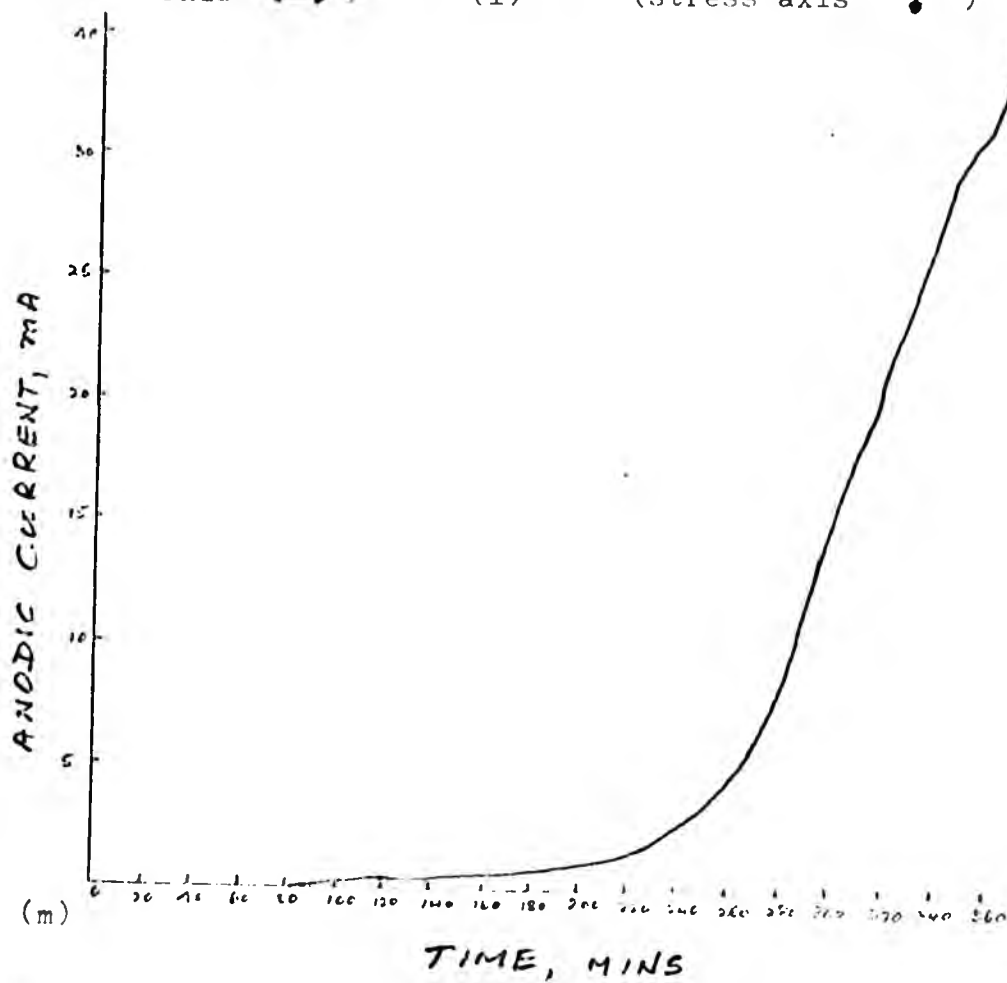
##### 4.8.1 Scanning electron microscopic examination

Results of the examination of rotating bend fatigue tested specimens using SEM are shown in Figure R 11.



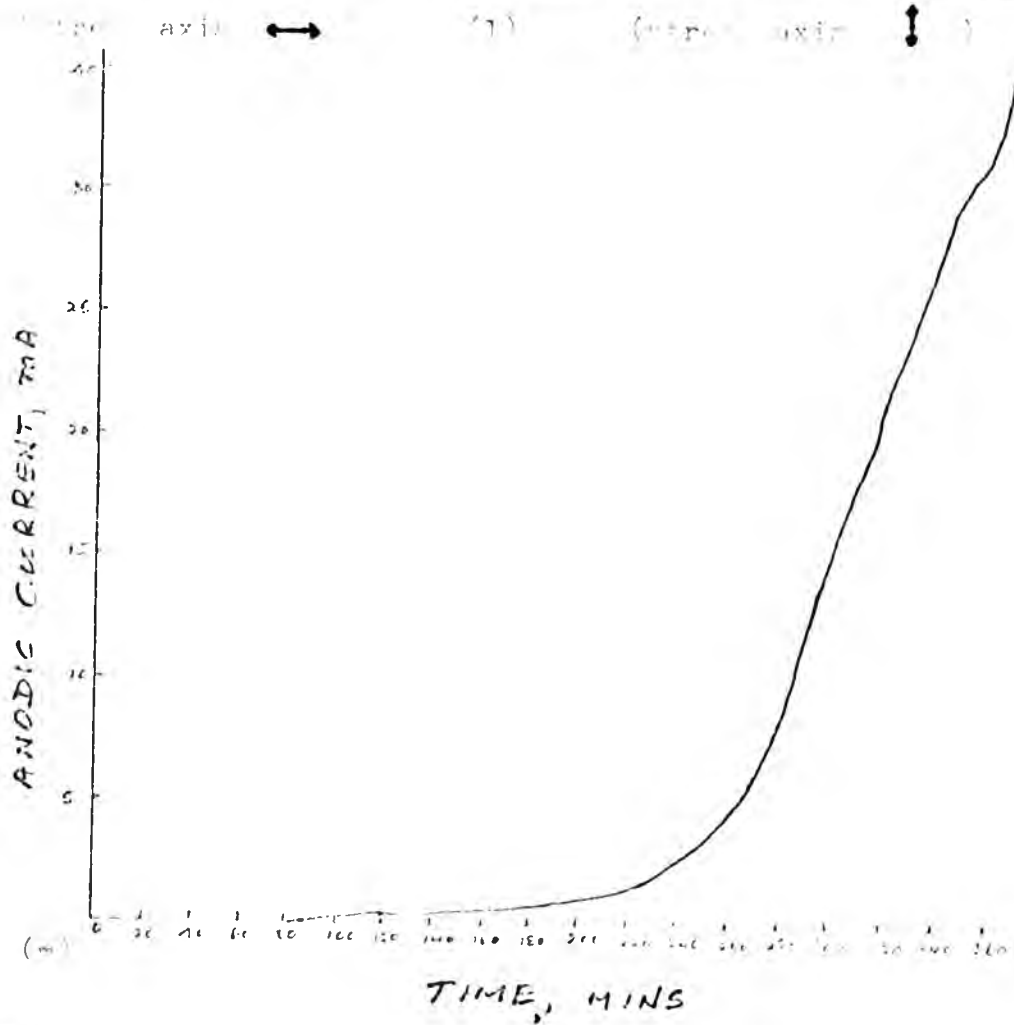
(k) (stress axis  $\rightarrow$ )

(l) (stress axis  $\downarrow$ )



Micrographs of the longitudinal surface of potential vs time (j) curve specimens after (k) 360 minutes exhibiting cracks and dissolution of the mill scale, and (l) 300 minutes showing joining of cracks. (m) Typical corrosion current vs time curve for mill scaled specimen at 170 MPa, R=-1, with an applied potential -440 mV (SCE).

Fig 9: Reverse bend fatigue test at 24 Hz.



(k) Longitudinal surface of potential vs time curve specimens after (k) 350 minutes exhibiting cracks and dissolution of the mill scale, and (l) 300 minutes showing joining of cracks. (m) Typical corrosion current vs time curve for mill scaled specimen at 120 MPa, R=-1, with an applied potential -440 mV (SCE).

(n) Reverse bend fatigue test at 1/4 Hz.





axial ↑

profile of the longitudinal surface of a corralled  
rock surface with curved bedding which is typical  
of the dissolution of mill scale.

increase in surface area to that of 4%.



(n) ( stress axis  $\updownarrow$  )

Micrograph of the longitudinal surface of a corrosion current vs time (m) curve specimen after 240 minutes exhibiting dissolution of mill scale.

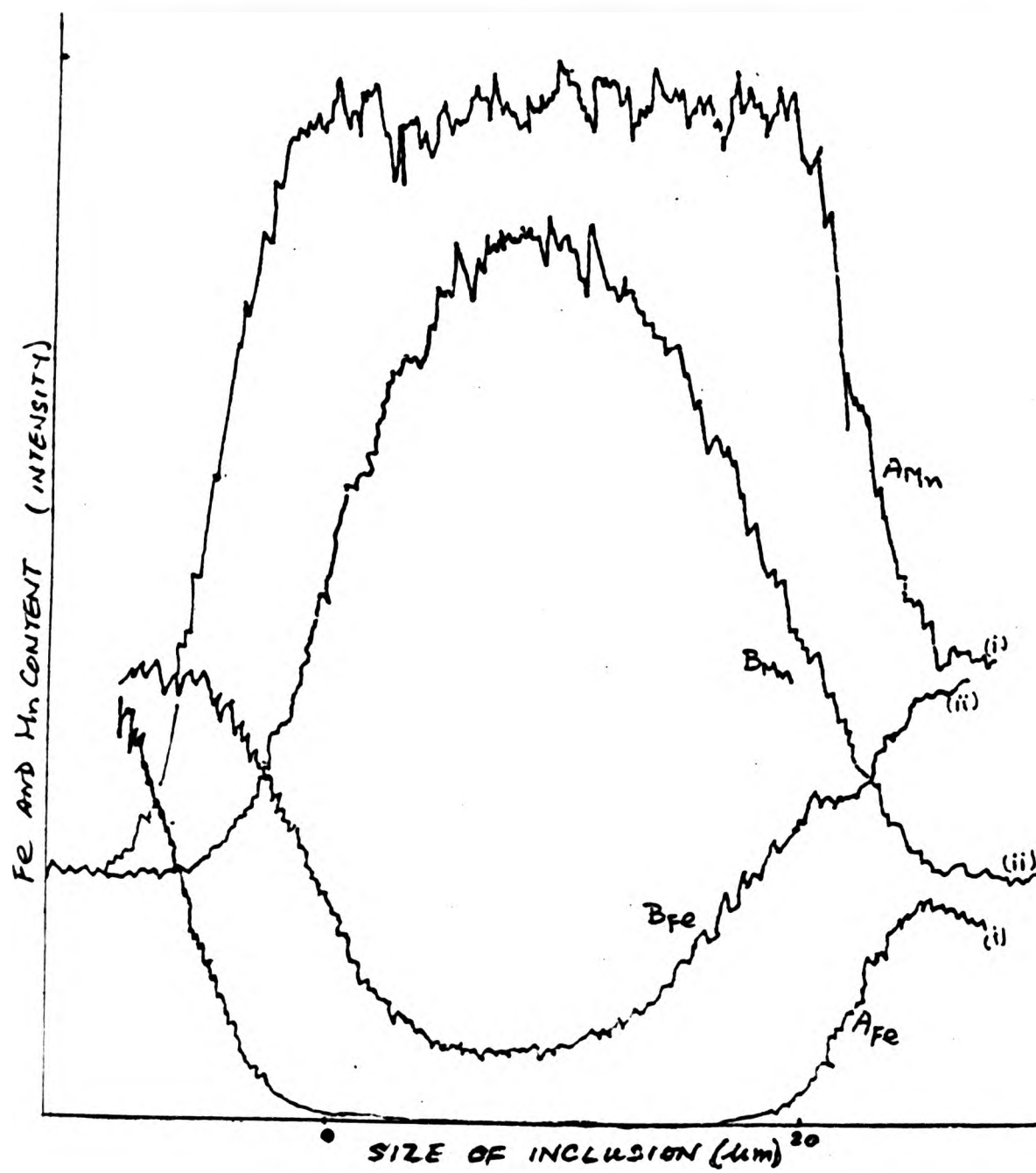
IR R 9: Reverse bend fatigue test at 24 Hz.



(n) ( stress axis ↑ )

Micrograph of the longitudinal surface of a corrosion current vs time (m) curve specimen after 240 minutes exhibiting dissolution of mill scale.

Fig R 9: Reverse bend fatigue test at 24 Hz.

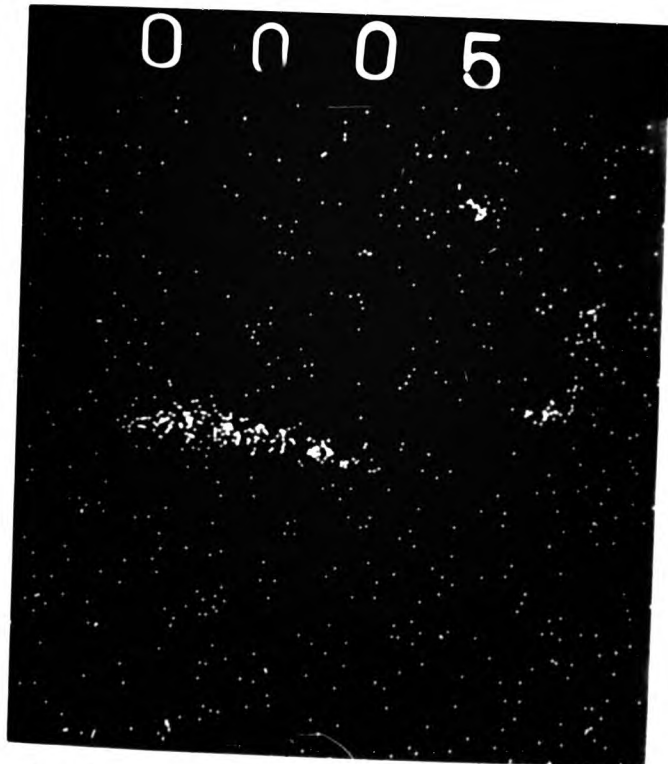


- (a) Electron probe microanalysis results of inclusions on wrought specimen surface prior to immersion test, exhibiting the presence of (i) only Mn (curve  $A_{Fe}-A_{Mn}$ ) and (ii) Fe and Mn (curve  $B_{Fe}-B_{Mn}$ ). It indicates that the presence of Fe in the inclusion reduces the Mn content.

Fig R 10: Examination results of the surface of mild steel specimens.



(i)



(ii)

(b) Electron probe microanalysis results of an inclusion on wrought specimen surface prior to immersion test, indicating presence of (i) S and (ii) Mn. x 1200

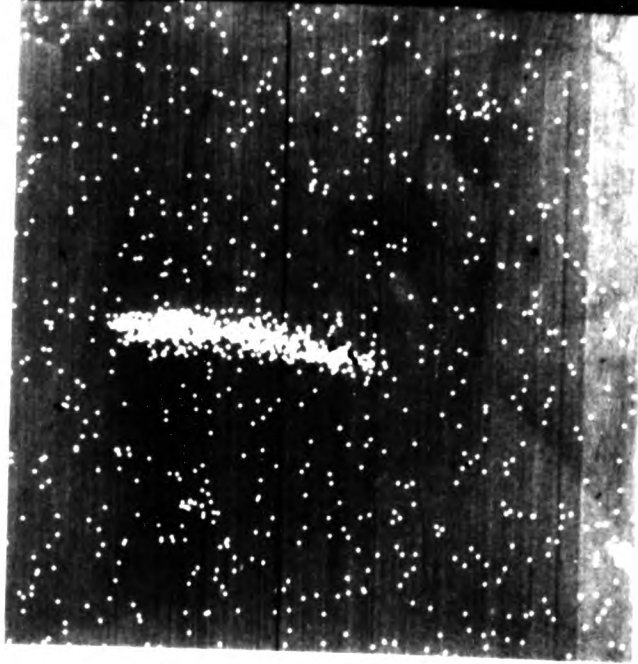
Fig. 10: Examination results of the surface of mild steel specimens.



Electron probe microanalytic profile of a specimen  
on the surface of a specimen surface prior to etching,  
indicating presence of Al at approx. 10% wt.

The concentration profile of Al is shown in the  
figure below.

0 0 0 4



0 0 0 5







(i)



(ii)



(iv)

(c) Electron probe microanalysis results of wrought specimen surface showing (i) inclusions and indicating the presence of (ii) Mn and (iii) S, and the absence of (iv) Si after immersion in 0.6 M sodium chloride solution for 5 mins. x 600

Fig. 10: Examination results of the surface of mild steel specimens.



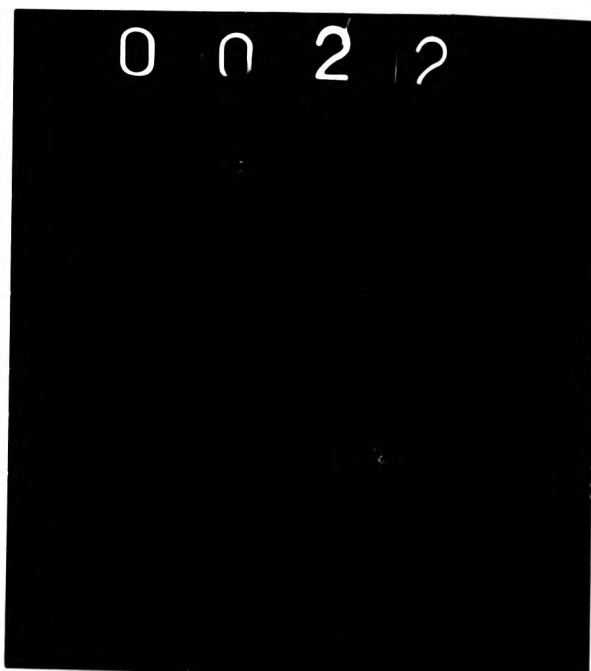
(i)



(ii)



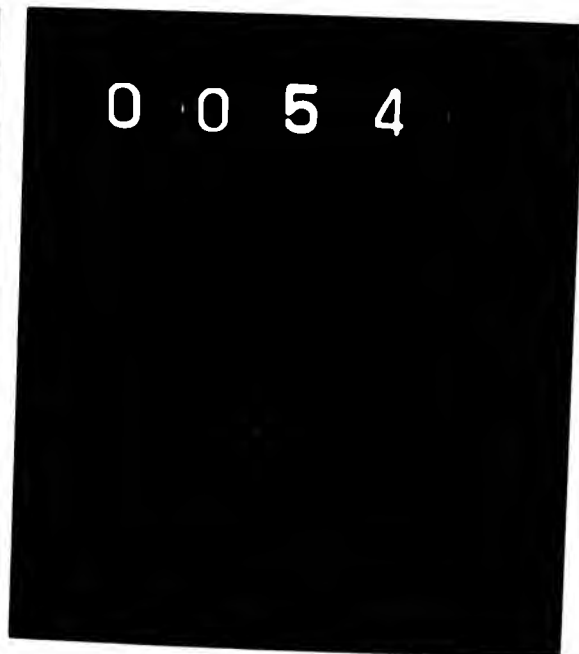
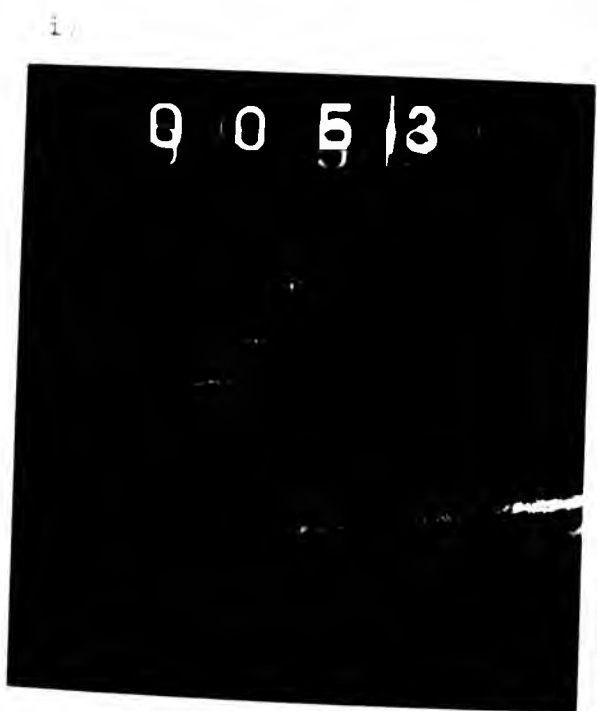
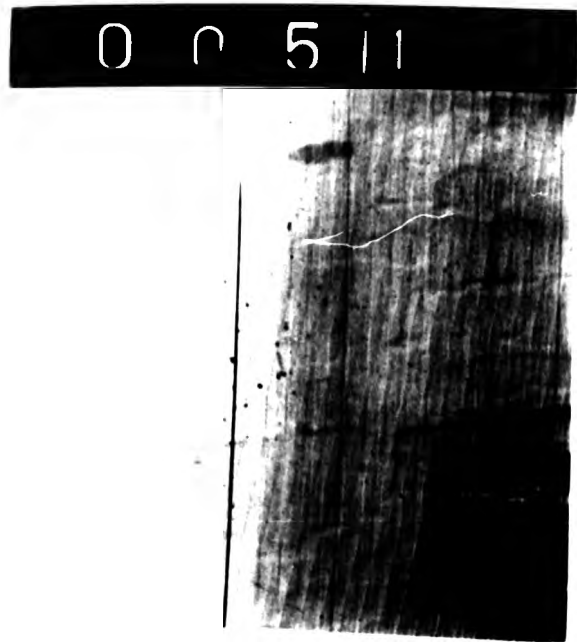
(iii)



(iv)

(c) Electron probe microanalysis results of wrought specimen surface showing (i) inclusions and indicating the presence of (ii) Mn and (iii) S, and the absence of (iv) Si after immersion in 0.6 M sodium chloride solution for 5 mins. x 600

Fig R 10: Examination results of the surface of mild steel specimens.



(iii)

(iv)

(d) Electron probe microanalysis results of wrought specimen surface showing (i) inclusions and indicating the presence of (ii) Mn and (iii) S, and the absence of (iv) Si after immersion in 0.6 M sodium chloride solution for 5 hours. x 300

Figure 10: Examination results of the surface of mild steel specimens.

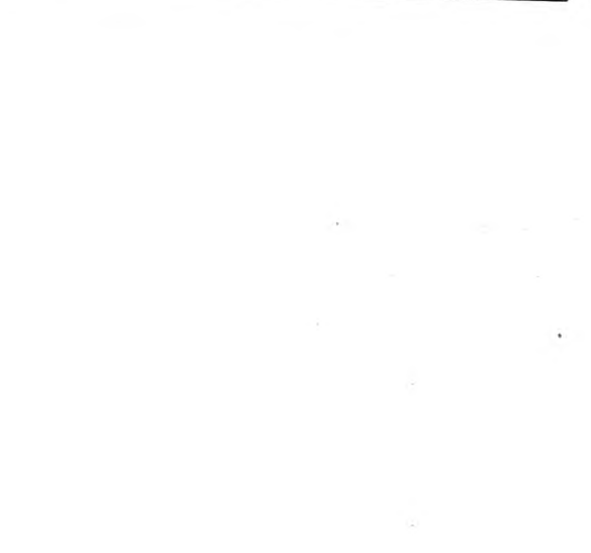
0 0 5 | 1



0 0 5 | 2



0 0 5 | 3



0 0 5 | 4





1. Fine electron micrograph of the surface of the specimen after immersion for nearly 2 hours in 0.1% aqueous solution of  $\text{Cu}^{2+}$  for 1 hour after immersion for 12 hours in 0.1% aqueous chloride solution.

2. Comparison results of the surface of the specimen.



(e)



(f(i))

Scanning electron micrographs of (e) wrought specimen after immersion for nearly 20 hours and (f(i)) annealed specimen (920°C for 3 hours) after immersion for 17 hours, in 0.6 M sodium chloride solution.

Fig R 10: Examination results of the surface of mild steel specimens.



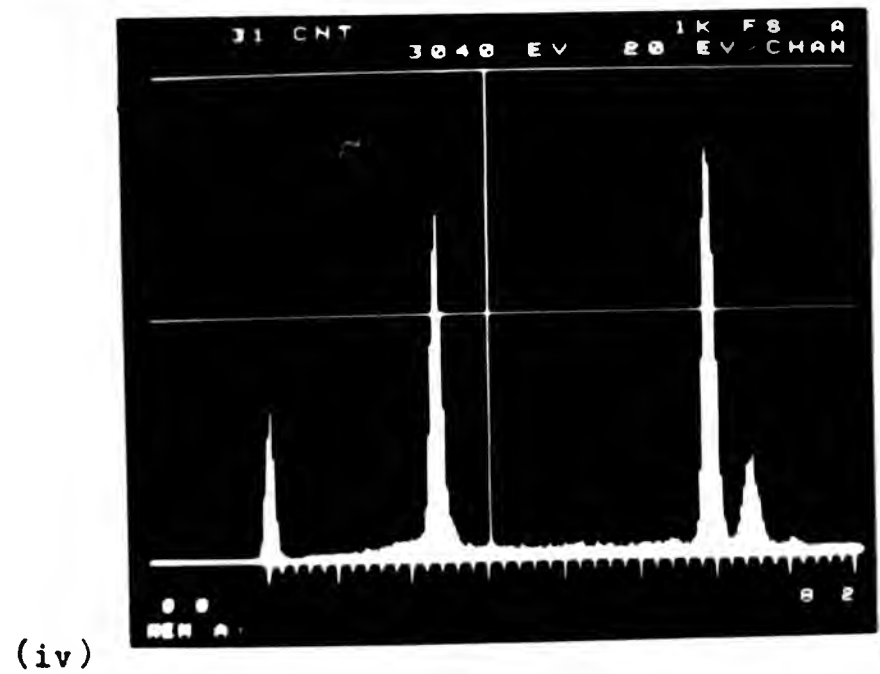
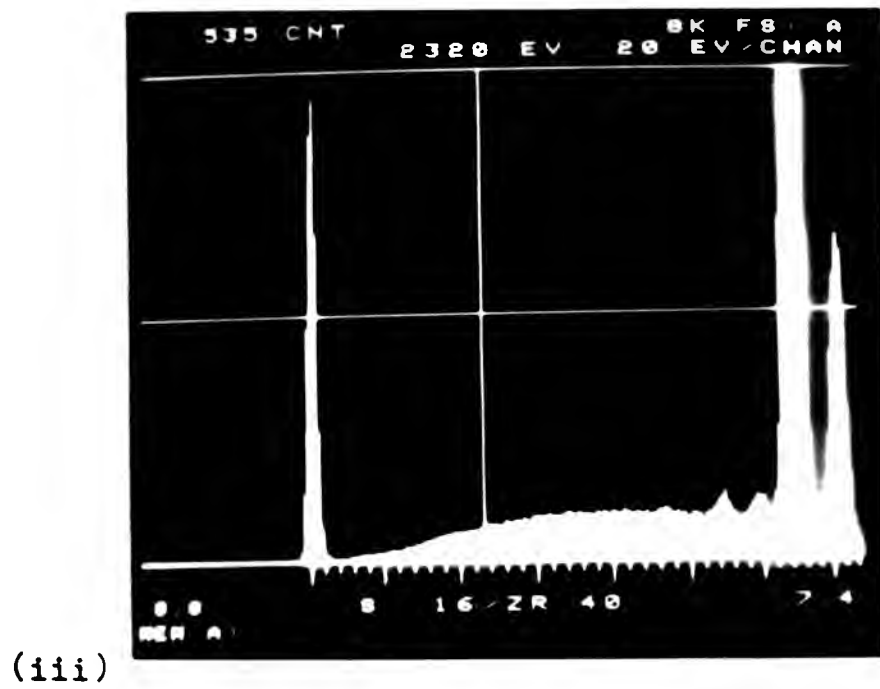
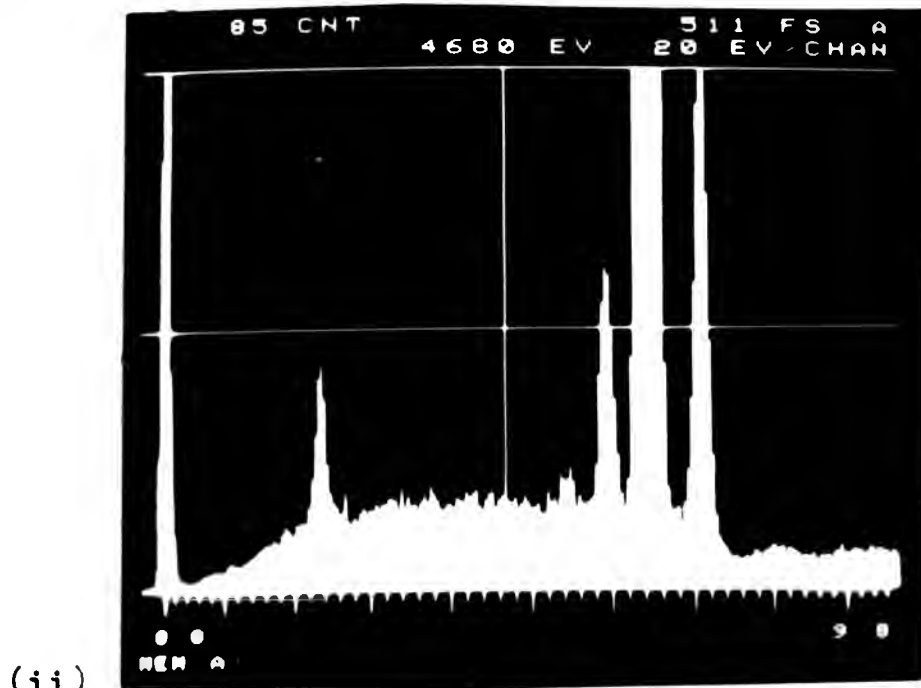
(e)



(f(i))

Scanning electron micrographs of (e) wrought specimen after immersion for nearly 20 hours and (f(i)) annealed specimen ( $920^{\circ}\text{C}$  for 3 hours) after immersion for 17 hours, in 0.6 M sodium chloride solution.

Fig R 10: Examination results of the surface of mild steel specimens.



(f) X-ray spectra analysis results of areas in (f(i)) indicated by (ii) "O" showing the presence of S, Mn, and Fe, (iii) "X" exhibiting the absence of S, and (iv) "\*" showing the presence of S (at 2.3), Mn (at 5.9), and Fe (at 6.4). Energy level vs intensity curves.

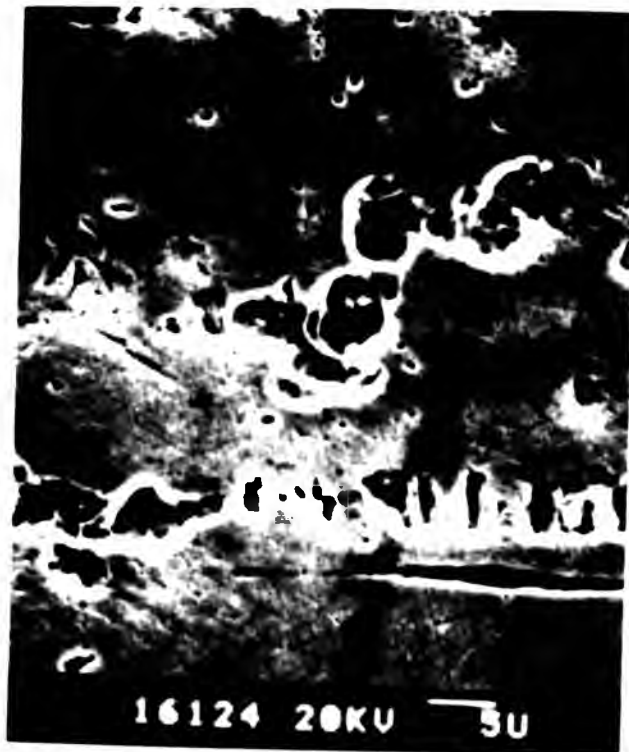
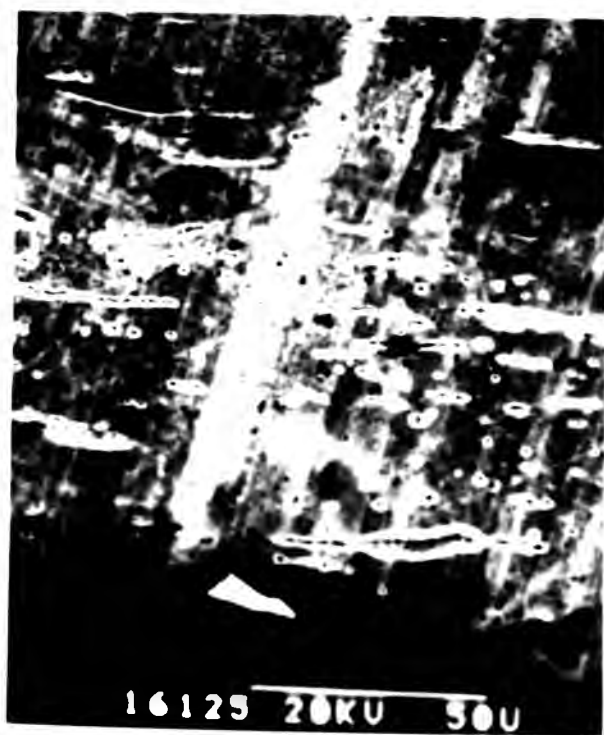
Fig R 10: Examination results of the surface of mild steel specimens.

The majority of tests were performed on as received specimens although a few tests were repeated with annealed specimens. A representative sample of micrographs have been included in Figure R 11.

Figure R 11a exhibits the surface of a specimen, annealed at  $920^{\circ}\text{C}$  for 3 hours in argon, which was rotated for approximately  $1.3 \times 10^6$  reversals without stress. The micrograph resembles that obtained after immersion tests (Figure R 10e).

On application of stress (183 MPa) dissolution at the inclusion - matrix interface was found to occur (Figure R 11b). Some of the inclusions also appear to have dissolved; the micrograph shows a region of high inclusion density. A similar result was also observed for a specimen tested at 197 MPa for 2,000 reversals (Figure R 11c). The region shown consists of elongated as well as a "shower" of smaller sulphide particles. The commencement of dissolution of these inclusions is shown in Figure R 11d.

Increasing the duration of the tests led to the dissolution of ferrite in the pearlitic area in addition to the dissolution in and around the inclusions (Figure R 11e). A further increase in the number of reversals at the same stress reveals localised corrosion at the matrix - inclusion interface leaving the inclusion isolated from the matrix. Localised corrosion also occurs in the vicinity of the inclusion creating micropits (Figure R 11f). Figure R 11g shows the tendency of these micropits in the ligaments between the sulphide particles in a high inclusion density region to coalesce. In the low density regions in which the inclusions are further apart, the tendency for amalgamation of the micro or macropits is not so discernible (Figure R 11h).



(a) (b) (c) (d)

Annealed specimens, 920°C for 3 hours in argon, (a) rotated without an applied stress after  $1.3 \times 10^6$  reversals showing high inclusion density area and (d) after 2000 reversals at 198 MPa exhibiting localised attack and breakdown of inclusions. Crystallographic pits are also observed. Wrought specimens (b) after 200 reversals at 183 MPa showing dissolution around some inclusions (surface shows presence of salt film) and (c) after 2000 reversals at 197 MPa exhibiting localised attack at inclusions.

Fig. 11: Rotating bend fatigue tests at 47 Hz, R=-1.



The following table lists the micrographs and their corresponding sample numbers and magnifications. The magnification is given in units of 50U (50 micrometers).

Micrograph Number	Sample Number	Magnification
20017	20KV	50U
41216	20KV	50U
16128	20KV	50U
16124	20KV	50U



16123 20KU 3U



41216 20KU 3U

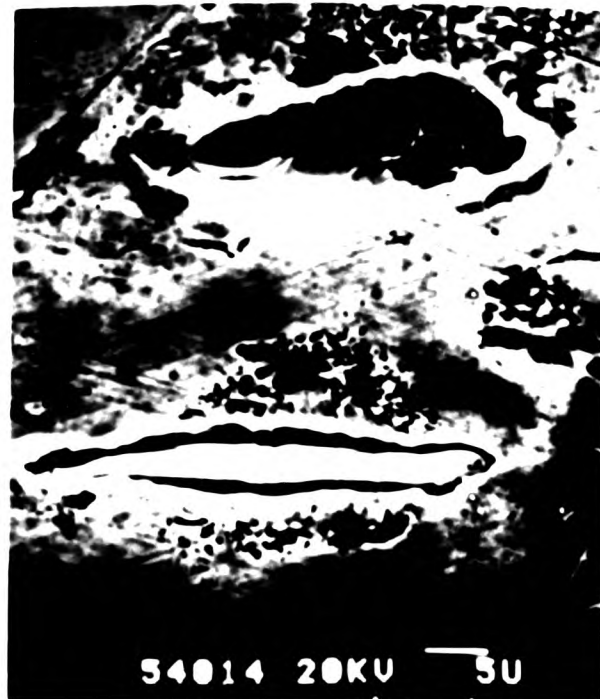


16123 20KU 3U



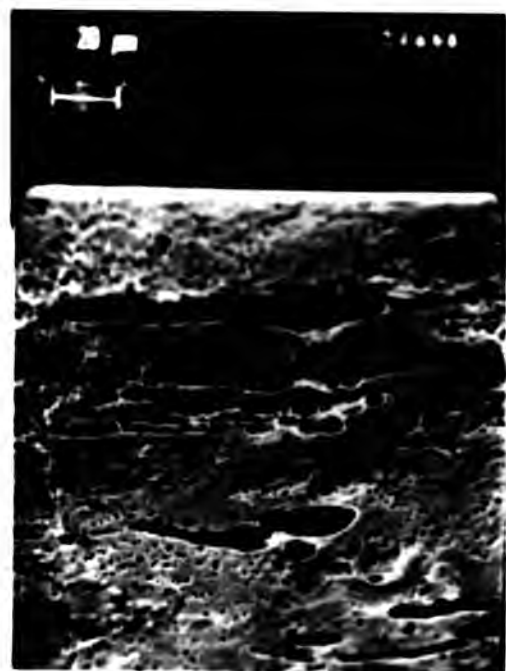
16124 20KU 3U





rough specimens after (e)  $6.1 \times 10^3$  reversals showing dissolution of ferrite in pearlitic area associated with an inclusion, (f)  $3.4 \times 10^4$  reversals showing localised corrosion in the vicinity of an inclusion, (g)  $7.5 \times 10^4$  reversals indicating coalescence of micropits in the ligaments between the inclusions in a high inclusion density region, and (h)  $1.06 \times 10^5$  reversals exhibiting localised attack around an inclusion. Stress = 193 MPa.

Fig. 11: Rotating bend fatigue tests at 47 Hz, R=-1.



(g)

(h)

rough specimens after (e)  $6.1 \times 10^3$  reversals showing dissolution of ferrite in pearlitic area associated with an inclusion, (f)  $3.4 \times 10^4$  reversals showing localised corrosion in the vicinity of an inclusion, (g)  $7.5 \times 10^4$  reversals indicating coalescence of micropits in the ligaments between the inclusions in a high inclusion density region, and (h)  $1.06 \times 10^5$  reversals exhibiting localised attack around an inclusion. Stress = 193 MPa.

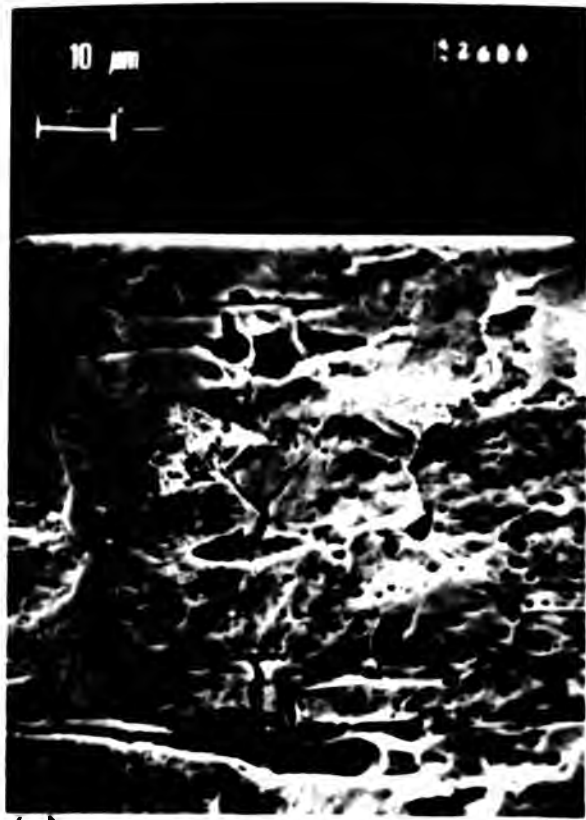
Fig R 11: Rotating bend fatigue tests at 47 Hz, R=-1.

Coalescence of the micropits, leading ultimately to the formation of what appears to be crack initiation in the transverse direction is shown in Figure R 11j. Dissolution and undermining of an inclusion is shown in Figure R 11k. The analysis results reveal the absence of S in the pit created by the removal of the sulphide particle (Figure R 11k (ii)) but the pitted area caused by localised attack around the inclusion contains S, Mn, and Fe (Figure R 11k (iii)); hexagonal pits are also observed in this micrograph (Figure R 11k (i)).

Figures R 11l and R 11m exhibit respectively areas containing relatively fewer and higher number of inclusions when the specimens are fatigue tested at 278 MPa,  $R = -1$ . Increasing the number of reversals to 3,000 and to 33,900 reversals show dissolution, undermining and detachment of the particles (Figures R 11n, R 11p, R 11q). The micrograph, Figure R 11q, resembles that in Figure R 11f, in that localised attack occurred on the matrix close to the inclusions. Thus it appears that dissolution of the matrix close to the inclusions is time dependent and not stress dependent.

It has been observed that in the high inclusion density region, dissolution appears to occur underneath the metal surface (Figure R 11r). As the number of reversals are further increased, coalescence of micropits to form macropits and linking of the macropits to create incipient cracks or microcracks in the transverse direction occurs (Figures R 11s and R 11t).

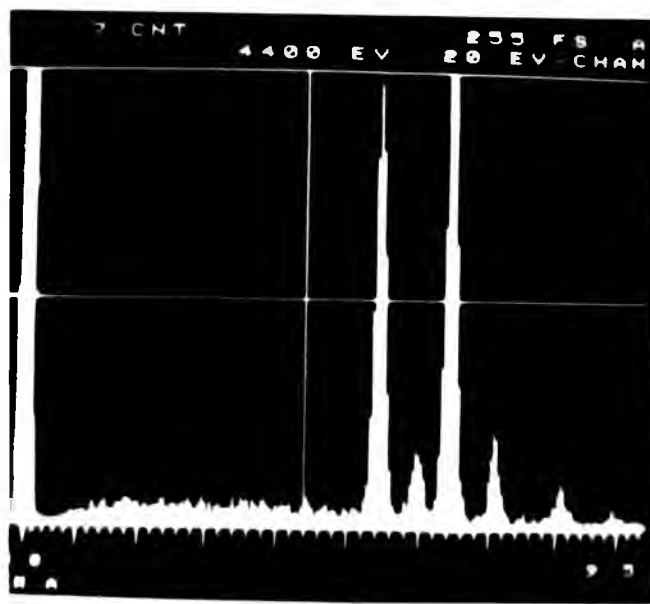
When the stress is further increased to 309 MPa dissolution is found to occur at the grain boundaries and in the pearlitic areas after  $2 \times 10^3$  reversals resulting in the formation of pits (Figure R 11u).



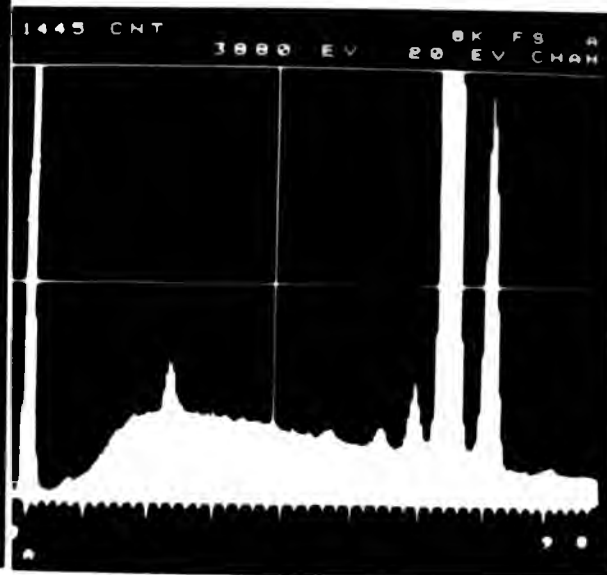
(j)



(k(i))



(k(ii))



(k(iii))

Wrought specimens after  $3.62 \times 10^5$  reversals (j) showing dissolution of inclusions and initiation of transverse microcracks from inclusions at 193 MPa, and (k(i)) exhibiting dissolution and spalling of an inclusion and localised corrosion in the vicinity of the inclusion at 198 MPa. Analysis results indicate (k(ii)) absence of S (at 2.3), and the presence of Cr (at 5.4), Mn (at 5.9) and Fe (at 6.4) in the pit, marked "x", and (k(iii)) the presence of S, Cr, Mn, and Fe in the corroded area, arrowed, around the inclusion; Energy level vs intensity curves.

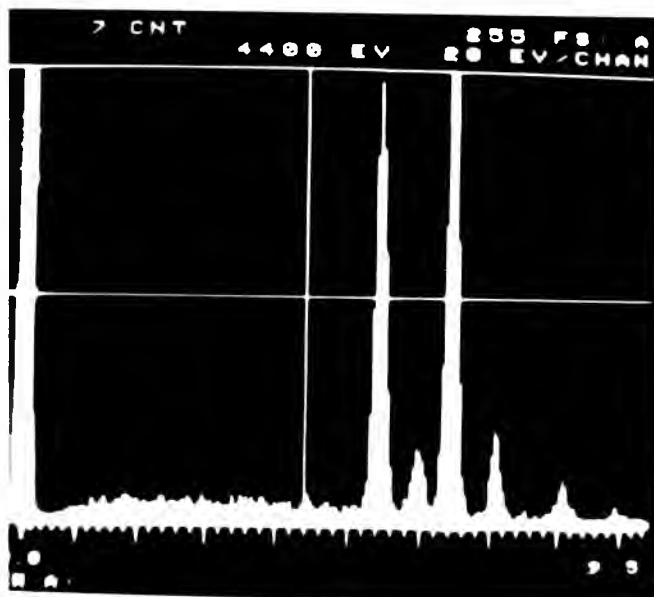
is R 11: Rotating bend fatigue tests at 47 Hz, R=-1.



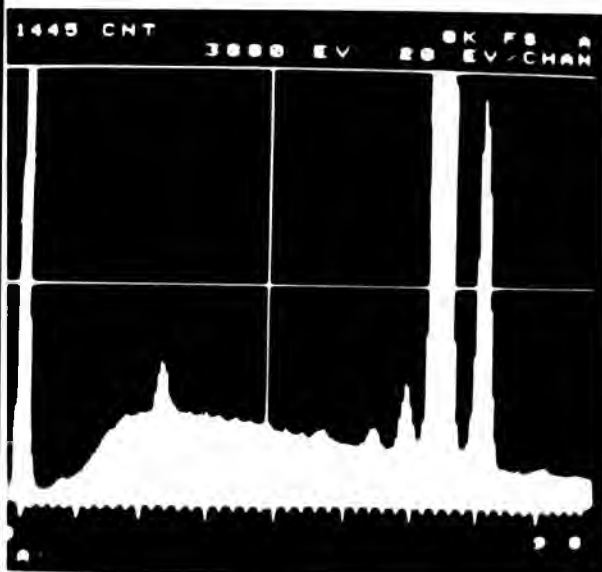
(h)



(i)



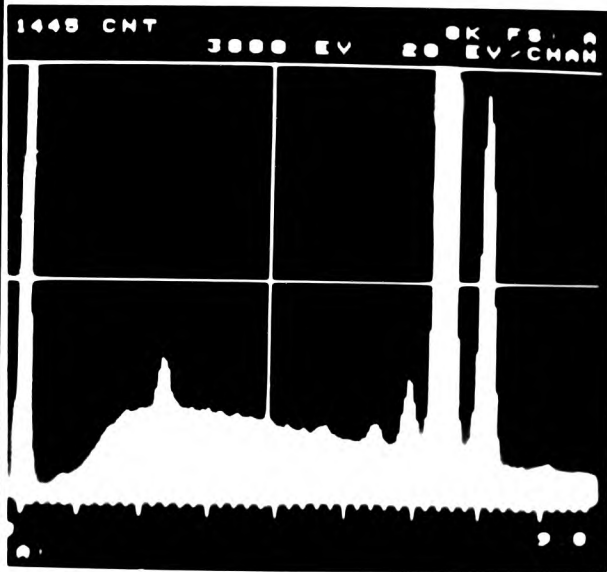
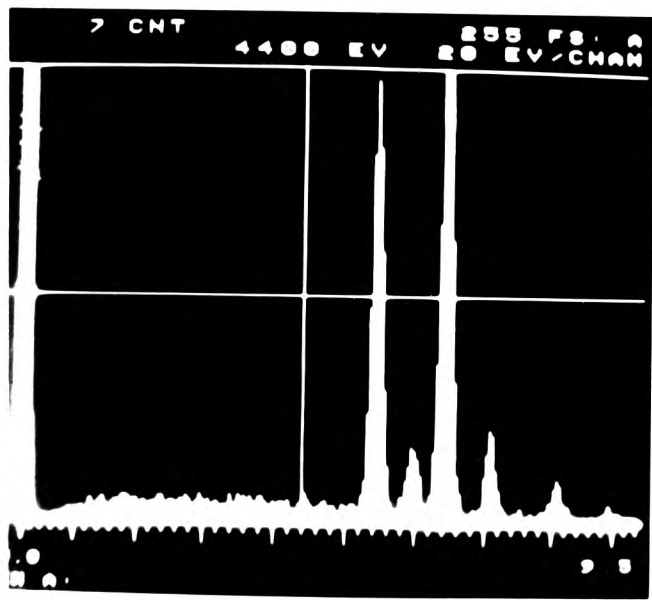
(j)



(k)

coupled specimens after  $4.07 \times 10^5$  revolutions (j) showing dissolution of inclusions and initiation of transverse microcrack from inclusions at 178 MPa, and (k(i)) exhibiting dissolution and swelling of an inclusion and localized corrosion in the pit adjacent to the inclusion at 198 MPa. Analysis results indicate (k(ii)) presence of Fe (at 2.3), and the presence of Cr (at 1.0), In (at 0.2), and Ni (at 0.2) in the pit, marked "x", and (k(iii)) the presence of Fe, Cr, Ni, and In in the corrosion product, marked "y". The EDS spectra and the corresponding activity curves are shown in Figures 10 and 11.

The micrographs of the specimens after 4.07 x 10<sup>5</sup> revolutions are shown in Figures 12 and 13.



)

( 1 )

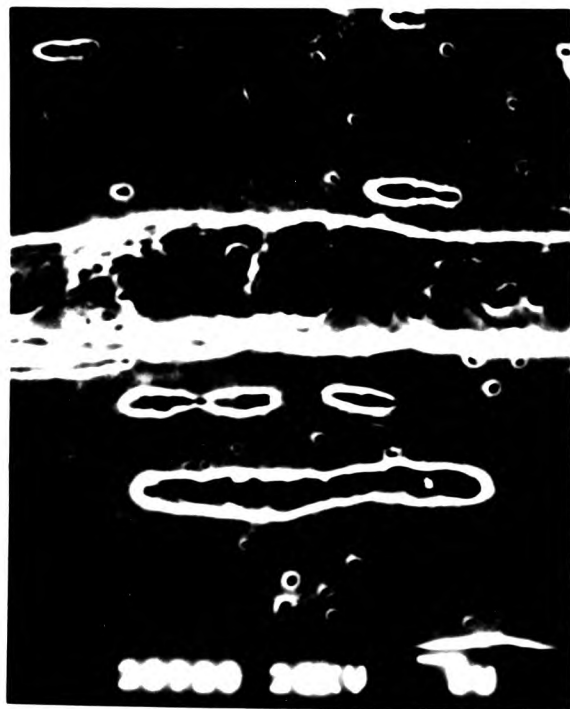




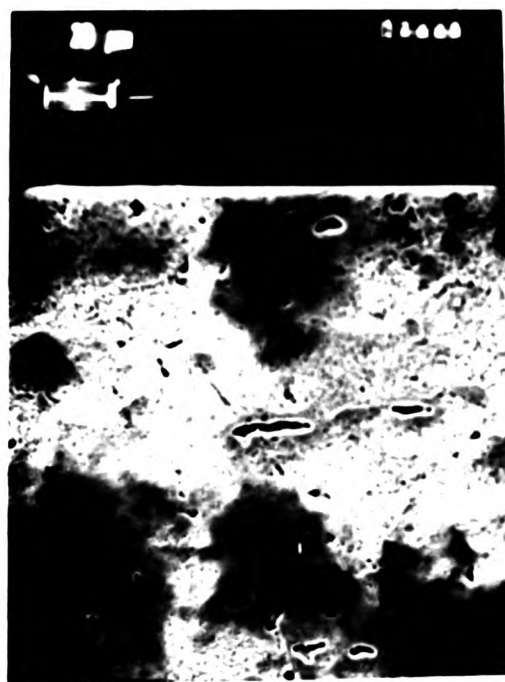
(l)



(m)



(n)



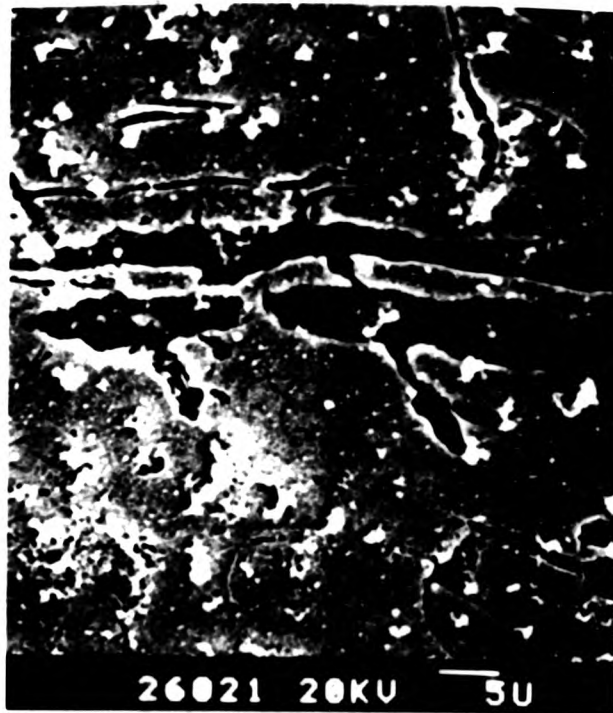
(p)

rough specimens after (l) 2000 reversals showing inclusions in the relatively low inclusion density region, (m) 2000 reversals exhibiting coalescence of the micropits, dissolution of the inclusions, and linking up of the macropits, (n) 3000 reversals showing dissolution of inclusions, and (p)  $3.4 \times 10^4$  reversals indicating absence of macropit linking in the low inclusion density region. Stress = 278 MPa.

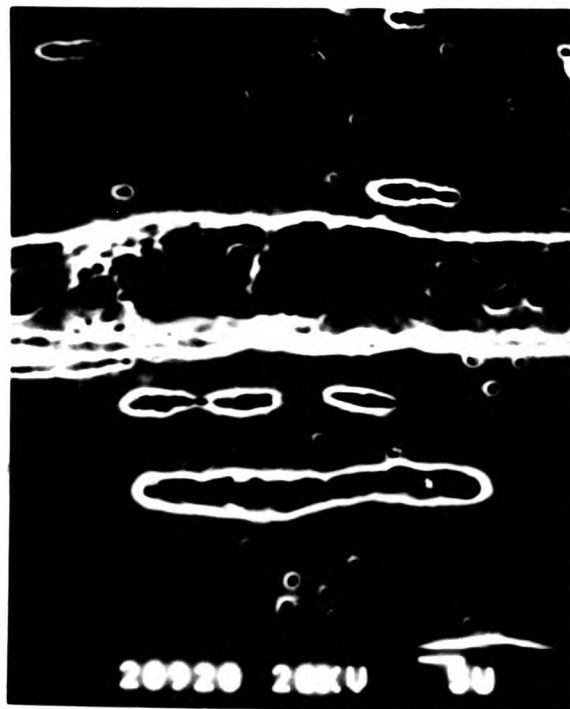
Fig. 1: Rotating bend fatigue tests at 47 Hz, R=-1.



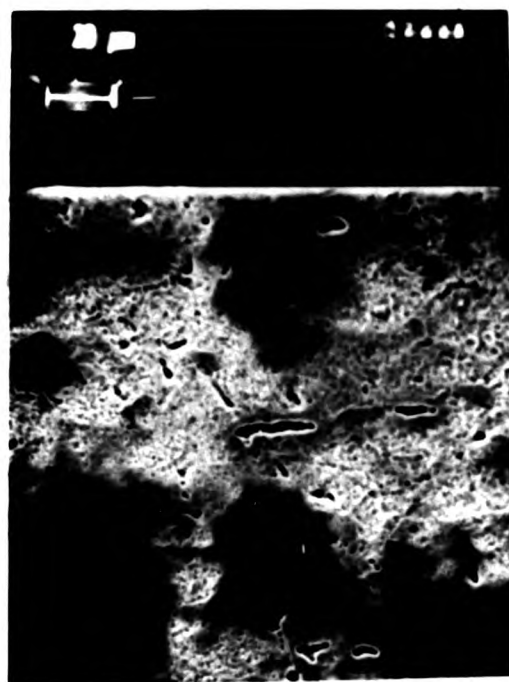
(l)



(m)



(n)



(p)

Wrought specimens after (l) 2000 reversals showing inclusions in the relatively low inclusion density region, (m) 2000 reversals exhibiting coalescence of the micropits, dissolution of the inclusions, and linking up of the macropits, (n) 3000 reversals showing dissolution of inclusions, and (p)  $3.4 \times 10^4$  reversals indicating absence of macropit linking in the low inclusion density region. Stress = 278 MPa.

Fig. 11: Rotating bend fatigue tests at 47 Hz, R=-1.



(q)



(r)



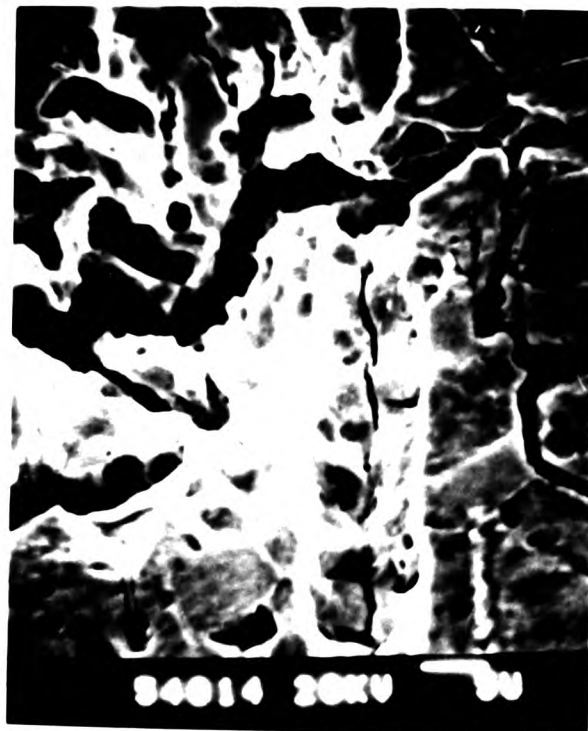
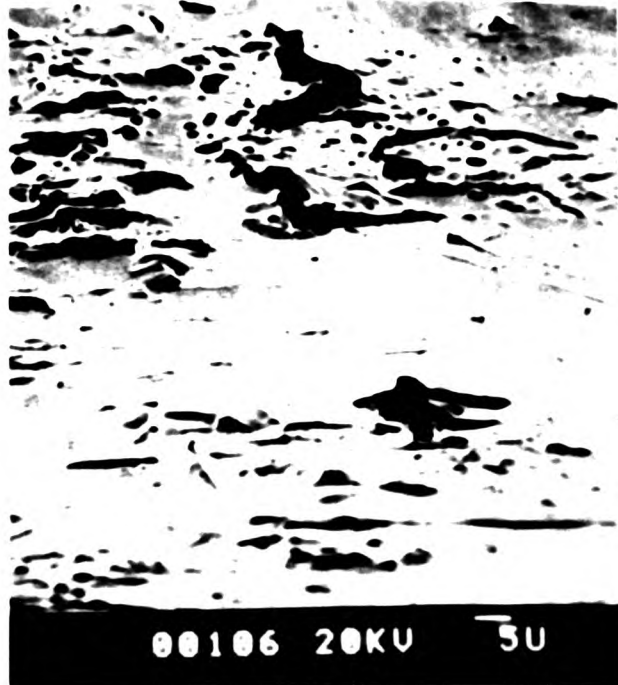
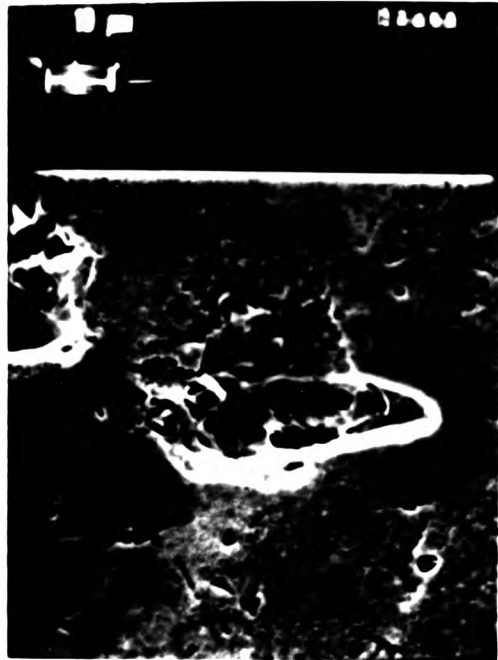
(s)



(t)

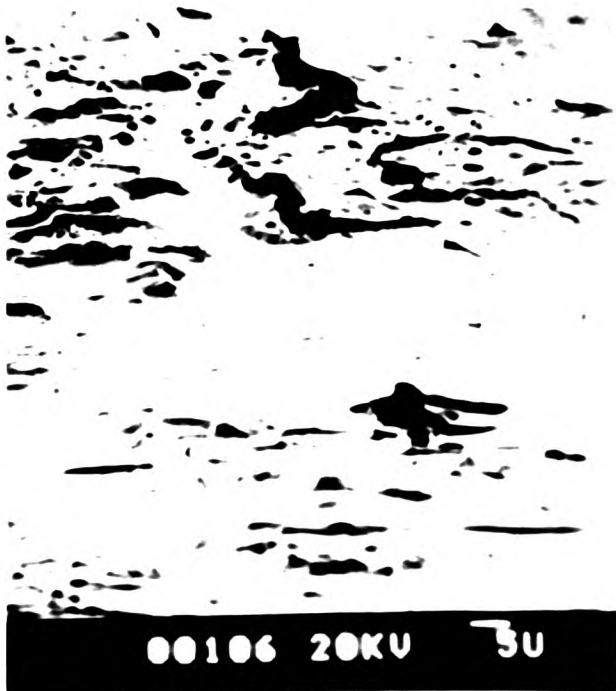
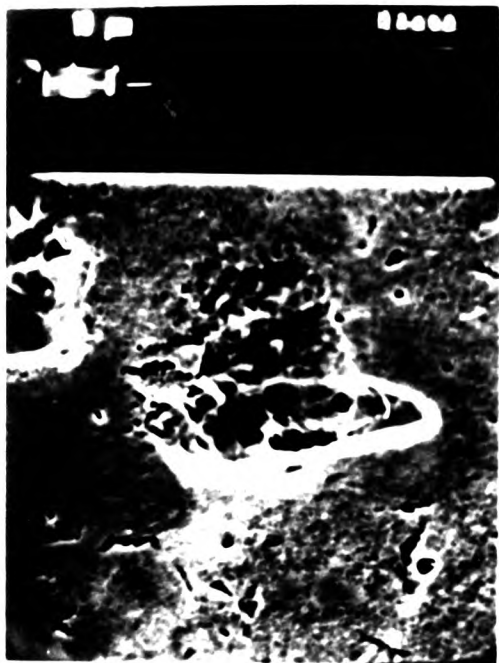
Wrought specimens after (q)  $3.4 \times 10^4$  reversals showing dissolution of inclusions and localised corrosion, (r)  $5.1 \times 10^4$  reversals exhibiting localised corrosion, (s)  $9.6 \times 10^4$  reversals indicating dissolution of inclusions and transverse cracks originated from these inclusions, and (t)  $4.38 \times 10^5$  reversals showing dissolution of inclusions and transverse cracks which lead to fracture. Stress = 278 MPa.

Fig. R 11: Rotating bend fatigue tests at 47 Hz, R=-1.



rough surface, after (a)  $3.4 \times 10^{-4}$  reversals showing  
 dissolution of inclusion and localized corrosion, (b)  $5.1 \times 10^{-4}$   
 reversals exhibiting localized corrosion, (c)  $1.5 \times 10^{-3}$  reversals  
 exhibiting dissolution of inclusions and transverse cracks  
 originate from these inclusions, and (d)  $1.5 \times 10^{-3}$  reversals  
 showing dissolution of inclusions and transverse cracks  
 originate from these inclusions.

The surface area of the test specimen is  $1.5 \text{ cm}^2$ .





41207 20KU 5U

Figure 11: Metallographic micrograph of a specimen after 2000 reversals at 300 MPa showing crack growth along grain boundaries and in acicular ferrite.

Figure 12: Rotating band fatigue tests at 40 Hz, R=-1.



(u)

Wrought specimen after 2000 reversals at 309 MPa showing dissolution along grain boundaries and in pearlitic areas.

Fig. R 11: Rotating bend fatigue tests at 47 Hz, R=-1.



(u)

Wrought specimen after 2000 reversals at 309 MPa showing dissolution along grain boundaries and in pearlitic areas.

Fig R 11: Rotating bend fatigue tests at 47 Hz, R=-1.

At this high stress level, all the phenomena, such as the dissolution and detachment of the inclusions, formation of hexagonal pits, linking up of the micropits to create incipient cracks in the transverse direction, are observed. However, the significance of dissolution appears to decrease and that of the stress appear to be predominant in the mechanism of the formation of incipient cracks thereby reducing the number of reversals required to nucleate microcracks. The close relationship between the inclusions and the formation of transverse cracks is shown in Figures R 11v and R 11w.

The pH value of the liquid at the mouth of the crevices or micropits on the external surfaces of the specimens which were rotated without stress for  $1.31 \times 10^6$  reversals was found to be approximately 4.5 whilst that for specimens tested at 193 MPa,  $R = -1$ , after  $3.4 \times 10^4$  reversals was between 3 - 3.5, indicating the contribution of stress in lowering the pH values. The application of cyclic stress appears to enhance the dissolution and hydrolysis of the metal within the crevices and micropits.

#### 4.8.2 Transmission electron microscopic examinations

Results of the examination of rotating bend fatigue tested specimens using transmission electron microscopy are shown in Figures R 12 - R 20.

Tests were performed mainly on as received material but one series of tests were carried out on specimens annealed at  $925^\circ \text{C}$  for 3 hours in argon, for comparison purposes. For the same reason some tests were performed in air. A few tests were also carried out using electropolished (10% perchloric acid/acetic acid) specimens in 0.6 M sodium chloride solution.



(v(i))



(v(ii))



(w(i))



(w(ii))

Wrought specimens (v) after  $1.61 \times 10^5$  reversals at 364 MPa indicating (i) the importance of mechanical factor at higher stresses and (ii) the linking of transverse cracks leading to fracture; after (w)  $1.01 \times 10^6$  reversals at 247 MPa exhibiting the close relationship between surface longitudinal and transverse cracks associated with (i) inclusions and (ii) formation of macropits.

Fig. 9.11: Rotating bend fatigue tests at 47 Hz, R=-1.



(v(ii))



(w(ii))

wrought specimens (v) after  $1.61 \times 10^5$  reversals at 264 MPa indicating  
 (i) the importance of mechanical factor at higher stresses and (ii)  
 the linking of transverse cracks leading to fracture; after (w)  $1.01 \times 10^5$   
 reversals at 242 MPa exhibiting the close relationship between  
 surface longitudinal and transverse cracks associated with (i)  
 inclusions and (ii) formation of macrovoids.

Fig. 1: Rotating bend fatigue tests at 47 Hz,  $R = -1$ .



Several tests, for each set of stress range, were performed and a representative sample of micrographs have been included in the results.

Figure R 12 exhibits the surface of the specimen after 5 and approximately 17 hours immersion in 0.6 M sodium chloride solution indicating dissolution of the inclusions and the matrix - inclusion interfaces (Figures R 12a - R 12f). Figure R 12g shows localised attack at the cementite - ferrite interfaces, micropits at the grain boundaries, and terminations and bends in the lamellar structures.

On the application of cyclic stress, 95 MPa,  $R = -1$ , dissolution of the ferrite in the pearlitic region is found to occur (Figure R 13a and Figure R 13b). Localised attack also occurs at the matrix - inclusion interface (Figure R 13c) after  $1.59 \times 10^5$  reversals.

Figure R 13d shows micropits and coalescence of micropits at the matrix - inclusion interface at  $3.18 \times 10^5$  reversals. At some of the inclusions microfissure nucleation in the transverse direction is also observed (Figure R 13e). Slip band formation is also found to occur (Figure R 13f).

As the number of reversals is further increased, microfissures tend to appear around the slip bands (Figure R 13g). Fracture of some of the inclusions and increasing dissolution at the matrix - inclusion interfaces also appear to occur (Figure R 13h): blisters surrounding the inclusion in the micrograph appear to be artifacts.

With increasing number of reversals, micropits tend to appear within the slip band (Figure R 13j) whilst further increase in the number of reversals reveal microcracks associated with the pearlitic region, slip bands and inclusions (Figure R 13k - R 13m). Etch pits and blisters in the matrix associated with inclusions are also found to occur at a higher number of reversals (Figure R 13n).

Several tests, for each set of stress range, were performed and a representative sample of micrographs have been included in the results.

Figure R 12 exhibits the surface of the specimen after 5 and approximately 17 hours immersion in 0.6 M sodium chloride solution indicating dissolution of the inclusions and the matrix - inclusion interfaces (Figures R 12a - R 12f). Figure R 12g shows localised attack at the cementite - ferrite interfaces, micropits at the grain boundaries, and terminations and bends in the lamellar structures.

On the application of cyclic stress, 95 MPa,  $R = -1$ , dissolution of the ferrite in the pearlitic region is found to occur (Figure R 13a and Figure R 13b). Localised attack also occurs at the matrix - inclusion interface (Figure R 13c) after  $1.59 \times 10^5$  reversals.

Figure R 13d shows micropits and coalescence of micropits at the matrix - inclusion interface at  $3.18 \times 10^5$  reversals. At some of the inclusions microfissure nucleation in the transverse direction is also observed (Figure R 13e). Slip band formation is also found to occur (Figure R 13f).

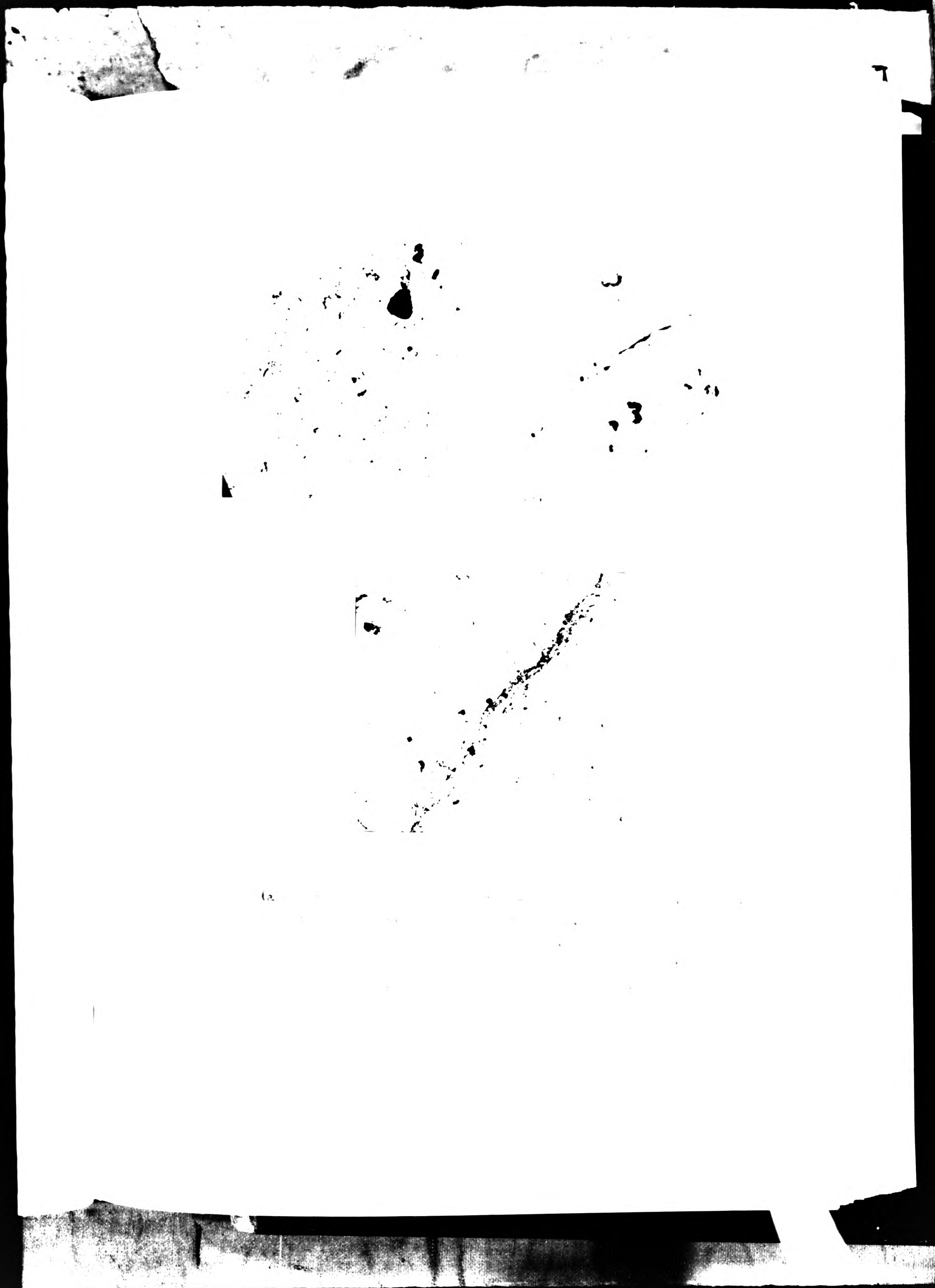
As the number of reversals is further increased, microfissures tend to appear around the slip bands (Figure R 13g). Fracture of some of the inclusions and increasing dissolution at the matrix - inclusion interfaces also appear to occur (Figure R 13h): blisters surrounding the inclusion in the micrograph appear to be artifacts.

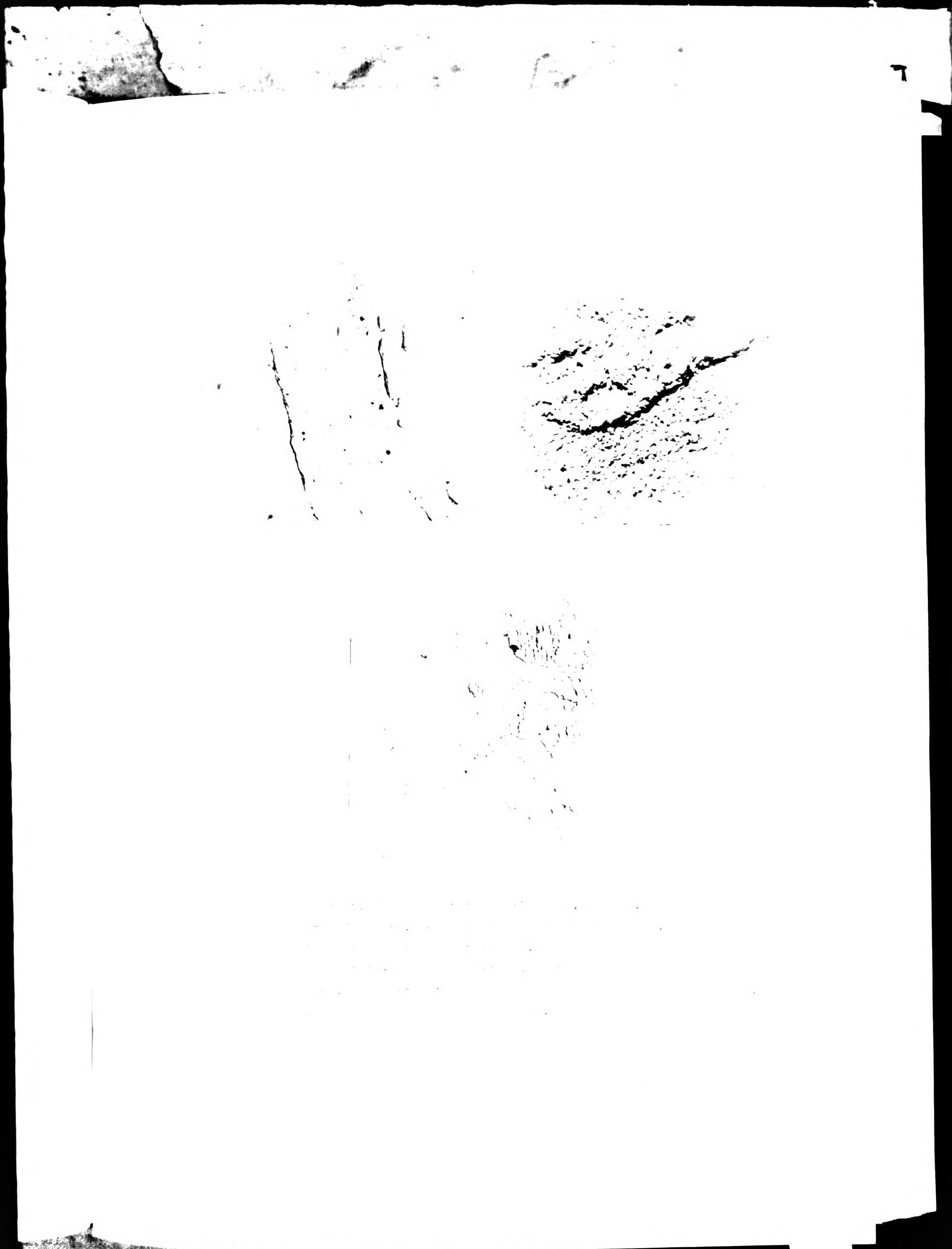
With increasing number of reversals, micropits tend to appear within the slip band (Figure R 13j) whilst further increase in the number of reversals reveal microcracks associated with the pearlitic region, slip bands and inclusions (Figure R 13k - R 13m). Etch pits and blisters in the matrix associated with inclusions are also found to occur at a higher number of reversals (Figure R 13n).

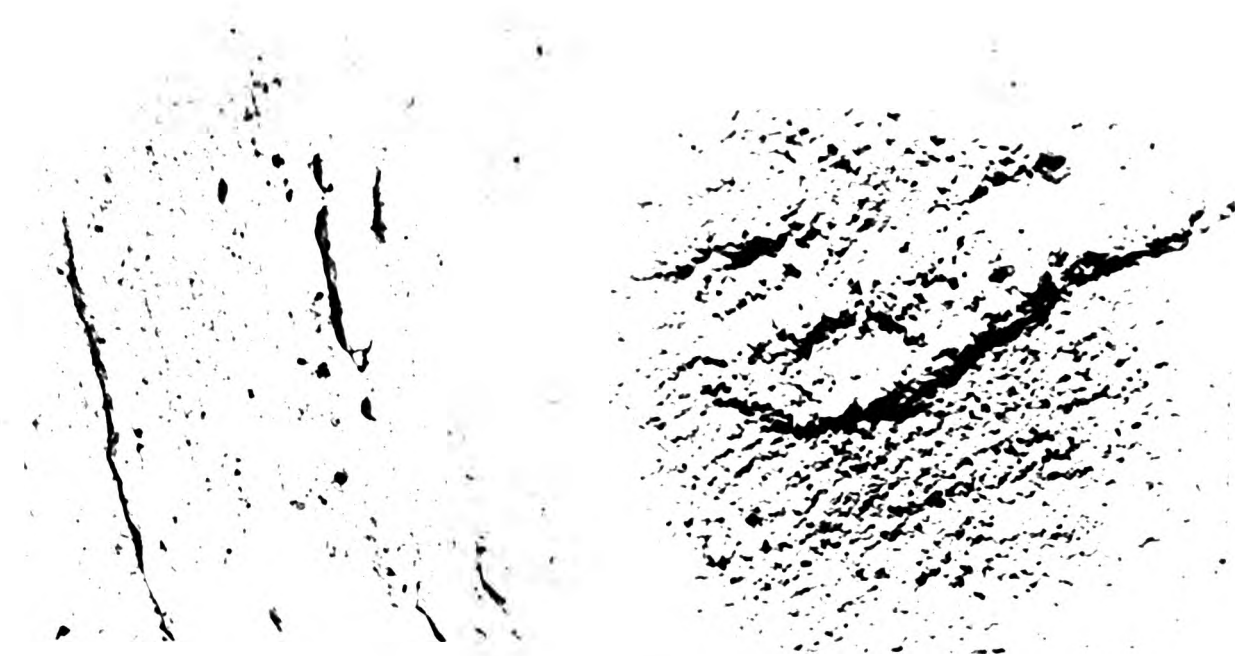


(a) reference state of matrix-inclusion interface, x 2000, microvoid formation at the interface, higher magnification (b), x 11200, immersion for 1 hour, and (c) dissolution of some of the inclusions and localised attack of the matrix close to the interface, x 2110, immersion for 1 hour.

Fig. 1: Examples on electron micrographs of carbon particles (a) and (b) showing the edge of the inclusion (left) and the matrix (right) and the interface (c) showing the localised attack of the matrix.



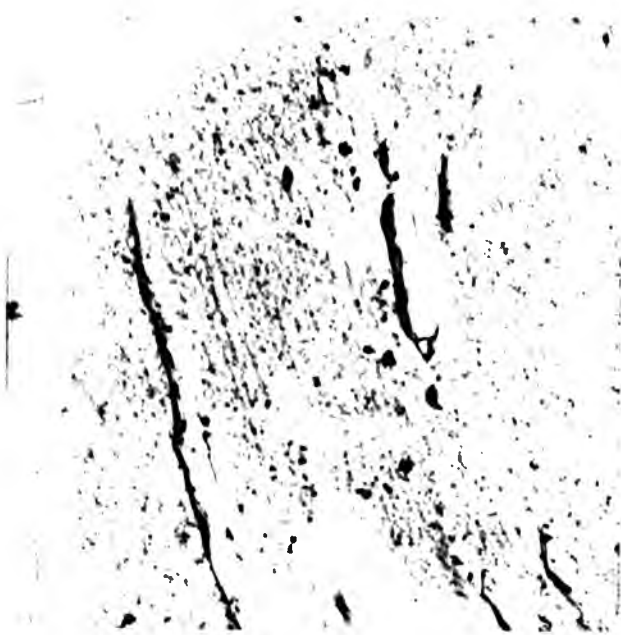




(f)

preferential attack at the inclusions, x 2125, immersion for nearly 17 hours, (e) higher magnification of (d), x 4025, indicating attack at the interfaces, and (f) localized attack at the cementite-ferrite interface, microvoids at the grain boundaries, and terminations and bends in the lamellar structure, x 4025, immersion for nearly 17 hours.

Transmission electron micrographs of carbon particles of various sizes in fatigue test specimens after immersion in 10% sodium chloride solution without stress.



(d)



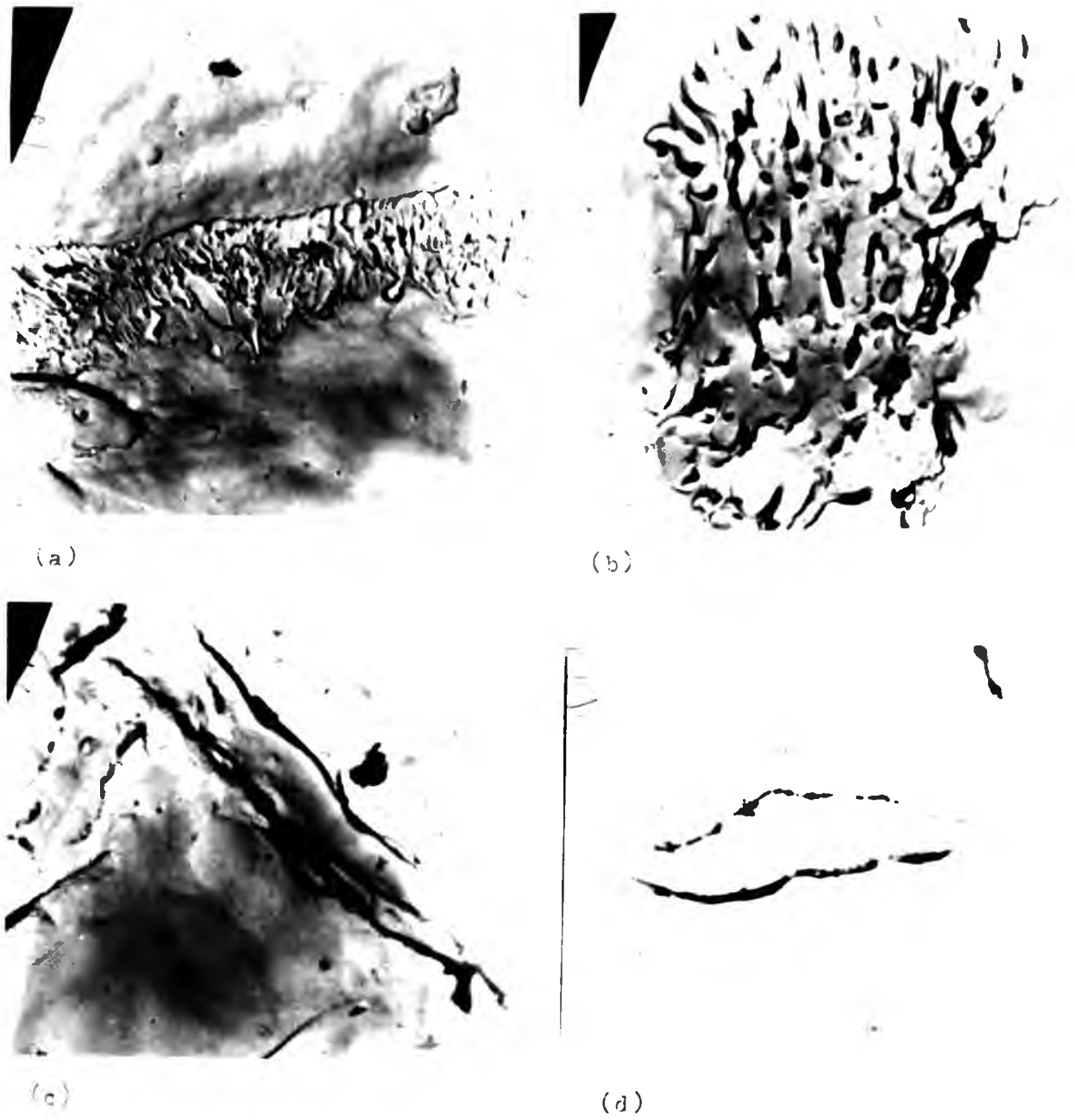
(e)



(f)

(d) Preferential attack at the inclusions, x 2182, immersion for nearly 17 hours, (e) higher magnification of (d), x 9727, indicating attack at the interfaces, and (f) localised attack at the cementite-ferrite interface, micropits at the grain boundaries, and terminations and bends in the lamellar structure, x 2182, immersion for nearly 17 hours.

12: Transmission electron micrographs of carbon replicas of rotating bend fatigue test specimens after immersion in 0.6 M sodium chloride solution without stress.



wrought specimens exhibiting (a) pearlitic region after  $1.59 \times 10^5$  reversals, x 3091, (b) higher magnification of (a), x 9727, indicating microvoid formation in the ferrite, (c) formation of microcrack at an inclusion after  $1.59 \times 10^5$  reversals, x 9727 and (d) coalescence of micropits to form macropits around an inclusion after  $3.18 \times 10^5$  reversals, x 9727.

Fig. R 13: Transmission electron micrographs of rotating bend fatigue tested specimens at 95 MPa,  $R=-1$ , 47 Hz.

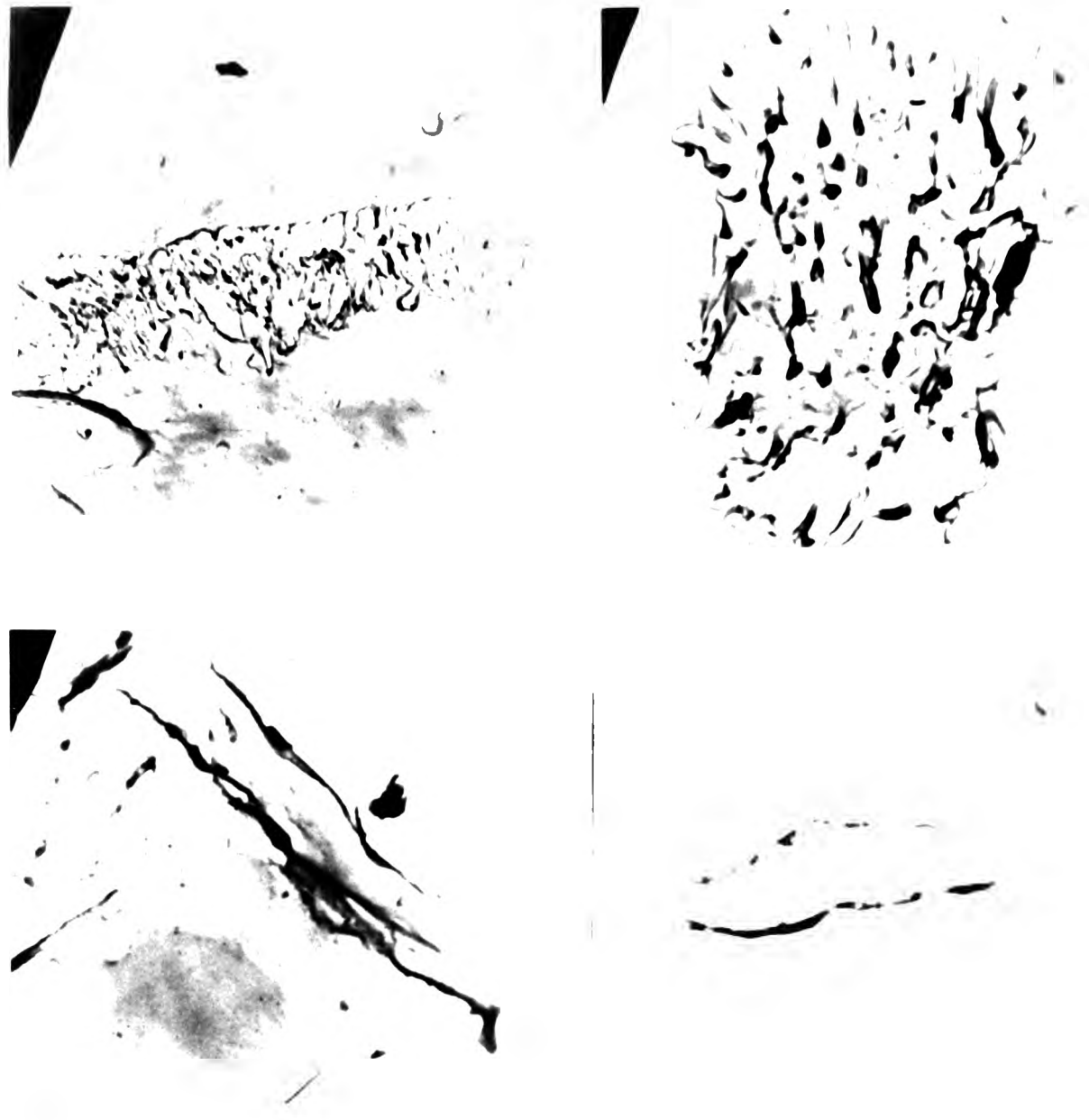
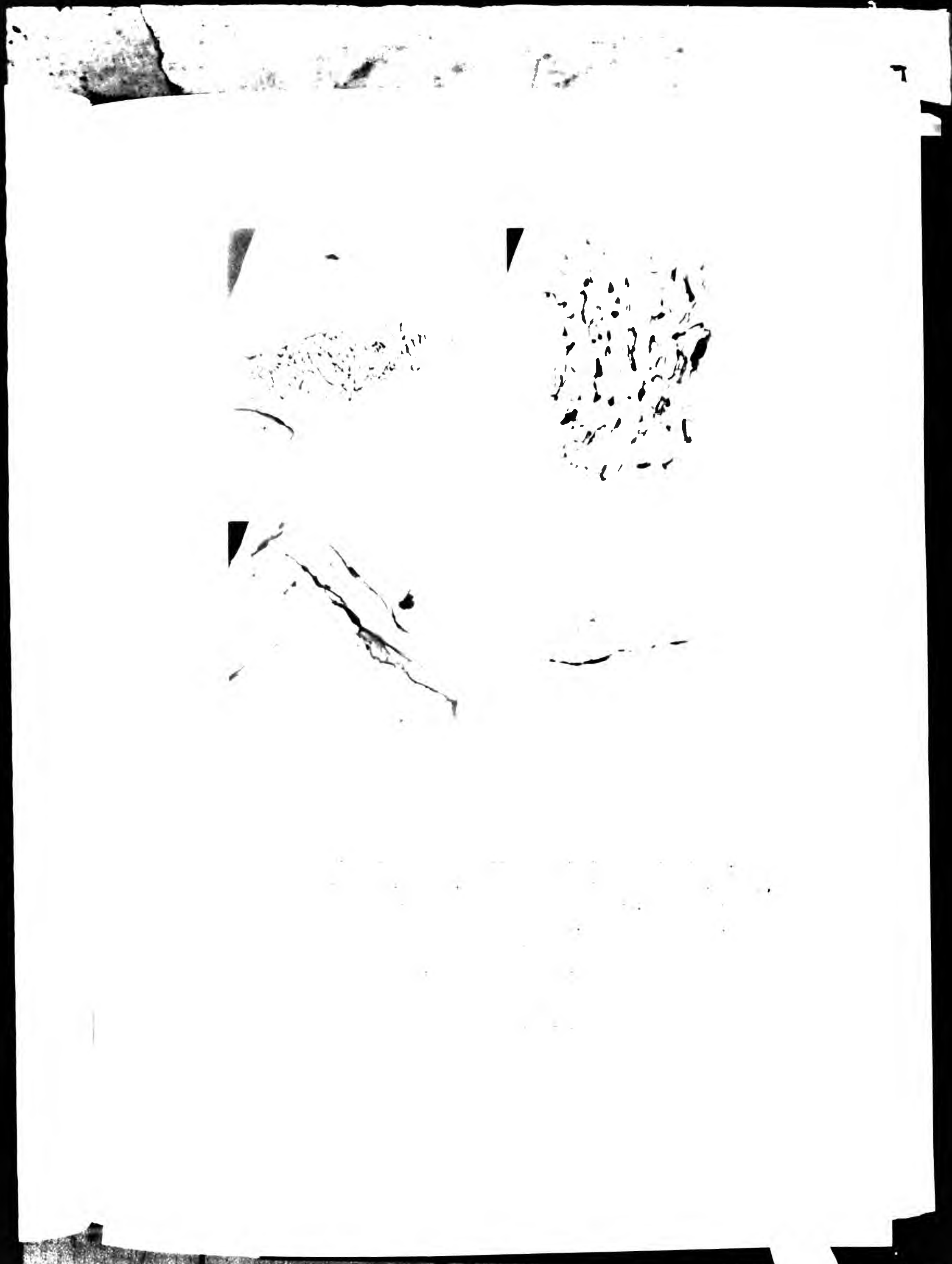


Figure 1. Transmission electron micrographs of retained pearlite in a  
 low alloy steel after cyclic loading at 200°C. (a) pearlitic region after  $1.5 \times 10^7$   
 reversals,  $\times 2000$ , (b) higher magnification of (a),  $\times 7000$ ,  
 highlighting microvoid formation in the ferrite, (c) formation  
 of microcrack or inclusion after  $2.5 \times 10^7$  reversals,  $\times 7000$ ,  
 (d) coalescence of microvoids to form macrovoids around an  
 inclusion after  $4.5 \times 10^7$  reversals,  $\times 7000$ .

Figure 2. Transmission electron micrographs of retained pearlite in a  
 low alloy steel after cyclic loading at 200°C.



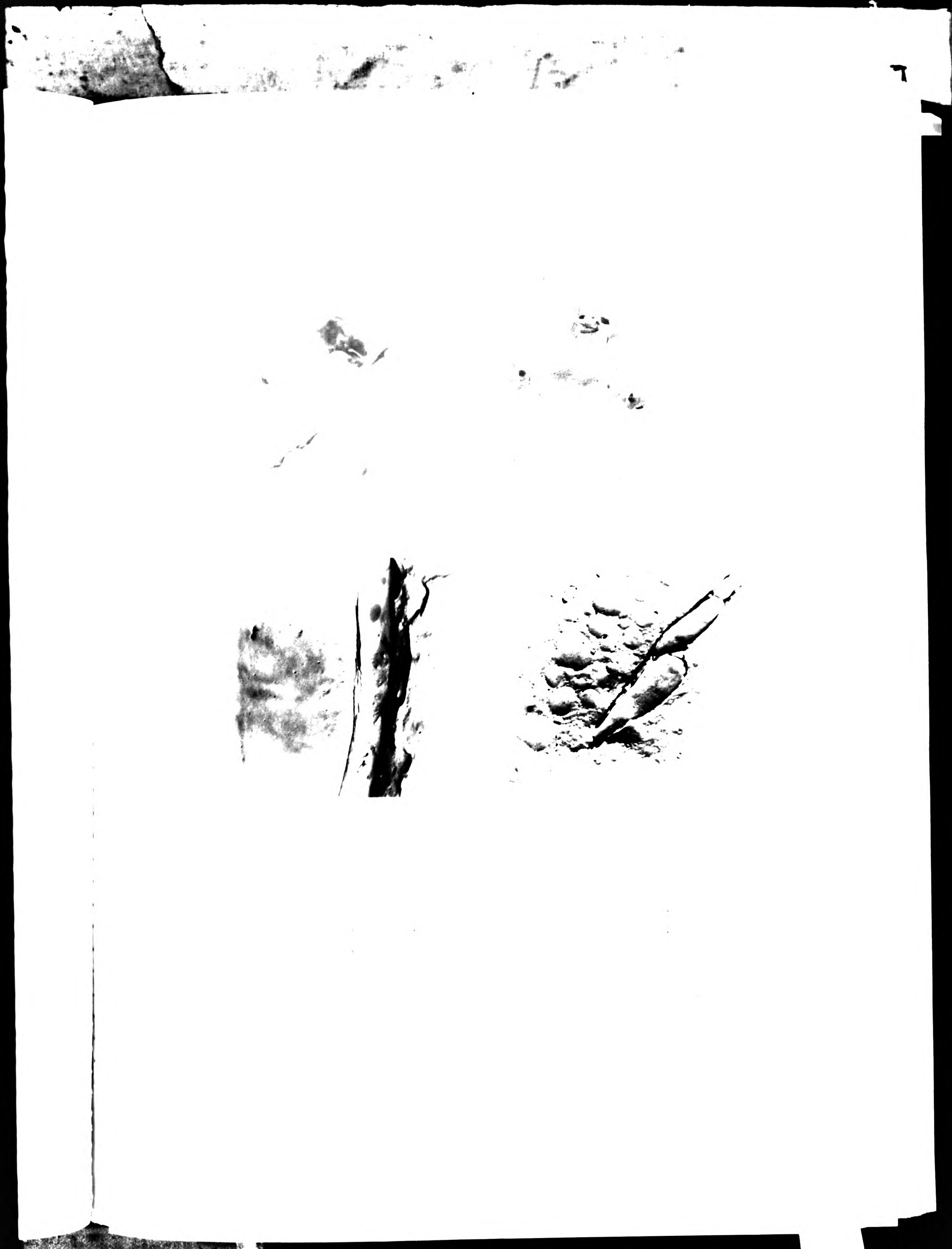




Figure 1: Transmission electron micrographs of rotating bend fatigue tested specimens of 7075-T6 Al<sub>2</sub>O<sub>3</sub> showing (a) formation of microfeature in the transverse direction from an inclusion after  $4.1 \times 10^5$  reversals,  $\times 4000$ , (b) slip band formation after  $4.1 \times 10^5$  reversals,  $\times 4000$ , (c) slip band and associated microfeatures after  $4.1 \times 10^5$  reversals,  $\times 4000$ , and (d) localized attack around an inclusion after  $4.1 \times 10^5$  reversals,  $\times 4000$ .

Figure 2: Transmission electron micrographs of rotating bend fatigue tested specimens of 7075-T6 Al<sub>2</sub>O<sub>3</sub>.



Wrought specimens exhibiting (e) formation of microfissure in the transverse direction from an inclusion after  $3.18 \times 10^5$  reversals, x 4900, (f) slip band formation after  $3.18 \times 10^5$  reversals, x 3091, (g) slip band and associated microfissures after  $4.16 \times 10^5$  reversals, x 9727, and (h) localised attack around an inclusion after  $4.16 \times 10^5$  reversals, x 9727.

Fig. 13: Transmission electron micrographs of rotating bend fatigue tested specimens at 95 MPa, R=-1, 47 Hz.



(j)



(k)



(l)



(m)

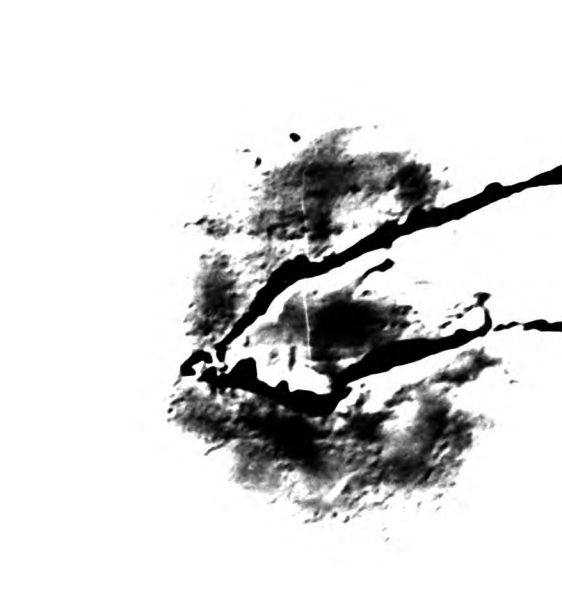
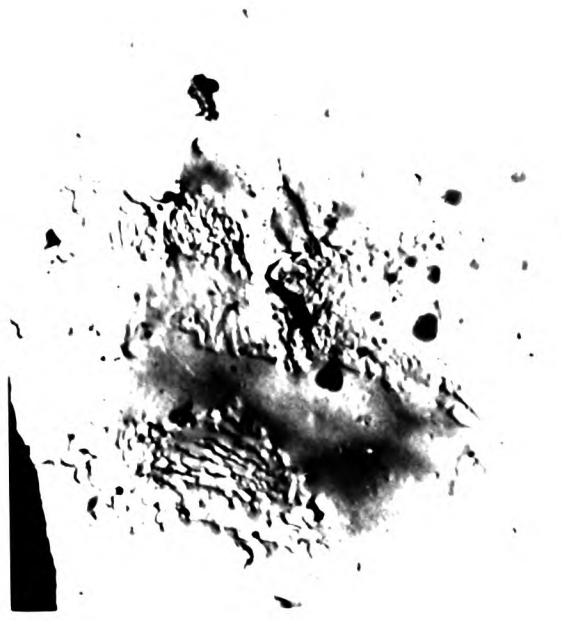
rought specimens exhibiting (j) microvoid formation in the pearlitic region and slip band with micropits after  $3.52 \times 10^5$  reversals,  $\times 9727$ , (k) microcracks associated with pearlitic region after  $7.28 \times 10^5$  reversals,  $\times 3091$ , (l) microcracks associated with slip bands after  $7.28 \times 10^5$  reversals,  $\times 2182$ , and (m) microcracks associated with an inclusion after  $7.28 \times 10^5$  reversals,  $\times 11273$ .

Fig. R 13: Transmission electron micrographs of rotating bend fatigue tested specimens at 95 MPa,  $R=-1$ , 47 Hz.



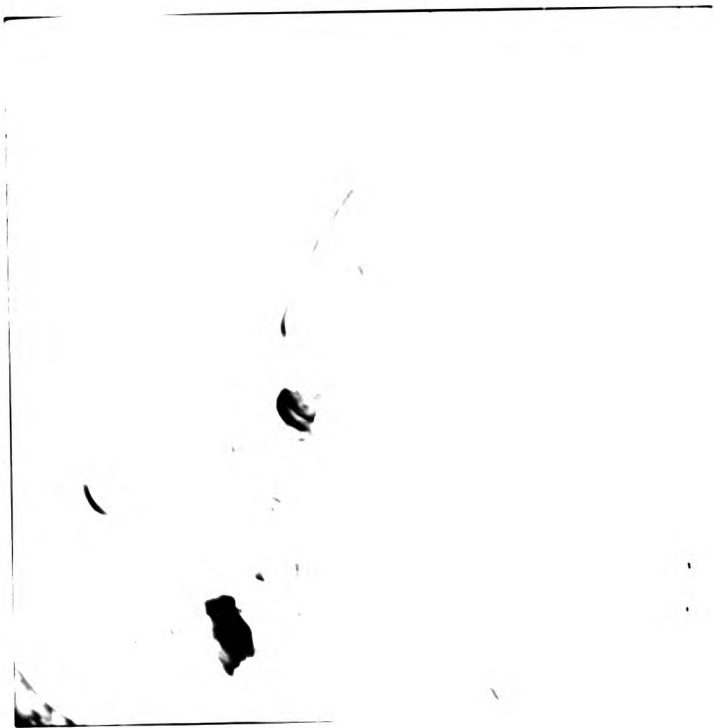
re-tilt specimens exhibiting (j) microvoid formation in the  
 pearlitic region and slip band with microvoids after  $7.5 \times 10^7$   
 reversals, x 2000, (k) microcracks associated with pearlitic  
 region after  $7.5 \times 10^7$  reversals, x 2000, (l) microcrack  
 associated with slip bands after  $1.3 \times 10^8$  reversals, x 2000,  
 and (m) microcracks associated with an inclusion after  $1.3 \times 10^8$   
 reversals, x 10000.

Fig. 14: Transmission electron micrographs of pearlitic specimens  
 tested specimens at 10 Min, 10-1, 10-2, etc.



result obtained exhibited inclusion with weak air ...  
located in the center close to the surface ...  
surface after a  $1.3 \times 10^4$  potential, x 100.

Fig. 4: Diagram for electron microscopy of rot ...  
... at  $100 \text{ kV}$ ,  $t = 1.6 \text{ sec}$ .



(n)

D wrought specimen exhibiting inclusion with etch pits and blisters in the matrix close to the matrix-inclusion interface after  $1.3 \times 10^6$  reversals, x 9727.

Fig R 13: Transmission electron micrographs of rotating bend fatigue tested specimens at 95 MPa, R=-1, 47 Hz.



(n)

Wrought specimen exhibiting inclusion with etch pits and blisters in the matrix close to the matrix-inclusion interface after  $1.3 \times 10^6$  reversals, x 9727.

Fig R 13: Transmission electron micrographs of rotating bend fatigue tested specimens at 95 MPa, R=-1, 47 Hz.

Applications of cyclic stress, 95 MPa,  $R = -1$ , on specimens annealed at  $925^{\circ}\text{C}$  for 3 hours in argon illustrate dissolution at the matrix - inclusion interface and the appearance of rectangular pits on the matrix in a high inclusion density region (Figure R 14a).

Localised attack at the ferrite - cementite interfaces, and terminations and bends in the cementite lamellae in the pearlitic region are found to occur (Figures R 14b and R 14c). Although these defects, such as bands and terminations of the cementite lamellae, have been observed in specimens with zero stress, they appear to become more prominent on the application of cyclic stresses.

Figure R 14d shows features resembling extrusion - intrusion effects associated with microcracks at triple points after  $6.25 \times 10^5$  reversals. With increasing number of reversals, coalescence of the microcracks in the ferrite of pearlitic regions is found to occur (Figure R 14e). Inclusions associated with blisters and intrusions are also observed (Figure R 14f). A deformed region containing etch pits is illustrated in Figures R 14g and R 14h. Figures R 14j - R 14m show microcracks and slip bands at grain boundaries and at the junction of the grain boundaries; these microcracks and slip bands appear to play a significant role with further increase in the number of reversals (Figures R 14n - R 14q).

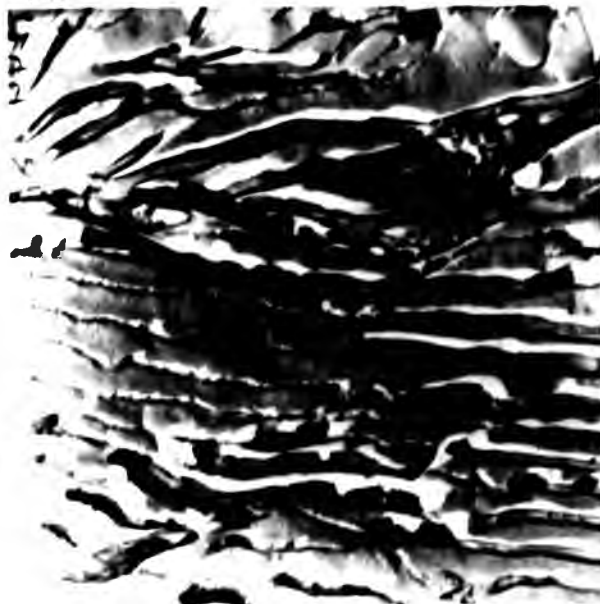
It should be emphasised that the number of reversals at which surface features tend to appear are not absolute values. Replicas were also taken at lower number of reversals but in many cases, examination of the replicas was not possible because of the breakage of the carbon films. This was found to occur if the changes in the surface morphologies were not sufficiently pronounced. Folding and disintegration of the carbon films were also observed when macrocracks appeared to develop.



(a)



(b)



(c)



(d)

Annealed specimens exhibiting (a) localised attack at the matrix-inclusion interface and rectangular pits after  $8.7 \times 10^4$  reversals  $\times 2182$ , (b) voids in pearlitic region after  $6.26 \times 10^5$  reversals  $\times 2182$ , (c) higher magnification of (b) indicating bends and terminations,  $\times 11273$ , and (d) extrusion-intrusion type feature at triple point after  $6.25 \times 10^5$  reversals,  $\times 2182$ .

Fig. 14: Transmission electron micrographs of rotating bend fatigue tested specimens at 95 MPa,  $R=-1$ , 47 Hz.



Sealed specimens exhibiting (a) localized attack at the matrix-inclusion interface and rectangular pits after  $2.7 \times 10^4$  reversals, (b) voids in pearlitic region after  $2.7 \times 10^4$  reversals, (c) higher magnification of (b) indicating bands and serrations,  $\times 1100$ , and (d) extrusion-intrusion type feature at triple point after  $2.7 \times 10^4$  reversals,  $\times 1100$ .

Fig. 1. Transmission electron micrograph of rotation-oxidation product in sealed specimen after  $2.7 \times 10^4$  reversals.

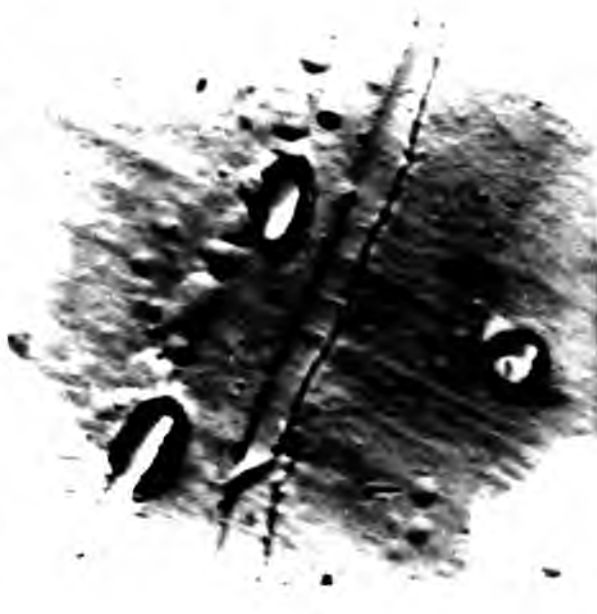


122

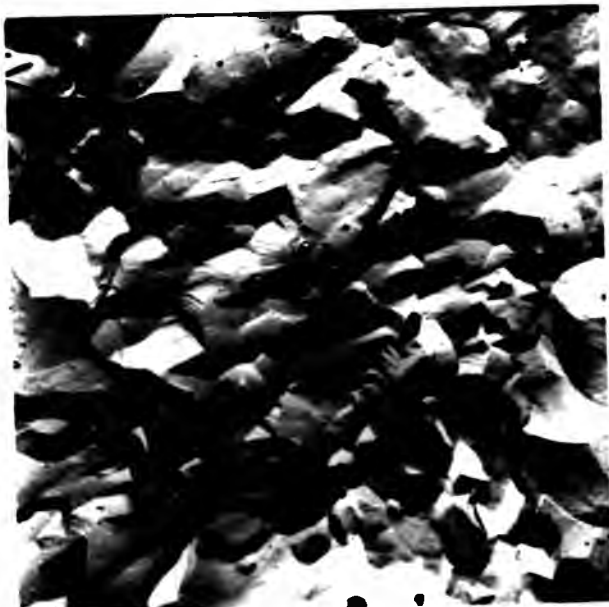




(e)



(f)



(g)



(h)

Annealed specimens exhibiting (e) linking up of micropits to form microcracks in pearlitic regions after  $1.05 \times 10^6$  reversals,  $\times 11273$ , (f) inclusions with features resembling blisters and intrusions after  $1.05 \times 10^6$  reversals,  $\times 11273$ , (g) inhomogeneous deformation on the surface resulting in microcrack formation after  $1.05 \times 10^6$  reversals,  $\times 2182$ , and (h) a chain of etch pits in the deformed area in (g),  $\times 8182$ .

Fig R 14: Transmission electron micrographs of rotating bend fatigue tested specimens at 95 MPa,  $R=-1$ , 47 Hz.



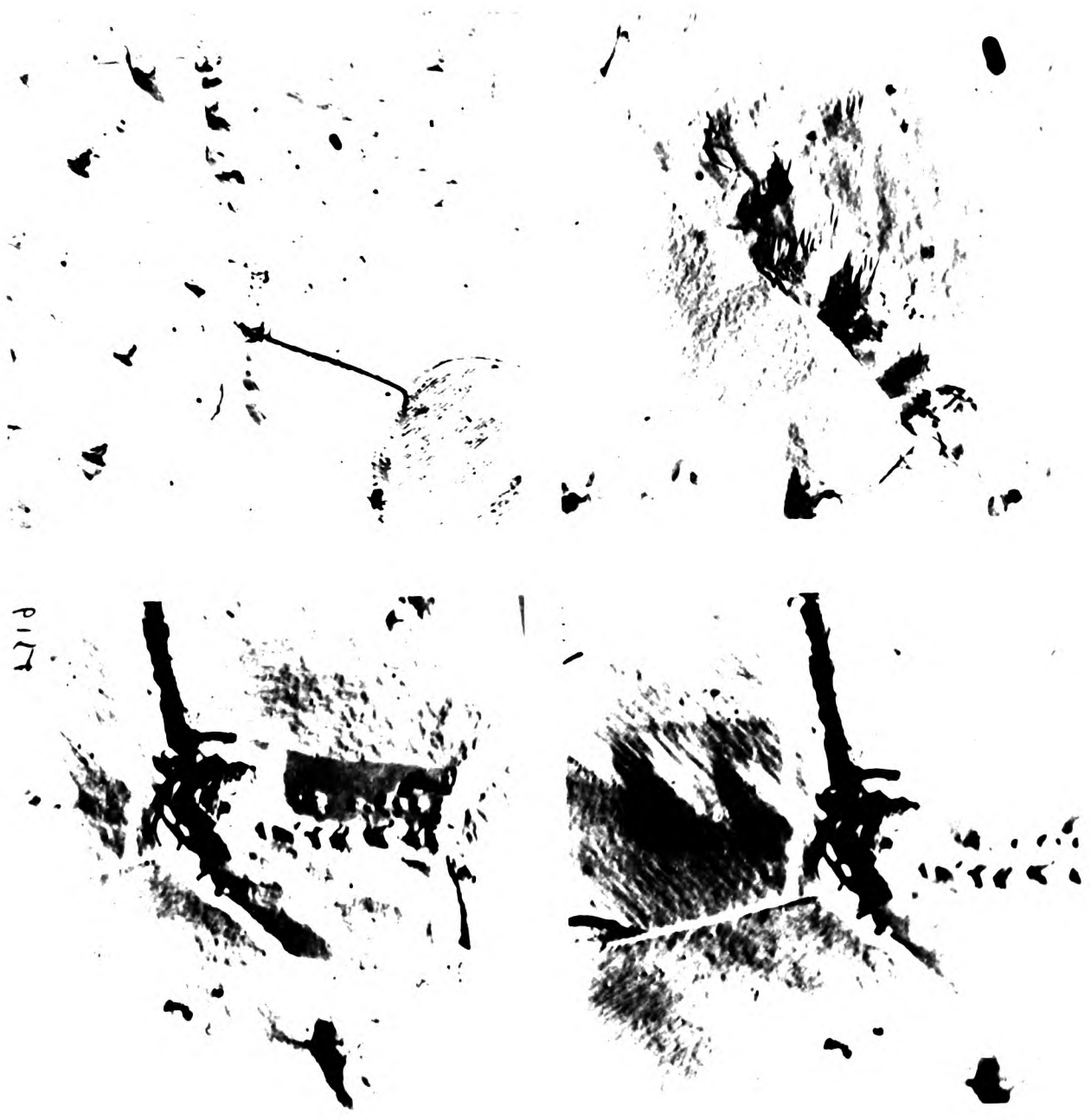
Annealed specimens exhibiting (e) linking up of microbits to form microcracks in pearlitic regions after  $1.05 \times 10^6$  reversals,  $\times 11273$ , (f) inclusions with features resembling blisters and intrusions after  $1.05 \times 10^6$  reversals,  $\times 11273$ , (g) inhomogeneous deformation on the surface resulting in microcrack formation after  $1.05 \times 10^6$  reversals,  $\times 2187$ , and (h) a chain of etch pits in the deformed area in (g),  $\times 8187$ .

Fig. 14: Transmission electron micrographs of rotating bend fatigue tested specimens at 950 Ma,  $\sigma = 1, 47$  Hz.



... regions exhibiting (a) linear ...  
 microcracks in pearlitic regions after ...  
 x 1000, (b) inclusions with features ...  
 after ... x 1000, (c) ...  
 formation on the surface resulting in ...  
 after ... x 1000, (d) ...  
 the deformed area at ... x 1000.

... electron micrograph of ...  
 ...



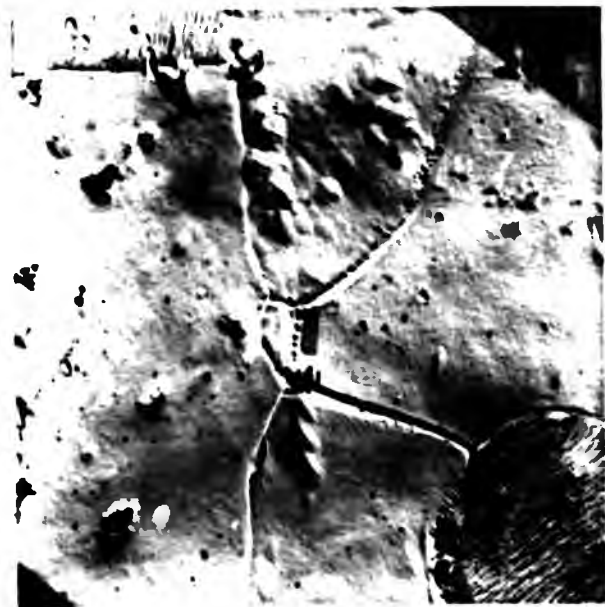
PIT



(m)

Uncoiled specimens exhibiting (j) subgrain formation at grain boundary junction, slip bands near grain boundary and microcrack formation after  $1.05 \times 10^6$  reversals, 2182, (k) higher magnification of the slipped region near grain boundary, x 4908, (l) etch pits and subgrain at the grain boundary junction in (j), x 918, and (m) microcrack formation at the grain boundary junction, x 2182.

14: Transmission electron micrographs of rotating iron specimen (specimen 10-10-1, 10-10-2).



(j)



(k)



(l)



(m)

Annealed specimens exhibiting (j) subgrain formation at grain boundary junctions, slip bands near grain boundary and microcrack formation after  $1.05 \times 10^6$  reversals, 2182, (k) higher magnification of the slipped region near grain boundary, x 4908, (l) etch pits and subgrain at the grain boundary junction in (j), x 8182, and (m) microcrack formation at the grain boundary junction, x 8182.

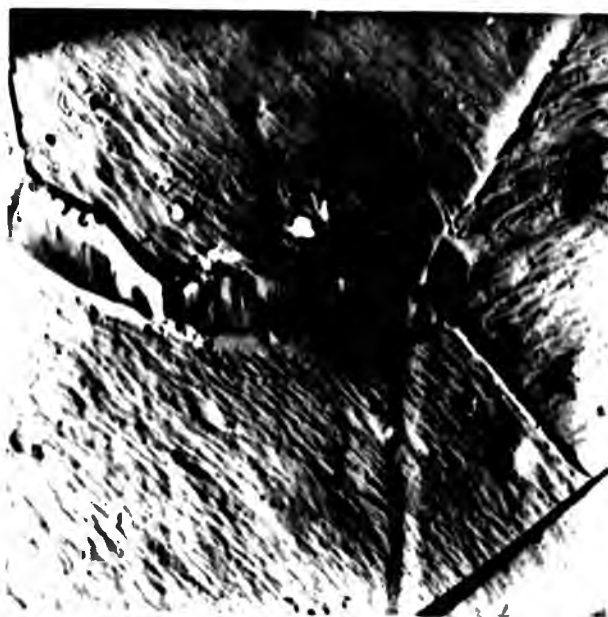
Fig R 14: Transmission electron micrographs of rotating bend fatigue tested specimens at 95 MPa,  $R=-1$ , 47 Hz.



(n)



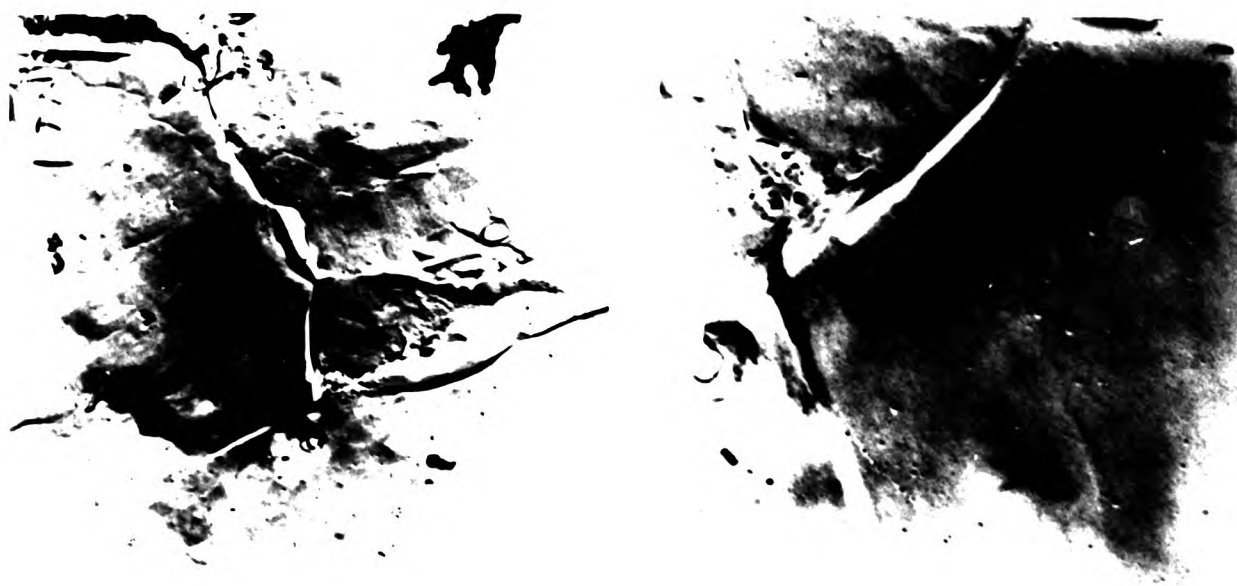
(p)



(q)

Annealed specimens exhibiting (n) localised attack and microcrack formation at the grain boundaries after  $1.31 \times 10^6$  reversals,  $\times 4909$ , (p) higher magnification of (n) indicating microcrack,  $\times 16273$ , and (q) deformation at the grain boundary after  $1.31 \times 10^6$  reversals,  $\times 6818$ .

Fig. 14: Transmission electron micrographs of rotating bend fatigue tested specimens at 95 MPa,  $R=-1$ , 47 Hz.



a

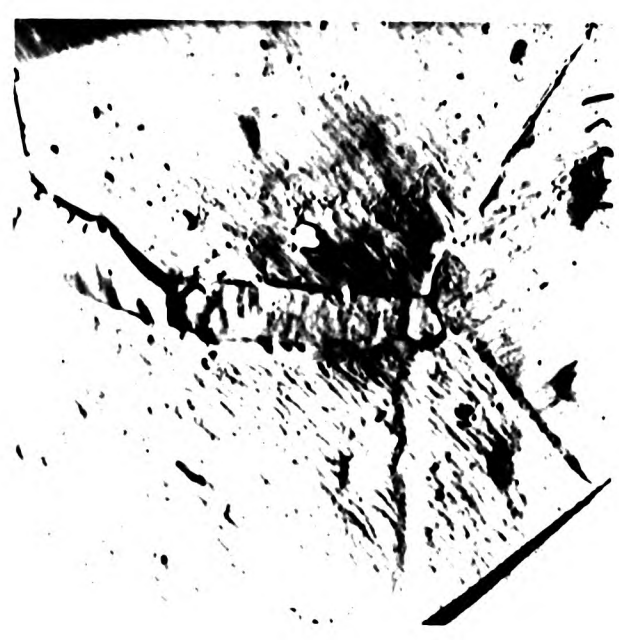


Fig. 1. Metal specimens exhibiting (a) localized attack and microcrack formation at the grain boundaries after  $1.35 \times 10^6$  reversals, (b) higher magnification of (a) indicating microcrack, (c) deformation of the grain boundary after  $1.35 \times 10^6$  reversals,  $\times 2000$ .

Fig. 2. Magnification electron micrograph of metal specimen after  $1.35 \times 10^6$  reversals,  $\times 10000$ .



n



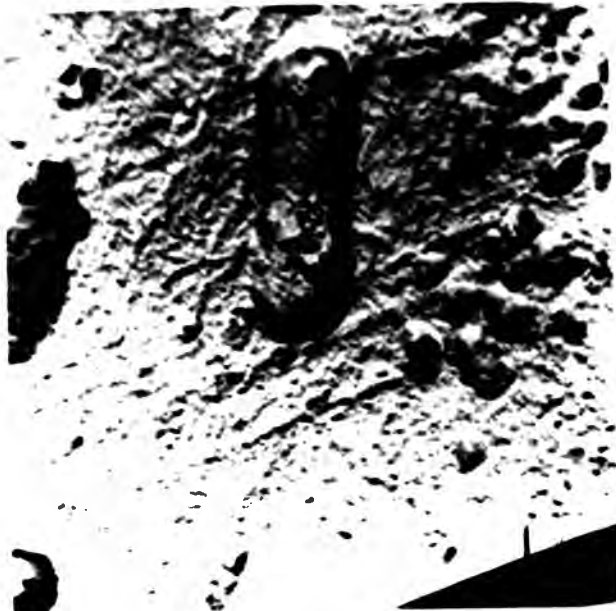
Figure R 15a - R 15c illustrate dissolution at the matrix - inclusion interface after  $2 \times 10^3$  reversals at 193 MPa,  $R = -1$ . Blisters associated with the inclusions are also observed. Figure R 15d shows dissolution at the ferrite - cementite interface and microvoid formation in ferrite of pearlite. With increasing number of reversals, dissolution of inclusions appears to occur (Figure R 15e). Microvoids also appear in slip bands after  $6.1 \times 10^3$  reversals (Figure R 15f) and Figure R 15g shows the formation of micropits at sub-boundaries. Linking of microvoids in pearlite regions are observed after  $7.5 \times 10^4$  reversals (Figures R 15h and R 15j). Coalescence of micropits in slip bands and around inclusions, and nucleation of microcracks in slip band are shown in Figures R 15k - R 15m.

In the low inclusion density regions, deformation and microcrack formation at the grain boundaries, and slip bands with micropits have been observed (Figures R 15n - R 15q). As the number of reversals are increased to  $10^6$ , linking up of microcracks at grain boundaries, around inclusions and at etch pits are found to occur (Figures R 15r and R 15s).

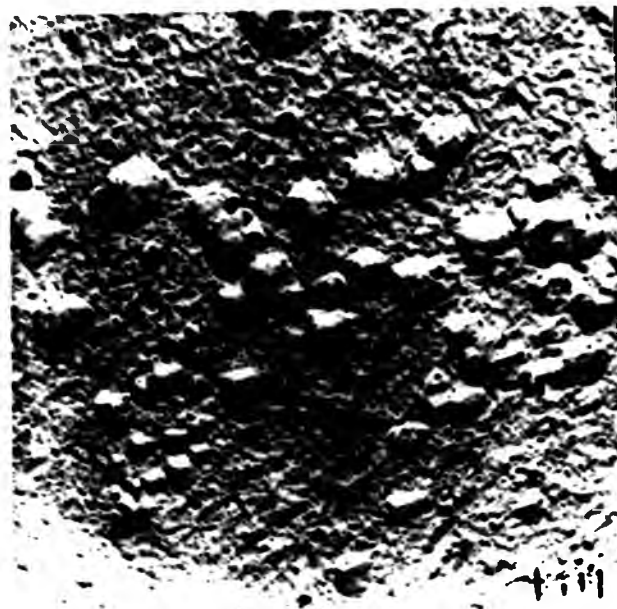
Figure R 16 shows the surface morphology at 247 MPa,  $R = -1$ . Preferential attack around elongated and spherical inclusions, and that in ferrite in the pearlitic region is shown in Figures R 16a - R 16d. Microfissure formation in the transverse direction appears to occur around  $3.3 \times 10^5$  reversals (Figure R 16e). Comparison of the micrographs (Figures R 13e and R 16e) shows that in the low inclusion density region, nucleation of microfissures in the transverse direction from the matrix - inclusion interface appears to occur at about the same number of reversals. In the high inclusion density region, however, the time to form microfissures in the transverse direction tends to be shorter (Figure R 15a).



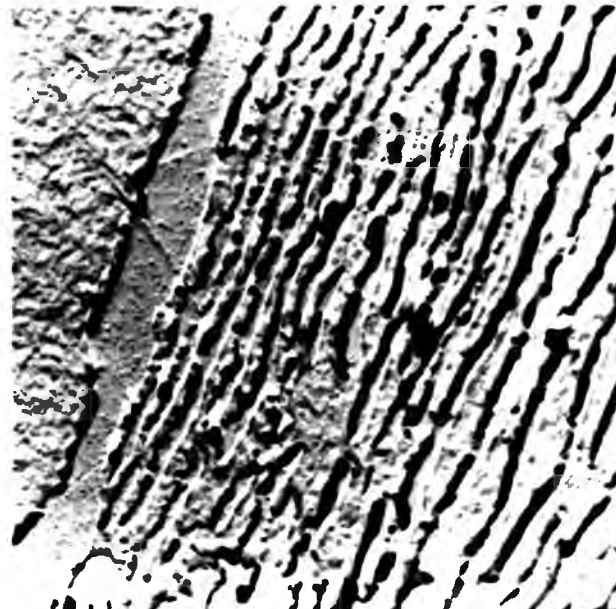
(a)



(b)



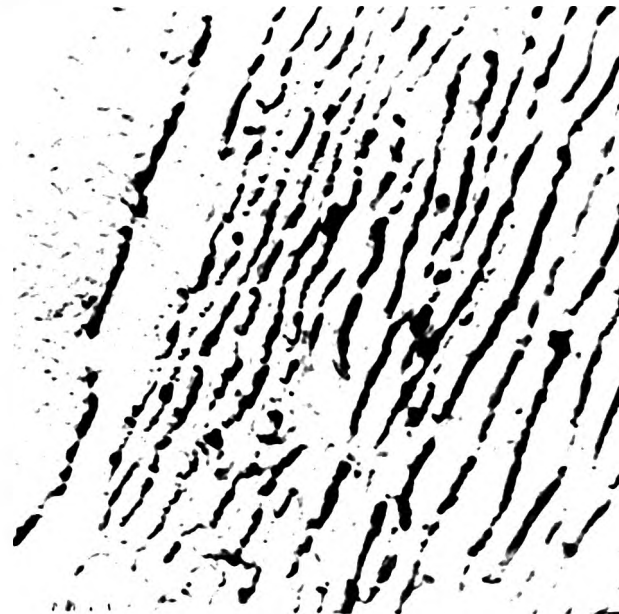
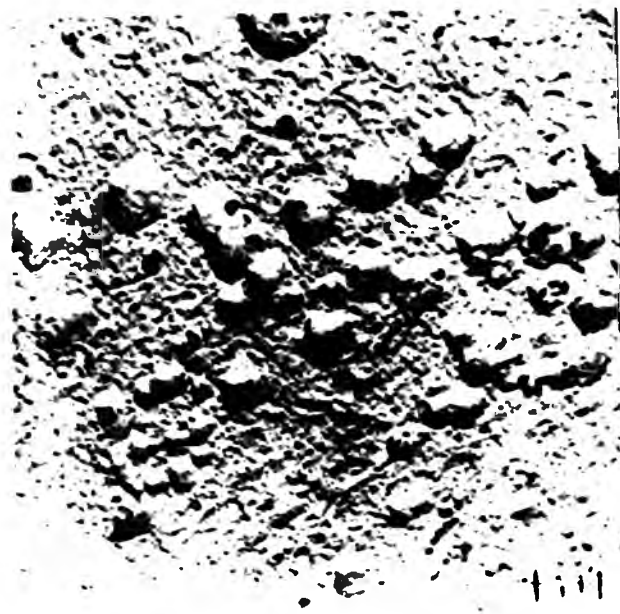
(c)



(d)

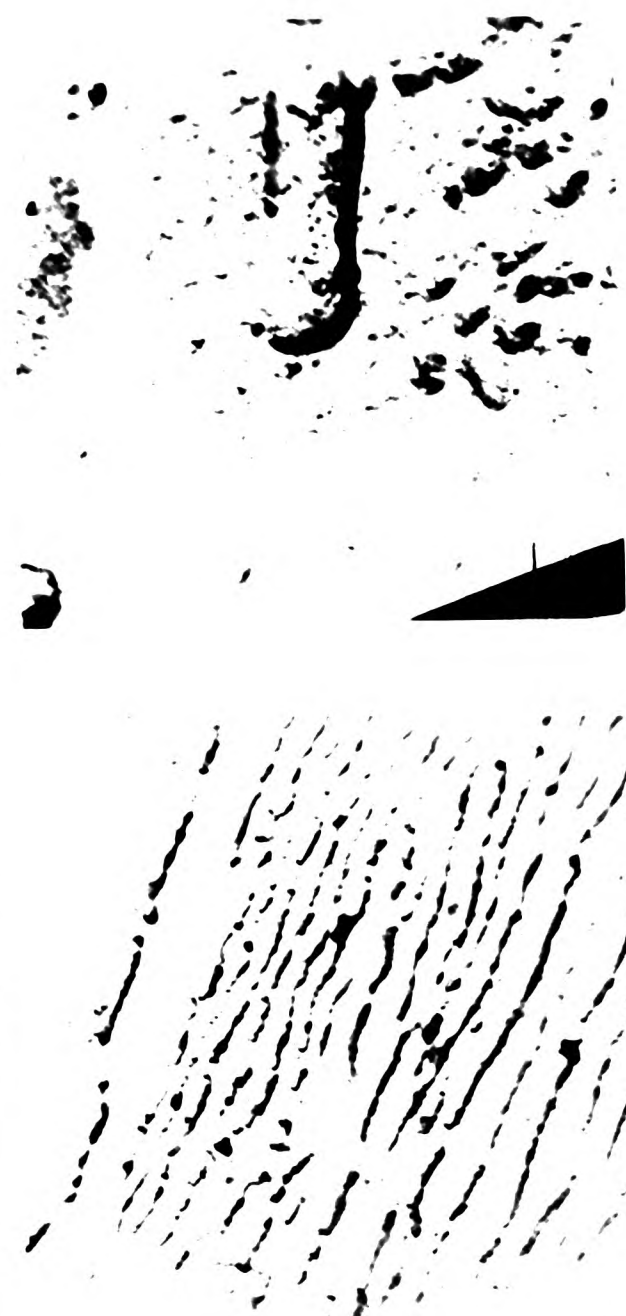
Wrought specimens after 2000 reversals showing (a) dissolution of the inclusion and at the matrix-inclusion interface; incipient crack formation is also indicated; x 11273, (b) slip band and blister formation, x 20455, (c) blisters with microcracks and pin holes (area adjacent to (b)), and (d) a pearlitic region; the lamellar structure contains terminations and bends; dissolution at the ferrite-cementite interface and microvoids in the ferrite matrix are also observed; x 20455

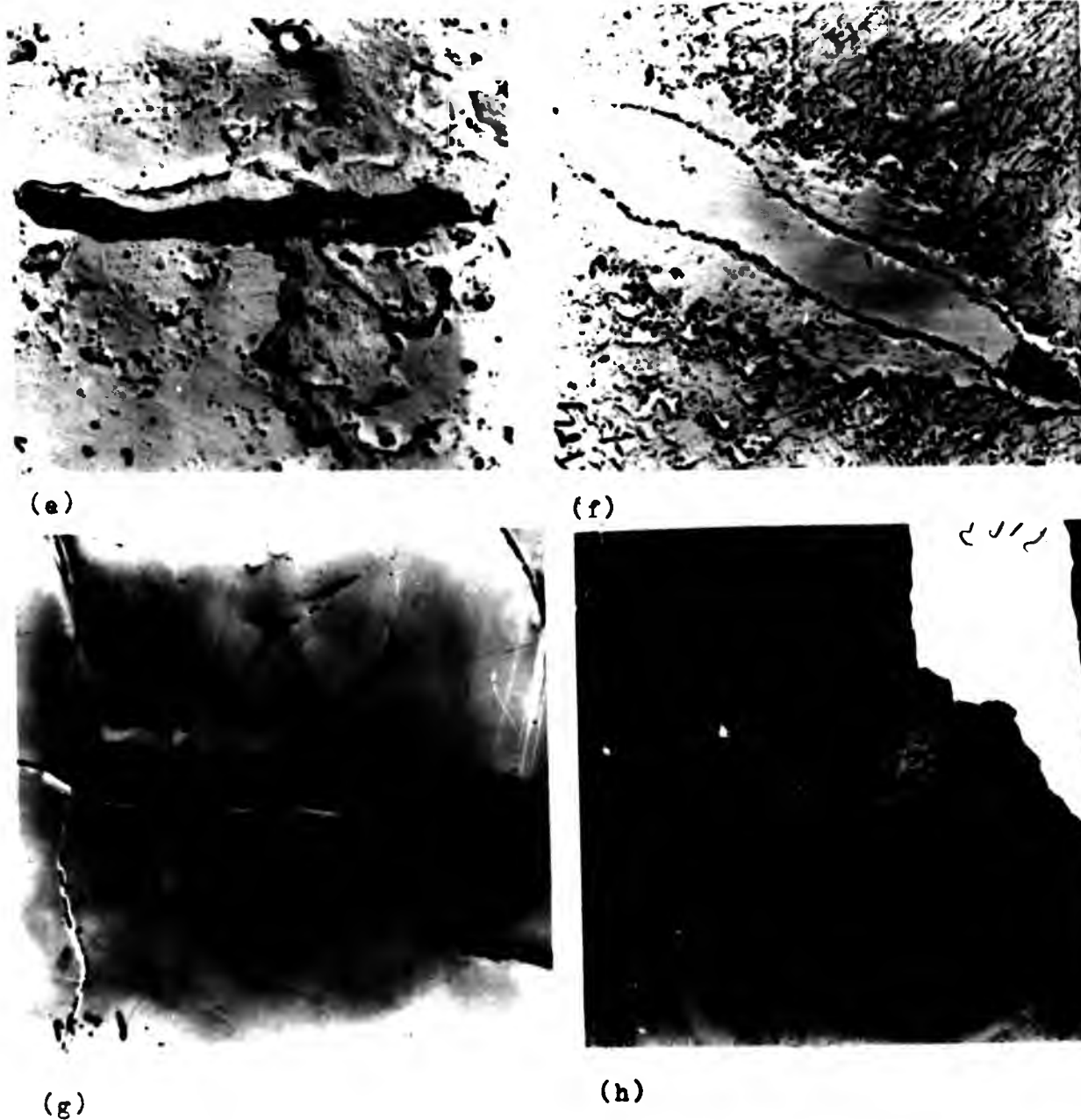
Fig. R 15: Transmission electron micrographs of rotating bend fatigue tested specimens at 193 MPa,  $R=-1$ , 47 Hz.



rough specimens after 2000 reversals showing (a) dissolution of the inclusion and at the matrix-inclusion interface; incipient crack formation is also indicated; x 11000, (b) slip band and blister formation, x 20000, (c) blisters with microcracks and pin holes (area adjacent to (b)), and (d) a pearlitic region; the lamellar structure contains terminations and bends; dissolution at the ferrite-cementite interface and microvoids in the ferrite matrix are also observed; x 20000.

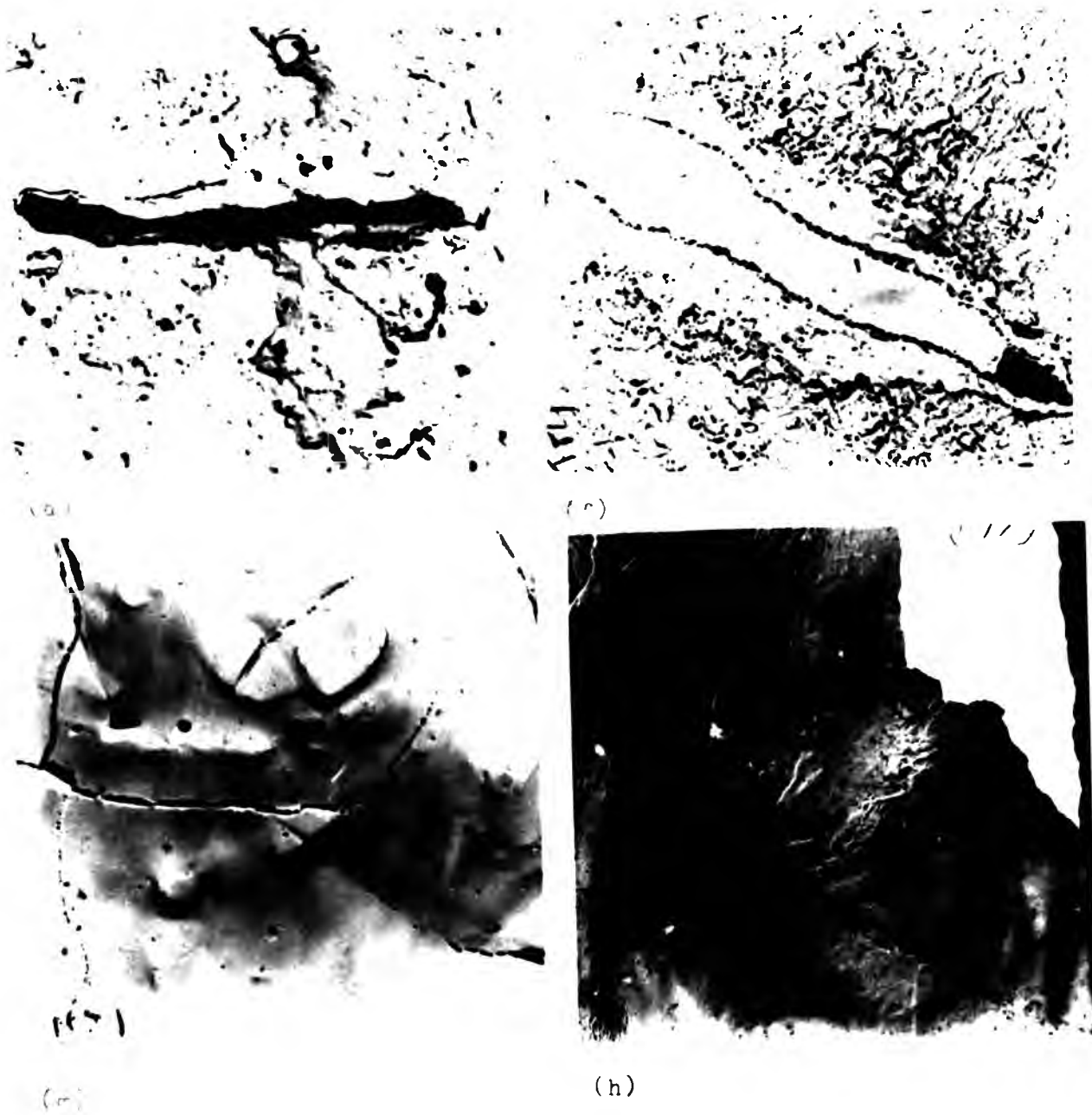
Fig. 1. Reproduction electron microscope micrographs of the surface of a specimen after 2000 reversals at 2000 Hz, 100°C.





Wrought specimens exhibiting (e) dissolution of an inclusion after 6100 reversals, x 9727, (f) slip band formation with microcracks outlining the band after 6100 reversals, x 9727, (g) surface rumplings and formation and linking of micropits indicating sub-boundaries after  $3.4 \times 10^4$  reversals, x 11273, and (h) coalescence of microvoids in pearlitic area after  $7.47 \times 10^4$  reversals, 2182.

Fig R 15: Transmission electron micrographs of rotating bend fatigue tested specimens at 193 MPa, R=-1, 47 Hz.



rough specimens exhibiting (e) dissolution of an inclusion after 6100 reversals, x 9727, (f) slip band formation with microcracks outlining the band after 6100 reversals, x 9727, (g) surface rumplings and formation and linking of micropits indicating sub-boundaries after  $7.4 \times 10^4$  reversals, x 11273, and (h) coalescence of microvoids in pearlitic area after  $7.47 \times 10^4$  reversals, 2182.

FIG. 15: Transmission electron micrographs of rotating bend fatigue tested specimens at 103 MPa, R=-1, 47 Hz.

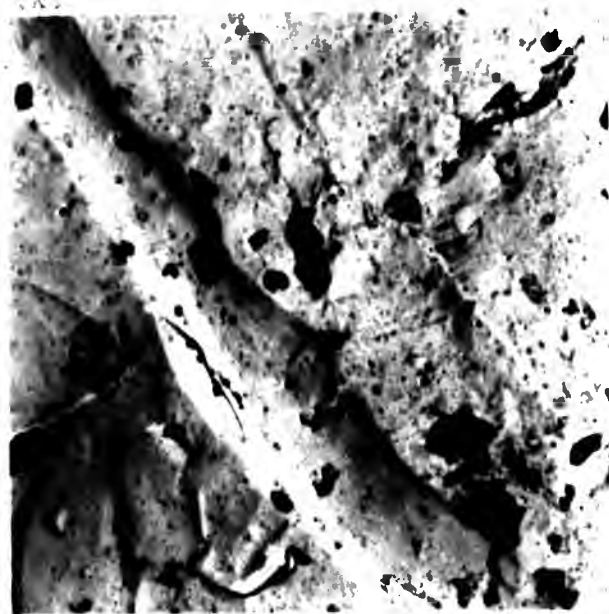
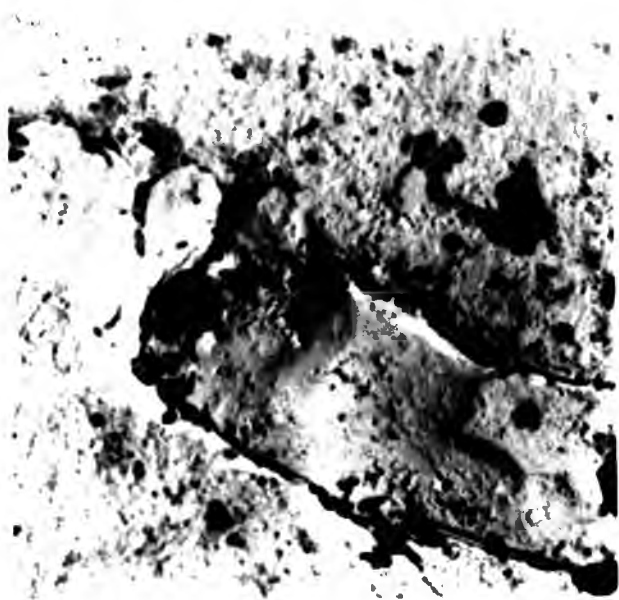
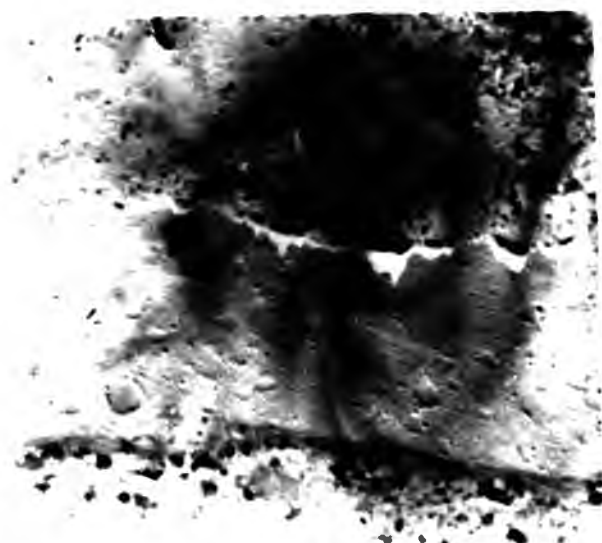


1570  
1571  
1572

... of the ...  
... of the ...  
... of the ...  
... of the ...  
... of the ...

... of the ...  
... of the ...

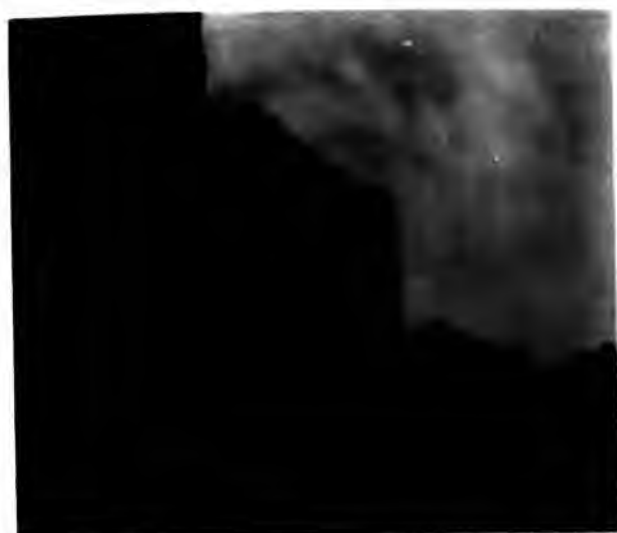




(m)

brought specimens exhibiting (j) coalescence of microvoids - higher magnification of (h), x 11273, (k) coalescence of microvoids at the edge of a slip band after  $7.47 \times 10^4$  reversals, x 11273, (l) microvoids around an inclusion and in the matrix close to the inclusion after  $3.52 \times 10^5$  reversals, x 11273, and (m) slip band with microcracks after  $3.52 \times 10^5$  reversals, x 3031.

Fig. 10. Transmission electron micrographs of rotation-fatigued lead specimens at 174 K,  $\sigma = -1, 47$  MPa.



(j)



(k)



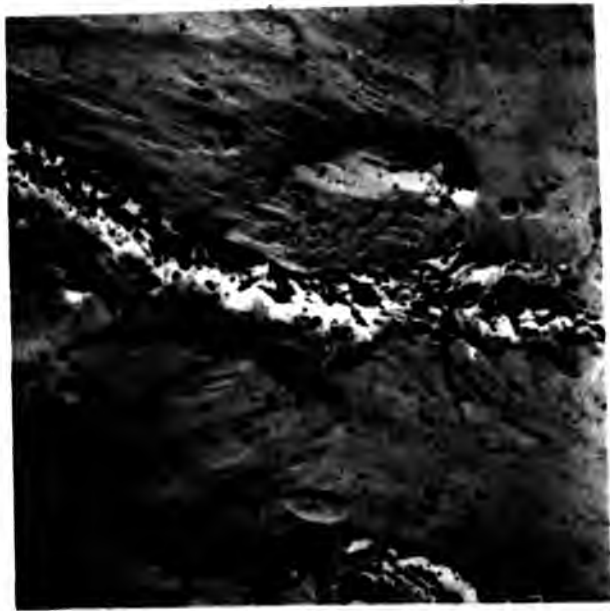
(l)



(m)

Wrought specimens exhibiting (j) coalescence of microvoids - higher magnification of (h), x 11273, (k) coalescence of micropits at the edge of a slip band after  $7.47 \times 10^4$  reversals, x 11273, (l) microvoids around an inclusion and in the matrix close to the inclusion after  $3.62 \times 10^5$  reversals, x 11273, and (m) slip band with microcracks after  $3.62 \times 10^5$  reversals, x 3091.

Fig R 15: Transmission electron micrographs of rotating bend fatigue tested specimens at 193 MPa, R=-1, 47 Hz.



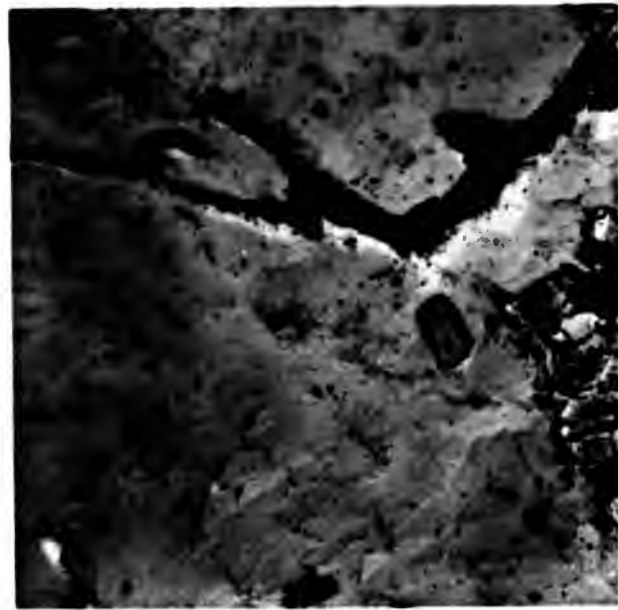
(n)



(p)



(q)



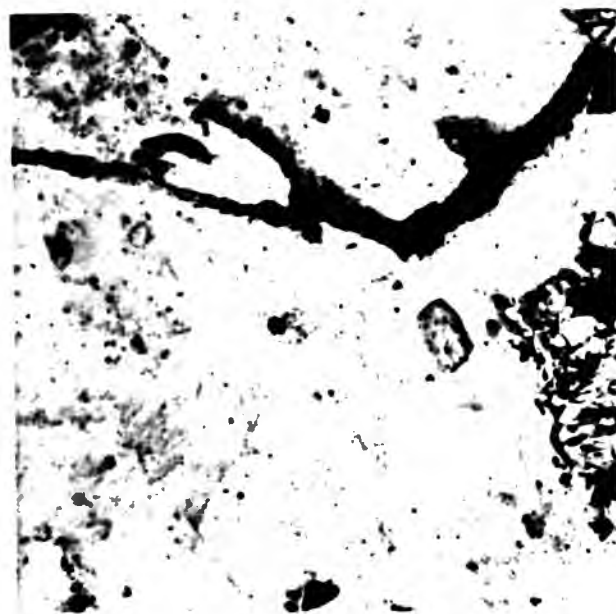
(r)

Wrought specimens exhibiting (n) deformed grain boundary region and microcracks with slip bands in adjacent grains after  $5.6 \times 10^5$  reversals, x 2182, (p) slip bands with micropits after  $5.6 \times 10^5$  reversals, x 2182, (q) higher magnification of (p), x 11273, and (r) microcracks associated with an inclusion after  $1.07 \times 10^6$  reversals, x 2182.

Fig R 15: Transmission electron micrographs of rotating bend fatigue tested specimens at 193 MPa, R=-1, 47 Hz.



(n)



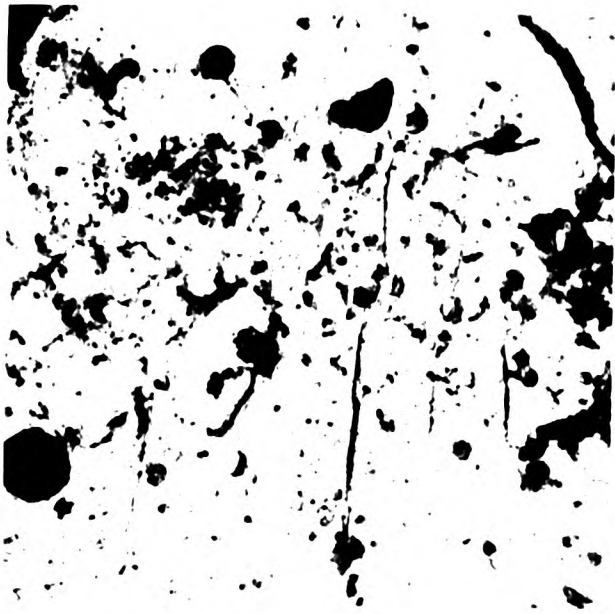
(r)

rough specimens exhibiting (n) deformed grain boundary region and microcracks with slip bands in adjacent grains after  $5.6 \times 10^6$  reversals, x 2182, (p) slip bands with micropits after  $5.6 \times 10^6$  reversals, x 2182, (q) higher magnification of (p), x 11273, and (r) microcracks associated with an inclusion after  $1.07 \times 10^7$  reversals, x 2182.

Fig. 5: Transmission electron micrographs of rotating bend fatigue tested specimens at 193 MPa,  $\sigma/\sigma_f = 1$ , 40 Hz.



Faint, illegible text or markings, possibly bleed-through from the reverse side of the page.

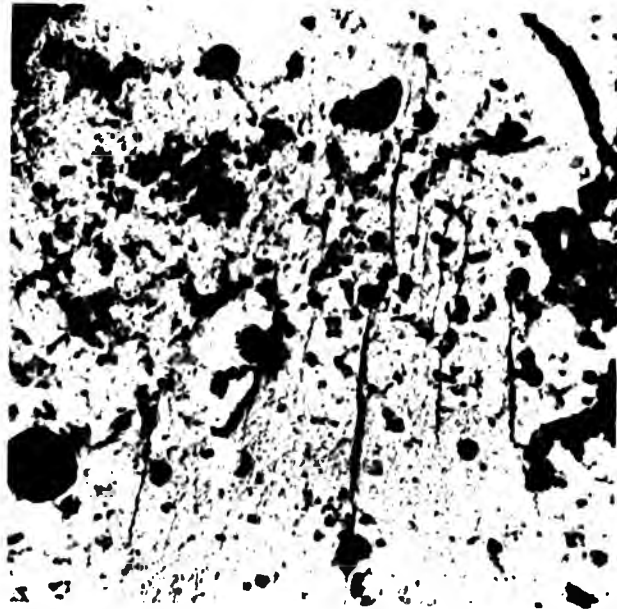


The following table shows the results of the analysis of the samples collected during the expedition to the Antarctic Peninsula in 1956-57. The data are presented in the form of a table with columns for the sample number, the date of collection, and the results of the analysis.



The results of the analysis of the samples collected during the expedition to the Antarctic Peninsula in 1956-57 are presented in the following table. The data are presented in the form of a table with columns for the sample number, the date of collection, and the results of the analysis.

The following table shows the results of the analysis of the samples collected during the expedition to the Antarctic Peninsula in 1956-57. The data are presented in the form of a table with columns for the sample number, the date of collection, and the results of the analysis.



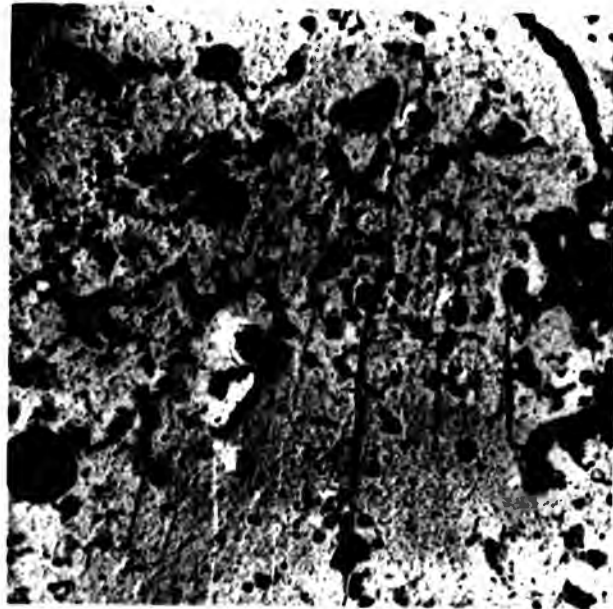
(c)  
rough specimen exhibiting microcracks associated with  
etch pits after  $1.39 \times 10^6$  reversals, x 4909.

Fig R 15: Transmission electron micrographs of rotating bend fatigue  
tested specimens at 103 MPa, R=-1, 47 Hz.



rough specimens exhibiting (a) micropits around inclusion and  
along grain boundaries, and coalescence of micropits after  $1.04$   
 $\times 10^5$  reversals, 3001, and (b) higher magnification of grain  
boundaries in (a), x 11273.

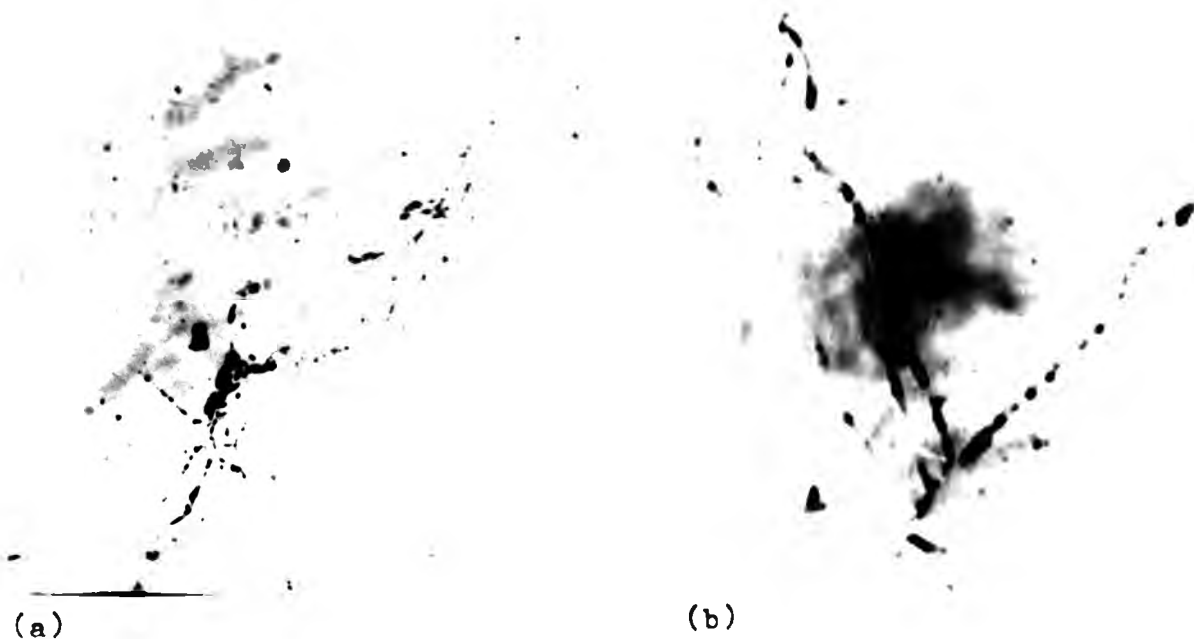
Fig R 16: Transmission electron micrographs of rotating bend fatigue  
tested specimens at 247 MPa, R=-1, 47 Hz.



(s)

Wrought specimen exhibiting microcracks associated with etch pits after  $1.39 \times 10^6$  reversals, x 4909.

Fig R 15: Transmission electron micrographs of rotating bend fatigue tested specimens at 193 MPa, R=-1, 47 Hz.



(a)

(b)

Wrought specimens exhibiting (a) micropits around inclusion and along grain boundaries, and coalescence of micropits after  $1.04 \times 10^5$  reversals, 3091, and (b) higher magnification of grain boundaries in (a), x 11273.

Fig R 16: Transmission electron micrographs of rotating bend fatigue tested specimens at 247 MPa, R=-1, 47 Hz.



(c)



(d)



(e)

Wrought specimens exhibiting (c) coalescence of micropits in the pearlitic area in (a), x 13727, (d) coalescence of micropits to form voids around a spherical inclusion after  $1.04 \times 10^5$  reversals, x 9727, and (e) initiation of microfissure in the transverse direction from matrix-inclusion interface after  $3.31 \times 10^5$  reversals, x 11273.

Fig R 16: Transmission electron micrographs of rotating bend fatigue tested specimens at 247 MPa, R=-1, 47 Hz.



(c)



(d)



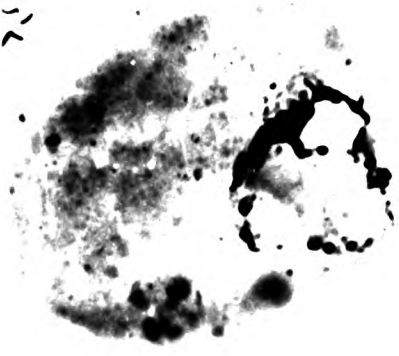
(e)

Wrought specimens exhibiting (c) coalescence of micropits in the pearlitic area in (a), x 13727, (d) coalescence of micropits to form voids around a spherical inclusion after  $1.04 \times 10^5$  reversals, x 9727, and (e) initiation of microfissure in the transverse direction from matrix-inclusion interface after  $3.31 \times 10^5$  reversals, x 11273.

Fig. R-16: Transmission electron micrographs of rotating bend fatigue tested specimens at 147 MPa, R=-1, 47 Hz.



252



These specimens exhibiting a coarseness of structure in the  
artificial area in fact, with a coarseness of structure in the  
artificial area around a central inclusion after 1.5 hr  
reversal, with a similar type of structure in the  
opposite direction from a cell, with a similar type of structure.

The specimens in the artificial area are similar to the  
specimens in the natural area.

Microvoids are found to occur due to the intersection of the slip bands and the inclusions (Figure R 16f). Increasing the number of reversals to  $10^6$  enhances the tendency of coalescence of the incipient cracks along grain boundaries, of micropits in the slip bands and nucleation of microcracks in the transverse direction, from the matrix - inclusion interface (Figures R 16g - R 16l).

Formation of slip bands have been observed after  $2 \times 10^3$  reversals at 278 MPa,  $R = -1$  (Figure R 17a). Microvoids also tend to form at the slip bands (Figure R 17b). Dissolution of the inclusions and that at the matrix - inclusion interface appear to be somewhat more rapid at the higher stress range (Figure R 17c) than at the lower one.

Localised corrosion at the matrix - inclusion interface is found to occur leaving the inclusion isolated from the matrix (Figure R 17c). Closer examination of the interfaces of some of the inclusions reveals the nucleation of transverse microcracks due to the coalescence of the micropits in the region close to the interface (Figure R 17d). That this region is contaminated with S has been shown in Figure R 11k. Dissolution at the ferrite - cementite interface is shown in Figure R 17e whilst Figure R 17f shows the formation of a microfissure.

Increasing the number of reversals at the same stress reveals blisters associated with inclusions (Figure R 17g), slip bands near a fractured inclusion (Figure R 17h) and a deformed region adjacent to an inclusion (Figure R 17j). This region appears to contain microfissures. Figure R 17k shows that the region immediately adjacent to the inclusions contain micropits and slip bands. Features resembling intrusions are also observed in the slip bands (Figure R 17l).



(f)



(g)



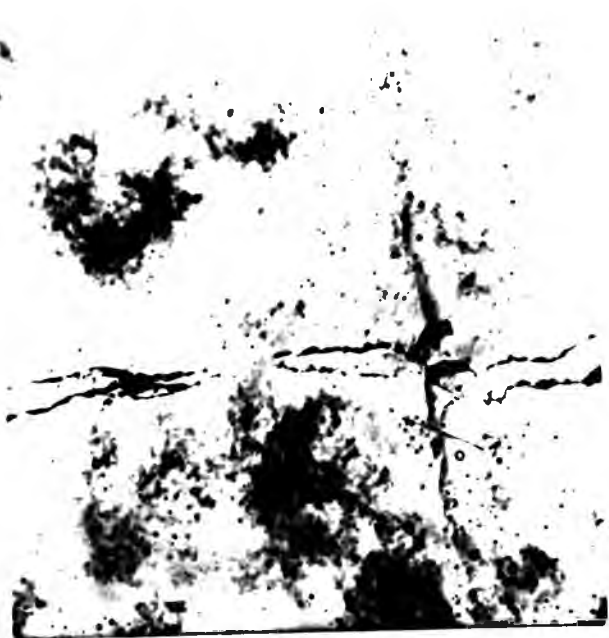
(h)



(j)

Wrought specimens exhibiting (f) intersection of inclusion and slip band resulting in microcrack formation after  $3.31 \times 10^5$  reversals, 2182, (g) extension of incipient crack in the transverse direction from matrix-inclusion interface and microcrack formation along grain boundaries after  $10^6$  cycles, x 6818, (h) formation of microcrack and voids around slip band with micropits within the band after  $10^6$  cycles, x 11273, and (j) macrocrack formation in the transverse direction from matrix-inclusion interface after  $1.01 \times 10^6$  reversals, x 9727.

Fig R 16: Transmission electron micrographs of rotating bend fatigue tested specimens at 247 MPa, R=-1, 47 Hz.



brought specimens exhibiting (f) intersection of inclusion and slip band resulting in microcrack formation after  $3.31 \times 10^5$  reversals, 2182, (g) extension of incipient crack in the transverse direction from matrix-inclusion interface and microcrack formation along grain boundaries after  $10^6$  cycles, x 6813, (h) formation of microcrack and voids around slip band with micropits within the band after  $10^6$  cycles, x 11771, and (i) macrocrack formation in the transverse direction from matrix-inclusion interface after  $1.01 \times 10^6$  reversals, x 3777.

Fig. 16: Transmission electron micrographs of rotating bend fatigue tested specimens at 247 MPa,  $\sigma/\sigma_u = 0.47$ .



The following is a list of the specimens collected during the expedition to the ...  
The specimens are arranged in the order in which they were collected. The first specimen is a ...  
The second specimen is a ...  
The third specimen is a ...  
The fourth specimen is a ...  
The fifth specimen is a ...  
The sixth specimen is a ...  
The seventh specimen is a ...  
The eighth specimen is a ...  
The ninth specimen is a ...  
The tenth specimen is a ...



(k)



drawn specimens exhibiting (k) slip bands in sub-grains, crack formation around sub-grain boundary and formation of rectangular pits after  $1.01 \times 10^7$  reversals,  $\times 3000$ , and (l) formation of macrocracks in pearlitic region, and rectangular pits after  $1.01 \times 10^7$  reversals,  $\times 10000$ .

Fig. 10: Transmission electron micrographs of martensite (k) and pearlitic region (l) of specimen after  $1.01 \times 10^7$  reversals.



(k)



(l)

Wrought specimens exhibiting (k) slip bands in sub-grains, crack formation around sub-grain boundary and formation of rectangular pits after  $1.01 \times 10^6$  reversals, x 3091, and (l) formation of macrocracks in pearlitic region, and rectangular pits after  $1.01 \times 10^6$  reversals, x 11273.

Fig R 16: Transmission electron micrographs of rotating bend fatigue tested specimens at 247 MPa, R=-1, 47 Hz.



(k)



(l)

Wrought specimens exhibiting (k) slip bands in sub-grains, crack formation around sub-grain boundary and formation of rectangular pits after  $1.01 \times 10^6$  reversals, x 3091, and (l) formation of macrocracks in pearlitic region, and rectangular pits after  $1.01 \times 10^6$  reversals, x 11273.

Fig R 16: Transmission electron micrographs of rotating bend fatigue tested specimens at 247 MPa, R=-1, 47 Hz.



(a)



(b)



(c)



(d)

Wrought specimens exhibiting (a) slip band with microvoid, between an inclusion and pearlitic region (not shown in the micrograph), x 4909, (b) higher magnification of (a), x 20455, (c) dissolution of an inclusion and at matrix-inclusion interface, x 20455, and (d) dissolution at matrix-inclusion interface and transverse microcracks in the region immediately adjacent to the interface, x 40000. After 2000 reversals.

Fig R 17: Transmission electron micrographs of rotating bend fatigue tested specimens at 278 MPa, R=-1, 47 Hz.



(a)



(b)



(c)



(d)

rought specimens exhibiting (a) slip band with microvoid, between an inclusion and pearlitic region (not shown in the micrograph), x 4909, (b) higher magnification of (a), x 20455, (c) dissolution of an inclusion and at matrix-inclusion interface, x 20455, and (d) dissolution at matrix-inclusion interface and transverse microcracks in the region immediately adjacent to the interface, x 40000. After 2000 reversals.

Fig. R 17: Transmission electron micrographs of rotating bend fatigue tested specimens at 278 MPa, R=-1, 47 Hz.



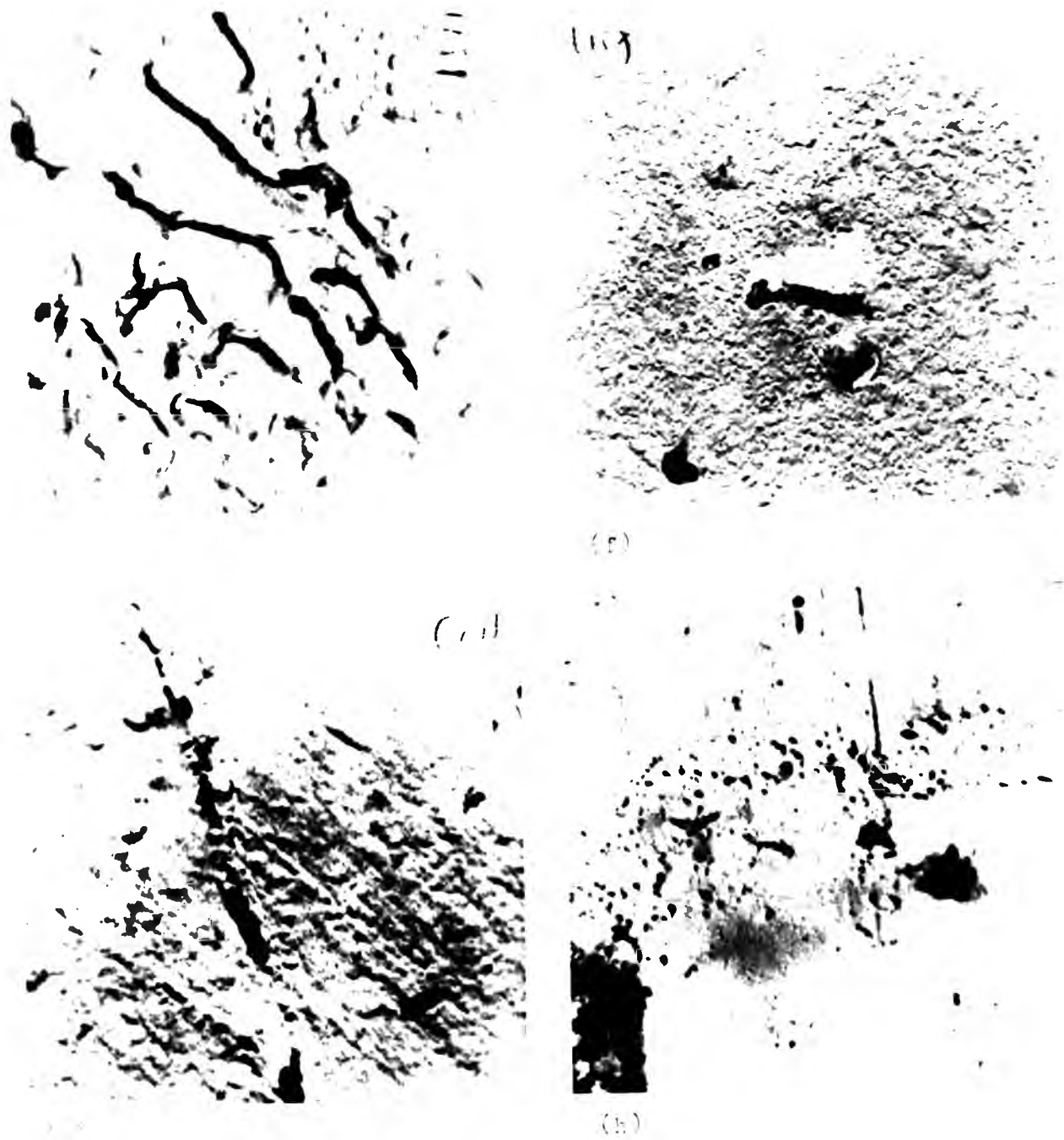
(b)



(d)

1189 specimens exhibiting (a) slip band with microvoid, between an inclusion and pearlitic region (not shown in the micrograph), x 4000, (b) higher magnification of (a), x 20455, (c) dissolution of an inclusion and at matrix-inclusion interface, x 20455, and (d) dissolution at matrix-inclusion interface and transverse microcracks in the region immediately adjacent to the interface, x 4000. After 2000 reversals.

Fig. 1. Transverse and electron micrographs of rotating bend fatigue fracture specimens at 200 Mpa, 10<sup>7</sup>, 47000.



rough specimens exhibiting (e) dissolution at the ferrite-cementite interface resulting in the formation of microfissure after 2000 reversals, x 40000, (f) formation of microcrack after 2000 reversals, x 20000, (g) inclusions with features resembling clusters after 3000 reversals, x 30132, and (h) slip bands near an inclusion after 3000 reversals, x 16273.

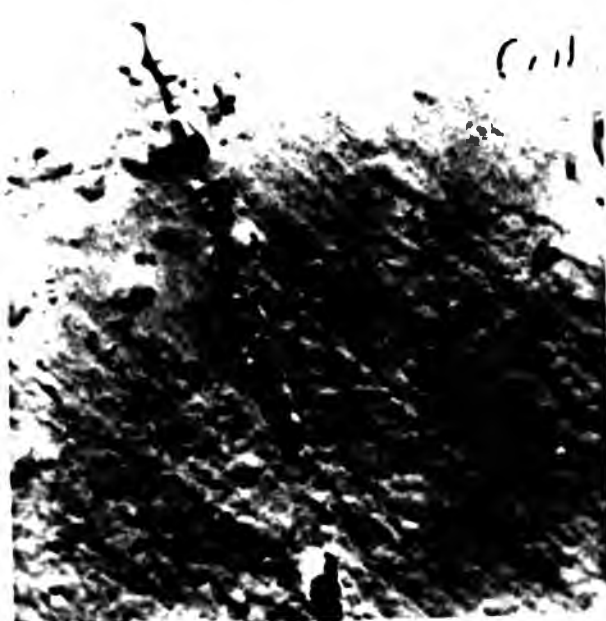
Fig. 1. Transmission electron micrographs of rotating bend fatigue tested specimens at 270 MPa,  $R = -1$ , 400 Hz.



(e)



(f)



(g)



(h)

rought specimens exhibiting (e) dissolution at the ferrite-cementite interface resulting in the formation of microfissure after 2000 reversals, x 40000, (f) formation of microcrack after 2000 reversals, x 20000, (g) inclusions with features resembling blisters after 3000 reversals, x 30182, and (h) slip bands near an inclusion after 3000 reversals, x 16273.

Fig R 17: Transmission electron micrographs of rotating bend fatigue tested specimens at 278 MPa, R=-1, 47 Hz.



(e)



(f)



(g)



(h)

Wrought specimens exhibiting (e) dissolution at the ferrite-cementite interface resulting in the formation of microfissure after 2000 reversals,  $\times 40000$ , (f) formation of microcrack after 2000 reversals,  $\times 20000$ , (g) inclusions with features resembling blisters after 3000 reversals,  $\times 30182$ , and (h) slip bands near an inclusion after 3000 reversals,  $\times 16273$ .

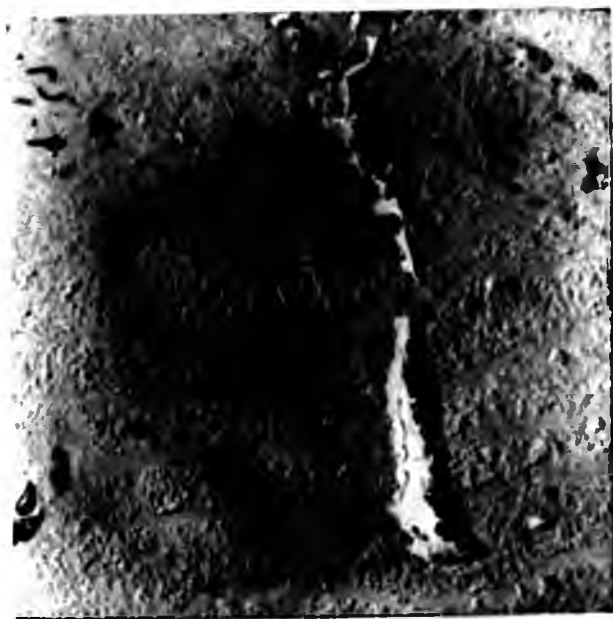
Fig R 17: Transmission electron micrographs of rotating bend fatigue tested specimens at 278 MPa,  $R=-1$ , 47 Hz.



(j)



(k)



(l)

Wrought specimens exhibiting (j) deformed region containing microfissures adjacent to inclusions, x 11273, (k) micropits in the matrix immediately adjacent to an inclusion, x 20455, and (l) intrusion effect, x 20455. After 3000 reversals.

Fig R 17: Transmission electron micrographs of rotating bend fatigue tested specimens at 278 MPa, R=-1, 47 Hz.



(j)



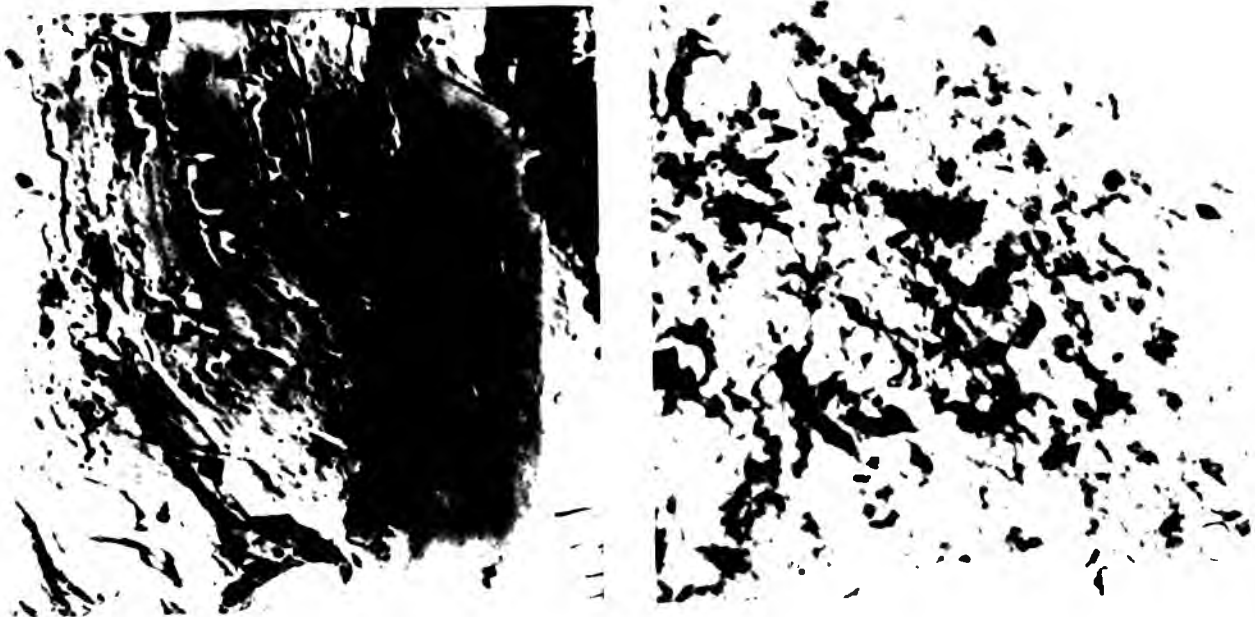
(k)



(l)

Wrought specimens exhibiting (j) deformed region containing microfissures adjacent to inclusions, x 11273, (k) micropits in the matrix immediately adjacent to an inclusion, x 20455, and (l) intrusion effect, x 20455. After 3000 reversals.

Fig R 17: Transmission electron micrographs of rotating bend fatigue tested specimens at 278 MPa, R=-1, 47 Hz.



(j)

(l)

brought specimens exhibiting (j) deformed region containing microfissures adjacent to inclusions, x 11200, (k) microvoids in the matrix immediately adjacent to an inclusion, x 8000, and (l) intrusion effect, x 20000. After 3000 reversals.

Fig. 1: Transmission electron micrographs of rotating beam fatigue tested specimens at 100000, 1-1, 100000.

The effect of increasing the number of reversals to  $3.4 \times 10^4$  for the high density regions and that in the pearlitic sites are shown in Figures R 17m - R 17p and in R 17q respectively. Formation of slip bands between the pearlitic zones is also observed (Figure R 17r). Localised attack around spherical and elongated inclusions are shown in Figures R 17s and R 17t. It has been observed that the presence of inclusions on the slip band path tend to arrest its passage at  $5.1 \times 10^4$  reversals (Figure R 17t).

Further increase in the test duration exhibits nucleation of microcracks in the transverse direction, from the matrix - inclusion interface (Figure R 17u). Slip bands near grain boundaries, dissolution of the inclusions in the high inclusion density region, and dissolution of ferrite in pearlite are observed at around  $4.38 \times 10^5$  reversals (Figures R 17v - R 17x).

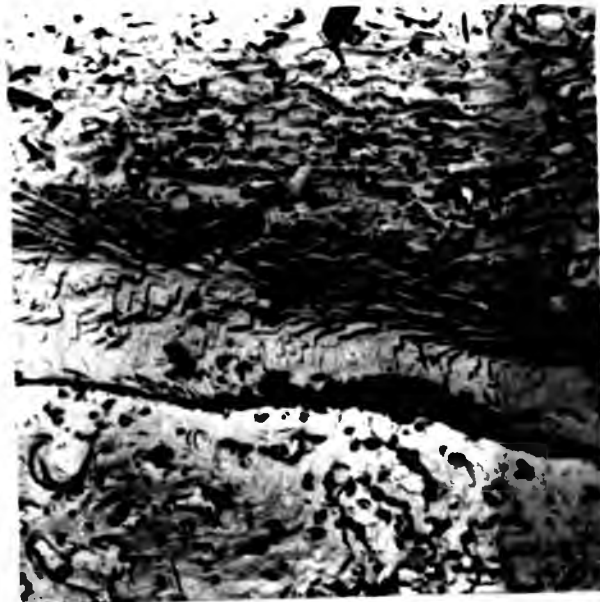
For comparison purposes, micrographs of carbon replicas obtained from air-fatigued specimen at 193 and 278 MPa,  $R = -1$ , are illustrated in Figure R 18.

The surface feature which deflected the slip bands observed in Figure R 18a is an elongated inclusion. Formation of slip bands and microcracks around an inclusion are found to occur around  $1.2 \times 10^6$  reversals (Figures R 18b and R 18c). The effect of a further increase in the number of reversals is shown in Figures R 18d - R 18g.

The influence of increasing the stress range to 278 MPa is shown in Figures R 18h - R 18m. Comparison of micrographs (Figures R 16f, and R 18j and R 18k) shows that slip bands appear to intersect the inclusions at lower stress range and at smaller number of reversals under corrosion fatigue conditions.



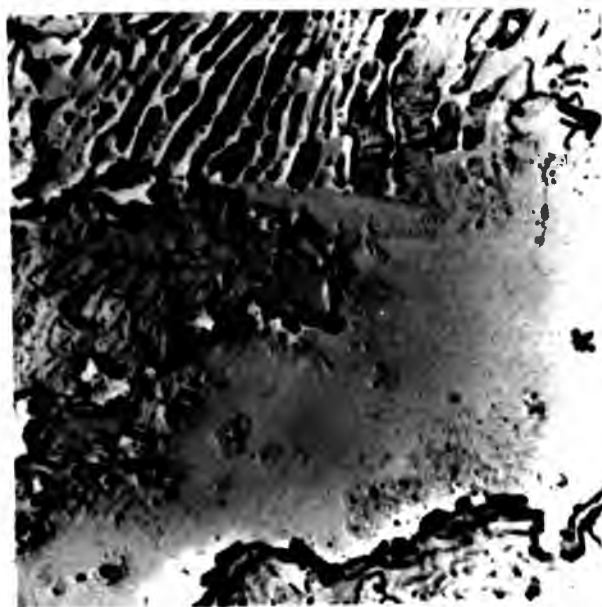
(m)



(n)



(p)



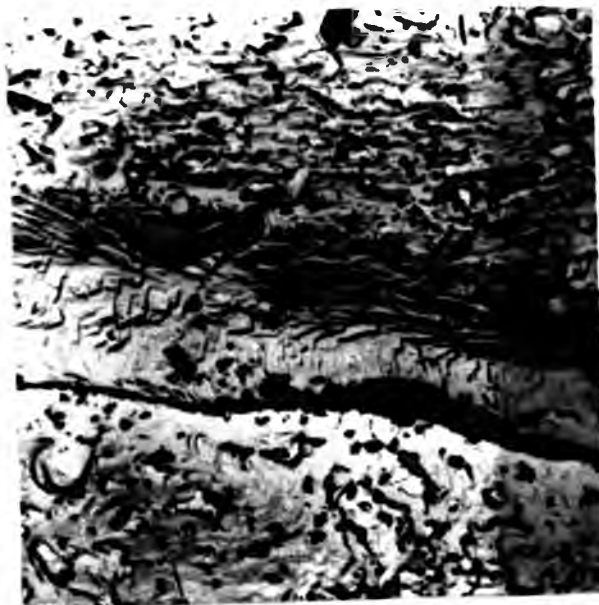
(q)

Wrought specimens exhibiting (m) dissolution at the matrix-inclusion interface, x 2132, (n) higher magnification of (m) indicating deformation of the inclusion, x 9727, (p) deformation and fracture of the inclusion, x 9727, and (q) dissolution of the ferrite in pearlitic region, x 9727. After  $3.4 \times 10^4$  reversals.

Fig R 17: Transmission electron micrographs of rotating bend fatigue tested specimens at 278 MPa, R=-1, 47 Hz.



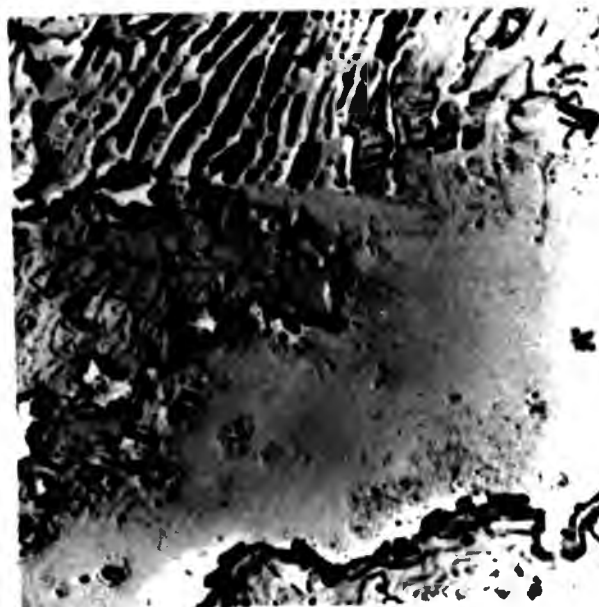
(m)



(n)



(p)



(q)

Wrought specimens exhibiting (m) dissolution at the matrix-inclusion interface, x 2132, (n) higher magnification of (m) indicating deformation of the inclusion, x 9727, (p) deformation and fracture of the inclusion, x 9727, and (q) dissolution of the ferrite in pearlitic region, x 9727. After  $3.4 \times 10^4$  reversals.

Fig R 17: Transmission electron micrographs of rotating bend fatigue tested specimens at 278 MPa, R=-1, 47 Hz.



(m)



(n)



(p)



(q)

Wrought specimens exhibiting (m) dissolution at the matrix-inclusion interface, x 2132, (n) higher magnification of (m) indicating deformation of the inclusion, x 9727, (p) deformation and fracture of the inclusion, x 9727, and (q) dissolution of the ferrite in pearlitic region, x 9727. After  $3.4 \times 10^4$  reversals.

R 17: Transmission electron micrographs of rotating bend fatigue tested specimens at 278 MPa, R=-1, 47 Hz.



(n)



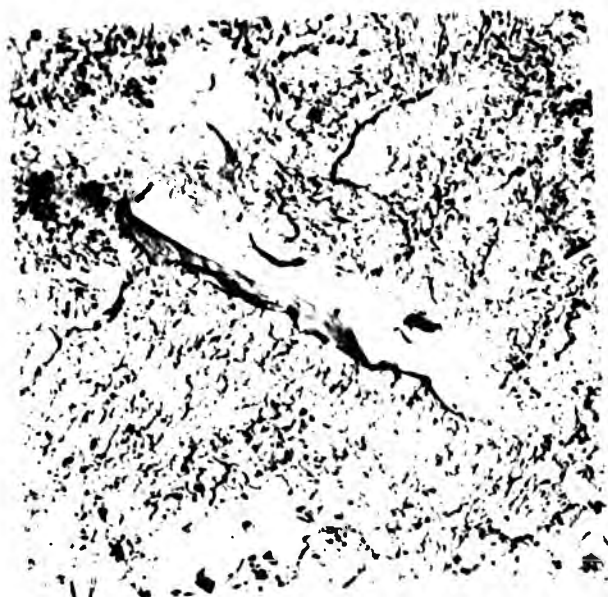
(p)



(o)

Wrought specimens exhibiting (m) dissolution at the matrix-inclusion interface,  $\times 2132$ , (n) higher magnification of (m) indicating deformation of the inclusion,  $\times 3777$ , (p) deformation and fracture of the inclusion,  $\times 3777$ , and (o) dissolution of the ferrite in pearlitic region,  $\times 3777$ . After  $1.4 \times 10^4$  reversals.

Fig. 1. Transmission electron micrograph of rotating beam fatigue tested specimens at 300 Hz,  $\sigma = 100$  MPa.



(r)

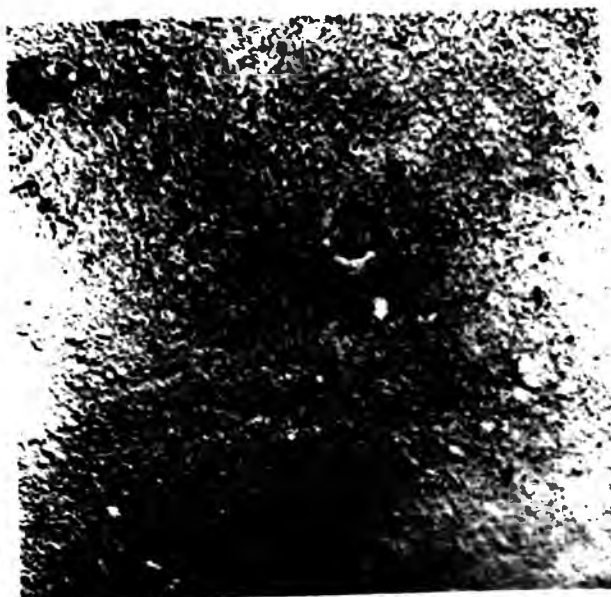


brought specimens exhibiting (r) slip band between two pearlitic regions after  $3.4 \times 10^4$  reversals,  $\times 2037$ , (s) dissolution around a spherical inclusion after  $5.11 \times 10^4$  reversals,  $\times 2037$ , (t) dissolution around a longitudinal inclusion and slip bands adjacent to the interface after  $5.11 \times 10^4$  reversals,  $\times 2037$ , and (u) formation of microcrack in the transverse direction after  $3.4 \times 10^4$  reversals,  $\times 8192$ .

Transmission electron micrographs of rotating bend specimen tested at  $200^\circ\text{C}$ ,  $\times 2037$ ,  $\times 8192$ .



(r)



(s)



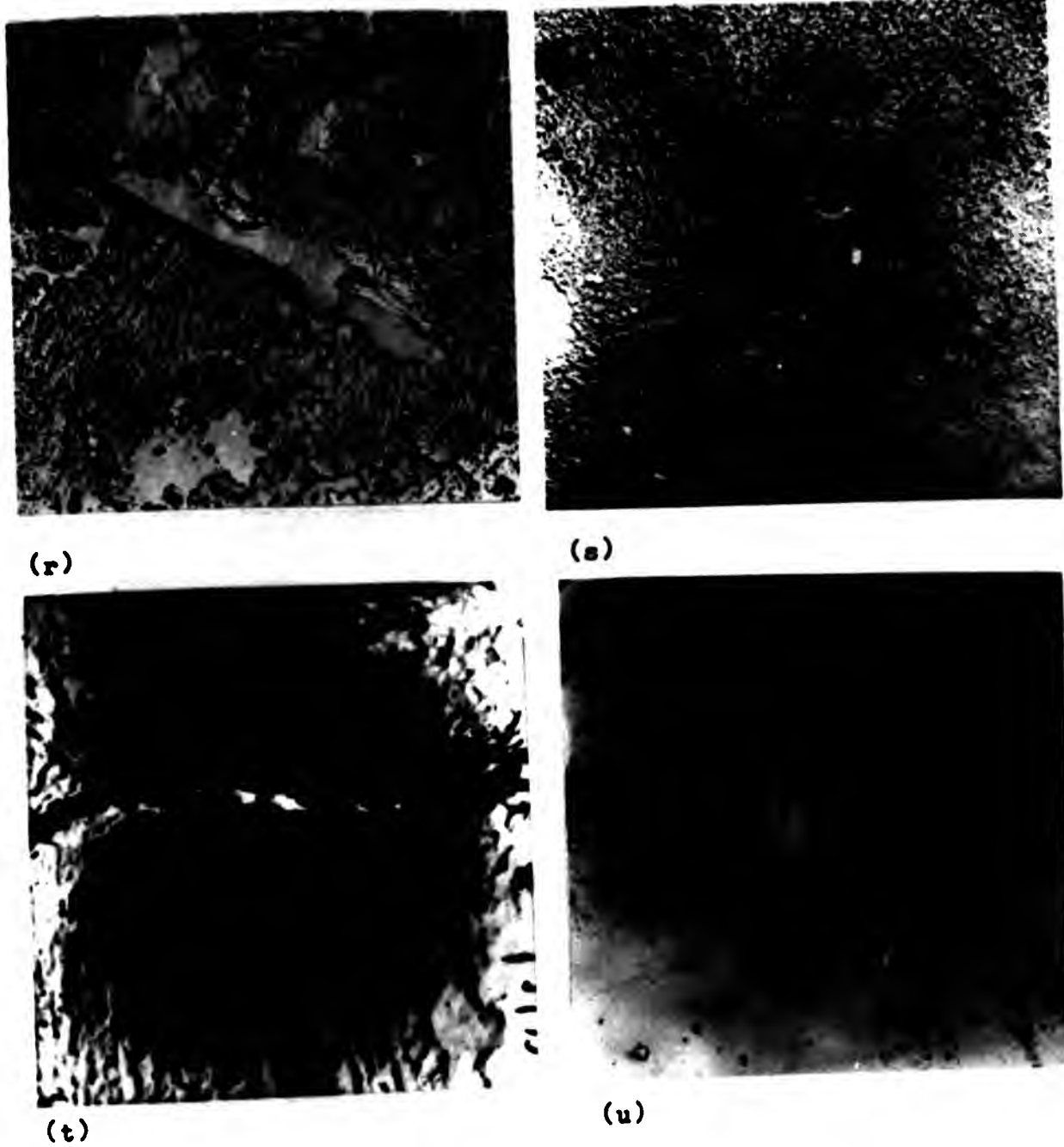
(t)



(u)

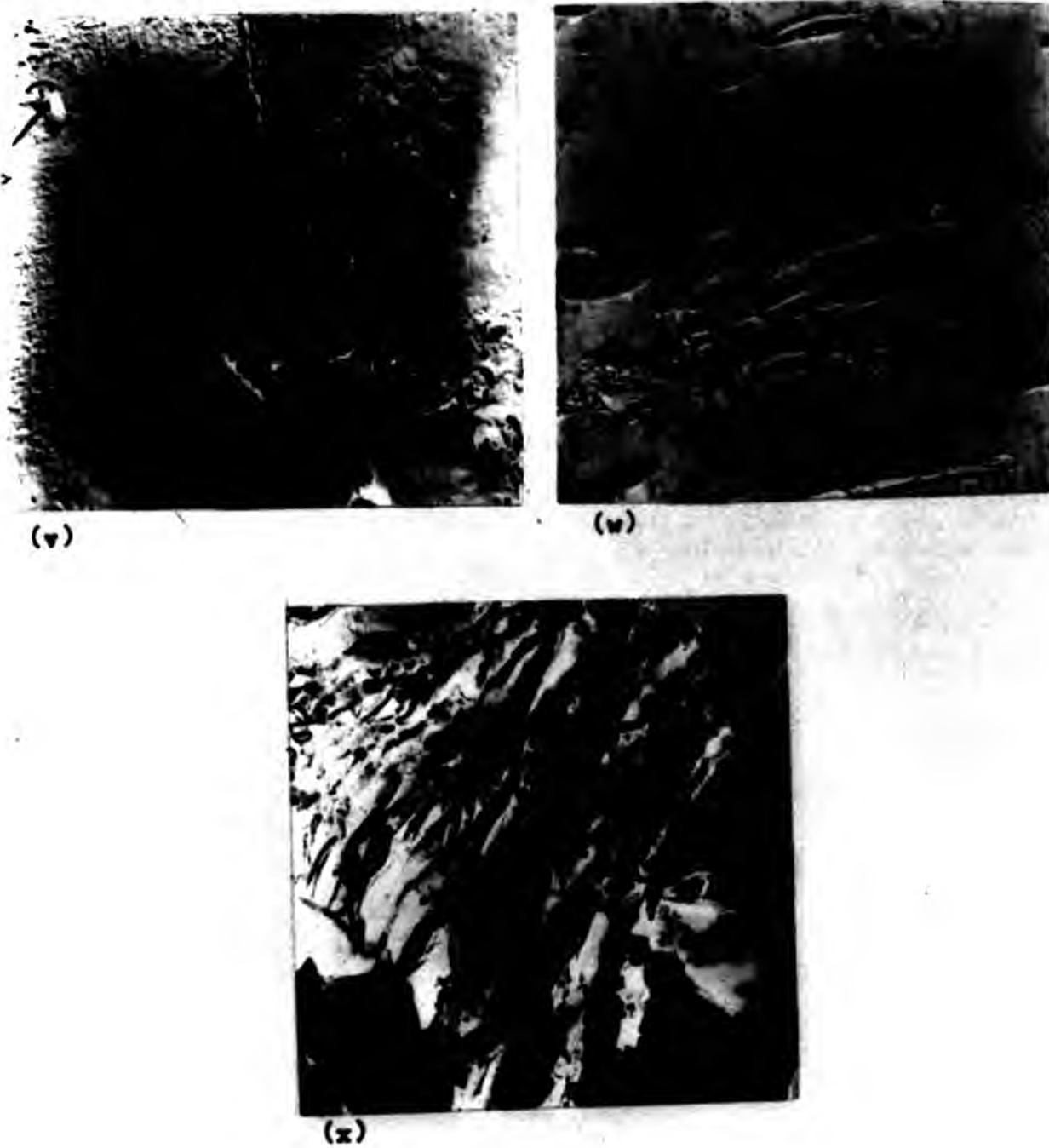
Wrought specimens exhibiting (r) slip band between two pearlitic regions after  $3.4 \times 10^4$  reversals,  $\times 2182$ , (s) dissolution around a spherical inclusion after  $5.11 \times 10^4$  reversals,  $\times 2182$ , (t) dissolution around a longitudinal inclusion and slip bands adjacent to the interface after  $5.11 \times 10^4$  reversals, 9727, and (u) formation of microcrack in the transverse direction after  $9.6 \times 10^4$  reversals,  $\times 8182$ .

Fig R 17: Transmission electron micrographs of rotating bend fatigue tested specimens at 278 MPa,  $R=-1$ , 47 Hz.



Wrought specimens exhibiting (r) slip band between two pearlitic regions after  $3.4 \times 10^4$  reversals,  $\times 2182$ , (s) dissolution around a spherical inclusion after  $5.11 \times 10^4$  reversals,  $\times 2182$ , (t) dissolution around a longitudinal inclusion and slip bands adjacent to the interface after  $5.11 \times 10^4$  reversals, 9727, and (u) formation of microcrack in the transverse direction after  $9.6 \times 10^4$  reversals,  $\times 8182$ .

Fig R 17: Transmission electron micrographs of rotating bend fatigue tested specimens at 278 MPa,  $R=-1$ , 47 Hz.



Wrought specimens exhibiting (v) slip bands near grain boundaries,  $\times 2182$ , (w) high inclusion density region,  $\times 2182$ , and (x) dissolution of ferrite in pearlitic area,  $\times 11273$ . After  $4.39 \times 10^5$  reversals.

Fig R 17: Transmission electron micrographs of rotating bend fatigue tested specimens at 278 MPa,  $R=-1$ , 47 Hz.



(v)



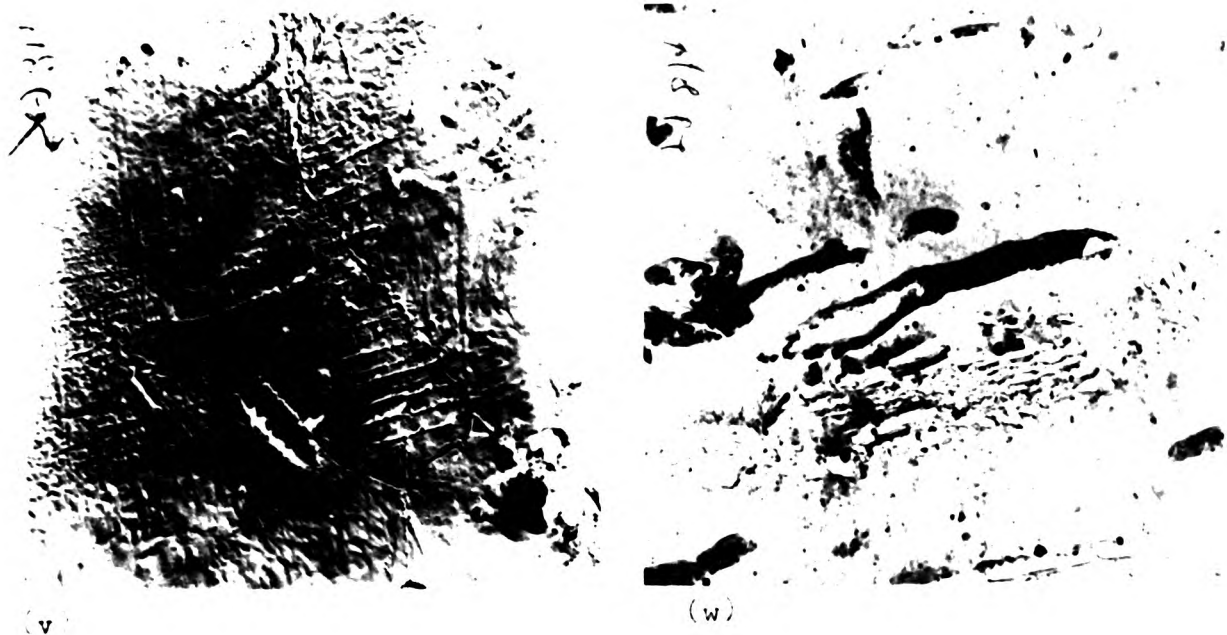
(w)



(x)

Wrought specimens exhibiting (v) slip bands near grain boundaries,  $\times 2182$ , (w) high inclusion density region,  $\times 2182$ , and (x) dissolution of ferrite in pearlitic area,  $\times 11273$ . After  $4.39 \times 10^5$  reversals.

Fig R 17: Transmission electron micrographs of rotating bend fatigue tested specimens at 278 MPa,  $R=-1$ , 47 Hz.



drawn specimens exhibiting (v) slip bands near grain boundaries,  $\times 2182$ , (w) high inclusion density region,  $\times 2182$ , and (x) dissolution of ferrite in pearlitic area,  $\times 11227$ . After  $4.33 \times 10^5$  reversals.

Fig. 17: Transmission electron micrographs of rotating bend fatigue tested specimens at 500 MPa,  $R=-1$ , 40 Hz.

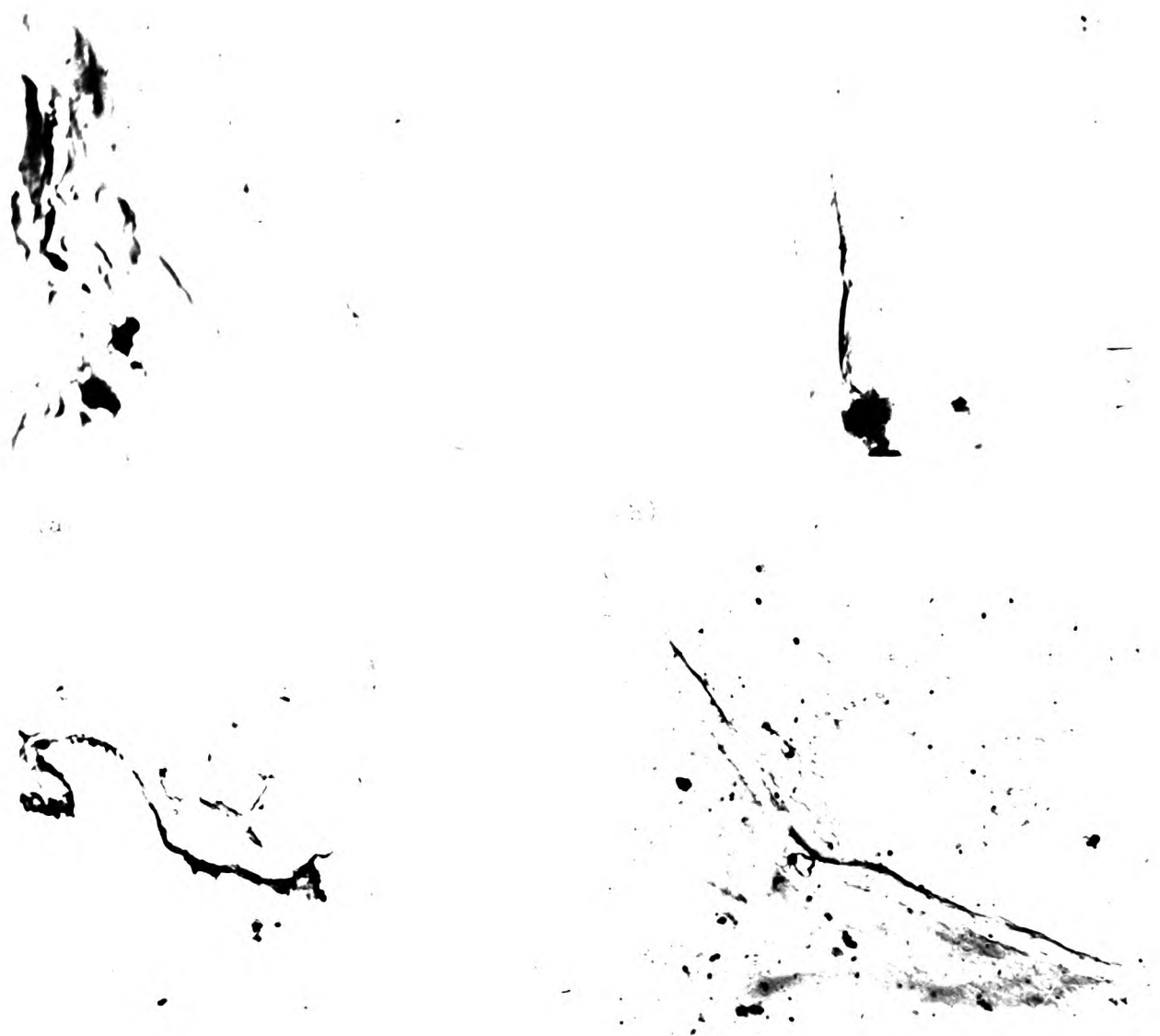
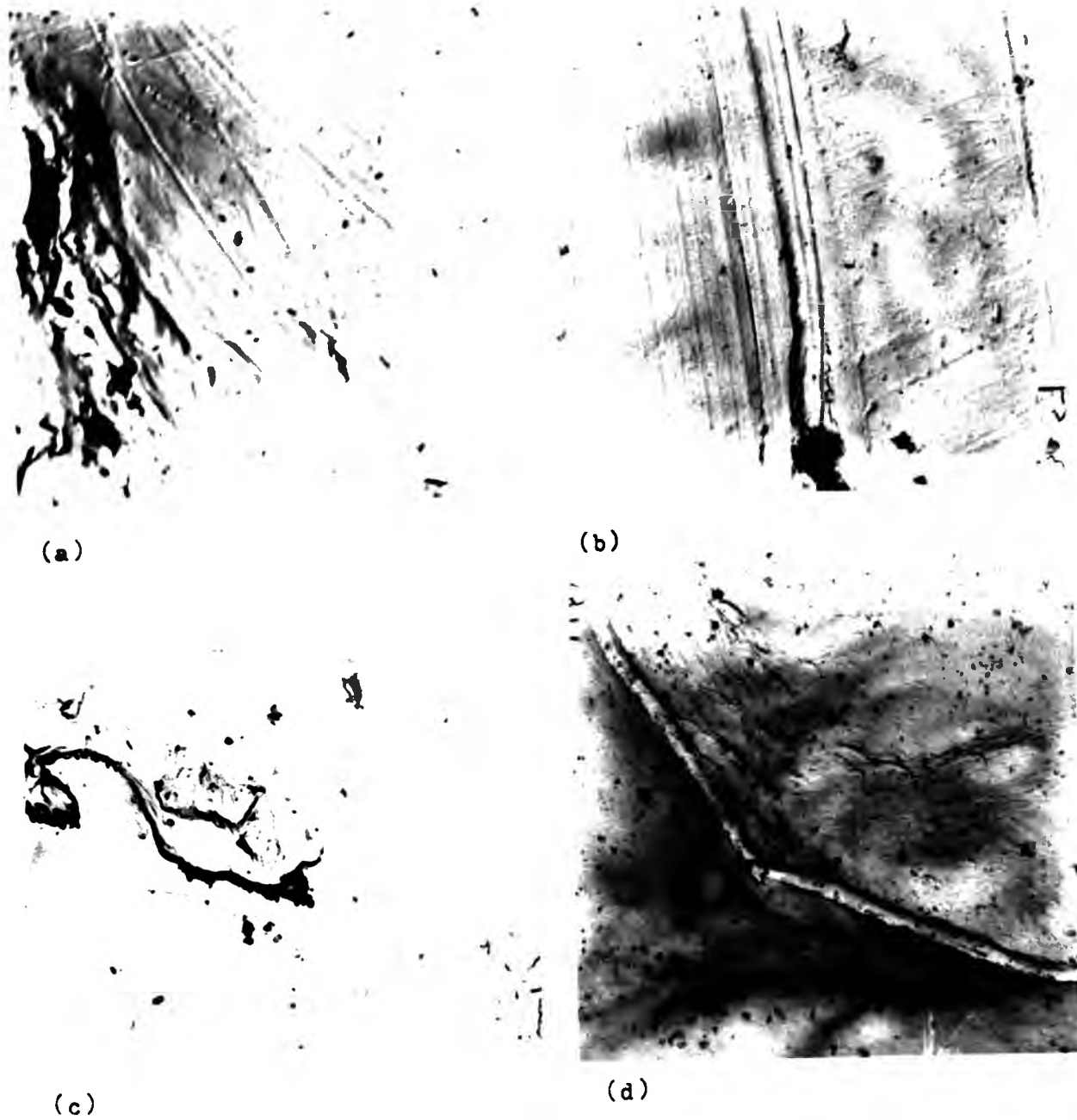


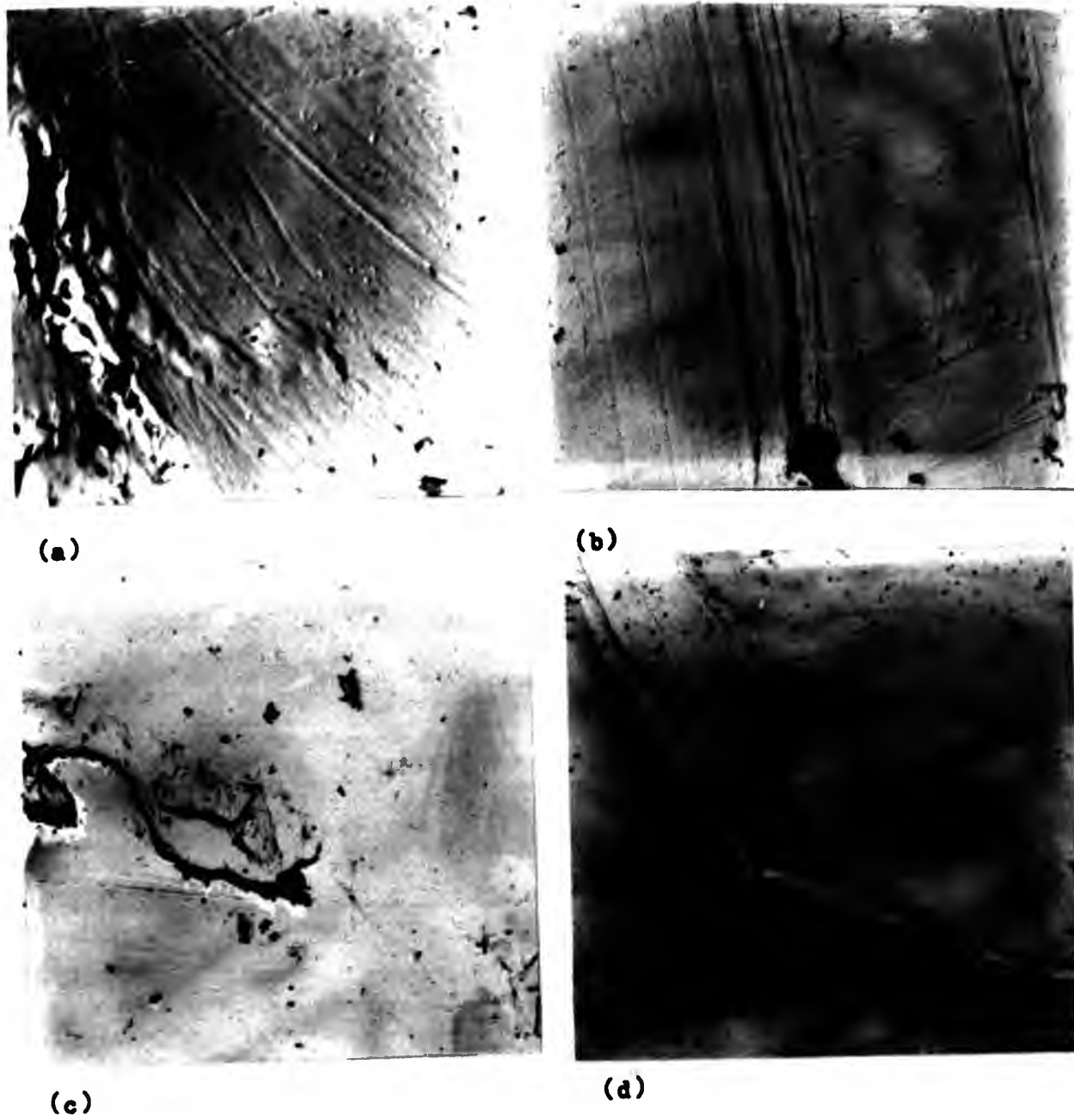
Fig. 1. Micrographs of polycrystalline specimens exhibiting (a) flow of slip bands near a surface defect after  $4.16 \times 10^7$  reversals,  $\times 11273$ , (b) discontinuation of slip bands at a void after  $1.7 \times 10^7$  reversals,  $\times 812$ , (c) microvoids at the matrix-inclusion interface after  $1.7 \times 10^7$  reversals,  $\times 4310$ , and (d) slip band changing direction at a surface defect after  $1.75 \times 10^7$  reversals,  $\times 1111$ . Stress  $10^8$  dyn/cm<sup>2</sup>.

Fig. 2. Diagram of the electron microscope of the specimen during cyclic loading.



Wrought specimens exhibiting (a) flow of slip bands near a surface defect after  $6.16 \times 10^5$  reversals,  $\times 11273$ , (b) discontinuation of slip bands at a void after  $1.2 \times 10^6$  reversals,  $\times 8182$ , (c) microvoids at the matrix-inclusion interface after  $1.2 \times 10^6$  reversals,  $\times 4909$ , and (d) slip band changing direction at a surface defect after  $1.75 \times 10^6$  reversals,  $\times 2182$ . Stress = 193 MPa,  $R = -1$ .

Fig. 18: Transmission electron micrographs of rotating bend fatigue tested specimens at 47 Hz in air.

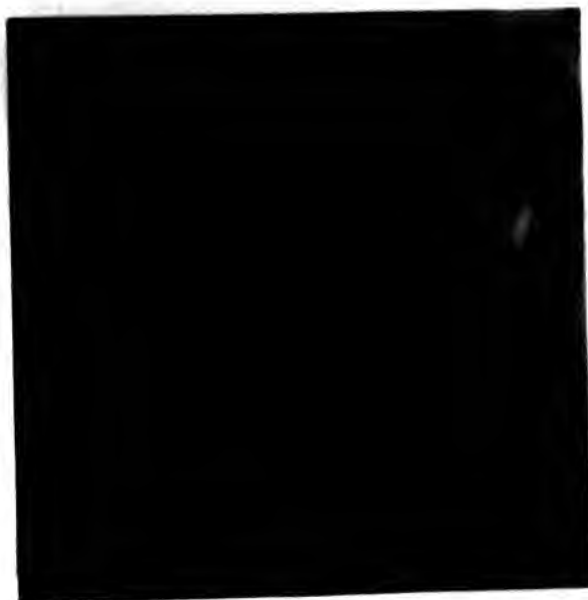


Wrought specimens exhibiting (a) flow of slip bands near a surface defect after  $6.16 \times 10^5$  reversals,  $\times 11273$ , (b) discontinuation of slip bands at a void after  $1.2 \times 10^6$  reversals,  $\times 8182$ , (c) microvoids at the matrix-inclusion interface after  $1.2 \times 10^6$  reversals,  $\times 4909$ , and (d) slip band changing direction at a surface defect after  $1.75 \times 10^6$  reversals,  $\times 2182$ . Stress= 193 MPa,  $R=-1$ .

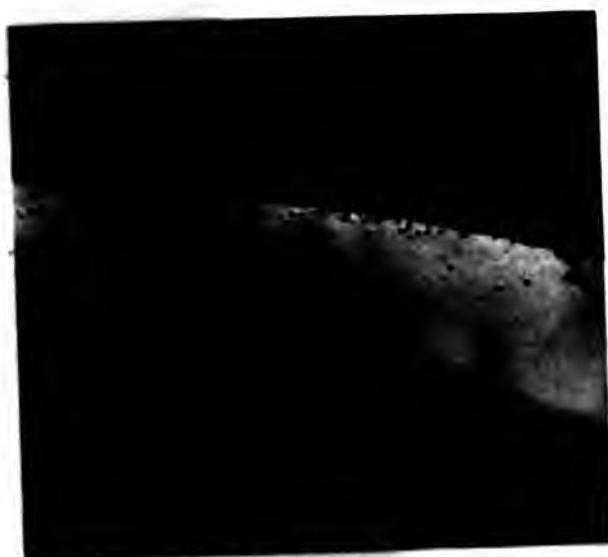
Fig 18: Transmission electron micrographs of rotating bend fatigue tested specimens at 47 Hz in air.



(e)



(f)



(g)



(h)

Wrought specimens exhibiting (e) slip band flow near surface defects after  $1.75 \times 10^6$  reversals at 193 MPa, x 2182, (f) widening of microvoids at the matrix-inclusion interface after  $2.34 \times 10^6$  reversals at 193 MPa, x 9727, (g) slip band with incipient microcrack and pores or micropits after  $2.34 \times 10^6$  reversals at 193 MPa, x 1627, and (h) slip bands after  $6.97 \times 10^4$  reversals at 278 MPa. The dark areas are artifacts. x 3182.  
R=-1.

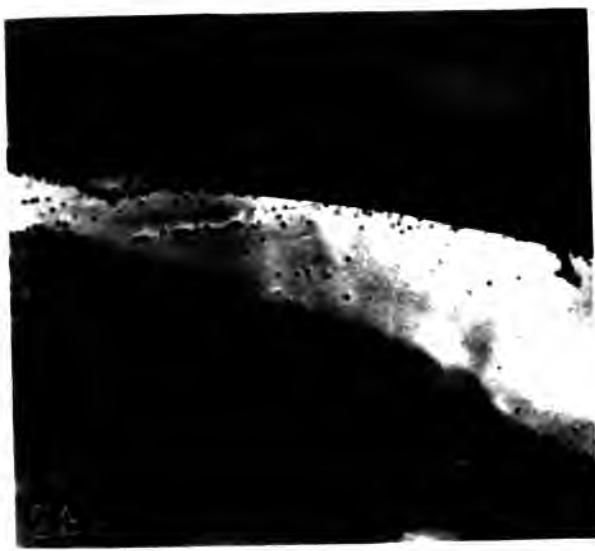
Fig R 18: Transmission electron micrographs of rotating bend fatigue tested specimens at 47 Hz in air.



(e)



(f)



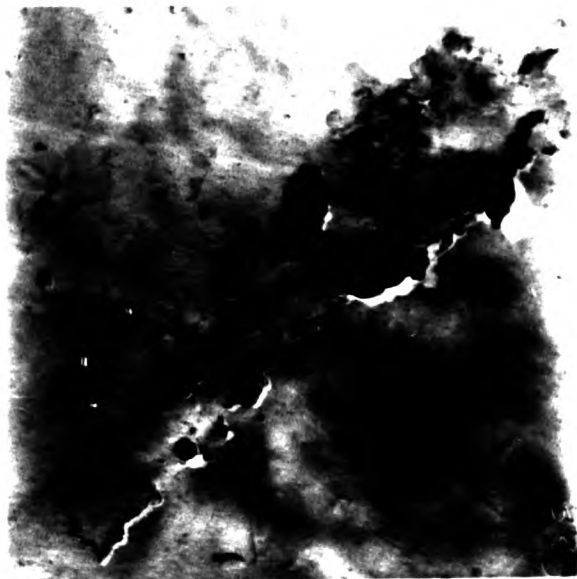
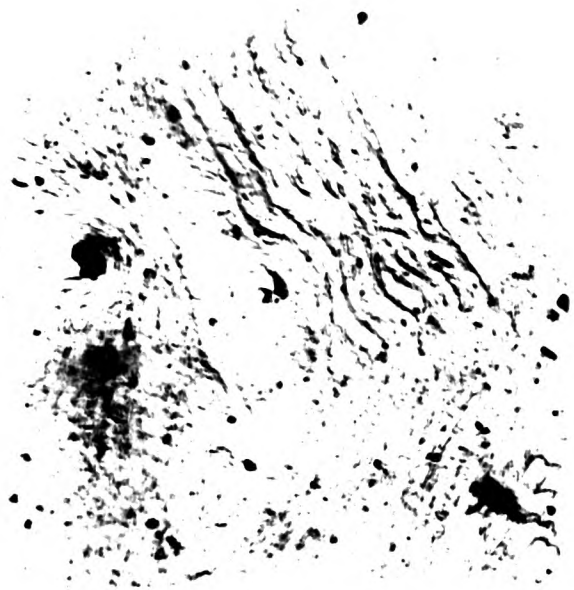
(g)



(h)

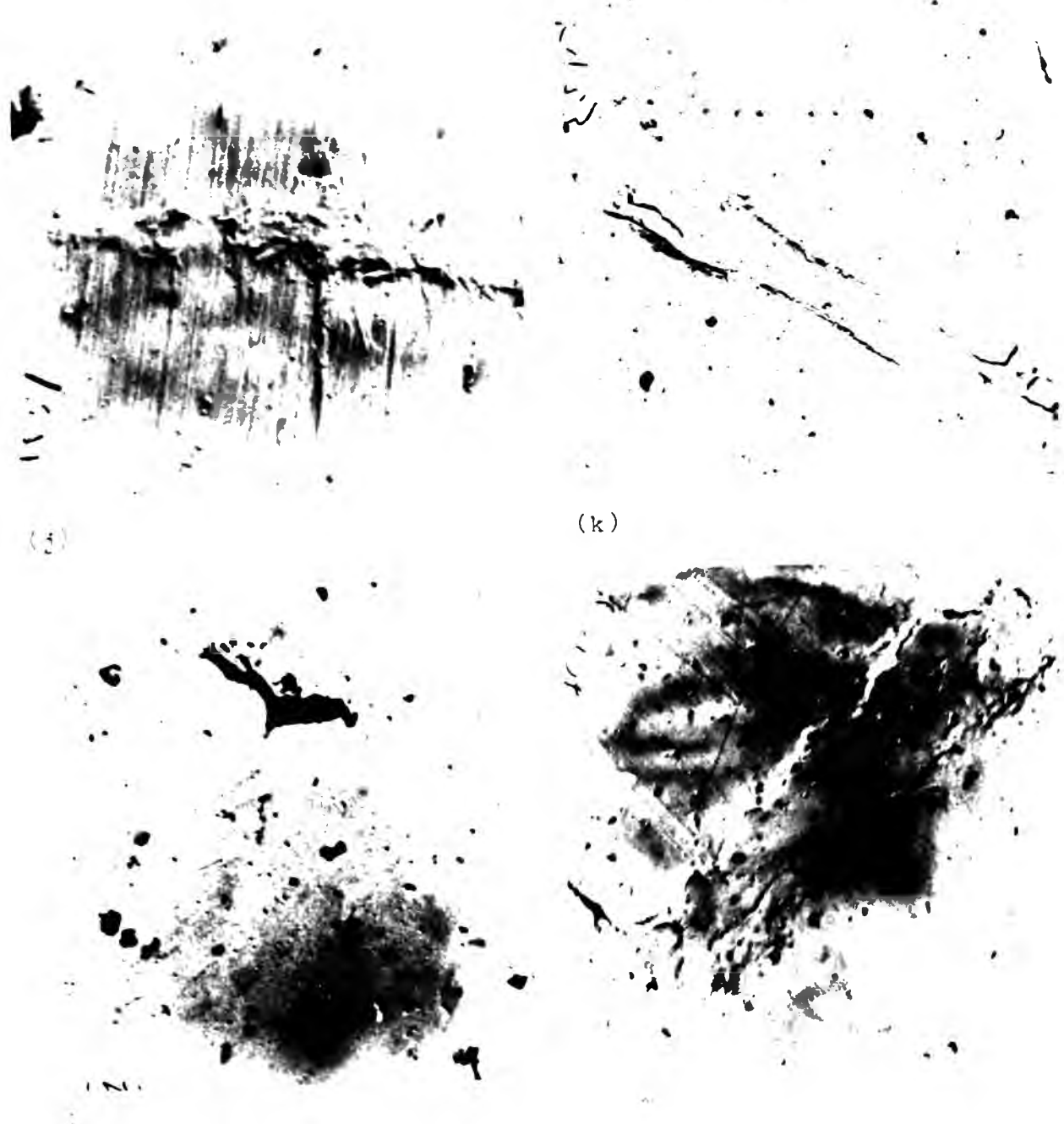
Wrought specimens exhibiting (e) slip band flow near surface defects after  $1.75 \times 10^6$  reversals at 193 MPa, x 2182, (f) widening of microvoids at the matrix-inclusion interface after  $2.34 \times 10^6$  reversals at 193 MPa, x 9727, (g) slip band with incipient microcrack and pores or micropits after  $2.34 \times 10^6$  reversals at 193 MPa, x 1627, and (h) slip bands after  $6.97 \times 10^4$  reversals at 278 MPa. The dark areas are artifacts. x 3182.  
R=-1.

i- R 18: Transmission electron micrographs of rotating bend fatigue tested specimens at 47 Hz in air.



round specimens exhibiting the slip and flow near surface effects after  $1.75 \times 10^7$  reversals at  $10^8$  psi,  $\gamma$  100, of loading of microvoids at the matrix-inclusion interface after  $1.75 \times 10^7$  reversals at  $10^8$  psi,  $\gamma$  100, of slip bands with adjacent microvoids and pores in specimens after  $1.75 \times 10^7$  reversals at  $10^8$  psi,  $\gamma$  100, and in slip bands after  $1.75 \times 10^7$  reversals at  $10^8$  psi,  $\gamma$  100, the microvoids are adjacent to the slip bands.

The slip bands in specimens after  $1.75 \times 10^7$  reversals at  $10^8$  psi,  $\gamma$  100, are adjacent to the microvoids.

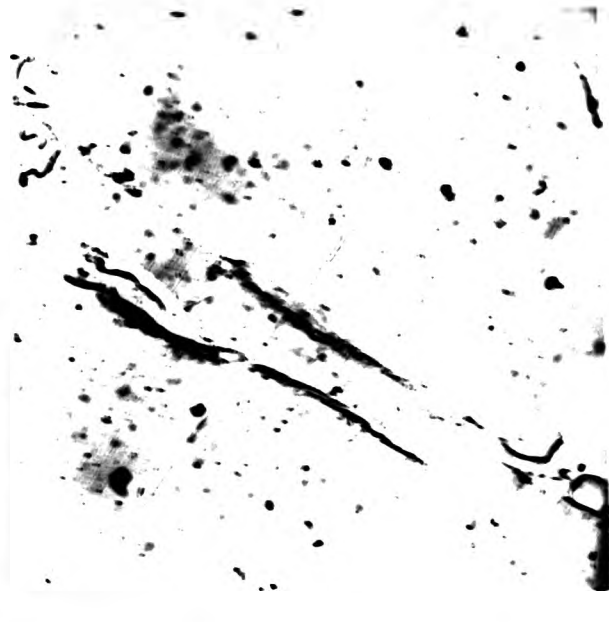


rough specimens exhibiting (j) slip bands intersecting an inclusion after  $3.7 \times 10^6$  reversals,  $\times 8000$ , (k) fracture of inclusion by slip bands after  $4.1 \times 10^6$  reversals,  $\times 8000$ , (l) formation of microvoids after  $4.2 \times 10^6$  reversals,  $\times 8000$ , and (m) microcrack at the matrix-inclusion interface after  $4.3 \times 10^6$  reversals,  $\times 8000$ . Stress  $100 \text{ MPa}$ ,  $\nu = 0.3$ .

Fig. 10: Transmission electron micrographs of rotating disk fatigue specimens at  $10^7$  cycles.



(j)



(k)



(l)



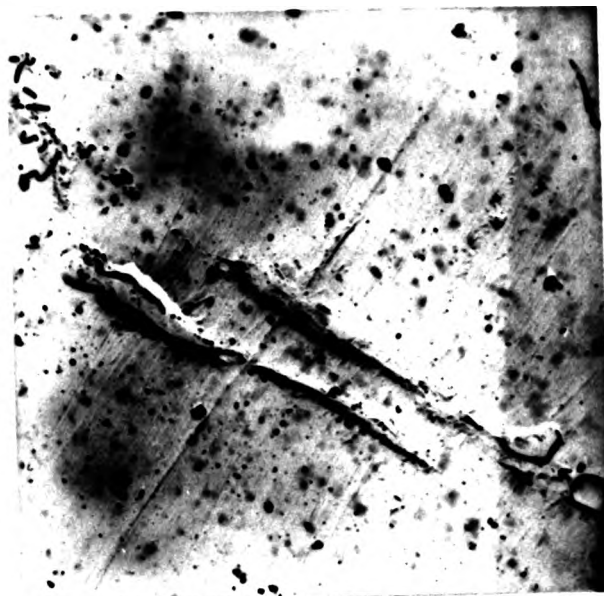
(m)

wrought specimens exhibiting (j) slip bands intersecting an inclusion after  $3.3 \times 10^6$  reversals,  $\times 8182$ , (k) fracture of inclusions by slip bands after  $4.2 \times 10^6$  reversals,  $\times 2182$ , (l) formation of microvoids after  $4.2 \times 10^6$  reversals,  $\times 2127$ , and (m) microcracks at the matrix-inclusion interface after  $4.2 \times 10^6$  reversals,  $\times 8182$ . Stress=278 MPa,  $R=-1$ .

Fig. 18: Transmission electron micrographs of rotating bend fatigue specimens at 47 Hz in air.



(j)



(k)



(l)



(m)

Wrought specimens exhibiting (j) slip bands intersecting an inclusion after  $3.3 \times 10^6$  reversals, x 8182, (k) fracture of inclusions by slip bands after  $4.2 \times 10^6$  reversals, 2182, (l) formation of microvoids after  $4.2 \times 10^6$  reversals, x 9727, and (m) microcracks at the matrix-inclusion interface after  $4.2 \times 10^6$  reversals, x 8182. Stress=278 MPa, R=-1.

Fig R 18: Transmission electron micrographs of rotating bend fatigue specimens at 47 Hz in air.

Transmission electron micrographs of specimens tested at 309 MPa,  $R = -1$ , in 0.6 M sodium chloride solution are shown in Figure R 19. Increasing the stress appears to enhance the mechanical effect rather than the corrosive one in that the fracture and spalling of the inclusions tend to occur more readily (Figure R 19a - R 19c). Figure R 19d shows features resembling those termed by Wood<sup>216</sup> as pores.

For comparison purposes, some of the specimens were electropolished in 10% perchloric acid/acetic acid mixture. Results of the transmission electron microscopic examination of these specimens tested at 193 MPa are shown in Figure R 20.

Figures R 20a and R 20b show preferential dissolution at the matrix - inclusion, ferrite - cementite and ferrite grain - pearlite colony interfaces after  $1.18 \times 10^5$  and  $4.84 \times 10^5$  reversals respectively. Microcrack formation is also observed in slip band adjacent to a pearlitic region. With an increasing number of reversals microcracks along grain boundaries (Figures R 20d and R 20e) and intrusions near triple point (Figure R 20f) are found to occur. Similar effects have been observed in annealed specimens at 95 MPa, at a smaller number of reversals (Figures R 14d and R 14n - q).



(a)



(b)



(c)



(d)

Wrought specimens exhibiting (a) localised attack around an inclusion resulting in microcrack formation after  $5 \times 10^4$  reversals, x 6818, (b) coalescence of microcracks in the inclusion after  $10^5$  reversals, x 16273, (c) fracture and dissolution of inclusion resulting in void formation after  $1.5 \times 10^5$  reversals, x 11273, and (d) slip band, pearlitic region and features resembling pores after  $2 \times 10^5$  reversals, x 2182.

Fig R 19: Transmission electron micrographs of rotating bend fatigue tested specimens at 309 MPa, R=-1, 47 Hz.



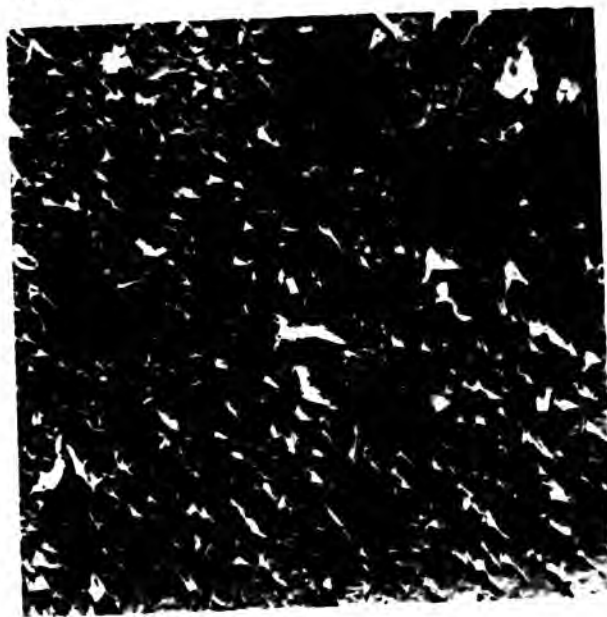
(a)



(b)



(c)



(d)

rought specimens exhibiting (a) localised attack around an inclusion resulting in microcrack formation after  $5 \times 10^4$  reversals,  $\times 6818$ , (b) coalescence of microcracks in the inclusion after  $10^5$  reversals,  $\times 16273$ , (c) fracture and dissolution of inclusion resulting in void formation after  $1.5 \times 10^5$  reversals,  $\times 11273$ , and (d) slip band, pearlitic region and features resembling pores after  $2 \times 10^5$  reversals,  $\times 2182$ .

Fig. 19: Transmission electron micrographs of rotating bend fatigue tested specimens at 300 MPa,  $R=-1$ , 47 Hz.

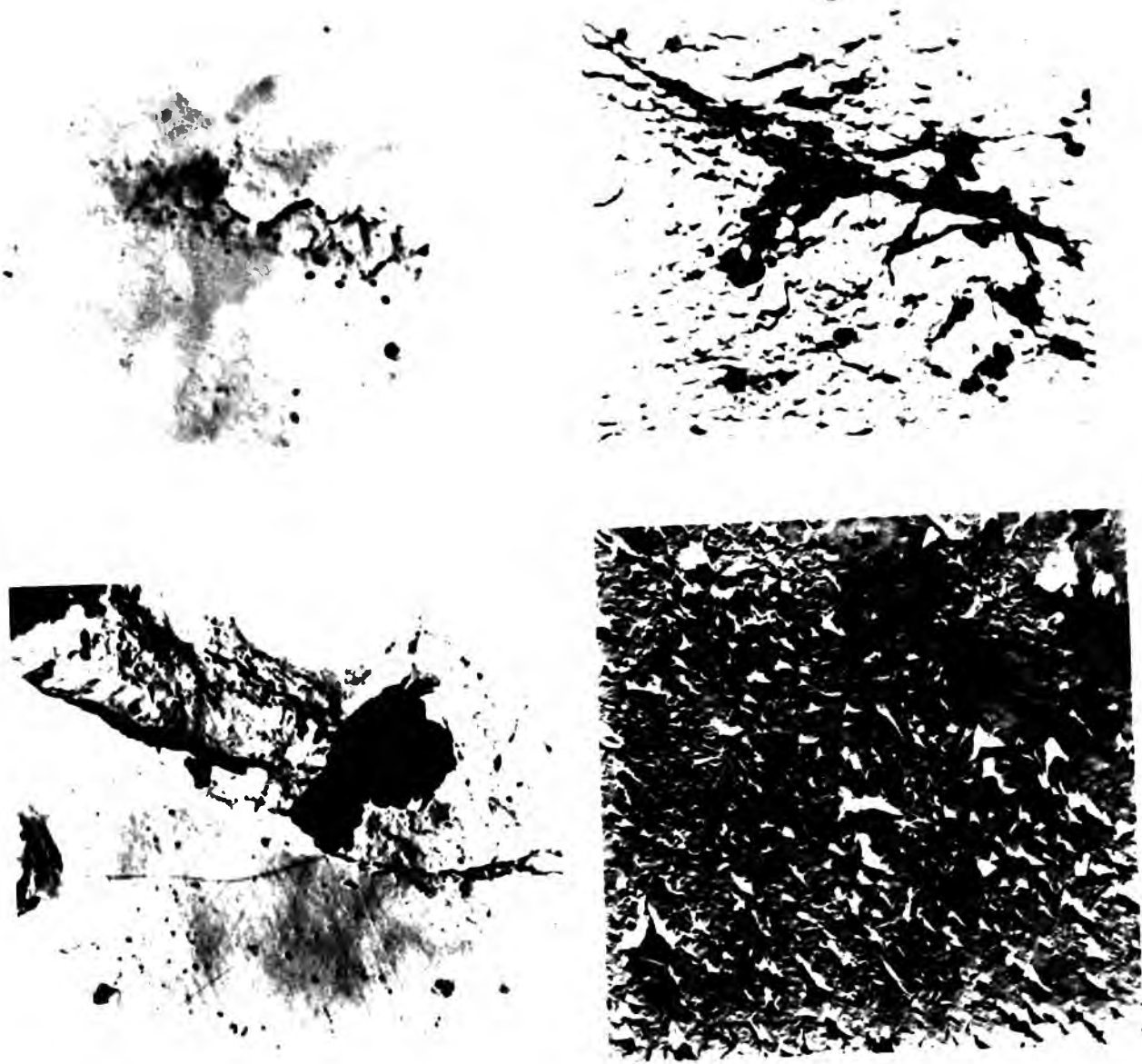


FIG. 1. Micrographs of wrought specimens exhibiting (a) localized attack around an inclusion resulting in microcrack formation after  $10^4$  reversals,  $\times 1000$ , (b) coalescence of microcracks in the inclusion after  $10^5$  reversals,  $\times 1000$ , (c) fracture and evolution of inclusion resulting in void formation after  $10^6$  reversals,  $\times 1000$ , and (d) porous, cellular region and features resembling cores after  $10^7$  reversals,  $\times 1000$ .

Fig. 1. Micrographs of wrought specimens exhibiting (a) localized attack around an inclusion resulting in microcrack formation after  $10^4$  reversals,  $\times 1000$ , (b) coalescence of microcracks in the inclusion after  $10^5$  reversals,  $\times 1000$ , (c) fracture and evolution of inclusion resulting in void formation after  $10^6$  reversals,  $\times 1000$ , and (d) porous, cellular region and features resembling cores after  $10^7$  reversals,  $\times 1000$ .

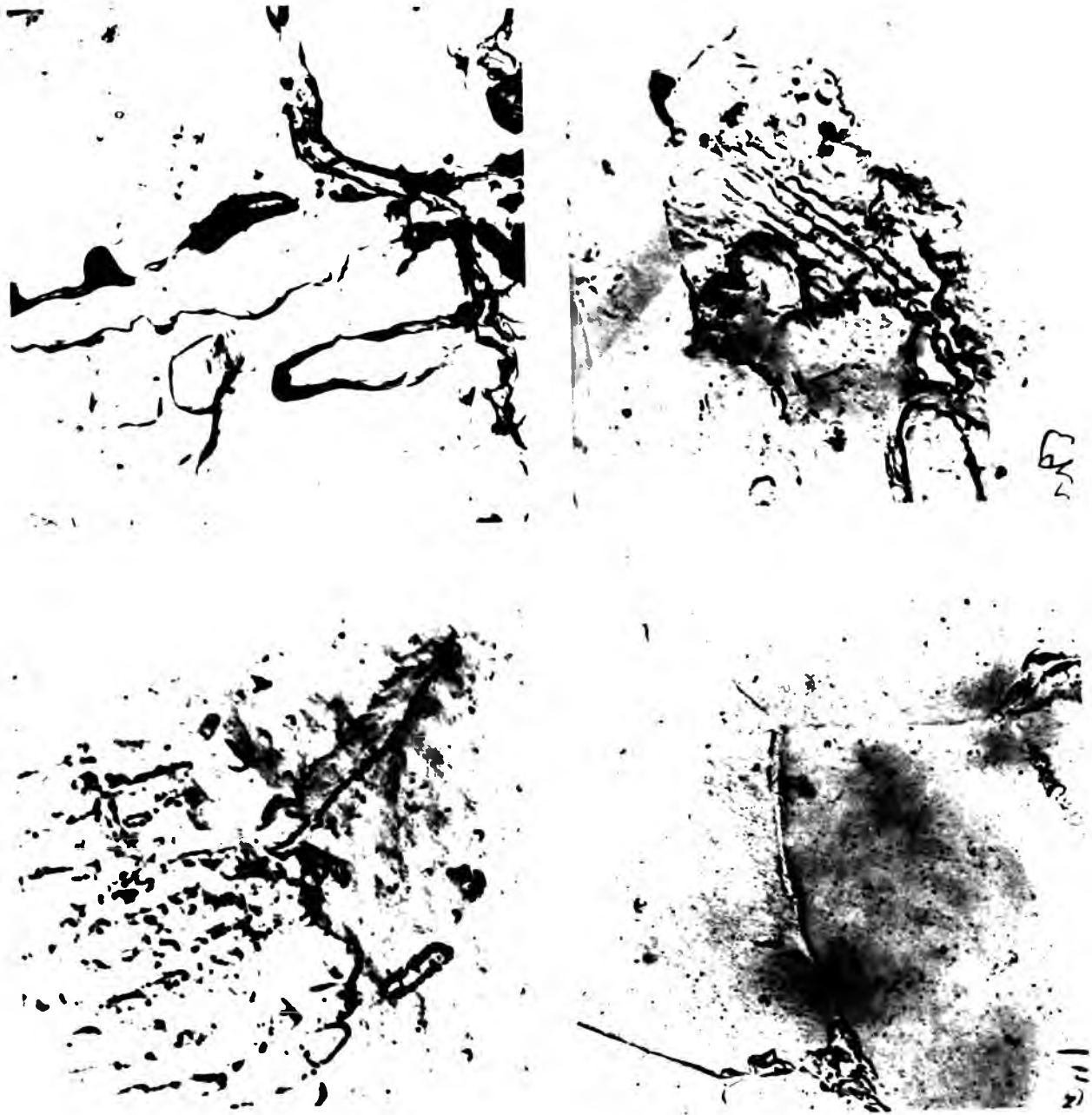
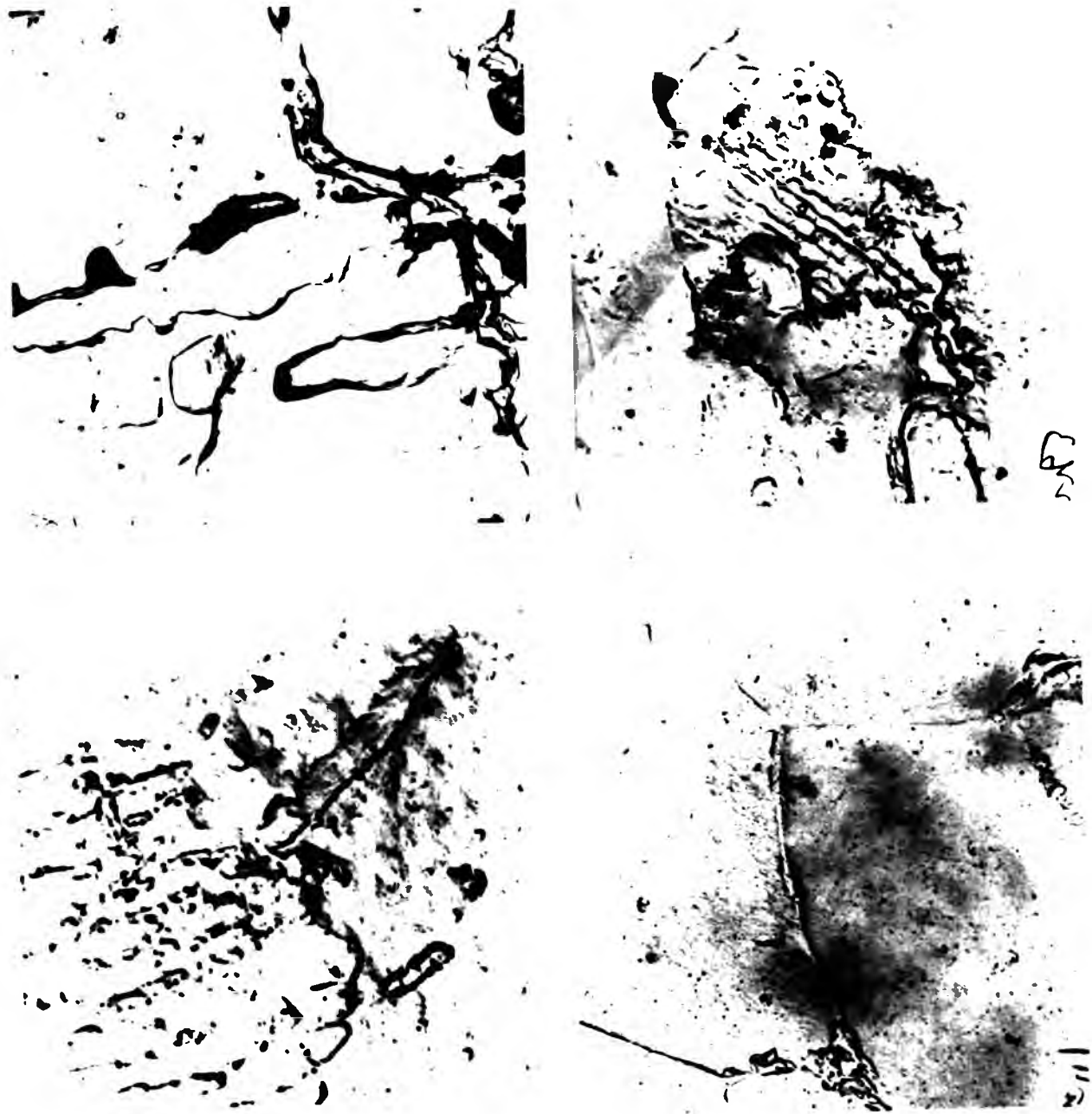


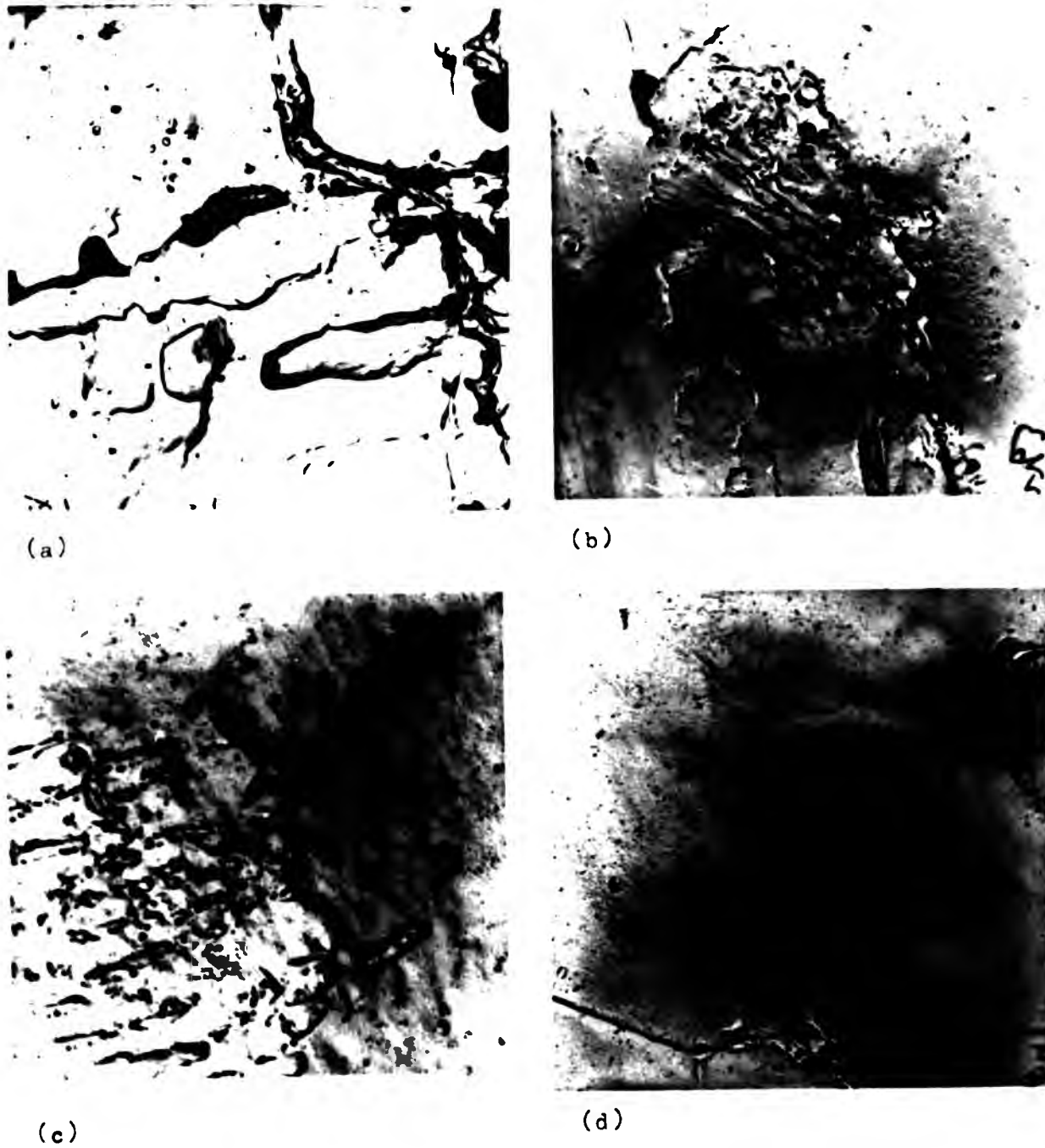
Figure 1. Micrographs of metal specimens exhibiting (a) localised corrosion around inclusions in a high inclusion density region after  $1.1 \times 10^7$  reversals,  $\times 3000$ , (b) microcracks in the ferrite in the pearlitic region after  $4.2 \times 10^7$  reversals,  $\times 1170$ , (c) microcrack around a slip band close to the pearlitic region after  $1.4 \times 10^7$  reversals,  $\times 1000$ , and (d) microcracks along grain boundaries,  $\times 1000$ .

Micrographs of metal specimens exhibiting (a) localised corrosion around inclusions in a high inclusion density region after  $1.1 \times 10^7$  reversals,  $\times 3000$ , (b) microcracks in the ferrite in the pearlitic region after  $4.2 \times 10^7$  reversals,  $\times 1170$ , (c) microcrack around a slip band close to the pearlitic region after  $1.4 \times 10^7$  reversals,  $\times 1000$ , and (d) microcracks along grain boundaries,  $\times 1000$ .



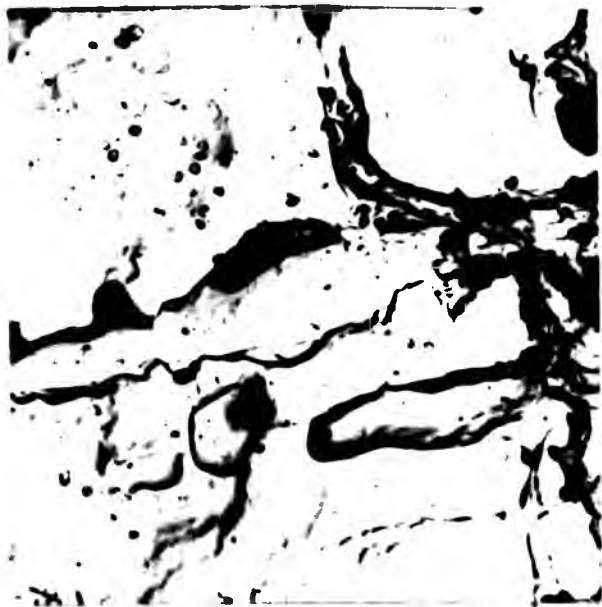
four specimens exhibiting (a) localised corrosion around inclusions in a high inclusion density region after  $1.10 \times 10^7$  reversals,  $\times 2000$ , (b) microcracks in the ferrite in the pearlitic region after  $4.24 \times 10^7$  reversals,  $\times 1100$ , (c) microcrack around a slip band close to the pearlitic region after  $1.4 \times 10^7$  reversals,  $\times 1000$ , and (d) microcrack along grain boundaries,  $\times 400$ .

4. Transmission electron micrographs of rotating disk specimens for the specimens of (a) (b), (c), (d) and (e) after 10<sup>7</sup> reversals.



Wrought specimens exhibiting (a) localised corrosion around inclusions in a high inclusion density region after  $1.19 \times 10^5$  reversals,  $\times 3091$ , (b) microcracks in the ferrite in the pearlitic region after  $4.84 \times 10^5$  reversals,  $\times 11273$ , (c) microcrack around a slip band close to the pearlitic region after  $1.04 \times 10^6$  reversals,  $\times 16273$ , and (d) microcracks along grain boundaries,  $\times 4909$ .

FIG. 20: Transmission electron micrographs of rotating bend fatigue tested specimens at 193 MPa,  $R=-1$ , 47 Hz. Electro-polished specimens.



(a)



(b)



(c)



(d)

Wrought specimens exhibiting (a) localised corrosion around inclusions in a high inclusion density region after  $1.19 \times 10^5$  reversals,  $\times 3091$ , (b) microcracks in the ferrite in the pearlitic region after  $4.84 \times 10^5$  reversals,  $\times 11273$ , (c) microcrack around a slip band close to the pearlitic region after  $1.04 \times 10^6$  reversals,  $\times 16273$ , and (d) microcracks along grain boundaries,  $\times 4909$ .

Fig R 20: Transmission electron micrographs of rotating bend fatigue tested specimens at 193 MPa,  $R=-1$ , 47 Hz. Eletropolished specimens.



Wrought specimens exhibiting (e) linking up of microcracks at triple points after  $1.85 \times 10^6$  reversals,  $\times 11273$ , and (f) features resembling intrusions near triple point after  $1.85 \times 10^6$  reversals,  $\times 8182$ .

Fig R 20: Transmission electron micrographs of rotating bend fatigue tested specimens at 193 MPa,  $R=-1$ , 47 Hz. Electropolished specimens.



brought specimens exhibiting (e) linking up of microcracks  
 at triple points after  $1.85 \times 10^6$  reversals,  $\times 11273$ , and  
 (f) features resembling intrusions near triple point after  
 $1.85 \times 10^6$  reversals,  $\times 8162$ .

Fig. 10: transmission electron micrograph of fatigue crack  
 fatigue tested specimens at  $1.85 \times 10^6$  reversals,  $\times 11273$ .  
 Electronically magnified.



... ..  
... ..  
... ..

... ..  
... ..

## 5 DISCUSSION

### 5.1 Introduction

The study has revolved around two aspects of corrosion fatigue of mild steel in an aqueous solution of sodium chloride, namely, the electrochemical aspects and the metallurgical examinations of the fatigue tested specimens using optical, scanning and transmission electron microscopy.

### 5.2 Anodic polarisation tests

The two principal modes of potentiostatic polarisation are the potentiokinetic and the potentiostatic step methods. Polarisation curves obtained by the potentiokinetic technique are considered to be less accurate than those obtained by the step method but are produced rapidly and are useful for comparative purposes<sup>156</sup>. Green and Leonard<sup>157</sup>, however, have suggested that traverse rate is the most important variable and that there is very little difference between the anodic curves obtained by the two different techniques, at the same rate of change of potential.

One important variable in the potentiokinetic method is the rate of scan of the potential<sup>157, 158</sup>. If the adsorption or desorption phenomenon of a soluble corrosion inhibitor is not anticipated the scanning rate may be as high as 500 V/h in the active region<sup>159</sup>. It has been suggested that for active-passive regions the rates of 0.5 V/h or less are essential. Leckie found that for type 304 stainless steel in 0.1 M sodium chloride solution,  $E_b$  was influenced by the scan rate<sup>160</sup>. Increasing the rate shifted  $E_b$  in the more noble direction.

The application of potentiostatic polarisation to corrosion phenomenon has been discussed in the literature <sup>161-169</sup>. Figure D1 shows a schematic potentiokinetic polarisation curve for a metal exhibiting passivity, e.g. iron in sulphuric acid.

In aerated neutral chloride solution corrosion of mild steel is generally under cathodic control and the main cathodic depolariser will be oxygen. Consequently, the rate of attack is primarily influenced by reduction kinetics and by the rate of transport of oxygen from the bulk solution to the corroding surface. The more rapid the transport of oxygen to the specimen surface the higher will be the rate of attack there; but with a metal such as iron which tend to be passivated if the oxygen concentration is high enough, this effect may be reduced by anodic polarisation.

In general, the surface of iron is covered completely by a poreless passivating layer when the applied potential is more positive than the Flade potential,  $E_p$ , which is defined as the potential at which a passive metal becomes active. Any local destruction of this passive metal will be arrested immediately in the absence of aggressive anions <sup>170</sup>. Even when starting with pre-active specimens in chloride containing media, a passive film will be formed, but the formation of pits has been observed <sup>171</sup>. When the chloride concentration is greater than or equal to 1 M, passivation is prevented and general dissolution occurs <sup>170</sup>.

According to Thomas <sup>155, 172</sup>, there are two distinct passivating oxide films. From the condition of active dissolution, a passivating film of lower oxidation state, rather similar to magnetite, is formed first. On increasing the potential in the positive direction, magnetite transforms to ferric oxide.

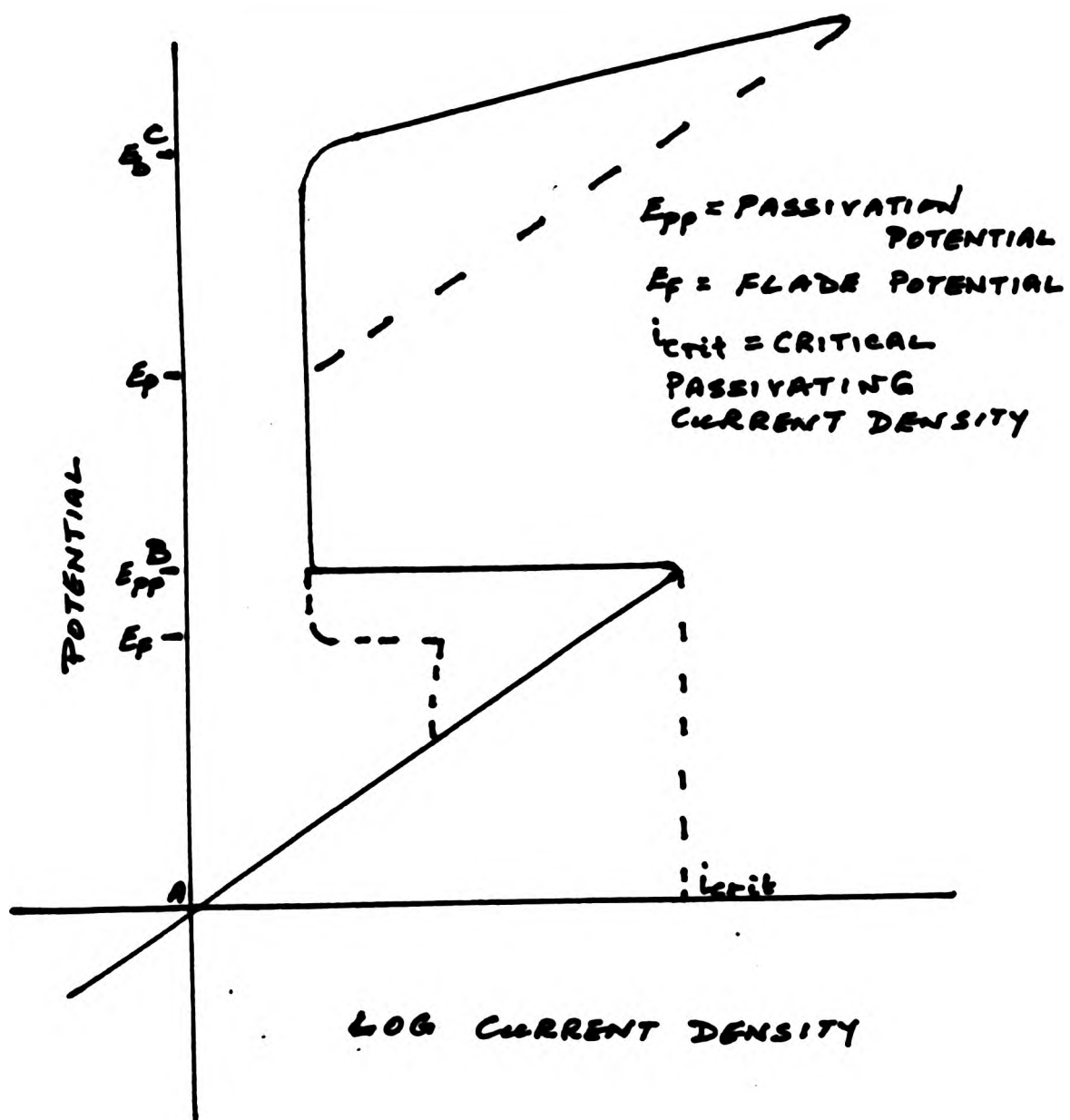
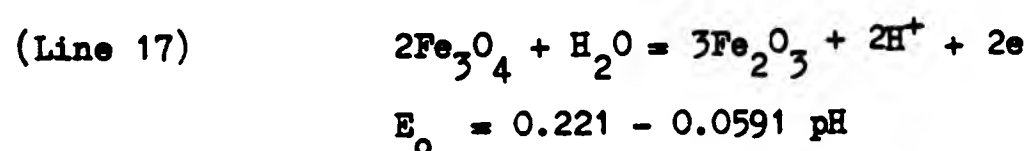
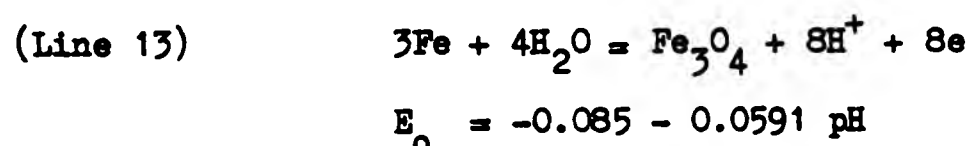


Fig D 1: Schematic potentiokinetic polarisation curve exhibiting active-passive transition.

In near neutral solution, two Flade potentials for iron may be observed <sup>172</sup>: one for ferric oxide and the other for the magnetite film (Figure D2). Reductive dissolution occurs at the Flade potential,  $E_F$ , of the ferric oxide film, whereby ferric ions on the oxide surface are reduced easily to soluble ferrous ions. The electrons necessary for this reduction are supplied by the oxidation of the metal to form cations. The film breakdown at  $E_F$  of ferric oxide is retarded by increase in pH and by the presence of dissolved oxygen. In the presence of aggressive anions, the oxide film is unstable at the breakdown potential,  $E_b$ , and at more positive potentials, when localised rupture occurs to initiate pitting.

The potentials for oxide forming reactions on iron <sup>173</sup> (Figure D3) are:



At pH 6.5,  $E_0$  for the formation of  $\text{Fe}_3\text{O}_4$  is -707 mV (SCE) and that for  $\text{Fe}_2\text{O}_3$  is -401 mV (SCE).

In stagnant solution, with zero stress, potentiostatic polarisation curve (Figure R 1b) show that the current is essentially constant over a range of potentials, -650 to -900 mV (SCE). The leakage current,  $i_{\text{pass}}$ , between -650 mV (SCE) and -900 mV (SCE) is approximately  $5 \mu\text{A}/\text{cm}^2$ . It is possible that an air-formed oxide film had been present on the specimen surface and the breakdown of this film is observed at -550 mV (SCE). After the tests the specimens were examined and found to be pitted.

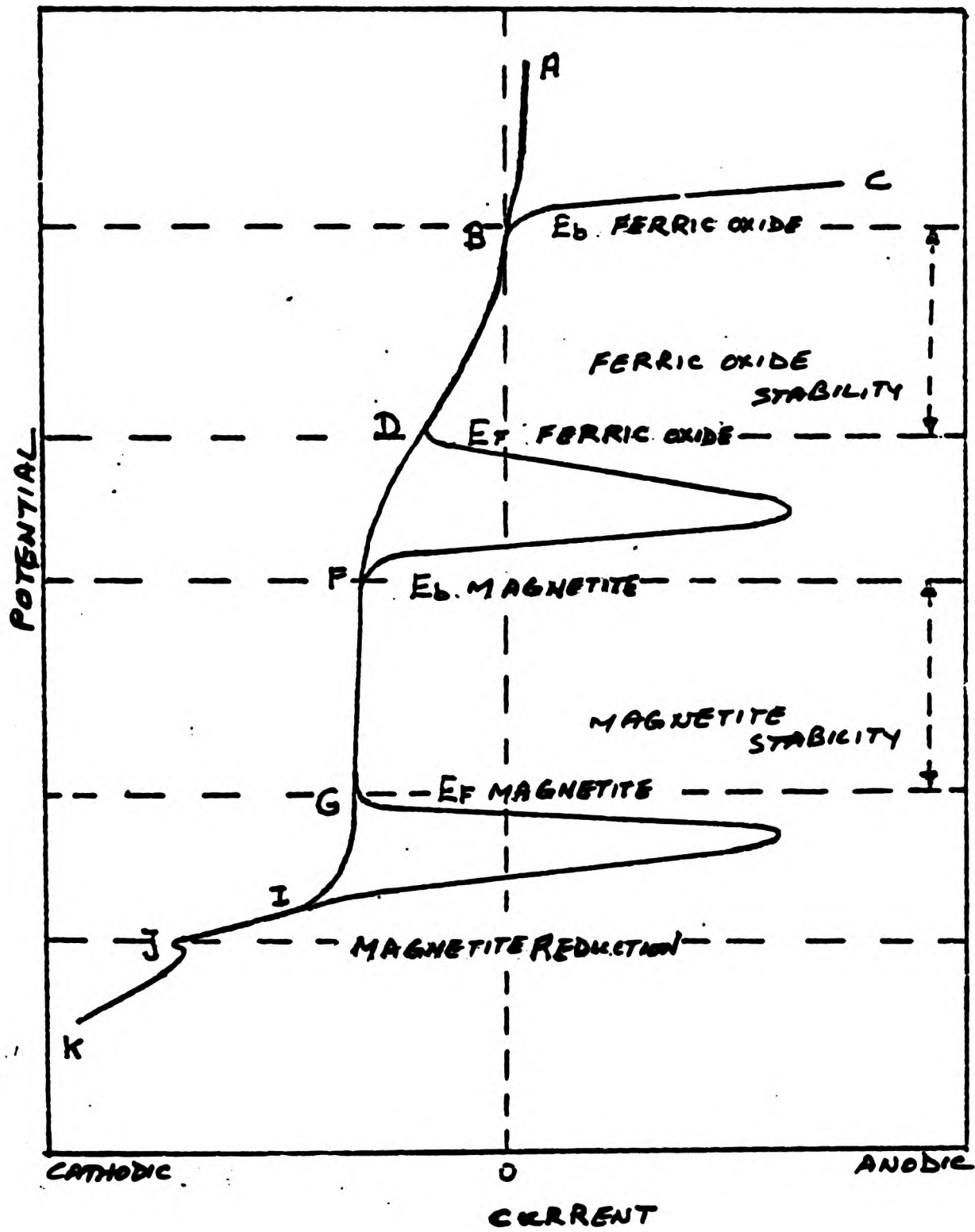


Fig D 2: Schematic polarisation curves for mild steel in air-saturated near-neutral solutions<sup>172</sup>.

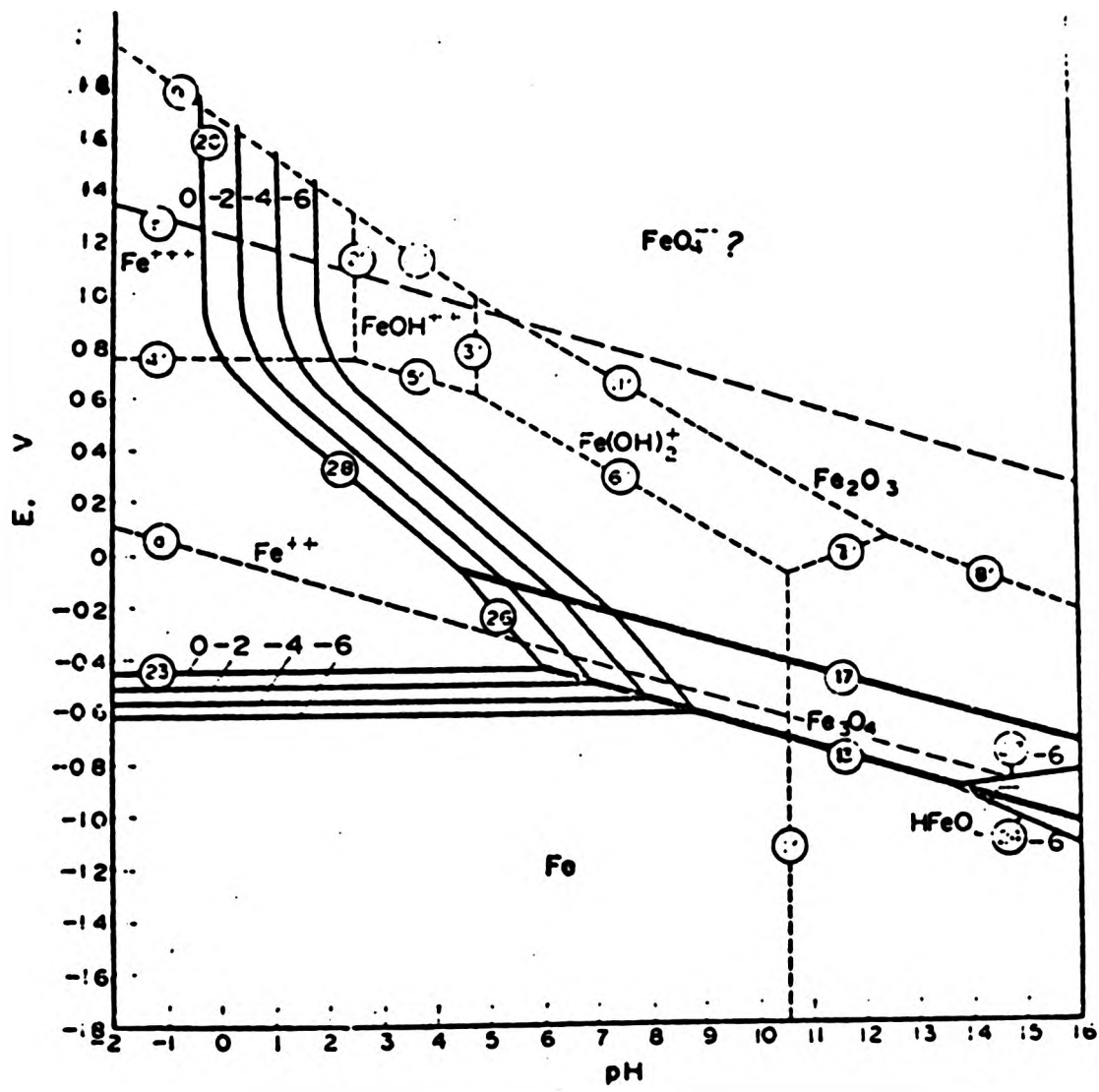


Fig D 3: Potential-pH equilibrium diagram for the iron-water system at 25°C<sup>173</sup>.

In flowing electrolyte, Figure R2, the zero current potential is 80 mV more positive than that found in stagnant solution possibly due to the increased transport oxygen. A narrow potential region of somewhat stable cathodic current corresponding to oxygen reduction has also been observed. A marked increase in current occurs at -700 mV leading to a current peak of  $1200 \mu\text{A}/\text{cm}^2$ , at approximately -550 mV. Between -550 and -520 mV (SCE), the anodic current appears to be constant. The current density then decreases to  $1150 \mu\text{A}/\text{cm}^2$  at -500 mV prior to a marked increase.

The calculated thermodynamic potentials <sup>173</sup> for the formation of  $\text{Fe}_3\text{O}_4$  and  $\text{Fe}_2\text{O}_3$  are -707 and -401 mV (SCE) respectively. The observed peak potential of -550 mV, however, is more positive than the potential for the formation of  $\text{Fe}_3\text{O}_4$ .

Thomas and Nurse <sup>174</sup> have suggested that the critical passivation potential in solutions of different anions, where passivation occurs relatively easily, varies with the pH in the range 6 to 12 according to:

$$E_{pp} = + 0.09 - 0.06 \text{ pH V (NHE)}$$

This pH dependence corresponds to oxide formation, but  $E_{pp}$ , the primary passivation potential, is slightly more positive than the thermodynamic potentials for the formation of the iron oxides and hydroxides <sup>174</sup>.

The critical passivation current density provides a measure of the ease of passivation and its magnitude depends on the balance between the effect of anion adsorption on ferrous ion dissolution and that on the stability and the protective nature of the passivating film.

The anion adsorption may hinder the ferrous ion dissolution process and may tend to reduce the current required for the metal surface to reach the critical passivation potential at which the passivating oxide starts to form. If the breakdown of the oxide film is not facilitated by the anions, the metal dissolution current tends to decrease as the film spreads across the surface. In the presence of aggressive anions, either the formation of oxide is prevented or a less protective film is formed. Consequently, higher currents and more positive potentials are required for the metal surface to achieve the state at which film formation is sufficient to induce a reduction in dissolution current <sup>174</sup>.

At pH 6.5,  $E_{pp}$  is calculated to be -540 mV (SCE). Hence it is considered that the peak potential observed in the polarisation curve corresponds to the primary passivation potential and a degree of overpotential is required for the formation of oxide film. This oxide film consists essentially of magnetite and the breakdown potential is -500 mV (SCE).

On application of a cyclic stress of 169 MPa at  $R = -1$ , the zero current is observed at a much more positive potential than that without applied stress both in stagnant and in flowing electrolyte. This is possibly due to oxygen transport being greater under cyclic stress conditions in flowing electrolyte than that in absence of stress.

Application of cyclic stress results in the formation of a hysteresis loop (Figures R 1a to R 3a). The amount of hysteresis is considered to be dependent on the time allowed for pitting <sup>175</sup>. The greater the pit depth the greater is the hysteresis. The time effect is possibly due to the increase in metal ion concentration, and hence lower pH and chloride ion concentration at the bottom of the pit <sup>175</sup>.

Other researchers have also suggested that the protection potential,  $E_p$ , is influenced by the composition of the solution inside the pit<sup>168</sup>. According to these investigators,  $E_p$  is more useful for practical purposes since it indicates the potential range more negative than  $E_p$  within which pitting cannot occur. However, Wilde<sup>176</sup> has suggested that  $E_p$  is not a unique parameter and is dependent on the sweep rates of the potential. The slower rate moves  $E_p$  to a more negative value. He explains that this is due to the chemical changes occurring inside the growing pit by hydrolysis of corrosion products and by the increased migration of chloride ions. Since  $E_p$  depends upon experimental procedures it cannot be used alone as a parameter against the propagation of existing pits in an engineering structure. He suggests that the potential difference  $E_b - E_p$  is a more useful criterion since this approximates the hysteresis loop area produced during the cyclic determination of  $E_b$  and  $E_p$ . The area of the loop obtained in a potentiokinetic sweep using a specimen with an artificial crevice provides a measure of the resistance to crevice corrosion in service, i.e. the greater the area the lower is the resistance<sup>177</sup>. The region between  $E_p$  and  $E_b$ , however, indicates imperfect passivation. Perfect passivation occurs in the potential - pH region between  $E_{pp}$  and  $E_p$  (Figure D1) in which neither initiation nor propagation of pits is possible<sup>178</sup>.

Wilde and Williams<sup>179</sup> have suggested that the presence of dissolved oxygen causes  $E_b$  to become more positive and enhances passivity. However, if crevices are present, the relationship between  $E_b$  and the resistance of a material to the breakdown of passivity and pit initiation becomes doubtful<sup>176</sup>.

Under cyclic stress the potential at which a marked increase in anodic current occurs is found to be -550 mV (SCE).

This potential is much more positive than that observed with zero stress in flowing electrolyte.  $E_p$  is  $-650$  mV which is the same as the zero current potential. This indicates that the growth of existing pits occurs above the zero current potential. Under cyclic loading condition, movement of the specimen leads to the stirring of the solution and hence enhances the supply of oxygen to the metal surface. Consequently, higher initial cathodic currents are observed at more positive potentials.

Potentiokinetic tests at zero stress in flowing electrolyte also exhibit an hysteresis loop. The protection potential is approximately  $-690$  mV (SCE) and the potential range,  $E_b - E_p$ , in which only existing pits tend to propagate but the initiation of new pits does not occur, is smaller than that found under cyclic loading condition in the potentiostatic test.

The potentiokinetic curve in stagnant solution with zero stress does not show any well defined breakdown potential. The potential at which a marked increase in current, indicating the onset of dissolution of iron, occurs is estimated to be approximately  $-690$  mV (SCE).

The potentiokinetic test (Figure R 4b) in flowing electrolyte shows that current remains cathodic to a much more positive potential than in stagnant solution. This may imply that the oxide film remains somewhat protective to more positive potentials and form better passivating characteristics in flowing solution possibly due to increased oxygen supply.

In all these experiments the specimens initially contained some air-formed oxide films. Essentially this film is composed of  $Fe_3O_4$  near the metal and  $\gamma-Fe_2O_3$  near the air-oxide interface <sup>180</sup>.

On exposure to solution, corrosion occurs when the rate of oxide breakdown is greater than the rate of repair by reaction with oxygen. The film may occur by either formation of new oxide due to adsorption and reaction of oxygen, by oxidation of ferrous ions produced during the corrosion process, or by anodic oxidation of ferrous ions at the active metal anode to ferric ion compounds<sup>181, 182</sup>.

The potential of the specimens immediately after immersion was found to vary between -500 mV and -590 mV (SCE) depending on whether the air-formed oxide film was allowed to form or not. If this potential is well above the potential at which a marked increase in current occurs then rapid breakdown of the oxide occurs. Corrosion takes place immediately on immersion and the rate increases until the potential falls into the region where the lower passivating film of magnetite is stable. Corrosion in this region occurs by the spread of the existing sites of breakdown. The more negative the breakdown potential of magnetite the greater is the amount of oxide which breaks down to form the initial corroding area.

The initial corroding area is also affected by the presence of sulphide inclusions. According to Eklund<sup>127, 183</sup>, the steel is completely covered by an oxide film except at the sites of sulphide inclusions. When such a steel is immersed in a corrosive liquid, the sulphide inclusions are polarised toward the potential of the oxide film. Initially the sulphides are anodic with respect to the oxide surface of the metal and tend to dissolve, increasing the sulphide-ion activity in their immediate vicinity. This "shower" of sulphide ions is adsorbed on the nearest oxide layer and the contaminated oxide quickly becomes anodic with respect to the unaffected oxide surface. Thus the film dissolves and the metal commences to corrode forming a micropit.

Gainer and Wallwork<sup>196</sup>, however, suggested that although Eklund<sup>183</sup> demonstrated the existence of an oxide film on MnS, the proposed model considered MnS inclusions to be devoid of an oxide covering. According to these researchers<sup>196</sup>, a more accurate suggestion may be that "sulphides support oxide films" but these contain many defects which permit direct exposure of the solution to the sulphide. It has been mentioned elsewhere that when specimens are exposed to 0.6 M sodium chloride solution for 30 seconds, initial attack occurs at the inclusion-matrix interface<sup>152</sup>.

The situation is further complicated by the stirring action of the electrolyte which enhances the supply of oxygen as well as that of chloride ions resulting in an increase in corrosion rate and the current density required to maintain passivity. The cyclic stress, under fully reverse loading conditions, produces a pumping action which may expel electrolyte from the pits. However, this effect may not be as severe as that expected in the case of a crack. The relatively more open nature of the pit limits closure during the compressive part of the cycle while it opens readily, like a crack, during the tensile part of the load cycle<sup>184</sup>.

In stagnant solution, both the potentiostatic and potentiokinetic curves (Figures R 1a and R 4a) are displaced from the cathodic to the anodic regions. This effect was also observed in potentiokinetic study elsewhere<sup>185</sup>. With U-bend specimens of wrought material of the same composition as the material used in this investigation it was found that in stagnant solutions the potentials at which a marked increase in anodic current occurred were -640 to -680 mV (SCE) at zero stress and -710 mV (SCE) under cyclic stress of 200 MPa at 1.78 Hz. The zero currents were observed at -820 mV (SCE) at zero stress and -650 mV (SCE) at 200 MPa.

The scan rate was somewhat higher, -3.5 mV per second. However, in all these tests, the specimen surface were cathodically reduced.

The general result of the present tests show that the application of cyclic stress (Figure R 3) modified the anodic polarisation characteristics as follows:

- (a) Zero current potential, calculated from the graphs, is more positive than that without stress.
- (b) The potential at which a marked increase in anodic current, indicating the dissolution of steel, occurs is more positive than that without an applied stress. Thus specimens will undergo passive film breakdown immediately on immersion to an extent which will be greater the more negative the "breakdown" potential. The existence of a protection potential,  $E_p$ , is also observed. If Figures R 3b and R 4b are considered then  $E_b - E_p$ , the potential range at which pits continue to grow but no new pits form, is larger than that without stress.
- (c) Corrosion potential,  $E_{corr}$ , is more positive than that without stress.
- (d) Corrosion current,  $i_{corr}$ , is higher than that without stress.

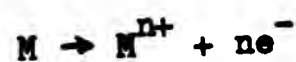
### 5.3 Scratching electrode test

The experimental results show a shift in potential in the negative direction with the passage of time until a steady state is achieved. Displacement of the surface film produces a shift in potential in the positive direction by almost 100 mV. This deviation, however, is not permanent and the potential within a short period becomes more negative than that observed prior to scratching of the surface.

It is possible that the displacement of the potential in the positive direction is due to the creation of a turbulent condition of the electrolyte near the specimen surface. During the performance trials, similar observations were made when air bubbles were introduced in the solution to create a turbulent condition. However, the shift in potential was small, approximately 10 mV. As the scale on the surface of the specimens thickened, potential became more negative with time. This tends to suggest that the shift in potential in the positive direction may be due to the agitation of the electrolyte, disturbing the equilibrium conditions at the surface-solution interface.

The movement of the potential in the more negative direction after the displacement of the surface film is due to the exposure of the bare surface to the corroding solution. This also corresponds to the increase in anodic current. The increment after the point "A" (Figure R 5a) is rather gradual indicating the formation of a surface film. This film or scale could be observed visually.

Materials with initially protective passive film can undergo localised corrosion if the breakdown of this film occurs due to differential elastic strain between the metal and the film or due to plastic strain producing an unfiled slip step. Metal dissolves at these exposed surfaces until the reaction:



ceases due to the healing of the passivating film or due to an accumulation of metal ion which cannot diffuse away <sup>186</sup>.

In flowing electrolyte, metal ions diffuse through the solution from the surface of a specimen. However, diffusion of metal ions from the tip of a crack or crevice to the bulk solution and that of oxygen to the crevice or crack tip may be difficult. This will result in a change of local chemical concentration and the rate controlling reactions inside the crevice or in the vicinity of a crack tip.

France and Greene<sup>187</sup> in considering crevice corrosion of mild steel in oxygenated sodium chloride solution, suggested that initially, dissolution of the metal and reduction of dissolved oxygen occur over the entire metal surface. Once the initial supply of oxygen has been exhausted the reduction process inside the crevice ceases due to the restricted access. Anodic dissolution within the crevice continues giving rise to an excess of positive metal ions which is balanced by the migration of chloride ions into the crevice. The metal ions tend to hydrolyse producing sparingly soluble metal hydroxide and hydrogen ions with a consequent decrease in pH. As the corrosion inside the crevice accelerates, the rate of reduction of dissolved oxygen outside the crevice and the rate of transfer of electrons increase.

Any model for a corroding metal under stress requires the inclusion of a rate of creation of bare surface as well as a passivation rate. Passivation rate is measured by the scratching electrode technique and this has recently been summarised by Knott<sup>186</sup>. In stainless steel or aluminium alloys, examples quoted by Knott, it has been shown that current rises rapidly to a maximum value when the surface of a specimen is scratched by a diamond stylus, and then decays exponentially. In the present investigation the instantaneous reaction was for the current to decrease momentarily when the specimen surface was scratched by a glass rod.

Recovery, however, was very rapid, and a small peak of the anodic current (Point A in Figure R 5a) and current decay were observed.

Mild steel in 0.6 M sodium chloride solution does not form a protective passive film. Therefore, reactions may occur both through the filmed and exposed area of the surface which may contain inhomogeneities, such as non-metallic inclusions. These chemical differences may affect the healing characteristics of the film. In addition, the environment inside a crevice may not be the same as that on a smooth surface specimen in a bulk solution. However, this scratching test shows the direction and the minimum change in potential and current produced when a fresh surface is exposed to the corroding solution.

#### 5.4 Measurement of potential inside a notch

Although corrosion fatigue tests were conducted on smooth surface specimens it was observed that micropits or cavities tend to develop at and around surface defects, and cracks appeared to initiate from these surface inhomogeneities.

Within the confines of a surface discontinuity the solution pH changes and potential differences may occur. The effect of flowing solution through the cell may be negligible within the discontinuity. The relevance of the measurement of the potential at a surface, where crevices or cracks tend to emerge, in relation to the potential inside the crevice has been reviewed<sup>188</sup>. However, the restricted geometry of a cavity also makes the measurements extremely difficult. This has led to the development of a wide variety of experimental techniques for determining the electrochemical conditions within the cavity from direct methods using microelectrodes to simulation methods using macrocells.

There are advantages as well as disadvantages in these techniques. In the case of microelectrodes, perturbation of the system may occur if these are inserted into a cavity. Probes may disturb the salt films which develop at the mouth of the cavity. However, if holes are made to accommodate the electrode near the bottom of the cavity by drilling through the side or bottom of the specimen, electrochemical conditions within the cavity may be altered or stress distribution, where there is an applied stress, may be affected <sup>188</sup>.

Artificial cavities have been used by many researchers to overcome some of the difficulties associated with direct measurements. These have been useful in providing data for testing the effects of variables, such as bulk conditions, potentials, geometry, etc. The results, however, cannot be directly related to real cavities.

Sufficient experimental data are not available to confirm changes in potential in pits relative to the external surface of mild steel exposed in chloride solutions. Use of large scale artificial pits, normally encounters difficulties due to the mixing of the bulk solution with that inside the pit resulting in a measure of uncertainty of the results. For this reason, in this investigation, a small notch was made on the specimen surface to simulate the condition within the pit.

The results (Figure R 6) show that an hour after the immersion the potentials on the external surface and that inside the notch were  $-610$  mV and  $-643$  mV (SCE) respectively. Both these potentials decayed with time and after 24 hours the respective potentials were  $-638$  mV and  $-673$  mV (SCE).

If the potentiostatic test results (Figure R 2) in flowing electrolyte are considered then the external surface potential,  $-610$  mV, is more negative than the "breakdown" potential,  $-500$  mV, of an oxide film. However, this potential is more positive than the potential at which a marked increase in anodic current occurs. Hence it appears that an unprotective film exists on the surface.

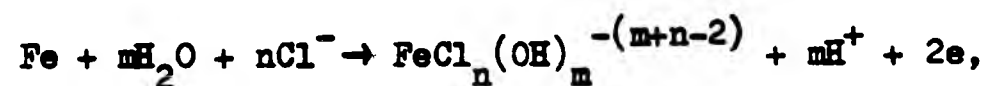
If the potentiokinetic test results (Table I) in flowing electrolyte are considered then the surface potential,  $-610$  mV, is more positive than the zero current potential as well as the potential at which a marked increase in anodic current is observed. However, the potential inside the notch,  $-643$  mV is above  $E_p$ ,  $-690$  mV. The final potentials after 24 hours are between  $-630$  mV and  $-690$  mV (Table I); hence it is expected that no new pits will be formed but the existing pits will tend to grow.

On application of a static stress of 15 MPa the potential of the external surface became more negative, from  $-638$  mV to  $-675$  mV (SCE). Potential inside the notch, however, remained practically the same. It was observed that application of tensile stress dislodged the capillary tube. It is possible that this action enhanced the mixing of the notch electrolyte with the bulk solution. When the specimen was left immersed in the solution under stress for 7 hours both these potentials moved in the more negative direction and became steady at around  $-690$  mV (SCE). When the load was reduced to zero, no immediate change in potential was recorded.

When a compressive stress of 100 MPa was applied, immediately after unloading, the potential at the external surface became more negative. After 60 minutes, the potential recorded was  $-710$  mV (SCE). It was not possible to measure the potential inside the notch since the capillary tube was displaced when the tensile stress was applied.

The pH values of the electrolytes extracted from the notch were found to be between 4.5 and 5. It is possible, however, that some oxidation of Fe<sup>2+</sup> ~~to~~ Fe<sup>3+</sup> could have taken place due to the presence of air in the capillary tube.

Lee et al <sup>189</sup> in investigating the potential and pH changes in an artificial crevice made on the surface of a 0.01% C steel observed that increasing the bulk chloride ion concentration accelerated the rate of pH change and produced more acidic conditions in the crevice. These researchers postulated that if the steel in the crevice behave as the anode of a local cell and dissolve according to the reaction



then the H<sup>+</sup> ion concentration will increase and the free Cl<sup>-</sup> ion concentration will decrease in the crevice. However, the decrease in Cl<sup>-</sup> ion concentration can be compensated by diffusion and migration of Cl<sup>-</sup> ions from the bulk solution. On chemical analysis of the solution extracted from the crevice they observed that in the case of aerated bulk solution containing 5 x 10<sup>-4</sup> M Cl<sup>-</sup>, total Cl<sup>-</sup> ion concentration, i.e. free plus complex Cl<sup>-</sup> ions, in the crevice after 24 hours immersion was approximately 1.5 x 10<sup>-3</sup> M. The free Cl<sup>-</sup> ion concentration was about 3.7 x 10<sup>-4</sup> M in the crevice. It was concluded that an increase in H<sup>+</sup> and total Cl<sup>-</sup> ion in the crevice accelerated the destruction of the passive film and hence the dissolution of metals. They found that after 100 minutes' immersion the potential inside the crevice was -700 mV (SCE) with anodic dissolution of steel occurring.

The extent of the potential drop in a cavity depends on the polarisation characteristics of the metal in the local environment,

the case of mass transport between the solution in the cavity and that in the bulk, and the conductivity of the solution. Turnbull<sup>188</sup> suggests the existence of limiting values of potential if the applied potential is moved to sufficiently positive or negative values. For structural steels in marine environments the potential drop in crevices of widely varying dimensions indicates that the potential drop will be less than 60 mV for applied potentials in the range -680 mV and -1000 mV (SCE). Polarisation of steel outside this range leads to limiting potentials in the crevice of -640 mV and -1100 mV (SCE) for anodic and cathodic polarisation respectively.

#### 5.5 Measurement of potential of specimen subjected to tensile stress

Attempts have been made to measure the potential of metals stressed in the region below the engineering yield stress. Peres<sup>190</sup> measured the potential of copper wire in acid copper sulphate solution for each load increment and obtained a linear relationship of potential vs strain in the initial stages of straining followed by a discontinuity resembling yield.

Taub et al<sup>191</sup> suggest that since fatigue failure originates from the surface, the endurance limit is expected to be closer to the surface elastic limit. Mechanical measurements cannot detect the elastic transition of microscopic localities. The surface undergoes plastic deformation at a lower stress level than the recorded elastic limit of the bulk.

In their investigation these researchers observed that the potential initially changed linearly with applied stress and then at a certain critical stress changed in the opposite direction thus resulting in a peak at that critical stress. They suggested that the generation of potential is a surface phenomenon which showed a marked change in behaviour as the weakest part of the metal surface deformed plastically.

According to Wagner <sup>192</sup>, potential is proportional to the stress. However, as some of the grains on the surface become plastic this linear relationship breaks down and the potential change decreases with increasing stress, the peak potential is suggested to be at the elastic limit of the surface material.

Using this method Taub et al <sup>191</sup> observed the surface elastic limit of  $16.5 \text{ Kg/mm}^2$ , i.e. 161.8 MPa, for 0.6% C steel in mixtures of pure methyl alcohol and water or nitric acid and suggested that in plain carbon steels only the ferrite was subjected to plastic deformation while the carbides were unaffected. They also found that the potential was affected by electrolyte composition, anode - cathode distance, conditions of electropolishing, and depolarisation.

Paul and Weiland <sup>193</sup> observed that in corrosion fatigue and in tensile tests on Ni/30 Mo and Cu, the negative shift in potential was due to the slip planes intersecting the surface. On stopping the deformation, the potential rapidly returned to almost the original value. The potential change was ascribed to the change in the structure. They observed that theoretically, for small deviations from the rest potential the potential shift should be directly proportional to the deformation rate and the polarisation resistance, assuming that the higher energy surface regions, where the slip planes intersect the surface, are responsible for the potential change.

In the present investigation the typical curves in Figure R 7 indicate the direction of changes observed while recording the potential after each load increment. The extent of potential change varied somewhat from specimen to specimen but the peaks were always at similar stress levels.

This appears to indicate the possibility of a change occurring on the material surface rather than to any change in the cell conditions. It also tends to favour, it seems partially, Taub's observation of a critical stress at which the potential changes direction resulting in a peak at that stress.

In this investigation it was found that after the peak the potential movement resumed its original direction and the decrease in potential was more rapid. Taub et al employed a different environment and used a different method of potential measurement. They measured the potential of the strained electrode against an unstrained one. The side effect in this procedure is uncontrollable.

The typical commercial metal contains inside each grain a network of dislocation lines and foreign atoms, precipitates and small angle boundaries that can act as obstacles to dislocations<sup>194</sup>. There may also be local groupings of dislocations around large foreign inclusions. Above a certain level of applied stress, some of these various dislocations are able to move between obstacles. This has been termed as "pre-yield micro strain" in which certain dislocations are able to move, either because the applied stress is enhanced by (i) local stresses or (ii) by stress concentrating features such as notches and sharp edged foreign inclusions or (iii) because such dislocations lie in favourably oriented grains. The overall plastic strain produced by these localised movements remains smaller than or comparable with the elastic strain, until the general yield stress is reached.

Although the curve for the annealed material (Figure R 7a) is somewhat different from that of the wrought material (Figure R 7b), the stress at which the peaks occur are below the yield stress of the material tested in air.

Plastic deformation of the bulk material has not been observed at these stresses. This tends to suggest that the sharp shift in potential in the opposite direction is possibly due to the "pre-yield micro strain" in which certain dislocations are able to move <sup>194</sup>.

It has been observed that if the electrolyte is 0.1 M sodium hydroxide instead of sodium chloride solution, no potential peak in the opposite direction occurs. At approximately 257 MPa the potential sharply changes in the negative direction. It is possible that below 257 MPa microscopic deformation of grains does not rupture the protective surface film and therefore the surface effects are obscured. The existence of a passivating film has been observed in the potentiokinetic study of mild steel in 0.1 M sodium hydroxide, pH 12.5, under a cyclic stress of 200 MPa,  $R = -1$ , at 1.78 Hz <sup>185</sup>. Breakdown of this film occurs at +560 mV (SCE).

The curves in Figure R 7 show that the sharp negative shift in potential accompanies plastic deformation of the bulk material and it decays exponentially with time. It is thought that the net decrease in potential is the resultant of the difference in the rate of production of new and active surface and the rate of its dissolution. If the straining reveals new crystal planes these will tend to dissolve preferentially and the surface in contact with the solution tends, after a certain time, to consist of more stable planes of electrochemical activity similar to that of unstrained metal <sup>195</sup>. There is thus a 'lifetime' for the activity of a newly emerged surface. Once the rate of formation of new surfaces equals the rate at which these become 'inactive' the steady state is reached.

At yield, slipping occurs and the emerging high index planes provide an increased dissolution activity. Preferential dissolution and disappearance of these planes into lower index planes accounts for the 'lifetime' of the active surface.

#### 5.6 Reverse bend fatigue tests - 0.02 to 0.2 Hz

The current vs time curve (Figure R 8a) shows that in stationary condition and in flowing solution, without any stress, the corrosion current tends to fluctuate. The control potential,  $-650$  mV (SCE), was below the potential at which a marked increase in anodic current is observed (Figures R 3b and R 4b). The specimen undergoes passive film breakdown immediately on immersion and before the control potential is applied. It is possible that dissolution occurs at these sites of breakdown and the fluctuations of current possibly indicate the 'lifetime' for activity of some of these sites due to the formation of a monolayer of anions, or due to the deposition of corrosion product, restricting or reducing further reactions.

When a compressive stress is applied, with a control potential of  $-660$  mV (SCE), fluctuation of corrosion current is also observed. During compression the microscopic surface area may decrease. However, the change in shape may rupture the surface film and expose bare metal to the corroding solution (Figure R 8b). This may explain the reason for corrosion current at compressive stress being greater than that at zero stress. Plastic deformation has been found to occur at around 199 MPa (Figure R 7b). Hence it may be reasonable to consider that application of tensile stress of 200 MPa also produces plastic deformation.

In iron, the (110), (112), and (123) planes function as slip planes.

Raicheff et al.<sup>95</sup> suggest that in iron wire, the high index planes (112) and (123) are likely to be more active for the dissolution process due to the lower binding energy of the surface atoms, since drawing of iron wire tends to develop (110) texture parallel to the wire axis. It has been observed that in copper the less close-packed plane, (110), has an exchange current density for deposition and dissolution about 10 times larger than the most closely packed (111) plane. Thus it has been suggested that at the outset of plastic deformation the current increases because the emerging high index planes provide an increased dissolution activity.

Slip bands on mild steel have been observed during the initial application of tensile stress<sup>91</sup>. These slip bands are partially removed by strain reversal to the zero strain position after compression and then accentuated and increased in number by the application of further compressive strain.

Whatever the mechanism, it appears that corrosion will occur quite readily with and without applied stress (Figures R 8a and R 8b).

The load - current vs time curves during the first minutes of a fatigue test at 198 MPa,  $R = -1$ , 0.07 Hz, at -560 mV (SCE) applied potential, are shown in Figure R 8c.

The precise manner in which the dissolution is influenced by deformation process depends upon whether any film was originally present on the surface and by the ability of such films to reform if they were ruptured during straining.

During plastic deformation, slip on the surface exposes fresh areas which are uncontaminated by any previous reactions, to the corroding solution. Thus preferential dissolution may occur on these sites.

When the current moves in the anodic direction the occurrence of the current peaks coinciding with the peaks of tensile and compressive stresses indicate the maximum dissolution effects when the rate of slip step generation is greatest. It is possible that the effect is related to an increase in surface area. The decay of current is possibly associated with the removal of active slip steps or kink sites on slip steps by the dissolution process<sup>91</sup>.

To observe the reason for the initial movement of the mean current in the cathodic direction, a specimen was left immersed in the electrolyte for 72 hours so that a scale, consisting possibly of hydrated oxide, would be formed. It is possible that pits were also formed but visual examination revealed no bare surface. On application of control potential and cyclic stress (Figure R 8c (i)) the mean current moved in the cathodic direction. The current decreased from approximately 0.32 mA to 0.20 mA in the first 48 reversals. This decrease is possible if the film is strong enough to withstand the cyclic stress, and progressively thickens to form a continuous layer covering the whole surface. However, this seems unlikely since in 0.6 M sodium chloride solution any film present on the surface is rather unstable and is not protective.

An alternative mechanism, ingress of a filmed slip step during reversed strain, has been proposed by Patel<sup>91</sup>. It is possible that when a slip step was formed, hydrated oxide scale reformed on the slipped surface and during the reverse slip this slip step was drawn into the metal surface leaving the scale intact. If slip occurred on the same plane again then the scale covered step would emerge and thus dissolution of metal would be retarded. However, since the film is not protective an anodic reaction would still be expected.

Before the mean current moves in the anodic direction there is a transition period when the mean current is practically stationary with the current maxima and minima tending to coincide with the tensile and compressive load cycles. It appears that a dwelling period exists during which the unstable film is finally undermined. At the end of this period, current peaks during the tensile cycle tend to be higher and occasional irregular high peaks are also observed.

When the specimen carries only the air formed film the tendency of the movement of the mean current remains the same. However, the period during which the mean current moves in the cathodic direction and that of the transition region are shorter (Figures R 8c (iii) and R 8c (iv)).

Potential vs time curve (Figure R 8d) shows a gradual decrease of potential. A steady value of  $-650$  mV (SCE) is attained after nearly 16 hours.

On the application of stress, the potential is found to decrease less rapidly at the outset of the test (Figure R 8e). During this test some irregular signals or peaks were noted. The magnitudes of these peaks, however, were too small to include in the graph.

The current vs time curve (Figure R 8f) shows that current initially decreases and then increases quite rapidly. Current peaks were observed. Similar peaks were also observed and found to be associated with the appearance of surface cracks<sup>185</sup>. At a higher stress, however, no pronounced peaks were observed, although current fluctuations were recorded (Figure R 8g). At this stress, 247 MPa, the initial decrease of current has also been observed. The period during which the current moves in the cathodic direction appears to be somewhat longer than that noted at 198 MPa (Figure R 8f).

It has been mentioned that during potential measurements occasional irregular signals or peaks were noted. For this reason, tests were performed at somewhat higher stress and at slower strain rate, i.e. at 247 MPa,  $R = -1$ , and at 0.02 Hz to record the irregularities. Figure R 8h shows the potential as a function of time. The inset in Figure R 8h shows the potential fluctuations on a compressed scale. The result shows that potential decreases somewhat rapidly with increasing number of cycles. At approximately 36 reversals the irregular signals or momentary shifts in potentials, in the more positive direction, resembling "spikes" were recorded. The magnitude of these spikes are approximately 5 mV. Immediately prior to the formation of these spikes, the potential seems to move slightly in the positive direction by about 2 mV. These smaller spikes are followed by somewhat larger spikes of amplitude approximately 10 to 15 mV. These spikes appear to be momentary shifts in potential in the negative as well as, occasionally, in the positive direction. The magnitudes of these spikes, however, vary. The potential tends to decrease somewhat more rapidly after these larger spikes than immediately before these spikes form.

The time interval between the smaller and larger spikes is between 0.4 to 0.9 minutes, i.e. approximately one - half of one reversal to nearly one reversal.

Some of the tests were discontinued immediately before and after the appearance of the first set of spikes and the surfaces were examined using optical microscopy. Areas of bright and dull bands of varying widths were noted on some regions of the specimen surface after the formation of the spikes. On the bright areas very little attack had occurred while the dull areas had been attacked more severely.

This type of "surface irregularities" was also observed on the rotating bend fatigue test specimens at 47 Hz. In the present test, examination of the surface using transmission electron microscopy was unsuccessful.

The bright and dull areas observed using optical microscopy appear to indicate the initial breakdown of the surface oxide film. The bright area is possibly cathodic while on the dull region both the metal dissolution and oxygen reduction occur.

The potential applied to the test piece in Figure R 8a was  $-650$  mV (SCE) which is more positive than that at which a marked increase in anodic current occurs (Figure R 4a). Thus on immersion of the specimen at this potential, a breakdown of the surface film is expected to occur. Application of compressive stress of 200 MPa shows an increase of the anodic current. Application of the tensile stress of the same magnitude after unloading the specimen causes a rapid increase of the current. The control potential in this test was  $-660$  mV (SCE). Since the specimens of the same dimensions were used, the relative increase of current density will also be similar. The actual area when the specimen is under stress is somewhat different than the one calculated prior to the application of stress. Hence current vs time has been plotted.

On application of cyclic stress of 198 MPa,  $R = -1$ , 0.2 Hz, the anodic current increases significantly (Figure R 8f). The applied potential of  $-560$  mV (SCE) is more positive than  $E_p$ , the protection potential, and the zero current potential (Table I). It is, however, more negative than the potential at which a marked increase in anodic current occurs. Enhancement of corrosion current is found to occur with the increase of stress (Figure R 8g).

Secondly, applications of cyclic stress indicate the presence of a region during which mean corrosion current initially moves in the cathodic direction. There is also a transition zone prior to the movement of the mean current in the anodic direction (Figure R 8c). This movement in the cathodic direction is reflected in Figures R 8f and R 8g.

Measurement of potential without stress show that the final potential is approximately  $-680$  mV (SCE) after nearly 300 hours (Figure R 8d). On application of cyclic stress of 198 MPa,  $R = -1$ , at 0.2 Hz, the decrease of potential was found to be somewhat slower initially than that without cyclic stress. The potential at around 240 hours is approximately  $-680$  mV (SCE) which is more negative than the zero current and protection potentials (Figures R 3 and R 8e). The potential decay, however, is more rapid when the stress is increased to 247 MPa (Figure R 8h).

#### 5.7 Reverse bend fatigue test - 24 Hz

Results of potential measurements of polished specimens at 24 Hz,  $R = -1$ , show that at 170 MPa (Figure R 9a) potential decay is slower than that at 277 MPa (Figure R 9e). Significant potential fluctuations are observed at higher stress and examination of the specimen surface after 90 minutes, i.e. approximately  $1.28 \times 10^5$  reversals, indicate the presence of cracks on the surface of the specimen (Figure R 9f). The cracks appear to initiate from inclusions and follow the grain boundaries to the neighbouring inclusion sites.

A second series of tests were interrupted at various intervals. The specimens were sectioned normal to the longitudinal surface, near those surface cracks observed in Figure R 9f, and then ground and polished in stages. Examination of the surface of a specimen after  $6.25 \times 10^5$  reversals reveals initiation of a crack from the bottom of a pit (Figure R 9g).

Figure R 9h shows the presence of a crack emanating from the pit after  $8.36 \times 10^5$  reversals. Examination of fracture surfaces of specimens tested at 170 MPa also shows existence of pits from which cracks tend to initiate (Figure R 9b).

Examination of the reverse sides of the specimens exposed to the ambient environment at 277 MPa did not show any surface cracks at  $6.25 \times 10^5$  reversals.

The transverse surface of a specimen tested at 277 MPa at approximately  $8 \times 10^5$  reversals exhibits formation and growth of a pit from the side exposed to the corrosive environment (Figure D 4a) while Figure D 4b shows the transverse surface sectioned normal to the side exposed to the ambient.

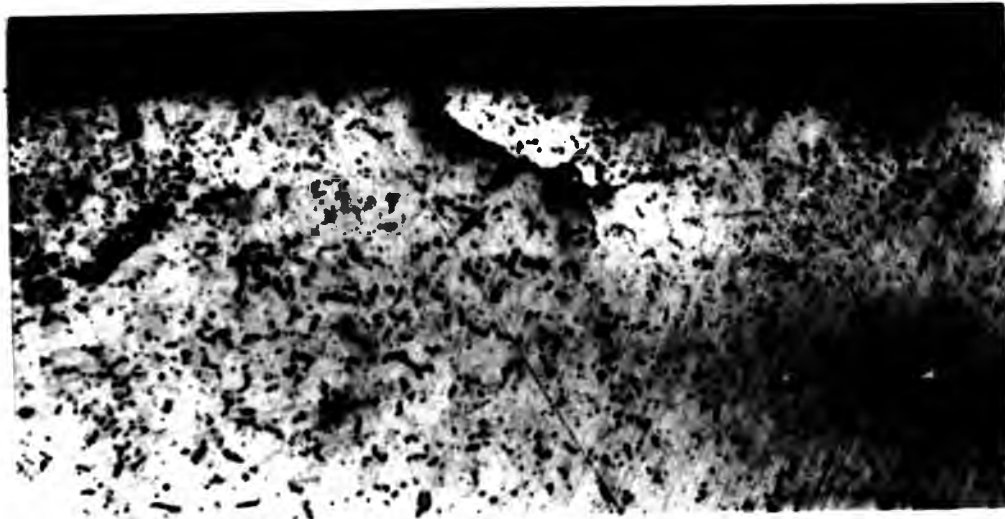
Potential measurements of the mill scaled specimens show that the initial potential fluctuation occurs after approximately 110 minutes, i.e. at around  $1.56 \times 10^5$  reversals (Figure R 9j). The test was discontinued when cracks were observed on the surface of the specimen. The surface of the specimen examined using scanning electron microscopy indicates mill scale dissolution at some places and appearance of cracks on the bare metal (Figure R 9k).

Potential fluctuation was also noted at around  $4.25 \times 10^5$  reversals, i.e. at approximately 300 minutes. A test was discontinued at this stage and the specimen surface was also examined using scanning electron microscopy. Figure R 9l shows the mill scaled surface at  $4.25 \times 10^5$  reversals indicating dissolution of mill scale at some places and the joining of crevices created at surface defects on the exposed metal surface.

Comparison of the two curves (Figures R 9a and R 9j) show that:



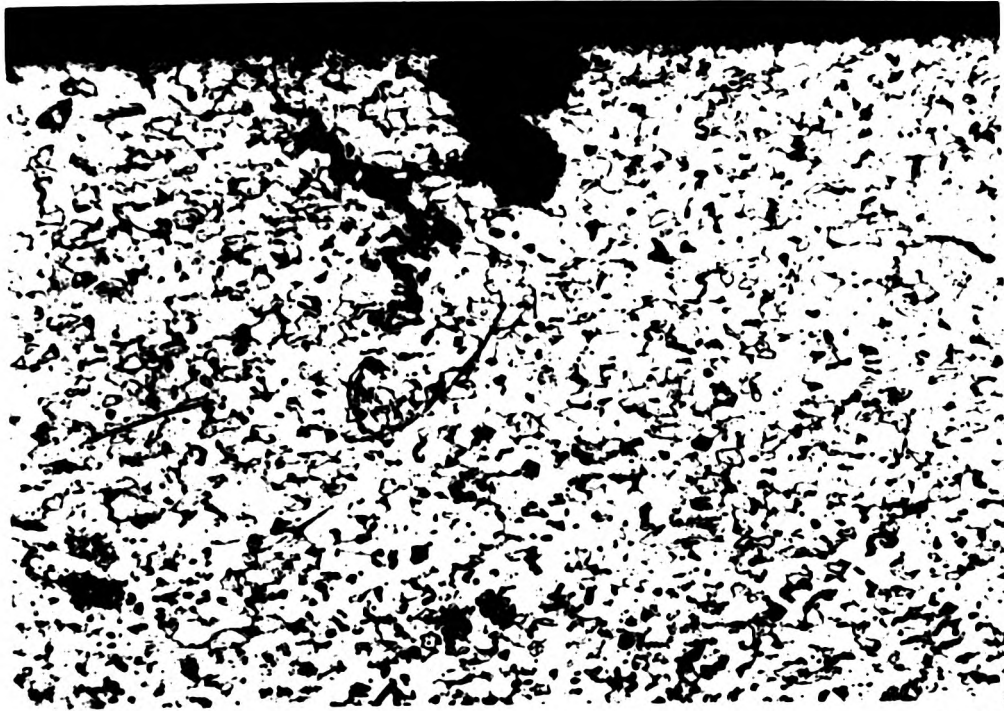
(a)



(b)

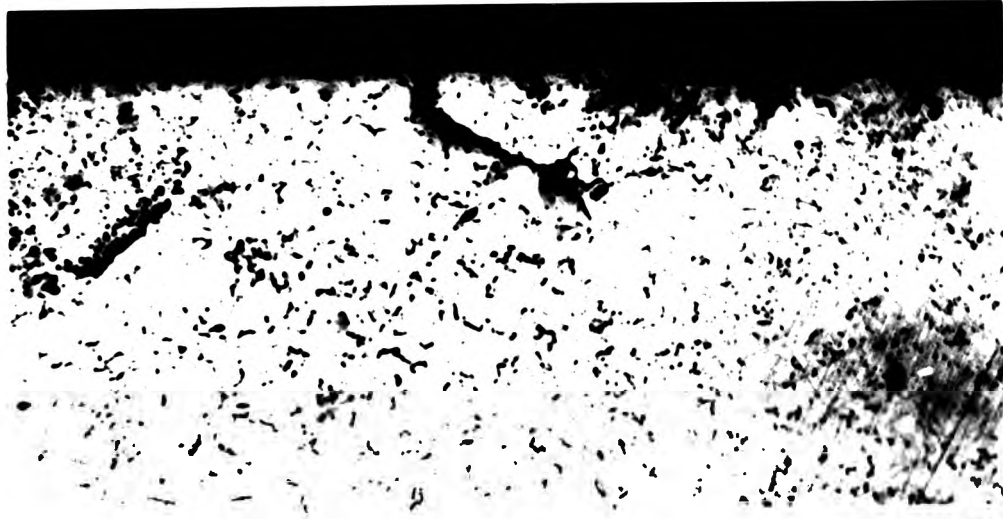
- (a) Transverse surface sectioned normal to the side exposed to the corrosive environment exhibiting growth of a pit,  
(b) transverse surface sectioned normal to the side exposed to ambient showing a crack.

Fig D 4: Micrographs of reverse bend fatigue tested specimen at 277 MPa,  $R=-1$ , 24 Hz, after  $8 \times 10^5$  reversals.



(a)

x75

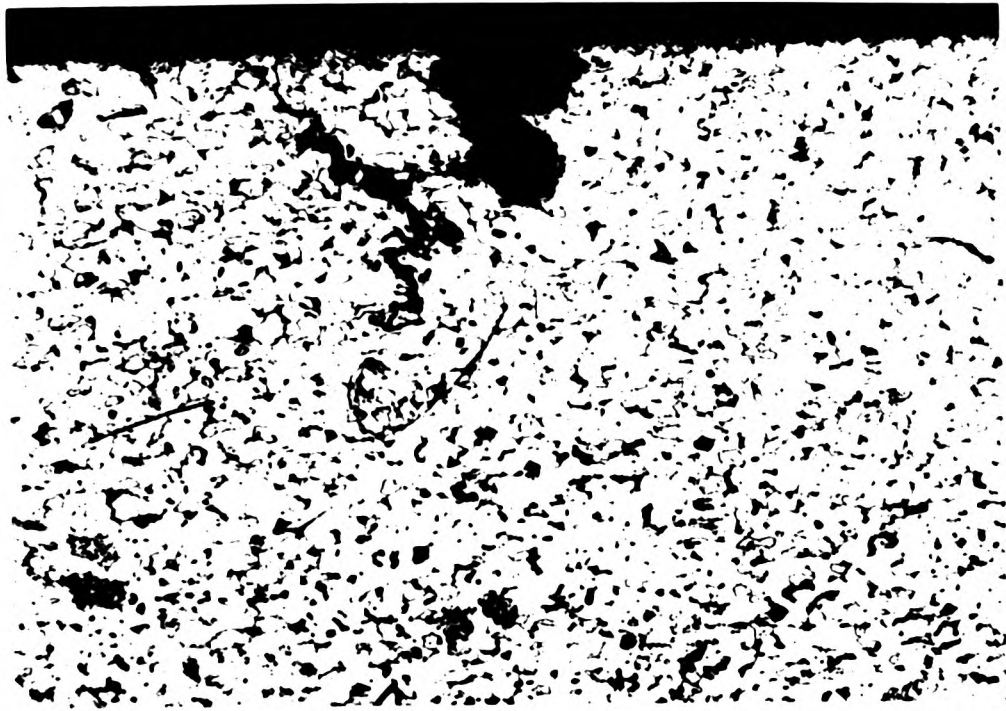


(b)

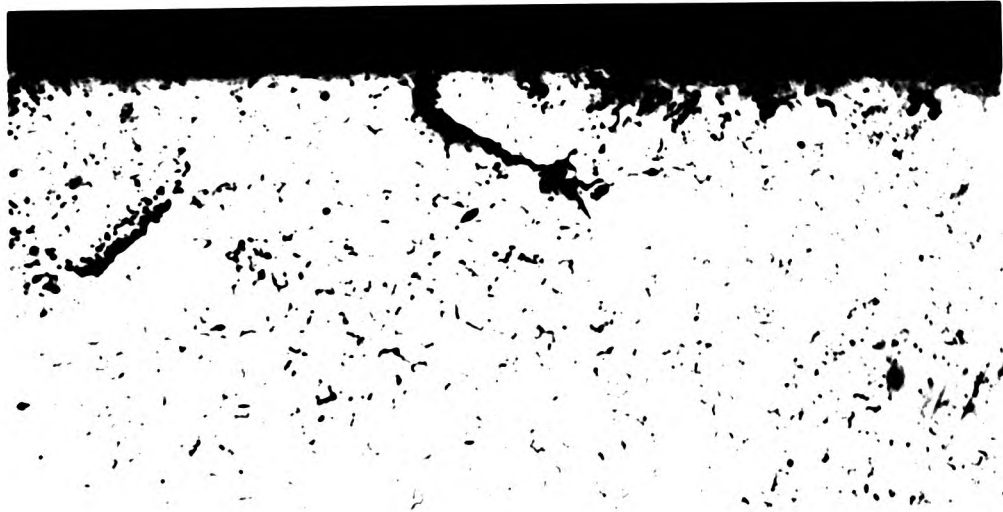
x100

- (a) Transverse surface sectioned normal to the side exposed to the corrosive environment exhibiting growth of a pit,  
(b) transverse surface sectioned normal to the side exposed to ambient showing a crack.

Fig. 4: Micrographs of reverse bend fatigue tested specimen at 277 MPa, R=-1, 24 Hz, after  $8 \times 10^5$  reversals.



x75



x100

(a) Transverse surface sectioned normal to the side extension to the corrosive environment exhibiting growth of scale, (b) transverse surface sectioned normal to the side extension to the solvent showing a crack.

(c) Micrograph of reverse bend failure of the material after 1000 hours, (d) Micrograph of reverse bend failure of the material after 1000 hours.

a) Potential of the mill scaled specimen immediately after immersion is more positive (-440 mV (SCE)) than that of the 1  $\mu\text{m}$  polished specimen (-650 mV (SCE)).

b) First potential peak or first significant potential fluctuation is observed at approximately  $7.1 \times 10^4$  reversals for polished specimen while the peak for mill scaled specimen appears at around  $1.56 \times 10^5$  reversals. Examination of the mill scaled specimen surface reveal that this potential fluctuation is associated with the change in surface morphology, e.g. dissolution of mill scale with the appearance of bare metal surface (Figure R 9l). Hence it is possible that for polished specimens, potential fluctuations are also associated with some change in surface morphology. Prior to the larger potential peaks, smaller peaks were also observed, but it was not possible to detect surface changes on the polished specimens at those peaks.

Similar changes in surface morphology have also been observed during tests at 277 MPa (Figures R 9e and R 9f).

Typical corrosion current vs time curves for polished and mill scaled specimens are shown in Figures R 9c and R 9m respectively. Anodic current appears to increase more rapidly for polished specimen than for the mill scaled specimen. Examination of the specimen surface on discontinuation of the test shows the presence of pits and dissolution of ferrites in pearlitic areas of the polished specimen (Figure R 9d). According to Staicopolus<sup>139</sup>, in 0.5 M sodium chloride solution, cementite acts as active cathodic sites since it does not polarise at low current densities. It appears that in Figure R 9d, ferrite is more active anodically than the carbide lamellae.

With a mill scaled specimen, the anodic current initially increases rather slowly. Rapid rise in current occurs around  $3.41 \times 10^5$  reversals, i.e. at around 240 minutes.

Examination of the specimen reveals breakdown of the scale at some sites and the presence of pits and cracks on the exposed surface. Comparison of the surfaces of the polished and mill scaled specimens (Figures R 9d and R 9n) show that although the polished specimen contained relatively numerous pits, the mill scaled specimen suffered more severe attack at the few exposed sites.

#### 5.8 Immersion tests

Results of immersion tests (Figure R 10) show the role of inclusions in the absence of stress. It was observed that the presence of Fe in the inclusion is associated with a corresponding reduction in the Mn content (Figure R 10a). S was present as shown in Figures R 10b - R 10d but Si was not detected.

Figures R 10e and R 10f show the results from specimens immersed in 0.6 M sodium chloride solution after 20 and 17 hours respectively. Immersion for upto 20 hours gives rise to the formation of surface islands or discoloured areas indicative of inhomogeneous corrosion (Figure R 10e). Such regions are normally associated with a high inclusion density. Specimens that had been annealed at 920° C for 3 hours in an argon atmosphere prior to immersion showed the formation and coalescence of micropits at the inclusion - matrix interface (Figure R 10f (i)). S was detected at those regions of the interface where dissolution has so far taken place (Figure R 10f (ii)). X-ray analysis does not show any S to be present in the matrix some few microns away from the inclusion (Figure R 10f (iii)). The analysis of the actual inclusions associated with this phenomenon of interface dissolution is shown in Figure R 10f (iv) and demonstrates the presence of Fe, Mn, and S.

According to Wranglen<sup>113, 115</sup>, active sulphide inclusions are surrounded by a matrix contaminated by sulphur and containing a fine dispersion of submicroscopically divided MnS precipitate. Gainer and Wallwork<sup>196</sup> have suggested that Wranglen offered no proof for the existence of such a sulphur contaminated matrix around active sulphide inclusions. Eklund<sup>183</sup> has also proposed that a submicroscopically divided MnS precipitate exists but is distributed uniformly throughout the matrix and not around certain active inclusions.

In the present tests it was observed that a S enriched band of ferrite exists around the inclusions but S does not appear to be distributed uniformly throughout the matrix as suggested by Eklund<sup>183</sup>. Corrosion occurs in the contaminated band (Figure R 10f (1)). Initiation of attack is found to occur at the matrix - inclusion interface shortly after immersion and the dissolution progresses with increasing period of immersion. In the previous tests (Figure R 8d), the potential of the specimen surface was found to be approximately -500 mV (SCE) immediately after immersion and about -650 mV (SCE) after nearly 20 hours of immersion. The initial potential is above while the final potential is below the "breakdown" potential observed in the polarisation study (Figure R 1b). Consequently as the potential of the specimen decays after immersion, growth of the existing micropits occur.

## 5.9 Metallurgical examinations: Rotating bend fatigue tests - 47 Hz

### 5.9.1 Scanning electron microscopic examination

Results of tests on specimens rotated without stress at 47 Hz with electrolyte being drip-fed show the formation of surface islands or discoloured areas associated with high inclusion density regions. The surface resembles that observed in immersion tests (Figure R 10e) suggesting that there is little, if any, difference due to the method of application of the electrolyte used in these tests.

On the application of cyclic stress, crystallographic etch pits (Figure R 11d) are found to occur indicating the formation of anodic sites by the emergent dislocations intersecting the surface. While the etch pits appear to be rectangular, some of the micropits seem to be round or hemispherical (Figure R 11d). On closer examination cavities were found at the base of these pits indicating the occurrence of reactions at the bottom of these micropits. The commencement of the dissolution of the elongated inclusions leading to possible spalling is also indicated in Figure R 11d.

Comparison of the Figures R 10f (i) and R 11d tend to indicate the rapid nature of the dissolution of the inclusions under cyclic stress. Fracture of some of the inclusions also appears to occur. No incipient cracks were found to emanate from either the crystallographic or from the round pits in and around the inclusions at these reversals.

Dissolution of ferrite in pearlitic areas has been found to occur at around 6,100 reversals at 193 MPa,  $R = -1$  (Figure R 11e).

The lamellar structure was found to contain terminations and bends. It was, however, not possible to detect whether these changes occurred during the fatigue tests.

Porter et al <sup>198</sup>, in their investigations on the behaviour of eutectoid steels under tensile stress, have observed the presence of imperfections such as lamellar terminations and twists, bends, ripples and changes in thickness of the cementite lamellae. According to these researchers, the lamellar structure can degenerate into ribbons of cementite, ~~performed~~ <sup>performed</sup> lamellae, or even isolated fragments and in a deformed specimen these features will be extremely difficult to separate from any changes caused by deformations.

Their study reveals that in coarse pearlites, slip steps form at the cementite - ferrite interface indicating that fracture of the cementite is preceded by local plastic flow. As the strain increases, voids form between the fractured ends and link up through the ferrite matrix. The fine pearlite, however, deforms by more homogeneous slip in both phases, and cementite is able to neck down in a ductile manner leading to extensive fragmentation at higher strains, but with little void formation. Microvoids eventually form and link up, but only close to the final fracture path. They conclude that the higher yield stress of the fine pearlite is able to operate many more dislocation sources in the ferrite - cementite interfaces resulting in finer slip in the ferrite than in the coarse pearlite.

Taylor et al <sup>61</sup> found a build up of dislocations in the ferrite in pearlitic steels during cycling. These researchers observed that slip bands and ferrite - cementite interfaces were among the major initiation sites.

Thus the microvoids created due to the deformation and fracture of the cementite and dissolution of the ferrite create capillary paths which tend to be the sites for entrapment of corrosive liquid <sup>143</sup>. Linking up of these microvoids to form macrovoids appears to be the precursor of incipient crack formation in pearlitic regions.

Under stress free conditions, dissolution at the matrix - inclusion interface is not as rapid as that under an applied cyclic stress. It has also been found that localised attack on the matrix immediately adjacent to the interface, creating microvoids, appears to depend on the number of reversals, indicating time dependence of the dissolution process of the matrix close to the inclusion. Figures R 11f and R 11q show the micrographs of the specimens subjected to 193 and 278 MPa respectively for  $3.39 \times 10^4$  reversals.

Slight longitudinal fissuring is sometimes found to be associated with these regions of localised corrosion. The increase of stress from 193 to 278 MPa does not appear to reduce the number of cycles to cause dissolution of the matrix immediately adjacent to the inclusions. Figures R 11h and R 11k also exhibit the dissolution of the same regions of matrices after  $1.06 \times 10^5$  and  $3.62 \times 10^5$  reversals respectively at 193 MPa. That these regions contain Mn and S has been shown in Figure R 11k. Further increase of stress tends to produce an increasing number of etch pits indicating an association between emergent dislocations and inhomogeneous rate of dissolution, active sites being formed at the point of intersection of the dislocation at the surface resulting in localised corrosion. It also appears that at lower stresses, such as around 193 MPa, and smaller number of reversals, dissolution of a few of the elongated inclusions does not occur quite as rapidly as that of the majority of the inclusions and the attack seems to be essentially localised dissolutions at the interfaces, gradually isolating these particles from the matrix (Figure R 11f). With increasing number of reversals these inclusions tend to deform and ultimately fracture. Analysis results do not appear to provide any reason for this variable behaviour.

Wood and Van Vlack<sup>199</sup> have observed that plastic deformation of inclusions occur at ambient temperature. Previously hot rolled B1113 steel containing sulphide inclusions was sectioned into cubes and deformed in 2% compression at room temperature. The deformation and fracture behaviour was observed on a median surface and on two externally polished surfaces. Their results showed that the plastic deformation of MnS was more common and fracture was less common within the metal than at the metal surface.

Dislocation markings within an internal sulphide particle were also observed during the 2% compression. The dislocation patterns were always aligned at approximately 45 degrees to the direction of the applied compressive load. MnS deformation followed the  $[110]$  (110) glide system, and the dislocations were seldom revealed by etching on planes other than the (110) planes. These researchers concluded that those inclusions which revealed dislocations were oriented with their MnS crystal axes essentially parallel to the cube edges of the sample. Similar deformation was also revealed for favourably oriented inclusions at the external surface of the sample. They also observed the redirection of the slip planes in the ferrite to coincide with the slip planes in the MnS inclusion on the external surface indicating the greater ability for dislocations to cross-glide in metals than in ionic solids. Inclusion fracture at the external surface almost always occurred along planes parallel to that of the stress application and at right angles to the external surface.

Hence it is possible that at low stresses in the early stages of the fatigue tests, some of the inclusions plastically deform because they are favourably oriented (Figure D 5). For others, dissolution, undermining and spalling appear to occur due to unfavourable orientation creating microcavities at the surface (Figures R 11g - R 11q). Initially, however, all the inclusions tend to dissolve to varying extents.

Analysis results show the presence of traces of Cr in addition to S, Mn, and Fe at most of the matrix - inclusion interfaces (Figures R 10f (ii) and R 11k, Energy level 5.4). This element was not detected at the inclusion itself (Figure R 10f (iv) and D 5). According to BS 970, Part-1, 1972, residual elements such as Cr in EN type steel are considered incidental.

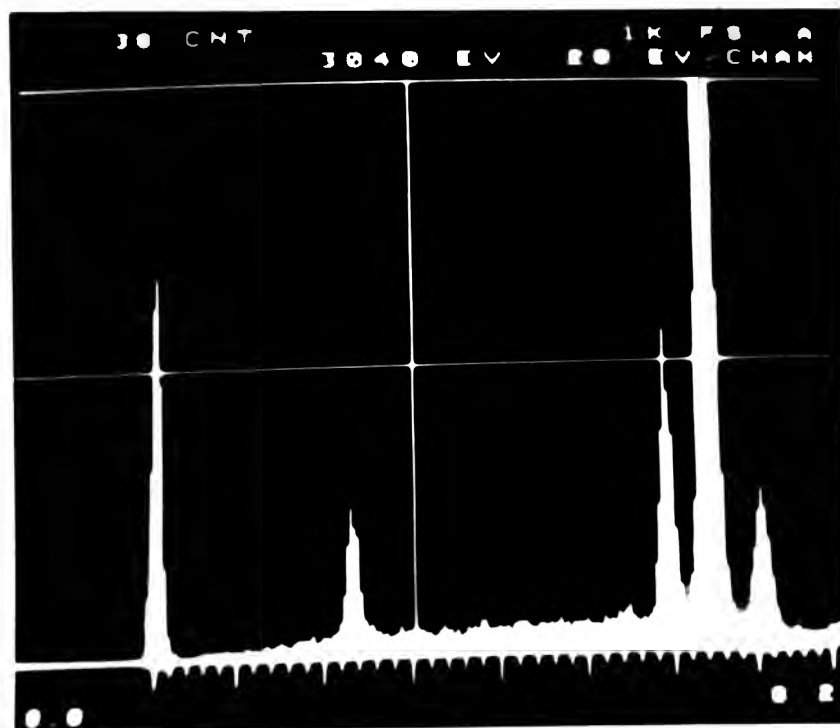
Dislocation markings within an internal sulphide particle were also observed during the 2% compression. The dislocation patterns were always aligned at approximately 45 degrees to the direction of the applied compressive load. MnS deformation followed the  $[110]$  (110) glide system, and the dislocations were seldom revealed by etching on planes other than the (110) planes. These researchers concluded that those inclusions which revealed dislocations were oriented with their MnS crystal axes essentially parallel to the cube edges of the sample. Similar deformation was also revealed for favourably oriented inclusions at the external surface of the sample. They also observed the redirection of the slip planes in the ferrite to coincide with the slip planes in the MnS inclusion on the external surface indicating the greater ability for dislocations to cross-glide in metals than in ionic solids. Inclusion fracture at the external surface almost always occurred along planes parallel to that of the stress application and at right angles to the external surface.

Hence it is possible that at low stresses in the early stages of the fatigue tests, some of the inclusions plastically deform because they are favourably oriented (Figure D 5). For others, dissolution, undermining and spalling appear to occur due to unfavourable orientation creating microcavities at the surface (Figures R 11g - R 11q). Initially, however, all the inclusions tend to dissolve to varying extents.

Analysis results show the presence of traces of Cr in addition to S, Mn, and Fe at most of the matrix - inclusion interfaces (Figures R 10f (ii) and R 11k, Energy level 5.4). This element was not detected at the inclusion itself (Figure R 10f (iv) and D 5). According to BS 970, Part-1, 1972, residual elements such as Cr in EN type steel are considered incidental.



(i)



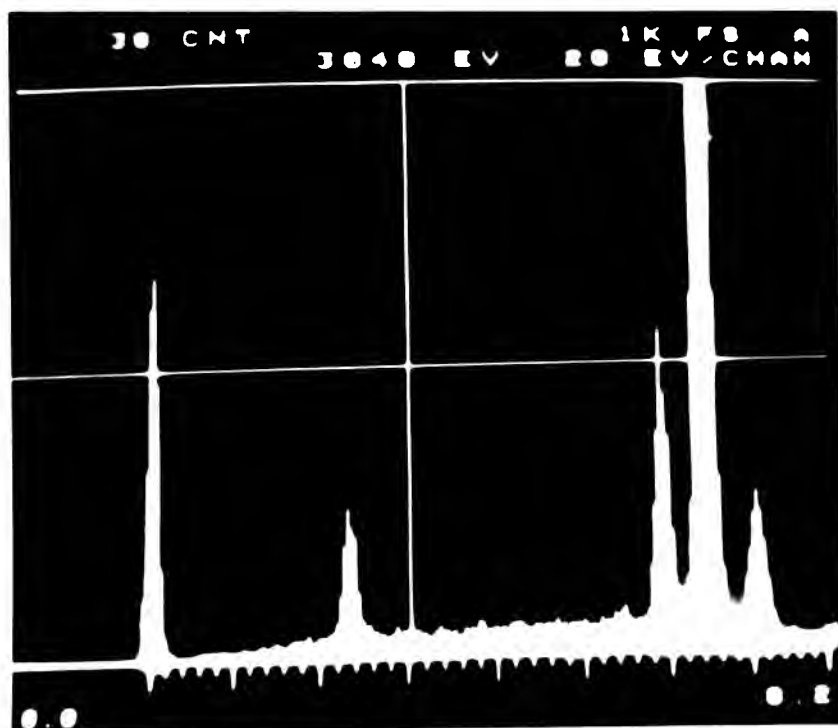
(ii)

(i) Dissolution of matrix-inclusion interface after  $3.62 \times 10^5$  reversals at 193 MPa,  $R=-1$ , 47 Hz. Analysis results (ii) of the inclusion (arrowed) exhibits the presence of S (at 2.3), Mn (at 5.9) and Fe (at 6.4) only. Energy level vs intensity curve.

Fig D 5: Scanning electron micrograph of rotating bend fatigue tested specimen.



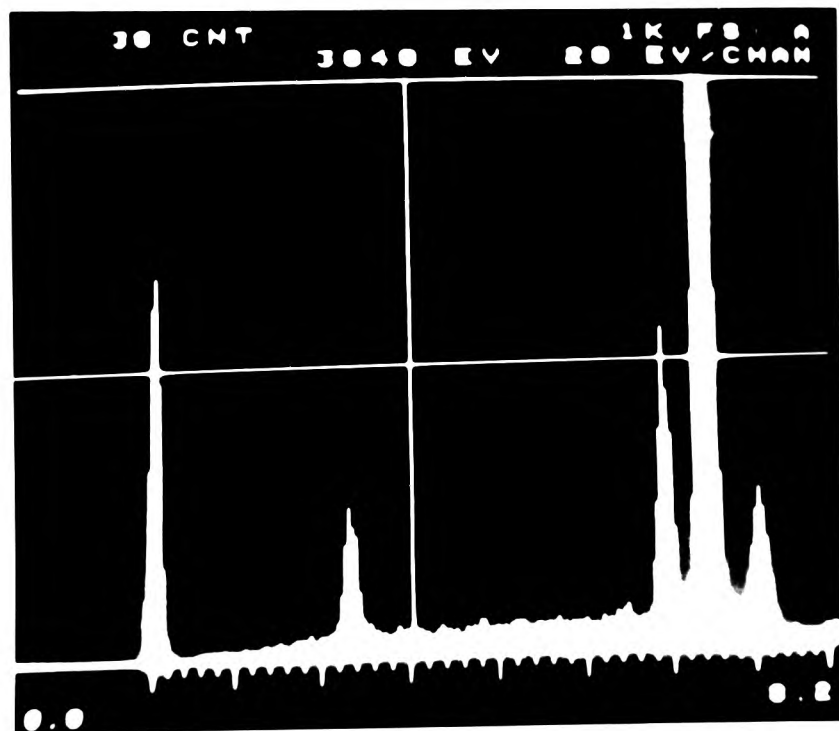
(i)



(ii)

(i) Dissolution of matrix-inclusion interface after  $3.6 \times 10^5$  reversals at 193 MPa, R=-1, 47 Hz. Analysis results (ii) of the inclusion (arrowed) exhibits the presence of S (at 2.3), Mn (at 5.9) and Fe (at 9.4) only. Energy level vs intensity curve.

Fig. 5: Scanning electron micrograph of rotating bend fatigue tested specimen.



(1) Evolution of matrix-inclusion interface after 1. x  
 10<sup>20</sup> reversals at 200°C, -1, 40 sec. Analysis results  
 (1) of the inclusion (arrow) exhibit the presence of  
 Fe (at 5.7), Mn (at 5.9) and Cu (at 8.9) only. See related  
 intensity curves.

(2) Scanning electron micrograph of particle of Fe<sub>2</sub>O<sub>3</sub> and  
 Mn<sub>2</sub>O<sub>3</sub> in matrix.

It has also been observed that impurity elements tend to segregate around defects, such as voids or cracks in a metal <sup>200</sup>. Figure D 6 shows the extent of P segregation around a defect in a nickel plated SAE 4130 steel. The matrix surrounding the defect appears to have very little P content. However, in this present investigation the presence or absence of Cr does not seem to affect the dissolution behaviour at the interfaces.

It has not been possible to establish whether any particular type of inclusions, such as (Mn, Fe) S<sub>x</sub> as suggested by Janik Czachor <sup>110</sup>, is the source of pit nucleation. In the immersion test (Figure R 10f (iv)), it was observed that the inclusions showing localised attack at the matrix - inclusion interface contain high Mn and S and smaller Fe peaks. Figure D 5, on the other hand, shows a smaller Mn peak in relation to that of Fe. A similar number of counts were taken for both these analysis. Although the analysis results are only qualitative ones, the intensities at the same number of counts may provide some indications of the quantitative nature of the elements present. Since both the inclusions (Figures D 5 and R 10f) tend to dissolve to a certain extent, it is possible that the variation in Mn or Fe content of the inclusions may not be a significant factor affecting the dissolution behaviour of the inclusions.

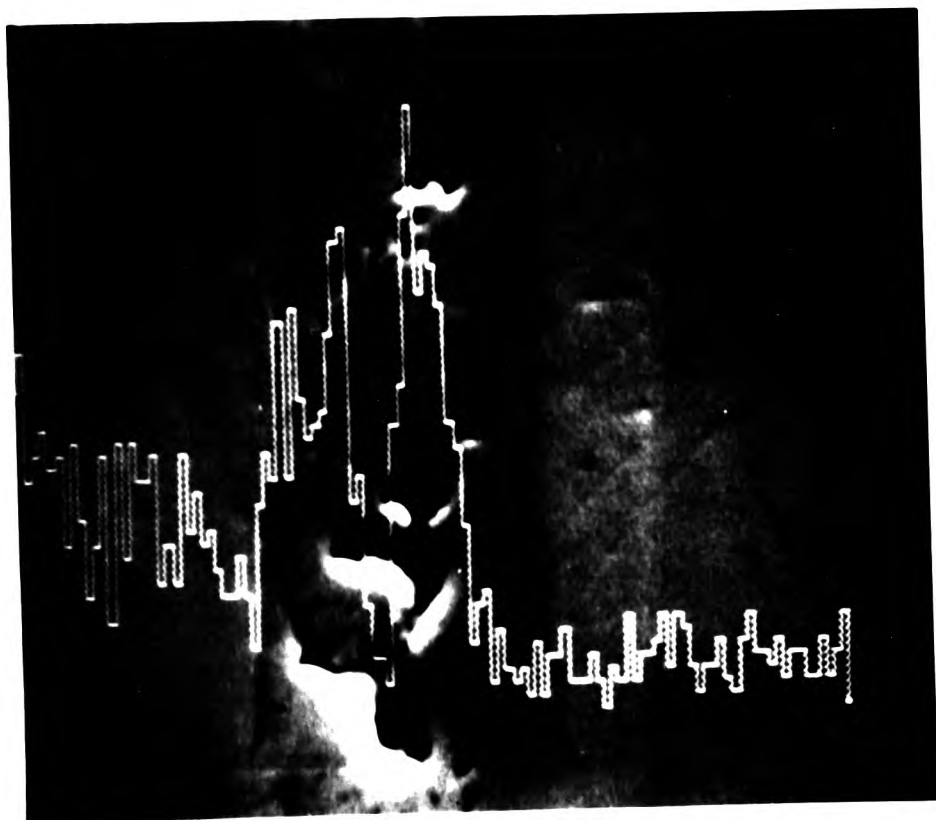
It is also possible that the presence of the Fe peak in the analysis results is due to the "tear drop" effect of the electron beam. Hence it may be postulated that the analysis results are influenced by the presence of the matrix surrounding the inclusions and hence the inclusions may contain only Mn and S. However, it appears unlikely since the presence of Cr which has been detected at the interfaces should also have been observed during the analysis of the inclusions themselves. This has not been found to occur.



Fig D 6: Scanning electron micrograph of an electroless nickel plated SAE 4130 steel exhibiting subsurface defects. Analysis results show concentration of P across the voids and in the bulk material. Left of the arrow is nickel deposit. x 1500.



Fig. D 6: Scanning electron micrograph of an electroless nickel plated SAE 4130 steel exhibiting subsurface defects. Analysis results show concentration of  $\mu$  across the voids and in the bulk material. Left of the arrow is nickel deposit. x 1500.



of certain selection process in a particular region  
labeled as "void" and exhibits a concentration of  
voids and in the full extent of left side, arranged  
right side, etc.

In some fatigue tested specimens, some of the inclusions were found to contain Si in addition to Mn and S, Figure D 7 shows the inclusions in a relatively low inclusion density region and the analysis results of the inclusions. Dissolution of the sulphide particles and at the interfaces appear to occur. Hence it may be considered that under the application of cyclic stress, all the inclusions containing S and Mn tend to dissolve and that the compositional differences do not have any significant influence on the dissolution process.

It has been suggested that the shape of the inclusions plays a significant role in pit nucleation <sup>119</sup>. For a given type of inclusions, spheroidised particles are less susceptible to corrosion than elongated and plastically deformed ones. For short immersion tests it may possibly be true. However, for longer periods of immersion (Figures R 10e and D 8), and under cyclic stress condition, the effect of the shape of the inclusions, especially in the high density regions, has not been observed.

On the basis of calculations using thermal expansion data, Brooksbank and Andrews <sup>201</sup> have suggested that crevices may exist around sulphide inclusions. Adrian et al <sup>130</sup> also have proposed that crevices form at the matrix - inclusion phase boundary upon cooling from the melting temperature due to the different coefficients of expansion. Examinations of the as-received material, however, do not indicate the presence of any voids at the matrix - inclusion interface.

In the high density regions, incipient attack appears to occur underneath the metal surface, close to the inclusions creating microcavities, (Figures R 11r, D 9 and D 10). Figure D 9 shows a schematic diagram of the dissolution underneath the metal surface.



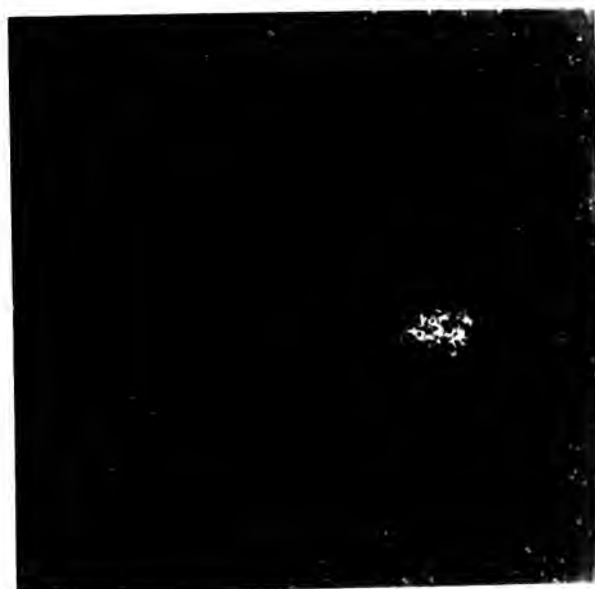
(i)



(ii)



(iii)



(iv)

Fig D 7: Electron microprobe analysis results showing (i) the cross section of the specimen, and the presence of (ii) Mn, (iii) S and (iv) Si. Rotating bend fatigue tested specimen at 309 MPa,  $R=-1$ ,  $4.17 \times 10^5$  reversals.

x 600

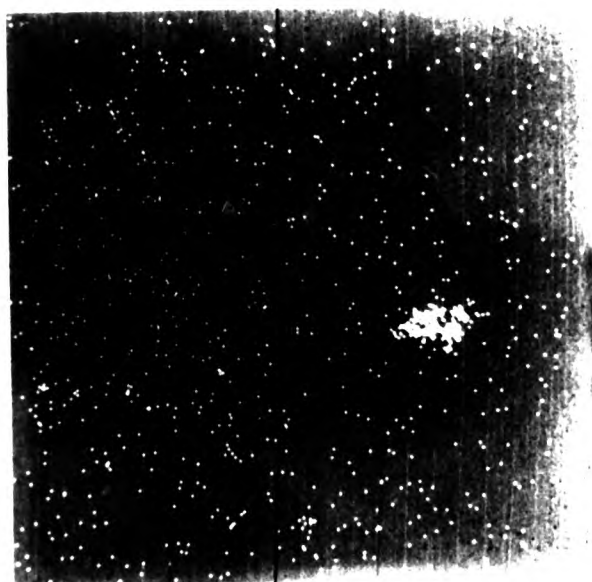
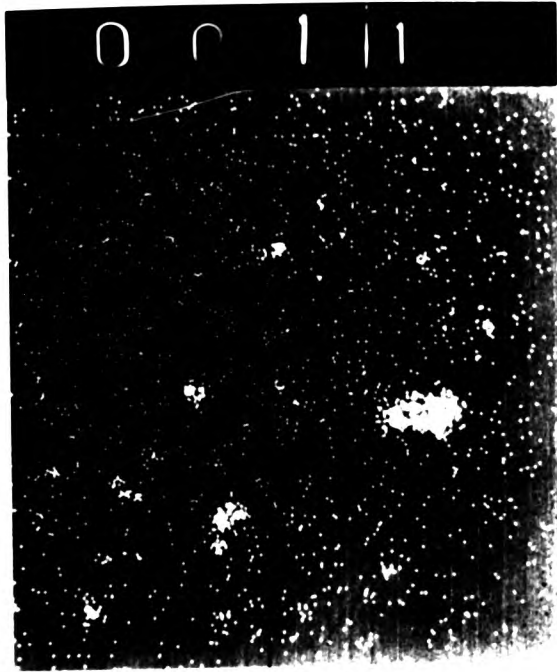
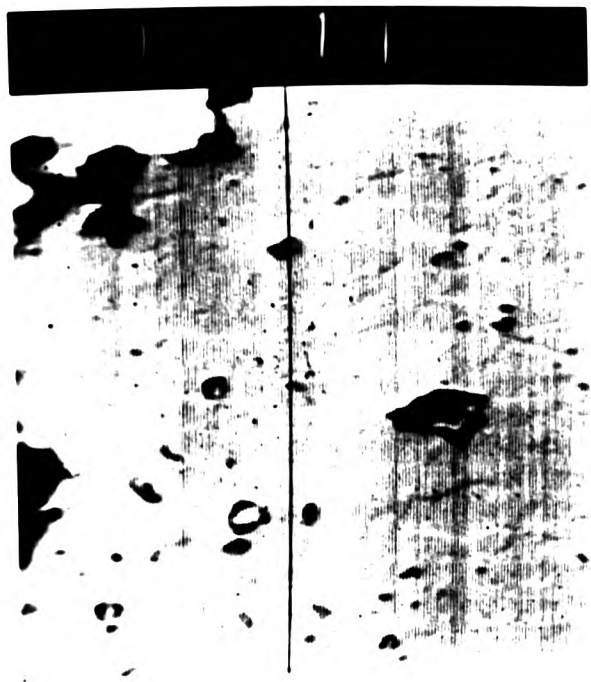


Fig. 1. Electron microprobe analysis results showing (a) the cross section of the specimen, and the presence of (b) Mn, (c) Si, and (d) Al. The specimens were tested at 4 kV, 10<sup>-7</sup> A, 10<sup>-8</sup> Torr, and 10<sup>-8</sup> Torr.

0 0 1 0



0 0 1 1



0 0 1 2

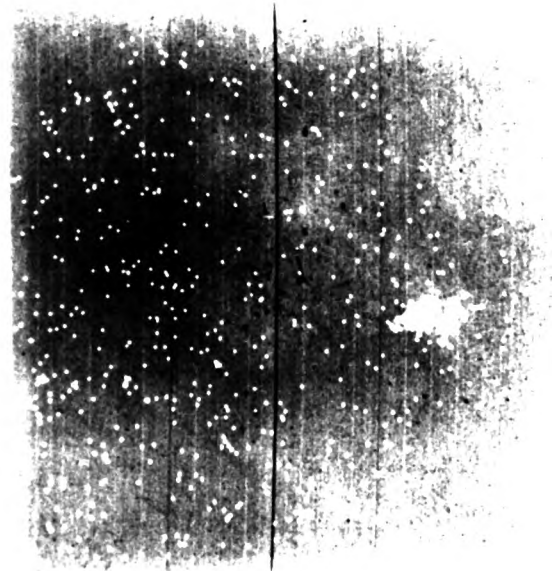
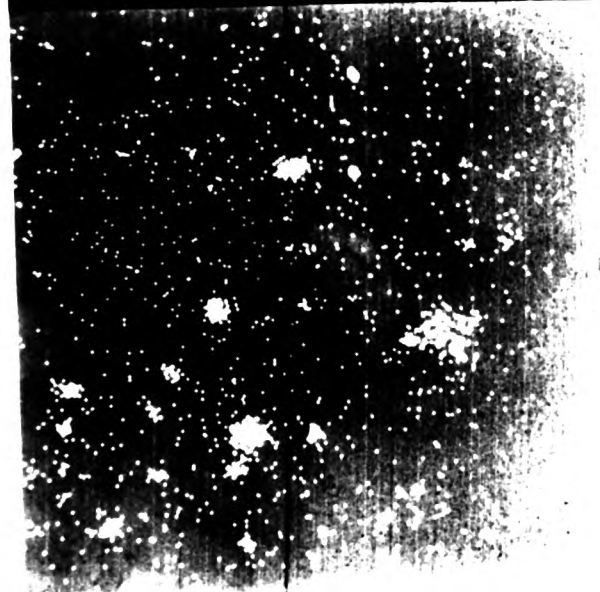




Fig D 8: Scanning electron micrograph showing dissolution of elongated and spheroidised shaped inclusions. Immersion test results after nearly 20 hours without stress.



Fig D 9: Schematic diagram of continued dissolution of sulphide inclusion and incipient attack on the metal close to the inclusion.



Fig. 8: Scanning electron micrograph showing dissolution of elongated and spheroidised shaped inclusions. Immersion test results after nearly 1 hours without stress.

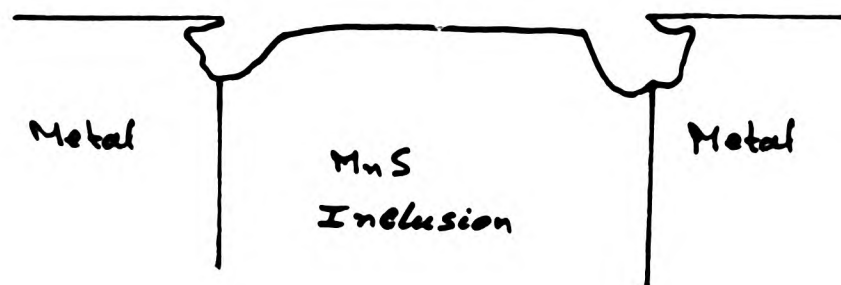


Fig. D.9: Schematic diagram of continued dissolution of sulphide inclusion and incipient attack on the metal close to the inclusion.



Micrograph showing MnS inclusions in metal matrix.



Schematic diagram of MnS inclusion in metal matrix.





Fig D 10: Scanning electron micrograph showing incipient attack on the metal creating a thin cover of intact metal on the surface. Wrought specimen after  $5.1 \times 10^4$  reversals at 278 MPa, R=-1.



Fig D 10: Scanning electron micrograph showing incipient attack on the metal creating a thin cover of intact metal on the surface. Wrought specimen after  $5.1 \times 10^4$  reversals at 278 MPa, R=-1.

In a high inclusion density region, dissolution at the interface and that of the inclusion may expose a new volume of inclusions, grain boundaries and pearlitic areas and attack around these sites may in turn expose a further volume of susceptible regions, resulting in the formation of cavities. The extension of these cavities sometimes may occur laterally, as shown in Figure D 9, as well as towards the centre of the specimen (Figures R 11k (i), R 11n, R 11r, and R 11w (ii)). These microcavities are also observed in the pits created by the dissolution and undermining of the sulphide particles (Figure R 11q). As the number of reversals are increased, coalescence of these microcavities occur resulting in the formation of macropits. It is also possible that the surface deformation assists the collapse of the covering metal on the specimen surface resulting in the appearance of the more conventional macropits. In the case of inclusions close to each other, the lateral retreat of metal due to the dissolution underneath the surface and the collapse of the cavity roof appears to breach the ligaments causing incipient crack formation in the transverse direction (Figure R 11m). In the high inclusion density region linking up of these incipient cracks to form microcracks occur by a cyclic sequence of inclusion "tunnel" formation by dissolution and ductile instability of ligaments under the applied load (Figure R 11w).

If the sulphide inclusions are further apart, then incipient cracks also tend to form but the lateral extension of the microcavities is not sufficient to breach the ligaments (Figure D 11). This incipient crack formation also occurs at etch pits (Figure D 12), in pearlitic areas (Figure R 11e) and at grain boundaries (Figure R 11u).



Fig D 11: Scanning electron micrograph of a wrought specimen after 2000 reversals at 278 MPa, R=-1, showing incipient crack formation from an inclusion.

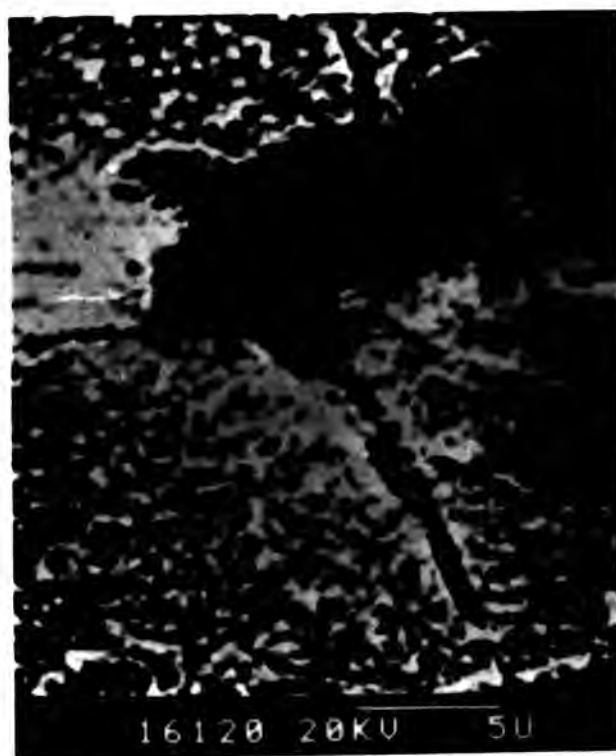


Fig D 12: Scanning electron micrograph of a wrought specimen after 2000 reversals at 198 MPa, R=-1, showing incipient crack formation from an etch pit in transverse direction.



Fig D 11: Scanning electron micrograph of a wrought specimen after 2000 reversals at 278 MPa, R-1, showing incipient crack formation from an inclusion.



Fig D 12: Scanning electron micrograph of a wrought specimen after 2000 reversals at 198 MPa, R-1, showing incipient crack formation from an etch pit in transverse direction.

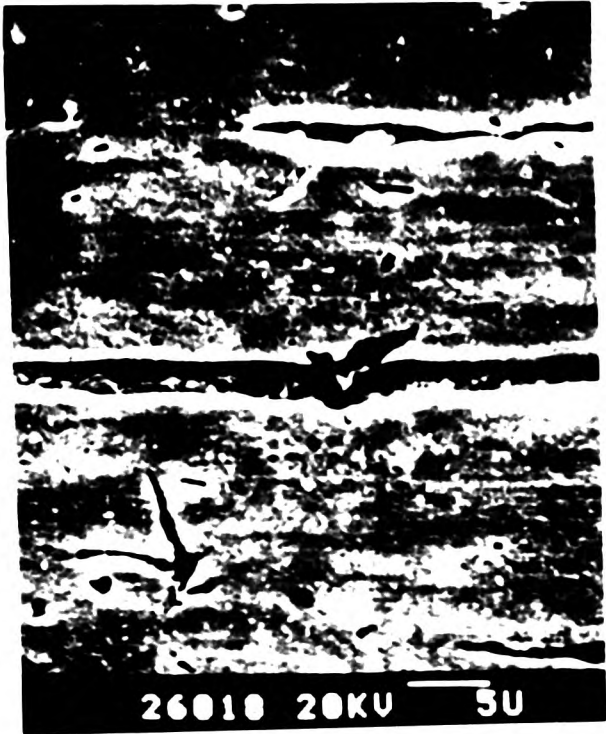


Fig. 10: Inclusion of graphite in the matrix of the graphite electrode after 1000 hours of operation at 2000°C, showing inclusion of graphite in the matrix.



The pH at the mouth of the crevices or micropits on the external surface of the specimen which was rotated without stress for  $1.31 \times 10^6$  reversals was found to be approximately 4.5 whilst that for specimens at 193 MPa,  $R = -1$ , after  $3.39 \times 10^4$  reversals was nearly 3 - 3.5. In a separate series of tests the potentials were measured after approximately the same number of reversals at which the pH values were measured. These were -630 mV (SCE) at zero stress and -550 mV (SCE) at 193 MPa.

Sandoz et al<sup>202</sup> used the freezing technique and subsequently analysed the solution in a stress corrosion crack for pH and concentration of metallic ions. Various steels including 13Cr/8Ni/Mo and 4340 steels were used. The pH values recorded were all of the order of 3.6 to 3.8 independent of steel compositions. The electrode potentials varied from approximately -500 to -700 mV (SCE) depending on the alloy.

Barsom<sup>203</sup> also applied the freezing and indicator paper technique to determine the pH in a corrosion fatigue crack for 12Ni/5Cr/3Mo steel in 0.6 M sodium chloride solution. The pH at the tip near the centre of the specimen was measured as 3 with a bulk pH of 7 in all the tests.

However, according to Turnbull<sup>131</sup> the freezing technique, although the easiest, is the least satisfactory technique for measurement of pH in corrosion fatigue studies because of possible changes in solution composition while the operation is being performed. To overcome his objections, in the present investigation the stressed specimens were frozen in situ without unloading.

It was observed that on the application of cyclic stress, the pH at the mouth of the micropits and crevices on the surface of the fatigue tested specimens was somewhat lower than that of the unstressed specimens although the latter had experienced a higher number of reversals. The observation of pH as low as 3 to 3.5 may imply some contribution from the hydrolysis of  $\text{Fe}^{3+}$  ions which are much more strongly hydrolysed than  $\text{Fe}^{2+}$  ions. This would be expected near the mouth of the crevices or crack where dissolved oxygen from the bulk solution can oxidise  $\text{Fe}^{2+}$  to  $\text{Fe}^{3+}$  ions. At the root of a pit or at the tip of a crack the oxygen concentration is expected to be low; hence production of an acid condition will be due to the hydrolysis of  $\text{Fe}^{2+}$  ions which, according to Thomas<sup>204</sup>, is unlikely to produce a pH below 4. However, the measured value may represent the minimum pH and since the measurement technique with and without applied stress were the same, the reduction in pH may indicate some contribution of the stress to create acidic conditions within the crevice on the specimen surface.

One of the significant effects of the developments of low pH, even at the mouth of the microcrevices around the inclusions, would be to stimulate the dissolution of the inclusion to produce more  $\text{HS}^-$  ions which could accelerate the dissolution of the steel surface in the crevice or pit. This dissolution process may produce fissures and cavities within the pits (Figures R 11d and R 11w (ii)).

According to Laird and Duquette<sup>11</sup>, pits produced on the surface of the steel exposed to salt solutions are normally hemispherical with the result that the accompanying stress concentration effect is low. However, in this investigation, not all the pits observed were hemispherical (Figure D 13). Moreover, even the wider pits do not contain smooth pit bases.



Fig D 13: Micrograph showing the formation of a pit indicating continuing electrochemical process at the base of the pit. Wrought specimen after  $3.81 \times 10^5$  reversals at 278 MPa,  $R=-1$ , 47 Hz. Etch: 2% Nital.



Fig D 13: Micrograph showing the formation of a pit indicating continuing electrochemical process at the base of the pit. Wrought specimen after  $3.81 \times 10^5$  reversals at 278 MPa,  $R=-1$ , 47 Hz. Etch: 2% Nital.



Fig. 13: Micrograph showing the formation of a pit  
indicating continuing electrochemical process at  
the base of the pit. Wrought specimen after  $2.5 \times 10^4$   
 $10^4$  reversals at 278 MPa, R<sub>s</sub>-1, 47 Hz. Size: 200 μm.

Figure D 14 shows the formation of crevices and fissures at the base of a "hemispherical" pit indicating continuing reactions at the base of the pit. Dissolution at the grain boundaries and at the sub-surface non-metallic inclusions were also found to occur (Figures D 13 and D 14). The localised activities at the root of the pit tend to alter the geometry of the pit, converting the crevices and fissures within the pit into microcracks.

Similar phenomenon may be observed in Figure R 9g in which initiation of a crack from the base of the pit of a reversed bend specimen stressed at 277 MPa,  $R = -1$ , 24 Hz, was found to occur.

It has been suggested that the sulphide inclusions have sufficient solubility to produce a significant local concentration of  $H_2S$  and  $HS^-$  ions <sup>113</sup>. In addition, chloride ions are also able to diffuse towards regions of high stress creating zones of high chloride concentration <sup>16</sup>. Stress concentrations around inclusions are formed as a result of applied external stresses <sup>205</sup>. Hence the activity of sulphide and chloride ions is possibly higher near the inclusions than in the bulk solution. Additionally, the presence of  $H_2S$  in an aqueous solution greatly increases the amount of hydrogen absorbed by steel. The dissolution of sulphide enhances the local transport of hydrogen into the metal as a result of the presence of  $H_2S$  at the solution - inclusion interface. Since the concentration of  $H_2S$  released by inclusions is only a small fraction of the total solution, the effect is expected to be highly localised.

Craig <sup>206</sup> estimates that the morphology and chemistry of sulphide inclusions can greatly affect the hydrogen penetration of steel and the susceptibility to hydrogen cracking.



Fig D 14: Micrograph showing the formation of crevices and fissures at the base of a "hemispherical" pit indicating continuing electrochemical process at the base of the pit. Wrought specimen at 177 MPa, R=-1, 47 Hr, after  $10^5$  reversals. Etch: 2% Nital.

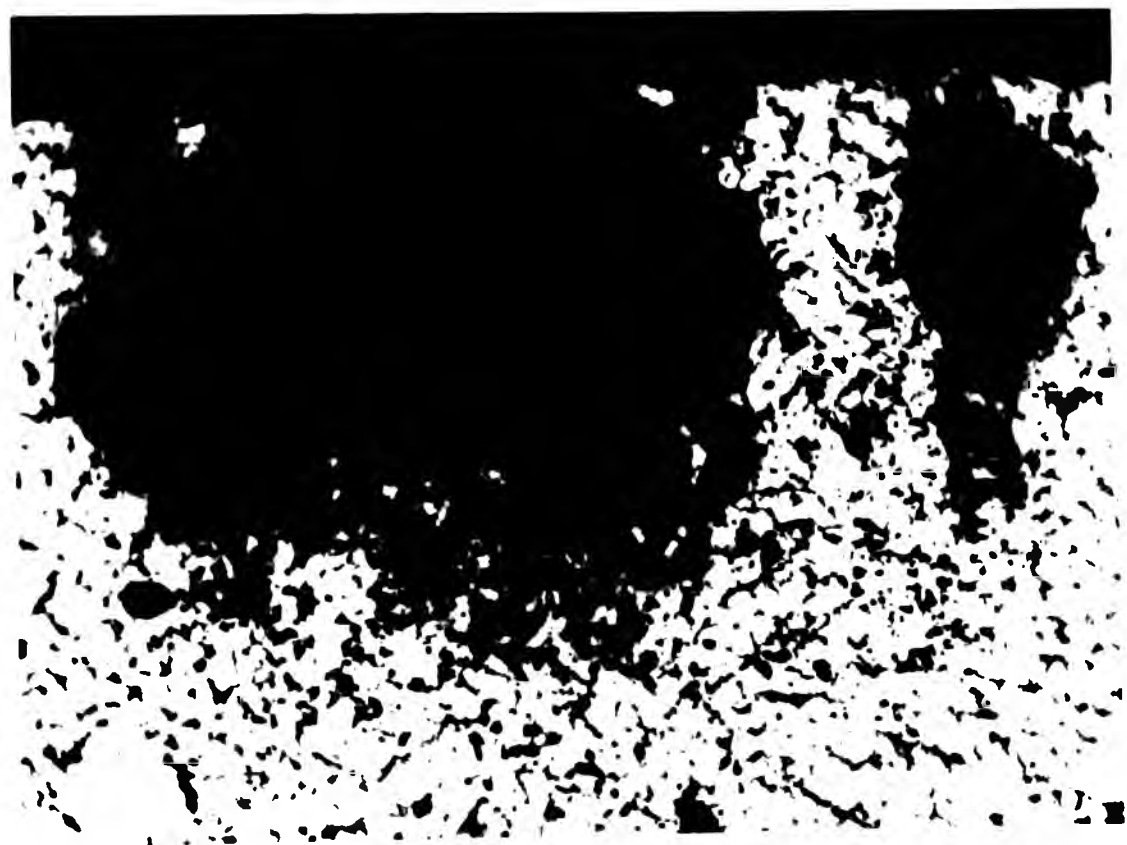
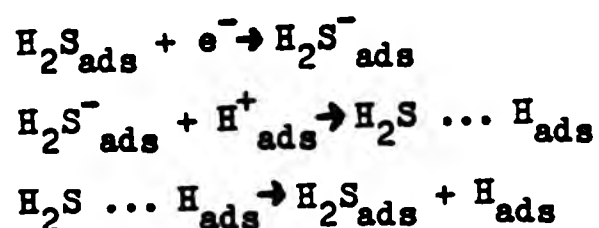


Fig D 14: Micrograph showing the formation of crevices and fissures at the base of a "hemispherical" pit indicating continuing electrochemical process at the base of the pit. Wrought specimen at 177 MPa,  $R=-1$ , 47 H . after  $10^5$  reversals. Etch: 2% Nital.

Spherical shaped sulphides enhance hydrogen cracking resistance from the standpoint of reduced hydrogen input whilst elongated inclusions tend to increase the amount of hydrogen adsorbed. He also suggests that Mn rich inclusions enhance hydrogen entry into metal.

Pumphrey <sup>207</sup> has observed that in mild steels containing elongated (Fe, Mn) S inclusions, H<sub>2</sub>S produced at the metal surface by the dissolution of the inclusions during corrosion in acid, promotes H<sub>2</sub> entry into the metal. Permeation rate increases with S content of the metal but only where the H<sub>2</sub>S supply can be maintained by inclusion dissolution. At lower temperature, e.g. 2° C, corrosive attack is confined essentially to the inclusions. Therefore, the H<sub>2</sub>S supply is reduced as initially exposed inclusions are dissolved. Permeation rates are lower through specimens oriented with the inclusions parallel to the surface as these are removed much more rapidly than inclusions oriented perpendicular to the surface. At higher temperature, such as 50° C, there is less anisotropy since the matrix dissolution is faster resulting in a further exposure of fresh inclusions and H<sub>2</sub>S supply.

Kawashima et al <sup>208</sup> studied the effects of strain rate, applied potential, pH, temperature and H<sub>2</sub>S concentration on sulphide cracking of mild steel and observed that nucleation sites of cracks appeared to be carbides in the pearlite, inclusions and/or grain boundaries. These researchers suggest that the dissolved species which promotes H<sub>2</sub> embrittlement in H<sub>2</sub>S solution is undissociated molecular H<sub>2</sub>S. The adsorbed molecular H<sub>2</sub>S accelerates proton discharge by the following reaction:



Thus the molecular  $H_2S$  adsorbed on the steel will act as a bridge - forming ligand for the proton discharge which thereby accelerates the discharge reaction and  $H_2$  entry into the metal promoting embrittlement. A small amount of  $H_2S$  in the solution affects the hydrogen electrode reaction.

According to Smialowska <sup>119</sup>, on application of stress the presence of a pit formed in the vicinity of a sulphide inclusion gives rise to piling up of stresses which favour local accumulation of  $H_2$  dissolved in the metal. This may result in nucleation of a crack.

Joshi <sup>209</sup> investigated the influence of density and distribution of sulphides on the sulphide stress cracking (ssc) of high strength steels containing 0.25 to 0.43 C / 0.008 to 0.014 P, and varying amounts of Mn and S. His results indicate that S and Mn precipitated at some grain boundaries, and in thicknesses not exceeding 100-150  $\text{\AA}$ , degrade the ssc properties of the material. The grain boundary S can influence the ssc behaviour in two ways. First the presence of S and P increases the crack nucleation and growth probabilities even in a non-hydrogen containing environment. Second is the enhancement of hydrogen diffusion along grain boundaries and the resultant increased embrittlement due to the presence of these elements at grain boundaries. It has been observed elsewhere that the crack nucleation probability is increased by the presence of segregated impurity elements <sup>210</sup>.

Cialone and Asaro <sup>211</sup> investigated the role of hydrogen in the ductile fracture of plain carbon steels containing 0.44 C. These researchers observed that void initiation occurred at lower strains and stresses in the presence of hydrogen although an equally important contribution to the ductility loss was from hydrogen accelerated void growth and coalescence.

This latter process takes place by the propagation of voids along the grain, and possibly subgrain, boundaries which interlink the cementite spheroids. The results indicate that hydrogen facilitates interface separation, possibly by accumulating at the boundaries during hydrogenation of the specimen. It was also found that approximately 15% of the voids were associated with MnS particles which would suggest that the sulphides cavitate more easily than carbides. They concluded that the initiation of voids in these ductile steels could not be viewed as simply a critical stress phenomenon but rather as a combined stress - plastic strain event.

According to Tetelman<sup>212</sup>, in corroded electrolytically charged or thermally charged specimens, excess hydrogen precipitates at inclusions or carbides in molecular form, causing the initiation of voids or microcracks. Surfaces of inclusions provides sites for the precipitation of hydrogen molecules. He has shown that the hydrogen pressure in these defects causes them to grow either by plastic deformation or by cleavage, depending on the intrinsic toughness of the particular steel and the shape of the nucleating particle. Microcrack or void coalescence, to form a macrocrack, occurs when a stress is applied to a hydrogenated structure.

Tiner<sup>213</sup> in his investigation of microprocesses in stress corrosion cracking of martensitic steels observed that cracks were initiated at several local sites by pit formation. Pits grew very slowly for a certain period. Eventually they attained certain depth and acuity, and a rapid but stable crack propagation commenced with moderate gas evolution. It was found that epsilon carbide particles could initiate cracks in steels. The epsilon carbide is able to absorb a considerable amount of hydrogen.

Thus it appears that localised corrosion occurs with the formation of pits and pits nucleate at sulphide inclusions with formation of an acidic environment within the pit. As a consequence, dissolution of the inclusions and metal occur with  $H_2S$  evolution. It seems likely that hydrogen discharge takes place on the steel surface, probably within the micro and macropits, and under the influence of  $H_2S$  and  $HS^-$ , the entry of hydrogen from the steel surface into the steel matrix is facilitated.

The localised activity within the micropits possibly occurs at internal sulphide inclusions, pearlitic areas, or at grain boundaries which may contain Mn and S as suggested by Joshi<sup>209</sup>. The presence of S at the grain boundaries may increase crack nucleation probabilities. Diffusion of hydrogen may also be enhanced at these boundaries.

It is also possible that if slip steps form in the metal within the crevices or pits, then as the pit opens hydrogen atoms are adsorbed on these slip steps formed during the previous cycle. During the next cycle the adsorbed hydrogen is swept in by the intrusion of the slip steps by the motion of mobile dislocation. This process is repeated during subsequent cycles.

Tien et al<sup>214</sup> proposed a similar dislocation sweep-in model, with respect to the mobile dislocations as a means for rapid transportation for the hydrogen atoms, for fatigue crack propagation. These researchers propose that the adsorption process is not a rate controlling step except at extremely high fatigue frequencies or when other gases present in the environment adsorb preferentially on the free surfaces and that the time for pick up and dumping at the grain boundaries is shorter than the fatigue cycle time.

Since dislocations cannot travel from grain to grain, it is considered that the hydrogen carrying dislocations must dump their loads at or near the grain boundary where the hydrogen atoms are then picked up by mobile dislocations originating near the grain boundary in the next grain.

Brown<sup>215</sup>, however, suggests that at high loading rates, approximately 100 Hz, with full reversal of stress, hydrogen cracking is unlikely to occur since hydrogen which may have tended to migrate to the effective sites during the tensile half cycle, is redistributed during compressive loading. Brown's argument may be valid for extremely high frequencies but it is conceivable that at 47 Hz, the time for pick up and dumping of hydrogen atoms at the grain boundaries is shorter than the fatigue cycle time.

Secondly, complete redistribution during compressive loading may be possible during full reversal of stress, if a pit behaves like a crack. Complete recontact of opposing faces of near perfect surfaces on closure is likely. However, the more open nature of the pits, and the imperfect surfaces of the opposing faces tend physically to obstruct interfacial recontact between opposing walls and prevent complete closure of the pits during unloading and compressive reversal.

The difference between a crack and a pit is that whereas access of the environment to the crack tip is limited, in the case of pits environment access is relatively easier and anodic dissolution may be possible even during complete reversal of stress since complete closure of the pit does not occur. This concept has been shown in Figure D 15. Figure D 14 shows the presence of a "hole" or microvoid due to material inhomogeneities, ahead of the fissure contributing directly to the initiation of a crack.

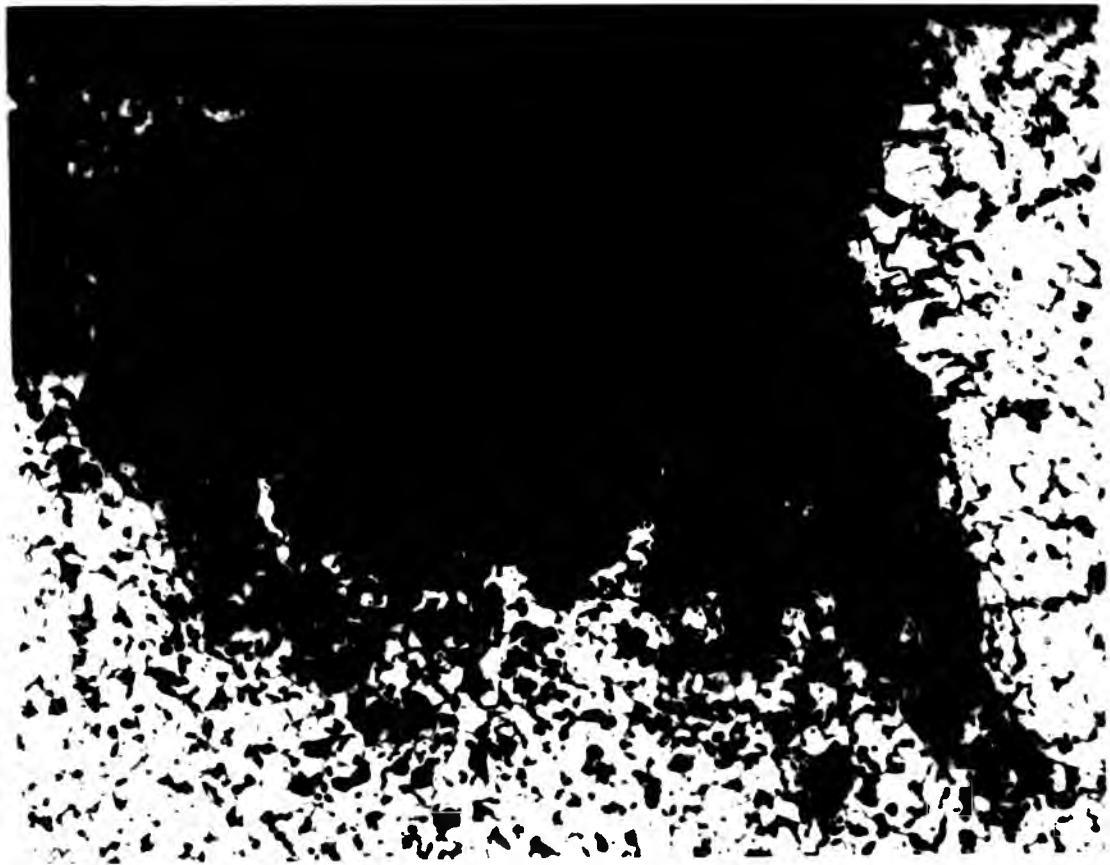


Fig D 15: Micrograph showing the initiation of a crack from the base of a pit. Wrought specimen after  $10^5$  reversals at 177 MPa,  $R=-1$ , 47 Hz. Etch: 2% Nital.

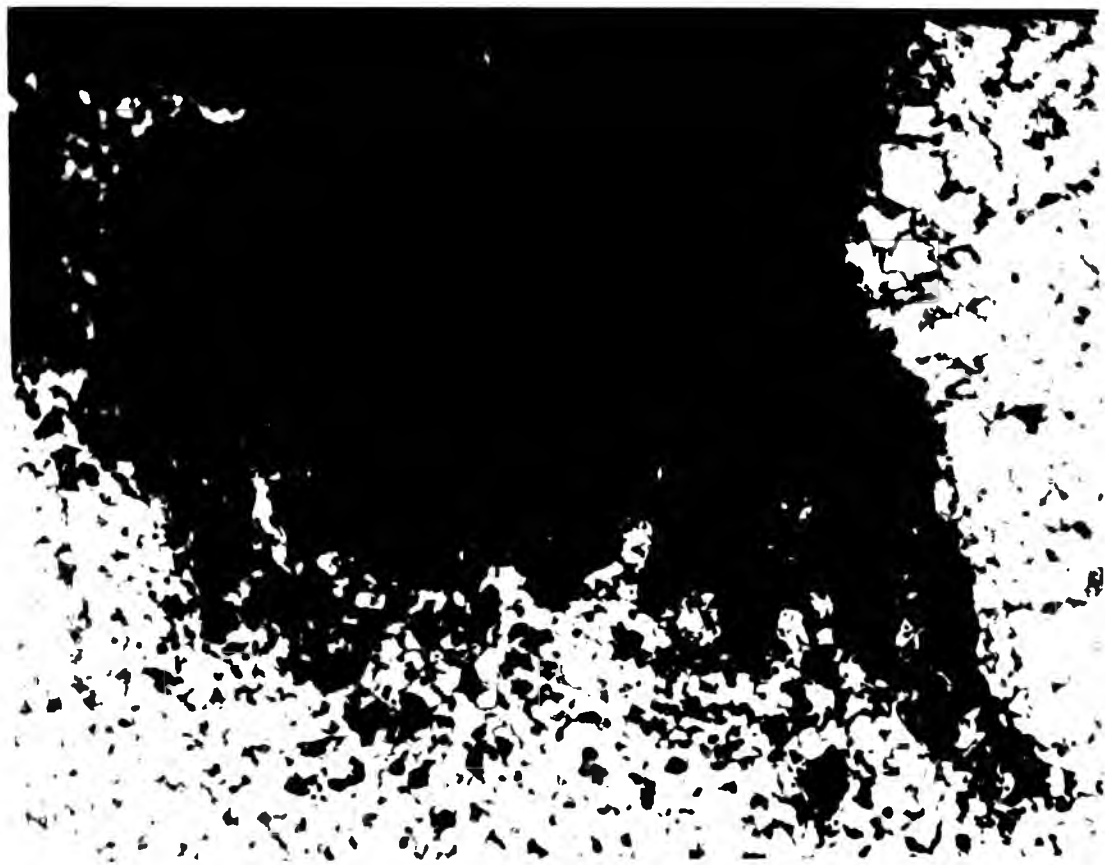


Fig. D 15: Micrograph showing the initiation of a crack from the base of a pit. Wrought specimen after  $10^5$  reversals at 177 MPa,  $R=-1$ , 47 Hz. Etch: 2% Nital.

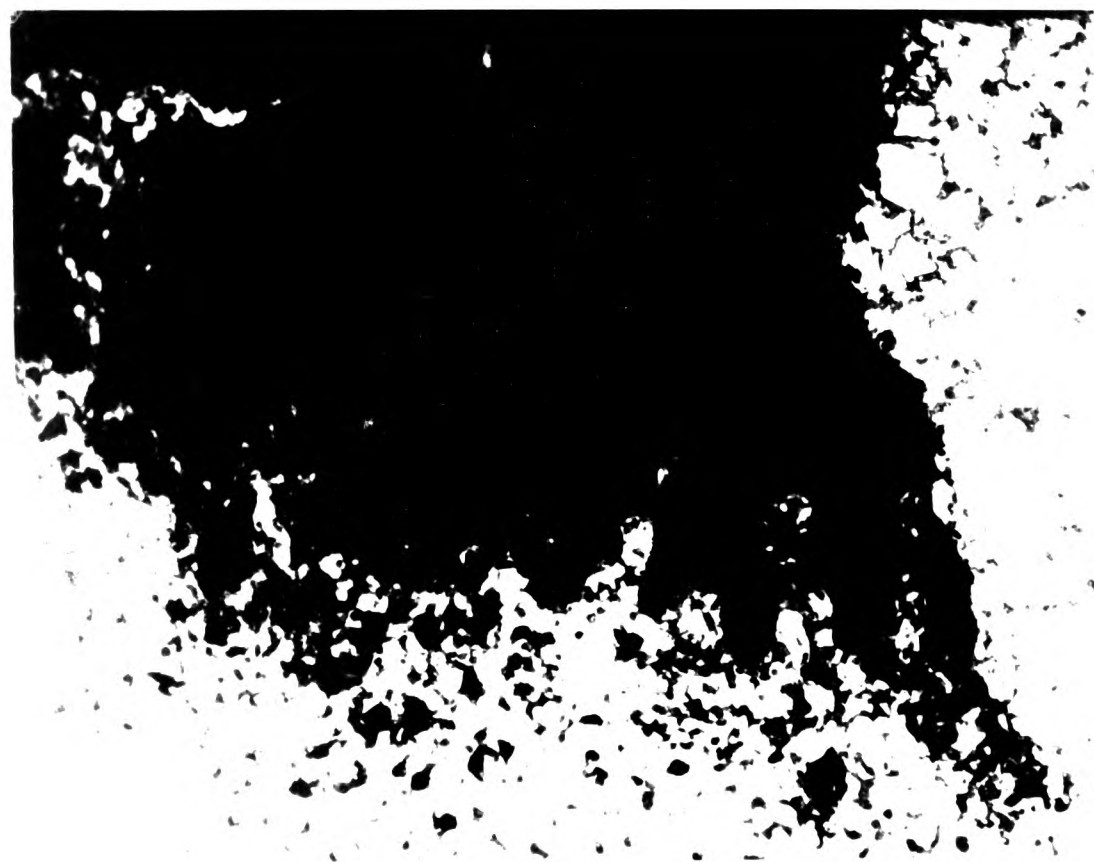


Fig. 1. Section showing the initiation of a crack from the edge of a pit. Wrought specimen after reversal at 700 MPa,  $\sigma_{max} = 4.7$  Hz. Rate: 20 MPa/s.

Following Figures R 9g and D 13 to D 15, it is proposed that on the application of cyclic stress, localised activities at the base of the pits tend to alter the geometry of the pits as shown in the schematically in Figure D 16.

Recently, Lindley et al <sup>184</sup> have also suggested that both pits and cracks open readily in response to the tensile part of the load cycle. However, crack closure can occur readily in sharp cracks during the compressive part of the load cycle whilst the more open nature of the pit limits crack closure, so that material at the tip of the pit is exposed to a greater overall stress range than would be experienced at the tip of a sharp crack.

Crack initiation may occur at subsurface defects, such as inclusions through the occurrence of local cyclic plastic deformation generating high local dislocation densities on slip planes thus leading to the formation of intrusions and extrusions. It is also possible that the dissolution at grain boundaries and pearlitic areas plays a significant role in the nucleation of cracks (Figures D 13 to D 15). Examination of the fractured surfaces shows that joining and extension of adjacent pits occurs leading to the initiation of a fracture crack (Figure D 17). This linking up of pits appears to take place mainly by dissolution along grain boundaries and subsurface defects (Figure D 18).

#### 5.9.2 Transmission electron microscopic examination

Results of tests on specimens immersed in 0.6 M sodium chloride solution for 5 and 17 hours show preferential attack at inclusions and in the pearlitic regions (Figure R 12). Examination reveals micropit formation and coalescence of micropits at the matrix - inclusion interface resulting in the nucleation of macropits.

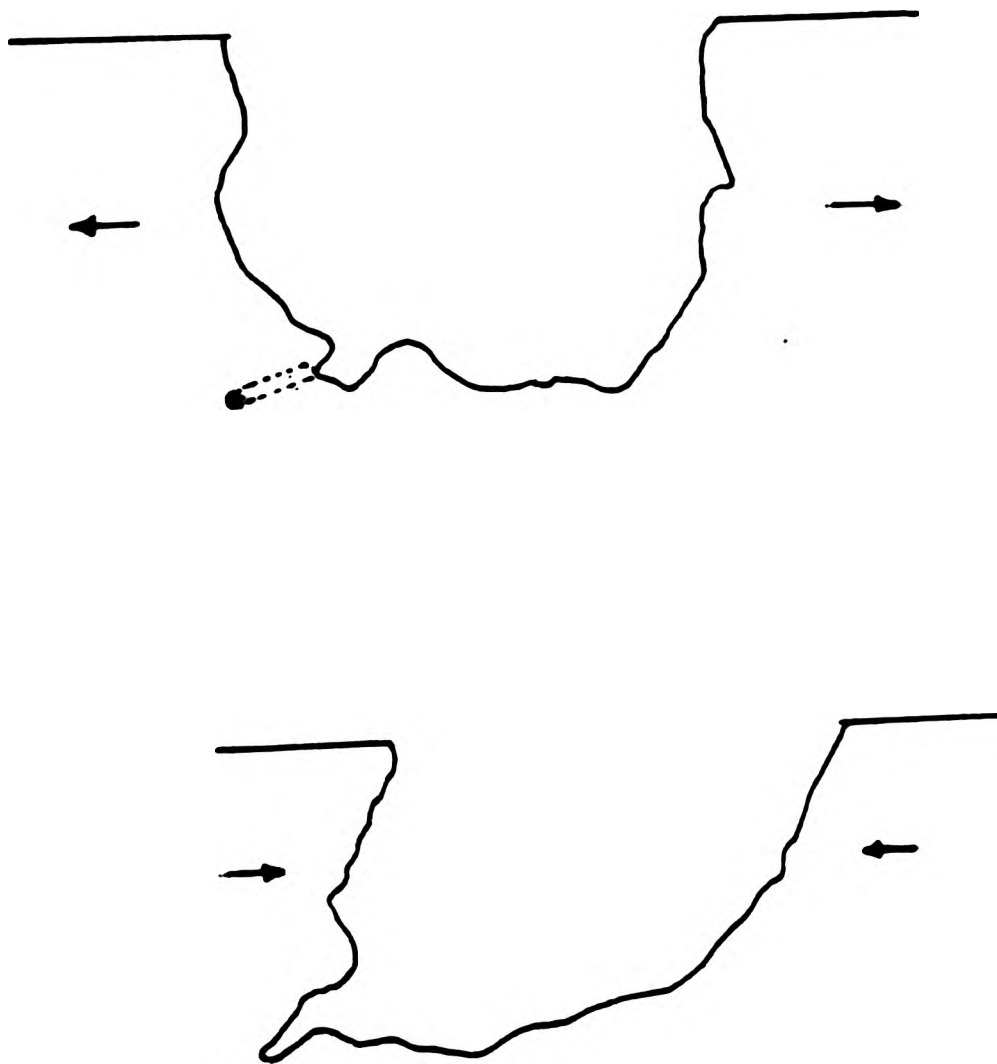


Fig D 16: Schematic diagram of a pit indicating the change in geometry due to the localised activities at the base of the pit.



Fig D 17: Micrograph of a fractured surface of a rotating bend fatigue tested specimen at 196 MPa, R=-1, after  $1.39 \times 10^6$  reversals exhibiting linking up and extension of two adjacent pits to form a crack.  
x 70.

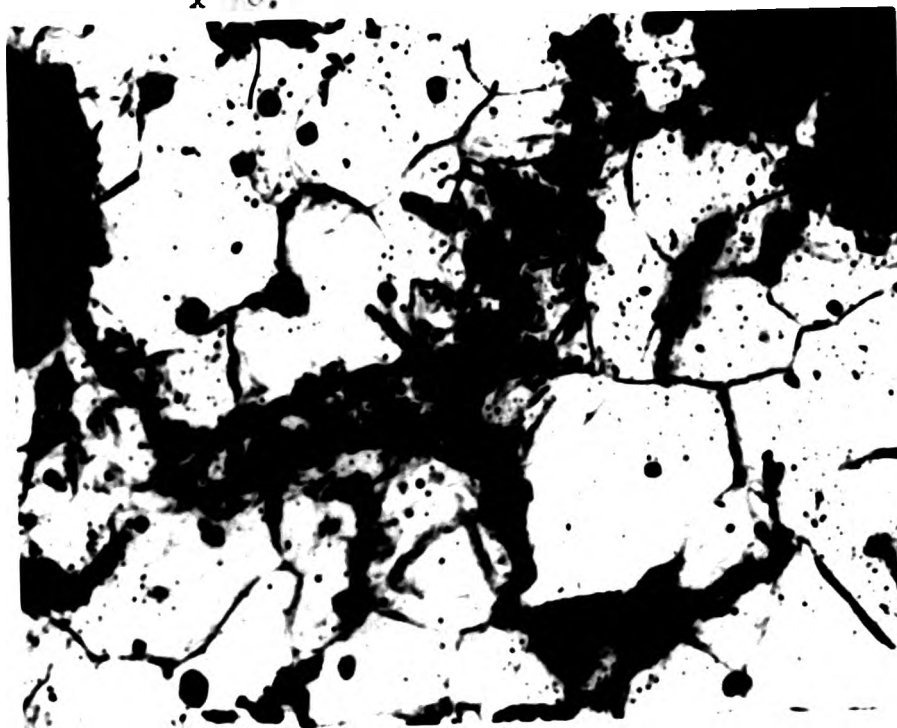


Fig D 18: Micrograph of a fractured surface of a rotating bend fatigue tested specimen at 177 MPa, R=-1, after  $10^6$  reversals exhibiting linking up of adjoining pits.  
x 700.



Fig. D 17: Micrograph of a fractured surface of rotating bend fatigue tested specimen at 106 MPa, R=-1, after  $1.39 \times 10^6$  reversals exhibiting linking up and extension of two adjacent pits to form a crack. x 700.

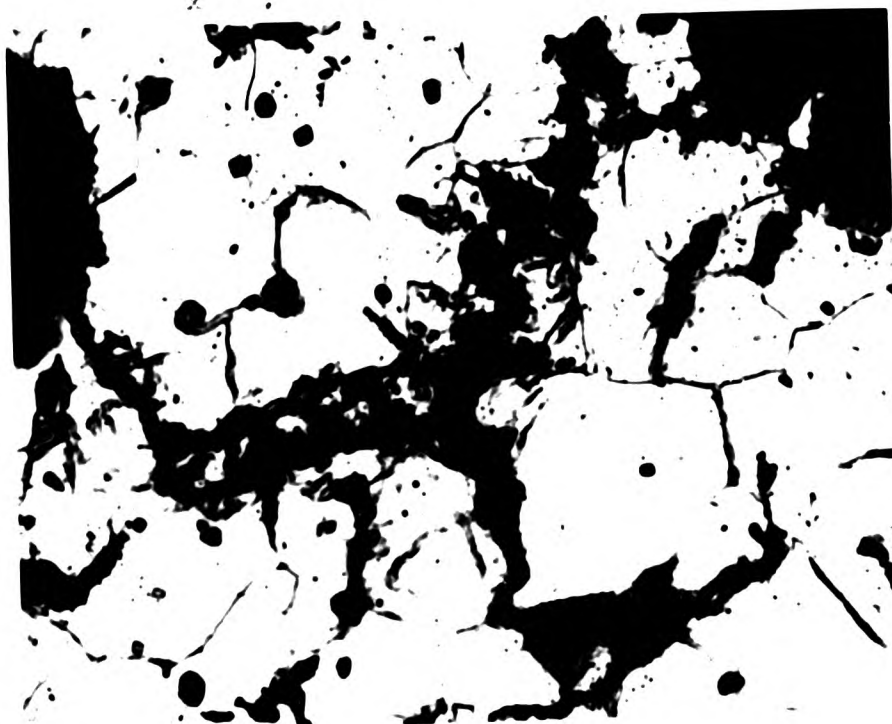
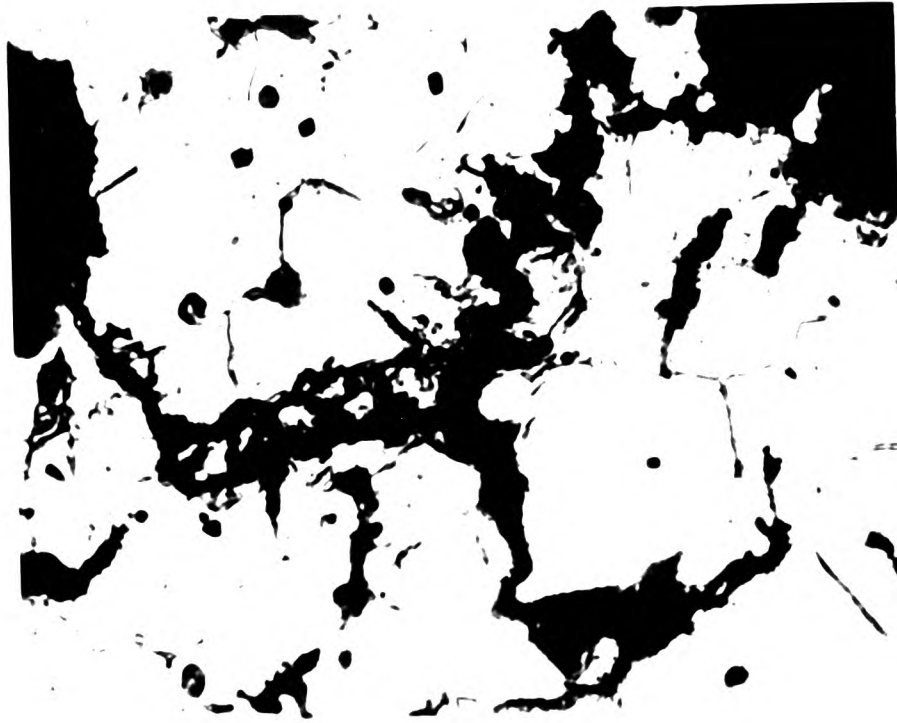


Fig. D 18: Micrograph of a fractured surface of a rotating bend fatigue tested specimen at 107 MPa, R=-1, after  $1.0^6$  reversals exhibiting linking up of adjoining pits. x 700.



The results appear to correspond to those obtained by using scanning electron microscopy (Figure R 10f (i)). Localised dissolution is also observed at the ferrite - cementite interface in the pearlite region. Examination also reveals terminations and bends in the lamellar structure (Figure R 12f).

On application of cyclic stress, dissolution at the matrix - inclusion interface appears to be more rapid than that at such interfaces unstressed. With stress at 95 MPa,  $R = -1$ , rectangular etch pits (Figure R 14a) are found to occur indicating the formation of anodic sites by the emergent dislocations intersecting the surface. Localised dissolution at the ferrite - cementite interface (Figures R 13a, R 13b, R 14b and R 14c) appears to be enhanced, and with increasing number of reversals, dissolution of ferrite and linking up of the micropits are found to occur (Figures R 13k and R 14e). The coalescence of micropits results in the formation of voids. It is possible that some degeneration of the lamellar structure, such as isolated fragments of cementite (Figure R 14c) may have occurred due to the application of cyclic stress. It is, however, difficult to separate such changes caused by deformation.

Examinations of micrographs reveal enhanced localised dissolution at the matrix - inclusion interface due to the cyclic stress. With an increasing number of reversals, micropits in the region close to the interface tend to coalesce; this appears to be a precursor to the formation of transverse microcracks from the interface (Figure R 13e). Fracture of some of the inclusions also occur with increasing duration of tests and/or with increasing stress (Figure R 17p). Microfissures also appear to nucleate from the tip of the inclusions (Figure R 13h). Blisters in the matrix surrounding the inclusion in this micrograph are possibly artifacts.

However, the appearance of etch pits and blisters associated with inclusions has been observed (Figures R 13n and R 14f).

It has been mentioned previously that hydrogen discharge may take place on the steel surface, probably within the micro and macropits, and under the influence of  $H_2S$  and  $HS^-$ , the entry of hydrogen from the steel surface into the steel matrix is facilitated. The presence of these blisters in the vicinity of the inclusions tends to suggest that hydrogen entry into the matrix, due to localised corrosion at sulphide inclusion, takes place and that at 47 Hz, the time for pick up and dumping of hydrogen atoms by mobile dislocations at grain boundaries is shorter than the fatigue cycle time.

Slip bands are found to occur with increasing number of reversals (Figures R 13g and R 13j). Micropits in slip bands also tend to appear with increasing number of reversals (Figures R 13j and R 16h) or with increasing applied stress (Figure R 14h). The features resemble those observed in the micrograph, Figure R 15g; the coalescence of the micropits appear to result either in subgrain formation in the matrix or microfissures in the slip bands. It has been observed that the individual micropits do not grow but that propagation occurs by linking.

Severe localised deformation has also been observed in annealed specimens at higher number of reversals (Figure R 14g). Etch pits, subgrain and microfissure nucleation at the grain boundary junctions are also found to occur (Figures R 14h - R 14q) at 95 MPa.

According to Wood <sup>216</sup>, crack initiation occurs with the formation of what may be termed as pores or voids. Distribution appears to be determined by a general principle that pores form preferentially where the microstructure is abnormally distorted.

A higher stress range produces coarse slip movements that reduce each grain to a disoriented substructure. The resulting subboundaries and the main boundaries themselves provide the abnormally distorted zones on which pores form; Figures R 17j and R 19d illustrate the distorted zones containing these pores. Hence they also determine the shape and distribution of the ensuing microcracks. These microcracks cross link readily resulting in the formation of macrocracks.

Smaller stress amplitudes tend to leave the grains nearly unrumpled <sup>216</sup>. However, it may be considered that slip concentrations may give rise to distortion zones with the formation of pores causing disintegration of the zones as the pores multiply. Cottrell and Strutt <sup>216</sup> in discussion with Wood, however, suggested that the pores were in fact etch pits developed at centres of strains as dislocation tangles and such tangles were characteristic of cyclic straining.

According to Wood <sup>216</sup>, slip in body centred cubic metals has a larger choice of slip planes and directions; moreover it can more readily cross from one slip plane to a neighbouring one. It has been suggested that regions beneath the fatigue slip bands are softer than the adjacent matrix <sup>217</sup>. It appears that this recovery facilitates further dislocation motions within the regions. In axially loaded copper single crystals, the soft zones have been found to penetrate some distance beneath the surface. Substructures have been observed within such persistent slip bands. The presence of substructures suggests that cross slip and climb are involved in the recovery process.

Comparison of the micrographs of the corroded (Figure R 16h) and uncorroded regions (Figure D 19) of the same specimen tested at 247 MPa,  $R = -1$ , show that the micropits in the slip bands are observed in both these sites at the same number of reversals. Under corrosion fatigue conditions at lower stress range, 95 MPa, and at higher number of cycles slip bands tend to intersect the inclusions creating voids (Figures R 14f and R 16f). In air fatigue, at lower stress range, 193 MPa, slip bands appear to be deflected by inclusions (Figures R 18d and R 18e) while at higher stresses, 248 MPa, and at somewhat higher number of reversals these bands intersect the inclusions resulting in microvoid formation. Intrusion - extrusion phenomena and slip band formation near the grain boundary region are also found to occur under corrosion fatigue conditions. These surface morphologies appear to indicate that the effects observed in air fatigue also occur in corrosion fatigue and that they play a significant role in crack nucleation.

Examination of fractured surfaces by using optical microscopy has shown that the extension of adjacent pits occur by linking and this leads to the nucleation of cracks which lead to fracture (Figures D 17 and D 18). This linking up of pits appears to take place mainly by a dissolution process along grain boundaries and sub-surface defects. Results of the examination of similar surfaces by using transmission electron microscopy are shown in Figure D 20. Figure D 20 (i) exhibits preferential attack along grain boundaries and pearlitic regions while Figure D 20 (ii) illustrates etch pits at the bottom of a pit, similar to that shown in Figure D 15, indicating preferential dissolution at the site of emergent dislocations.



(i)

(ii)

Fig D 19: Transmission electron micrographs of wrought specimen showing (i) micropits in the slip band and microcracks at the matrix-slip band interface, and (ii) linking of micropits creating microcracks in the slip band. Outside corroded zone, 247 MPa, R=-1, after  $10^6$  reversals; x 16273 and x 11273 respectively.



(i)



(ii)

Fig D 20: Transmission electron micrographs of wrought specimen showing (i) linking of adjacent pits by dissolution along grain boundaries and pearlitic regions, x 2182, and (ii) etch pits at the tip of a fissure in a pit, x 6818. 197 MPa, R=-1,  $7.86 \times 10^5$  reversals.



Fig D 19: Transmission electron micrographs of wrought specimen showing (i) micropits in the slip band and microcracks at the matrix-slip band interface, and (ii) linking of micropits creating microcracks in the slip band. Outside corroded zone, 247 MPa, R=-1, after  $10^6$  reversals; x 16273 and x 11273 respectively.

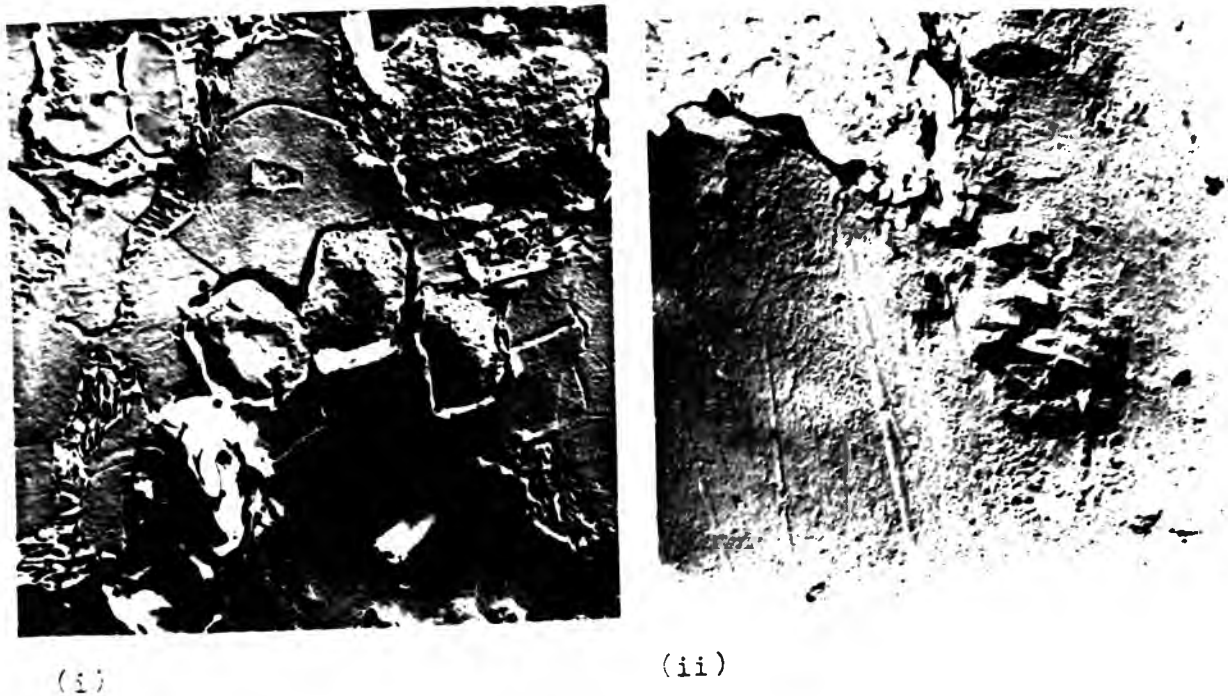


Fig D 20: Transmission electron micrographs of wrought specimen showing (i) linking of adjacent pits by dissolution along grain boundaries and pearlitic regions, x 2182, and (ii) etch pits at the tip of a fissure in a pit, x 6818. 197 MPa, R=-1,  $7.86 \times 10^6$  reversals.



(ii)

Fig. 19: Transmission electron micrographs of wrought specimen showing (i) micropits in the slip band and microcracks at the matrix-slip band interface, and (ii) linking of micropits creating microcracks in the slip band. Outside corroded zone, 242 MPa, R=-1, after  $10^6$  reversals; x 11277 and x 11277 respectively.



(ii)

Fig. 20: Transmission electron micrographs of wrought specimen showing (i) matrix-slip band interface with micropits and microcracks, and (ii) linking of micropits creating microcracks in the slip band. Outside corroded zone, 242 MPa, R=-1, after  $10^6$  reversals; x 5117 and x 5117 respectively.

The results of this series of tests show that the application of cyclic stress enhances the formation of micro and macropits at inclusions, in pearlitic regions and at grain boundaries. Generation of etch pits is also facilitated due to application of cyclic stress. Subgrain formation, slip band and intrusion phenomena have also been observed. Slip bands also appear to form between the pearlitic regions on the specimen surface thus providing a path for the nucleation of a microcrack by linking the voids created in these regions. These voids are created by the dissolution of the ferrite - cementite interfaces and dissolution of ferrite in pearlitic areas. Microcracks also tend to nucleate in the slip bands and along the grain boundaries near the triple points.

Inclusions act as nucleation sites for hydrogen blisters, and microcracks and pin holes in these blisters have been observed.

With low applied stress, it appears that the dissolution mechanism is the predominant reaction while at higher stress ranges, mechanical factors, such as fracture and spalling of inclusions, tend to predominate. It also appears that in low inclusion density regions nucleation of microcracks may occur at slip bands, etch pits, pearlitic regions and at grain boundaries. In the high density regions, these may also play a significant role, but their effects may be somewhat overshadowed by the influence of dissolution reactions at and around inclusions. Etch pits have been observed in the matrix close to the inclusions indicating that the inclusions induce stresses and generate dislocations in the surrounding metal 119.

#### 5.10 General discussion

Results of anodic polarisation studies indicate that on the application of cyclic stress in a flowing electrolyte the zero current potential, calculated from the graphs obtained in the potentiostatic experiments, becomes more positive compared with that without stress. The potential at which a marked increase in anodic current occurs, indicating the dissolution of metal, also becomes more positive than that without applied stress.

Specimens will undergo film breakdown immediately on immersion to an extent which will be greater the more negative the potential at which the marked increase in anodic current occurs. Comparison of Figures R 3b and R 4b indicate that  $E_b - E_p$ , the potential range at which pits continue to grow but no new pits form, is larger with applied stress than that in the absence of stress.

In these experiments, the cathodic current and/or cathodic potential, where appropriate, was applied as the specimen was immersed in the solution. This procedure should prevent breakdown of the oxide film on steel on initial immersion. Breakdown of the film will occur as the anodic sweep makes the potential more positive. The breakdown potentials obtained in this investigation are not clearly defined. This tends to suggest that the breakdown is not that of a completely protective film. It may be postulated that the cathodic treatment reduces the oxide film at localised areas where the film is thin or susceptible to reduction thus exposing the underlying metal which starts to corrode as the potential becomes more positive than the cathodic protection potential. Hence the initial increase in anodic current will be due to the dissolution of the areas where the film has already broken down.

In flowing electrolyte and under cyclic stress conditions, the extra movement introduced into the solution increases the oxygen supply to the metal, resulting in increased cathodic currents as observed in Figures R 2 and R 3. It will also produce more positive zero current potentials. When the potential is swept to more positive values, the anodic current required to change the potential tends to decrease the cathodic current by the same amount. Hence, the faster the potential sweep rate in the positive direction, the smaller will be the cathodic current and thus the larger is the anodic current. This may partly explain the reason for the very negative zero current potentials observed in stagnant solutions (Figures R 1a and R 3a). The breakdown potential is little affected by the movement but the marked increase in anodic current is expected to be observed from a larger cathodic current, as shown in Figure R 4b <sup>204</sup>.

Mild steel in 0.6 M sodium chloride solution does not form a protective film. Therefore, reactions may occur both at the filmed and exposed area of the surface which contain inhomogeneities, such as non-metallic inclusions. These differences may affect the healing characteristics of the film. The breakdown of the surface film produces a shift in potential in the more negative direction and the corrosion current tends to increase, indicating corrosion of the exposed metal.

Measurements of the potentials on the external surface and inside a notch indicate that a potential difference exists in the absence of stress.

The experimental observations show that the determinations of potentials inside the notch were not particularly successful when the stress was applied because of the movement of the flexible capillary tube.

However, the results do suggest that the potential inside a notch is somewhat more negative than that on the external surface in the absence of stress and that the potential of the external surface becomes slightly more negative on the application of compressive stress.

Measurements of corrosion currents indicate that corrosion occurs quite readily with and without an applied stress. On application of a static compressive stress, namely 200 MPa, with a control potential of -660 mV (SCE), the corrosion current is found to be higher than that at zero stress indicating enhanced corrosion of the metal. Application of a static tensile stress of the same magnitude after unloading the specimen causes a rapid increase of the anodic current.

The cyclic load - current vs time curves (Figure R 8c), during the initial stages of a fatigue test at 198 MPa,  $R = -1$ , at 0.07 Hz show an initial decrease of the anodic current. This indicates that the surface film becomes more protective possibly because of the precipitation of the corrosion products due to the dissolution of the anodic areas thereby partially plugging these sites.

It is also possible that the alternating stress tends to breakdown the surface film resulting in a competitive reaction with the stifling of the anodic areas due to the precipitation of the corrosion products at these sites predominating initially, and the film breakdown being the main effect at longer times.

On application of cyclic stress of 198 MPa at  $R = -1$ , 0.2 Hz, the anodic current increases significantly. Further increase in corrosion current occurs with increasing stress. Potential spikes were observed during the fatigue tests at 247 MPa, 0.02 Hz after an incubation period.

Examination of the specimen surfaces by using optical microscopy revealed areas of bright and dull bands of variable width after the observation of spikes. On the bright areas very little attack had occurred while the dull areas had been attacked more severely. It is possible that these areas indicate the initial breakdown of the oxide film and may contain high inclusion density regions, pearlitic colonies and slip bands. It has been observed during the examinations of the surfaces using scanning and transmission electron microscopy that dissolution of the inclusions, of the matrix - inclusion interfaces and ferrite - cementite interfaces in the pearlitic regions commences in the early stages of the fatigue tests. Slip bands<sup>also</sup> tends to form.

Tests with mill scaled and polished specimens have also indicated that potential fluctuations are associated with changes in surface morphologies. A rapid rise in corrosion current is found to occur due to the breakdown of the mill scale at some sites. Severe attack was observed at the few exposed sites on the mill scaled specimens while the polished specimens suffered relatively less severe corrosion since the exposed sites in the latter case were comparatively numerous. It was observed that the potential (Figure R 8h) decreased somewhat more rapidly after the formation of the spikes. Hence it is possible that the perturbation observed in the potential vs time curve (Figure R 8h) may be some indication of the breakdown of the oxide film due partly to the formation and development of the slip bands.

According to Pelloux et al <sup>218</sup>, the process of corrosion fatigue crack nucleation can be described most simply as the perturbation of the normal fatigue crack initiation mechanisms by environmental interactions, so that any unknowns relating to fatigue crack initiation also apply to corrosion fatigue.

The dislocation arrangements leading to the formation of a fatigue crack have been studied extensively <sup>219, 220</sup>. Depending upon the cyclic strain amplitude, the dislocations in the bulk are arranged in veins or bands of dipoles, or in cell walls and have been found to exist in the bulk away from the persistent slip band but also within a few hundred Å of the free surface. Within the persistent slip band, the dislocations are arranged in a well defined ladder or cell structure. It has been suggested that the persistent slip bands are formed not only from newly generated dislocations but also by transfer of the matrix dislocations into the slip band structure. However, Pelloux et al <sup>218</sup> suggest that the dislocation arrangements associated with persistent slip bands have been characterised only for the simplest, oxide free single crystals.

In the present investigation, metallographic examinations indicate that preferential dissolution at inclusions and in pearlitic regions causes stress concentration around these phases leading to the formation and development of slip bands. Microcracks tend to develop at the edges of these bands possibly because of the localised dissolution which is easier from sites on the slip steps than from unstepped crystal surface <sup>72</sup>. Nucleation of microcracks was also observed within the slip bands due to the coalescence of the micropits. These micropits develop at the centres of strain such as dislocation tangles, as suggested by Cottrell and Strutt in discussion with Wood <sup>216</sup>.

Lucas and Klesnil<sup>220</sup> also suggest that the persistent slip bands contain a large number of dislocation tangles.

The nucleation of microcracks at grain boundaries may result from plastic strain and plastic folding (Figures R 14p and R 14q) at grain boundaries due to the differences in orientation between the adjoining grains. Since each grain has a different orientation, the distribution of strain between the grains is hindered at the grain boundaries. This constraining effect of grain boundaries and the inhomogeneity of strain distribution possibly accounts for the grain boundary deformation. It is possible that the strain disparity in adjacent grains produce a squeezing action on the material near the deformed boundary causing extrusion-like defects.

The results of the present study indicate that the cyclic stress enhances the formation and penetration of pits. Pitting occurs at the inclusions, matrix - inclusion interfaces and in pearlitic areas due to the nucleation of micropits, coalescence of micropits to macropits, and due to the linking up of macropits. This extension of macropits also result in the formation of incipient cracks. Generation of etch pits is also facilitated by the application of cyclic stress; incipient cracks tend to form at these etch pits.

The incidence of crack nucleation depends upon the number of reversals and applied stress and in the main cracks tend to initiate in the high inclusion density regions. Pitting and electro-chemical reactions within the pits appear to play a significant role in crack initiation in the presence of inclusions.

With low applied stress, it appears that the dissolution mechanism is the predominant reaction. At higher applied stress, mechanical factors, such as deformation and spalling of inclusions, deformation and fracture of carbides creating voids, fracture of inclusion ligaments in the high density regions, all play a significant part in the nucleation process. Some or all of these mechanisms also appear to occur at low stresses with a higher number of reversals. In the pearlitic regions and with low applied stress, incipient cracks tend to form in ferrite indicating possible dissolution control mechanism.

It was also observed that inclusions act as nucleation sites for hydrogen blisters. This may assist the formation of cracks.

## 6 CONCLUSIONS

6.1 Results of anodic polarisation tests show that on application of cyclic stress:

6.1.1 Zero current potential becomes more positive than that in the absence of stress.

6.1.2 The potential at which a marked increase in anodic current occurs, indicating the dissolution of metal, is more positive than that in the absence of an applied stress. Thus the specimens undergo film breakdown immediately on immersion to an extent which will be greater the more negative the potential at which a marked increase in corrosion current occurs.

Since the breakdown potential is not clearly defined it is believed that the breakdown is not that of a completely protective film.

6.1.3 The potential range at which pits continue to grow but no new pits form is larger than that in the absence of stress.

6.2 A potential difference exists between the external surface and inside a notch.

6.3 Application of both the static tensile and compressive stresses produces anodic current which is higher than that in the absence of stress, indicating enhanced corrosion of metal.

6.4 Application of cyclic stress tends to break down the surface film resulting in a competitive reaction with the stifling of the anodic areas, due to the precipitation of corrosion products at these sites, predominating initially and the film breakdown being the main effect at longer times.

Hence, an initial decrease of anodic current is observed. With increasing number of reversals anodic current increases rapidly. Enhancement of corrosion current occurs with the increase of stress.

- 6.5 A sulphur enriched band of ferrite exists around the inclusions in the steel and corrosion occurs in this contaminated band both in the presence and absence of applied stress.

Under cyclic stress condition, an effect attributable to inclusion shape, especially in the high density region, has not been observed.

- 6.6 Cyclic stress enhances the formation and penetration of pits. Pitting occurs at the inclusions and matrix - inclusion interfaces due to nucleation and coalescence of micropits. Generation of etch pits is also enhanced by the application of cyclic stress. Incipient cracks in the transverse direction nucleate at these pits.

- 6.7 Cracks in the transverse direction tend to initiate more rapidly in the high inclusion density regions than in the low density ones.

- 6.8 Preferential attack occurs at the ferrite - cementite interfaces and on the application of alternating stress ferrite in the pearlite undergoes dissolution. The microvoids created due to the deformation and fracture of the cementite, and the dissolution of the ferrite, create capillary paths resulting in the entrapment of corrosive liquid. Linking up of these microvoids appears to be the precursor of incipient crack formation in pearlitic regions.

Cracks also nucleate at the ferrite grain - pearlitic colony interfaces.

- 6.9 Cracks tend to nucleate in the slip bands, at the slip band-matrix interfaces and at grain boundaries.

6.10 With low applied stress, the dissolution mechanism appears to be the predominant reaction. At higher applied stresses, mechanical effects play a significant role in the nucleation process.

Inclusions appear to be the predominant surface defects from which cracks initiate readily irrespective of applied stress levels.

6.11 Inclusions act as nucleation sites for hydrogen blisters. This may assist the formation of cracks.

References

- 1 B.P.Haigh, JIM, 18, 55, 1917
- 2 D.J.McAdam Jr, Proc. ASTM, 26, 224, 1926
- 3 D.J.McAdam Jr, Trans Amer Soc Steel Treat, 11, 335, 1927
- 4 D.J.McAdam Jr and G.W.Geil, Proc. ASTM, 28, 696, 1928
- 5 D.J.McAdam Jr, *ibid*, 31, 259, 1931
- 6 H.J.Gough, JIM, 49, 17, 1932
- 7 A.J.Gould, Iron and Steel, 24, 7, 1951
- 8 P.T.Gilbert, Met Rev, 1, 379, 1956
- 9 R.B.Waterhouse, Fatigue of Metals, Inst of Met, 105, 1955
- 10 D.J.Duquette, Corrosion Fatigue, NACE-2, 12, 1972
- 11 C Laird and D.J.Duquette, *ibid*, 88
- 12 R.M.Pelloux, R.E.Stoltz and J.A.Moskovitz, Mat Sci and Eng, 25, 193, 1976
- 13 R.N.Parkins, Met Tech, 9, 122, 1982
- 14 V.Rollins, B.Arnold and E.Lardner, Br Corr J, 5, 33, 1970
- 15 C.Patel, T.Pyle and V.Rollins, Met Sci, 11, 185, 1977
- 16 C.Patel, Corrosion, 36, 665, 1980
- 17 A.J.Gould, Engineering, 141, 495, 1936
- 18 I.Cornet and S.Golan, Corrosion, 15, 262t, 1959
- 19 M.Watanabe and Y.Mukai, Conf on Welding in Offshore Structure, The Welding Inst, 1974
- 20 M.T.Simnad and U.R.Evans, JISI, 156, 531, 1947
- 21 F.J.Radd, L.H.Crowder and L.H.Wolfe, Corrosion, 16, 415t, 1960
- 22 D.J.Duquette, PhD Thesis, MIT, 1968
- 23 K.Endo and Y.Miyas, Bull Japan Soc Mech Eng, 1, 374, 1958
- 24 H.J.Gough and D.G.Sopwith, JISI, 127, 301, 1933
- 25 H.J.Gough and D.G.Sopwith *ibid*, 135, 293, 1937
- 26 A.J.Gould, JISI, 161, 11, 1949

- 27 J.W.Knight, Corrosion Fatigue, Welding Research Council, N.Y,  
7, No. 3, 1977
- 28 N.Inglis and G.F.Lake, Trans Faraday Soc, 27, 803, 1931
- 29 T.H.Burnham, Trans Inst Marine Eng, 46, 1, 1934
- 30 A.M.Binnie, Engineering, 128, 190, 1929
- 31 P.Mehdizadeh, R.L.McGlassen and J.E.Landers, Corrosion 22, 325,  
1966
- 32 H.Kitagawa, Fracture Mechanics Approach to Ordinary Corrosion  
Fatigue of Unnotched Steel Specimens, Univ of Connecticut, 1973
- 33 N.Thompson and N.J.Wadsworth, Adv Phys, 7, 72, 1958
- 34 J.A.Ewing and J.C.Humphrey, Phil Trans, A 200, 241, 1903
- 35 H.J.Gough, S.J.Wright and D.Hanson, JIM, 36, 173, 1926
- 36 H.J.Gough and D.Hanson, Proc Roy Soc, A 104, 538, 1923
- 37 N.Thompson, N.J.Wadsworth and N.Louat, Phil Mag, 1, 113, 1956
- 38 G.C.Smith, Proc Roy Soc, A 242, 189, 1957
- 39 P.A.Jaquet, Int Conf on Fatigue of Metals, I Mech E, London,  
1956
- 40 P.J.E.Forsyth and C.A.Stubbington, Nature, 175, 767, 1955
- 41 P.J.E.Forsyth, Proc Roy Soc, A 242, 198, 1957
- 42 P.J.E.Forsyth, Nature, 171, 172, 1953
- 43 P.J.E.Forsyth, JIM, 83, 395, 1955
- 44 C.A.Stubbington and P.J.Forsyth, JIM, 86, 90, 1957
- 45 P.J.E.Forsyth, Symp on Basic Mech of Fatigue, ASTM 237, 1959
- 46 J.C.Grosskreutz, Phys Stat Sol, 47, 357, 1971
- 47 W.A.Wood, S.Cousland and K.R.Sargent, Acta Met, 11, 643, 1963
- 48 W.D.Dover and W.J.D.Jones, Br J Appl Phys, 18, 1257, 1967
- 49 E.E.Lauffer and N.N.Roberts, Phil Mag, 14, 65, 1966
- 50 P.Lukas, M.Klesnil and J.Kvejci, Phys Stat Sol, 27, 545, 1968
- 51 S.J.Basinski, Z.S.Basinski and A.Howie, Phil Mag, 19, 899, 1969
- 52 A.H.Cottrell and D.Hull, Proc Roy Soc, A 242, 211, 1957
- 53 A.J.Kennedy, Process of Creep and Fatigue of Metals,  
J.Wiley & Sons Inc, N.Y, 331, 1963

- 54 N.F.Mott, Acta Met, 6, 195, 1955
- 55 N.Thompson, Int Conf on Atomic Mech of Fracture,  
J.Wiley & Sons Inc, N.Y, 1959
- 56 A.J.McEvily and E.S.Machlin, Fracture, J.Wiley & Sons Inc, N.Y,  
450, 1959
- 57 P.Neumann, Acta Met, 17, 1219, 1969
- 58 J.B.Clark and A.J.McEvily, Acta Met, 12, 1359, 1964
- 59 C.A.Stubbington, *ibid*, 931, 1964
- 60 J.T.McGrath and W.J.Bratina, *ibid*, 15, 329, 1967
- 61 J.G.Taylor, P.E.Warin and P.Watson, Fracture, 2, 681, 1977
- 62 D.J.Duquette and H.H.Uhlig, Trans ASM, 61, 449, 1968
- 63 D.J.Duquette and H.H.Uhlig, *ibid*, 62, 839, 1969
- 64 A.R.Jack and A.Peterson, The Influence of Env on Fatigue,  
I Mech E, 75, 1977
- 65 T.Hodgekiess, Mech of Env Sensitive Cracking of Materials,  
Metals Soc, 1977
- 66 N.L.Person, Mat Perf, 22, Dec 1975
- 67 U.R.Evans, The Corrosion and Oxidation of Metals,  
Edward Arnold Ltd, London, 360, 1960
- 68 W.G.Johnston, Progress in Ceramic Science, 2, 1962
- 69 W.H.Robinson, Techniques of Metal Research, 2, 291, 1968
- 70 A.H.Cottrell, Dislocations and Plastic Flow of Metals,  
Oxford Univ Press, 1953
- 71 A.J.Forty and G.C.Frank, J of Phys Soc of Japan, 10, 656, 1955
- 72 N.Cabrerra and M.M.Levine, Phil Mag, 1, 450, 1956
- 73 D.Whitwham and U.R.Evans, JISI, 165, 76, 1950
- 74 F.Lihl, Metall, 4, 130, 1950
- 75 H.Spahn, Metalloberflache, 16, 299, 1962
- 76 H.H.Uhlig, Corrosion and Corrosion Control,  
J.Wiley & Sons, N.Y, 100, 1963
- 77 Z.Foroulis and H.H.Uhlig, J Electrochem Soc, 111, 522, 1964
- 78 N.D.Greene and G.A.Salzman, Corrosion, 20, 293 t, 1964
- 79 J.C.Finley and J.R.Myers, Corrosion, 26, 150, 1970

- 80 M.Doruk, *Corr Sci*, 8, 317, 1968
- 81 H.H.Uhlig, *Corrosion Fatigue*, NACE-2, 270, 1972
- 82 R.Revie and H.H.Uhlig, *Corr Sci*, 12, 669, 1972
- 83 R.Revie and H.H.Uhlig, *Acta Met*, 22, 619, 1974
- 84 M.T.Simnad and U.R.Evans, *Proc Roy Soc, A* 188, 372, 1947
- 85 C.Benedicks, *Int Conf on Surface Reactions*, Pittsburg, 196, 1948
- 86 D.Phillips and N.Thompson, *Proc Phys Soc*, 63B, 839, 1950
- 87 S.Harper and A.Cottrell, *ibid*, 331, 1950
- 88 R.Roscoe, *Nature*, 133, 912, 1934
- 89 E.Andrade and R.Randall, *Proc Phys Soc*, 65B, 445, 1952
- 90 I.R.Kramer, *Trans Met Soc AIME*, 221, 989, 1961
- 91 C.Patel, PhD Thesis, Lanchester Polytechnic, Coventry, 1976
- 92 E.A.G.Liddiard, J.A.Whittaker and H.King, *1st Int Conf on Met Corr*, 482, 1961
- 93 T.Broom and A.Nicholson, *JIM*, 89, 183, 1960
- 94 C.Laird and G.C.Smith, *ibid*, 163, 1960
- 95 J.A.Whittaker, *ibid*, 91, 346, 1962
- 96 W.L.Holshouser and J.A.Bennett, *Proc. ASTM*, 62, 683, 1962
- 97 J.A.Bennett, *Acta Met*, 11, 799, 1963
- 98 J.S.Jackson, *Proc of the Int Cong on Fatigue of Metals*, I Mech E, 500, 1956
- 99 D.P.Smith, *Hydrogen in Metals*, Chicago Univ Press, 1947
- 100 C.M.Hudgins, B.M.Casad, R.L.Scroedar and C.C.Paton, *J of Pet Tech*, 23, 283, 1971
- 101 W.H.Hartt, J Fluet and T.Henke, *Offshore Tech Conf*, Paper OTC 2380, 1975
- 102 J.Kochera, J Tralmer and P.Marshall, *ibid*, Paper OTC 2604, 1976
- 103 R.T.Foley, *Corrosion*, 26, 58, 1970
- 104 Z.Szklarska-Smialowska and M.Janik-Czachor, *Corr Sci*, 7, 65, 1967
- 105 W.Schatt and H.Worch, *Corr Sci*, 9, 869, 1969; 11, 623, 1971
- 106 M.Janik-Czachor, *Br Corr J*, 6, 57, 1971
- 107 M.Smialowski, Z.Szklarska-Smialowska, M.Rychoik and A.Szumner, *Corr Sci*, 9, 123, 1969

- 108 G.Wränglen, *Corr Sci*, 9, 585, 1969
- 109 Z.Szklarska-Smialowska, A.Szumner and M.Janik-Czachor,  
*Br Corr J*, 5, 159, 1970
- 110 M.Janik-Czachor, A.Szumner and Z.Szklarska-Smialowska,  
*Br Corr J*, 7, 90, 1972
- 111 Z.Szklarska-Smialowska, *Corrosion*, 28, 388, 1972
- 112 A.Szumner and M.Janik-Czachor, *Br Corr J*, 9, 216, 1974
- 113 G.Wränglen, *Corr Sci*, 14, 331, 1974
- 114 G.R.Wallwork and B.Harris, *Localized Corrosion*, NACE-3, 292,  
1974
- 115 G.Wränglen, *ibid*, 462, 1974
- 116 L.J.Gainer and G.R.Wallwork, *Corrosion*, 35, 435, 1979
- 117 V.Scotto, G.Ventura and E.Traverso, *Corr Sci*, 19, 237, 1979
- 118 N.D.Greene and M.G.Fontana, *Corrosion*, 15, 25 t, 1959
- 119 Z.Szklarska-Smialowska and E.Lunarska, *Werkstoffe und Korrosion*,  
32, 478, 1981
- 120 L.Tronstad and J.Sejersted, *JISI*, 127, 425, 1933
- 121 J.E.Stead, *JISI*, 94, 5, 1916
- 122 M.Stern, *J Electrochem Soc*, 102, 663, 1955
- 123 P.H.Salmon Cox and J.A.Charles, *JISI*, 203, 493, 1965
- 124 H.J.Cleary and N.D.Green, *Corr Sci*, 7, 821, 1967
- 125 Z.A.Foroulis and H.Uhlig, *J Electrochem Soc*, 112, 1177, 1965
- 126 G.Eklund, *Clean Steel*, Rep of the Roy Swedish Academy of Eng Sci,  
1, 152, 1971
- 127 G.Eklund, *Localized Corrosion*, NACE-3, 477, 1974
- 128 R.A.King and D.S.Wakerley, *Br Corr J*, 8, 41, 1973
- 129 R.A.King, J.D.A.Miller and J.S.Smith, *ibid*, 137, 1973
- 130 H.Adrian, *Corr Sci*, 17, 143, 1977
- 131 A.Turnbull, National Physical Laboratory, Teddington, Middx,  
Private Communication
- 132 J.G.Parker, *Br Corr J*, 8, 124, 1973
- 133 P.E.Manning, C.E.Lyman and D.J.Duquette, *Corrosion*, 36, 247, 1980

- 134 N.D.Tomashov, Theory of Corrosion and Protection of Metals, McMillan & Co, N.Y, 1966
- 135 T.P.Hoar and D.Havenhand, JISI, 133, 239, 1936
- 136 Z.A.Foroulis, Corr Sci, 5, 39, 1965
- 137 R.W.Manuel, Corrosion, 3, No. 10, 1947
- 138 U.R.Evans, The Corrosion and Oxidation of Metals, Edward Arnold Ltd, London, 456, 1960
- 139 D.N.Staicopolus, J Electrochem Soc, 11, 1121, 1963
- 140 J.A.S.Green and R.N.Parkins, Corrosion, 24, 66, 1968
- 141 J.Flis, Corr Sci, 10, 745, 1970
- 142 C.J.Cron, J.H.Payer and R.W.Staehle, Corrosion, 27, 1, 1971
- 143 R.L.Chance, Corrosion, 33, 108, 1977
- 144 R.N.Parkins, Proc 8th Int Cong on Met Corr, Mainz, 3, 2181, 1981
- 145 R.N.Parkins, Br Corr J, 14, 5, 1979
- 146 V.Rollins, C.Patel, and T.Pyle, Int Conf on Mech Env, Cracking of Materials, Metals Soc, 367, 390, 1977
- 147 C.Patel, Proc 8th Int Cong on Met Corr, Mainz, 1, 381, 1981
- 148 J.K.Tien, R.J.Richards, O.Buck and H.L.Marcus, Scripta Met, 9, 1097, 1975
- 149 J.Moskovitz and R.M.Pelloux, Proc 2nd Int Conf on Mech, Behaviour of Metals, ASTM, 295, 1976
- 150 R.N.Parkins, Abstract, Conf on Defects and Cracks Initiation in Env Sensitive Cracking, Univ of Newcastle upon Tyne, 1981
- 151 D.J.Lees, Mech of Env Sensitive Cracking of Materials, Metals Soc, 557, 1977
- 152 G.P.Ray and R.A.Jarman, Br Corr J, 15, 226, 1980
- 153 R.A.Cottis and Z.Hussain, Proc 8th Int Cong on Met Corr, Mainz, 467, 1981
- 154 J.Congleton, Univ of Newcastle upon Tyne, Private Communication
- 155 A.D.Mercer and J.G.N.Thomas, 3rd Eur Sym on Corr Inhib, Ferrara, 1970
- 156 J.A. von Fraunhofer and C.H.Banks, Potentiostat and its Applications, 131, 1972, Butterworth & co, London
- 157 N.D.Greene and R.B.Leonard, Electrochem Acta, 9, 45, 1964

- 158 R.Littlewood, *Corr Sci*, 3, 99, 1963
- 159 J.M.West, *Br Corr J*, 5, 65, 1970
- 160 H.P.Leckie, *J Electrochem Soc*, 117, 1152, 1970
- 161 N.D.Greene, *Corrosion*, 18, 136 t, 1962
- 162 I.Dugdale and J.B.Cotton, *Corr Sci*, 3, 239, 1963
- 163 M.Pourbaix, *ibid*, 239, 1963
- 164 M.Pourbaix, *ibid*, 5, 677, 1965
- 165 E.D.Vernik, *Proc 5th Int Conf on Met Corr*, Tokyo, 1972
- 166 D.Gilroy and J.E.O.Mayne, *Br Corr J*, 1, 102, 1965
- 167 P.E.Morris and R.C.Scarberry, *Corrosion*, 28, 444, 1972
- 168 S.Smialowska and M.Czachor, *Localised Corrosion*, NACE-3, 1974
- 169 L.L.Shreir, *Corrosion*, 2, 20:123, 1976, Newnes-Butterworth,  
London
- 170 H.H.Strehblow and B.Titze, *Corr Sci*, 17, 461, 1977
- 171 H.H.Strehblow and J.Wenners, *Z.Physik Chem*, 98, 199, 1975
- 172 J.G.N.Thomas and J.D.Davies, *Br Corr J*, 12, 108, 1977
- 173 M.Pourbaix, *Atlas d'Equilibres Electrochimiques*, 309, 1963  
Ganthier-Villars et Cie, Paris
- 174 J.G.N.Thomas and T.J.Nurse, *Br Corr J*, 2, 13, 1967
- 175 V.Hospadaruk and J.Petrocelli, *J Electrochem Soc*, 13, 878, 1966
- 176 B.E.Wilde, *Corrosion*, 28, 283, 1972
- 177 L.L.Shreir, *Corrosion*, 2, 20:70, 1976, Newnes-Butterworth,  
London
- 178 L.L.Shreir, *ibid*, 1:158
- 179 B.E.Wilde and E.Williams, *J Electrochem Soc*, 117, 775, 1970
- 180 M.Cohen, *Corrosion - 75*, Paper No. 132, 1975, Toronto
- 181 J.L.Leibenguth and M.Cohen, *J Electrochem Soc*, 119, 987, 1972
- 182 K.Hashimoto and M.Cohen, *ibid*, 121, 37, 1974
- 183 G.Eklund, *Scand J Met*, 1, 331, 1972
- 184 T.Lindley, P.McIntyre and P.J.Trant, *Met Tech*, 9, 135, 1982
- 185 H.Warnecke, *M.Sc Thesis*, 1980, City of London Polytechnic

- 186 J.F.Knott, Met Tech, 9, 86, 1982
- 187 W.D.France and N.D.Greene, Corrosion, 24, 247, 1968
- 188 A.Turnbull, National Physical Laboratory, Teddington,  
To be published
- 189 Y.H.Lee, Z Takehara and S.Yoshizawa, Corr Sci, 21, 391, 1981
- 190 A.Peres, Bull Res Council, Israel, 6c (1), 2, 1957
- 191 A.Taub, E.Uygur and S.Dirnfield, Appl Mat Res, 5, 76, 1966
- 192 C.Wagner, Thermodynamics of Alloys, 1952,  
Addison-Wesley Publishing Co, Mass
- 193 M.Paul and H.Weiland, Electrochim Acta, 14, 1025, 1969
- 194 A.H.Cottrell, An Introduction to Metallurgy, 1967,  
Edward Arnold Ltd, London
- 195 R.G.Raicheff, A Damjanovic and J.O'M.Bockris, J Chem Phys,  
47, 2198, 1967
- 196 L.Gainer and H.Wallwork, Rev on Coatings and Corr, III (1),  
49, 1978
- 197 G.P.Ray, Trans Inst of Met Finishing, 56, 168, 1978
- 198 D.A.Porter, K.E.Easterling and G.D.Smith, Mech of Deformation  
and Fracture, 87, 1978, Lulea, Sweden
- 199 L.E.Wood and C.H.Van Vlack, Trans ASM, 56, 771, 1963
- 200 G.P.Ray, Unpublished work
- 201 D.Brooksbank and K.W.Andrews, JISI, 595, June 1968
- 202 G.Sandoz, C.T.Fujii and B.F.Brown, Corr Sci, 10, 839, 1970
- 203 J.M.Barsom, Int J Frac Mech, 7 (e), 163, 1971
- 204 J.G.N.Thomas, National Physical Laboratory, Teddington, Middx,  
Private Communication
- 205 R.Kiesling and H.Nordberg, Clean Steel, Rep of the Roy Swedish  
Academy of Eng Sci, Stockholm, Sweden, 1, 159, 1971
- 206 B.D.Craig, Corrosion, 34, 282, 1978
- 207 P.H.Pumphrey, ibid, 36, 537, 1980
- 208 A.Kawashima, K.Hashimoto and S.Shimodaira, ibid, 32, 321, 1976
- 209 A.Joshi, ibid, 34, 47, 1978
- 210 R.Viswanathan and A.Joshi, Met Trans, 6A, 2289, 1975

- 211 H.Cialone and R.Asaro, *ibid*, 10A, 367, 1979
- 212 A.S.Tetelman, Proc Conf Fund Aspects of Str Corr Cracking,  
NACE, 446, Sept, 1967
- 213 N.A.Tiner, *ibid*, 461, Discussion
- 214 J.K.Tien, R.Richards, O.Buck and H.L.Marcus, Scripta Met,  
9, 1079, 1975
- 215 B.F.Brown, Corrosion Fatigue, NACE-2, 26, 1972
- 216 W.A.Wood, Fracture, Proc 1st Tewksbury Sym, 62,  
Melbourne, Aug, 1963
- 217 A.S.Tetelman and A.J.McEvily, Fracture of Structural Materials,  
357, John Wiley & Sons, Inc, London, 1967
- 218 R.M.Pellour, R.E.Stoltz and J.A.Moskovitz, Mat Sci Eng,  
25, 193, 1976
- 219 J.T.Fourie, Corrosion Fatigue, NACE-2, 164, 1972
- 220 P.Lucas and M.Klesnil, *ibid*, 118, 1972

Attention is drawn to the fact that the copyright of this thesis rests with its author.

This copy of the thesis has been supplied on condition that anyone who consults it is understood to recognise that its copyright rests with its author and that no quotation from the thesis and no information derived from it may be published without the author's prior written consent.

**IV**